A Broadband EPR Spectrometer Using Transmission Line Microwave Probes

Zur Erlangung des akademischen Grades einer

DOKTORIN DER INGENIEURWISSENSCHAFTEN (Dr.-Ing.)

von der KIT-Fakultät für
Elektrotechnik und Informationstechnik
des Karlsruher Instituts für Technologie (KIT)

angenommene

DISSERTATION

von

M.Sc. Selina Eckel
geb. in Heidelberg

Tag der mündlichen Prüfung: 16.03.2026

Hauptreferent: Prof. Dr.-Ing. Ahmet Çağrı Ulusoy
Korreferent: PD Dr. rer. nat. Benno Meier

Zusammenfassung

Die Elektronenspinresonanz-Spektroskopie (EPR) ist eine nichtinvasive Messmethode zur Untersuchung von Proben mit ungepaarten Elektronen. Ihre Anwendungsfelder reichen von Biologie, Chemie und Physik bis hin zu Materialwissenschaften und Medizin und ermöglichen unter anderem Einblicke in Spin-Defekte in Halbleitern, oxidativen Stress sowie Quantenspeicher. In der EPR absorbieren ungepaarte Elektronenspins unter einem extern angelegten Magnetfeld Mikrowellenstrahlung bei Erfüllung der Resonanzbedingung und erlauben damit einen spektroskopischen Zugang zu ihrer lokalen magnetischen Umgebung. Konventionelle EPR-Spektrometer sind schmalbandige, resonatorbasierte Systeme, die typischerweise im Reflexionsbetrieb bei festen Frequenzen betrieben werden, beispielsweise bei 10 GHz, 35 GHz und 94 GHz, während das Magnetfeld zur Erfassung der Resonanz variiert wird. Für komplexe oder bislang unbekannte paramagnetische Systeme liefern Messungen bei nur einer Frequenz jedoch häufig ein unvollständiges Bild. Zur Trennung verschiedener Wechselwirkungen innerhalb der Probe sind daher Messungen bei mehreren Frequenzen erforderlich, was in der Praxis den Einsatz mehrerer großer und teurer Spektrometer voraussetzt. Darüber hinaus lassen sich bestimmte Wechselwirkungen, insbesondere die Nullfeldaufspaltung, nur dann direkt bestimmen, wenn kein äußeres Magnetfeld angelegt wird und stattdessen die Frequenz über einen großen Bereich durchgestimmt werden kann. Dies ist mit schmalbandigen resonatorbasierten Spektrometern nicht möglich. Die Entwicklung eines kompakten und breitbandigen On-Chip Spektrometers würde Messungen bei unterschiedlichen Frequenzen deutlich zugänglicher machen und die EPR-Spektroskopie auf neue Anwendungen sowie Probengeometrien erweitern.

Diese Arbeit untersucht Entwurfsstrategien auf System- und Komponentenebene zur Realisierung eines breitbandigen On-Chip-EPR-Spektrometers. Hierbei wird das Anregungsfeld über eine planare Leitung (TL) anstelle eines Resonators in die Probe eingekoppelt, wodurch ein kontinuierlicher Betrieb

bis 110 GHz möglich wird. Der Verzicht auf einen Resonator führt jedoch typischerweise zu einer geringeren Empfindlichkeit, da die Feldüberhöhung des Mikrowellen-Magnetfeldes entfällt. Zusätzlich ist das schwache EPR-Signal durch das dominante Transmissionssignal überlagert. Diese Herausforderungen sowie allgemeine Anforderungen an breitbandige Mikrowellensysteme werden in dieser Arbeit untersucht und gezielt adressiert.

Auf Systemebene werden drei Detektionsarchitekturen identifiziert, analysiert und demonstriert: Quadratur-Detektion, Interferometrie und Lock-in-Detektion. Der interferometrische Ansatz unterdrückt das Transmissionssignal durch destruktive Interferenz, während es bei der Quadratur-Detektion in der Nachverarbeitung entfernt wird. Für den interferometrischen Aufbau wird ein neuer Algorithmus entwickelt, der Absorption und Dispersion mit weniger Abtastpunkten und kürzerer Messzeit voneinander trennt. Das Lock-in-Verfahren trennt Transmissions- und EPR-Signal im Frequenzbereich und detektiert die Absorption direkt. Dieser Ansatz kombiniert eine hohe Rauschunterdrückung mit den geringsten Anforderungen an die Hochfrequenz-Komponenten. Basierend auf dieser Analyse wird ein vollständiges TL-basiertes EPR-Spektrometer mit Lock-in-Detektion realisiert, das aus kommerziellen Komponenten sowie den in dieser Arbeit entwickelten TL-Koppelstrukturen besteht. Zusätzlich wird ein Post-Processing-Schema entwickelt, um den Einfluss eines unerwünschten Interferenzpfads infolge der Magnetfeldmodulation zu korrigieren. Eine anschließende Rauschanalyse identifiziert das Amplitudenrauschen des Signalgenerators und potentiell das Flicker-Rauschen des Detektors als dominierende Rauschquellen. Der Vergleich mit einem High-End-EPR-Spektrometer auf Resonatorbasis zeigt die wesentlichen Unterschiede zum hier entwickelten TL-Ansatz. Beim Betrieb beider Spektrometer kurz vor Erreichen der Sättigung der Probe ist die höhere Empfindlichkeit des Resonatorsystems hauptsächlich auf Unterschiede im Rauschverhalten sowie auf die räumliche Überlappung zwischen Mikrowellen-Magnetfeld und Probenvolumen zurückzuführen. Durch On-Chip-Integration und verbesserte Schaltungsarchitekturen wird erwartet, dass Verluste und Rauschen reduziert werden können, um die Empfindlichkeit zu erhöhen.

Auf Komponentenebene werden TL-Koppelstrukturen und integrierte Schaltungen entwickelt, um Magnetfeldstärke, Feldhomogenität sowie die breitbandige Signalverstärkung und -detektion zu optimieren. Elektromagnetische Simulationen und Experimente liefern Entwurfsrichtlinien für

koplanare Wellenleiter (CPW) und Mikrostreifenleitungen (MSL), die auf die Maximierung der Mikrowellen-Magnetfeldstärke abzielen. Von den beiden Konfigurationen bietet die CPW-Geometrie die höhere Magnetfeldstärke. Darüber hinaus wird eine invertierte Mikrostreifenleitung untersucht und entwickelt, die im Vergleich zu CPW- sowie konventionellen MSL-Geometrien eine homogenere Feldverteilung im probenzugänglichen Bereich ermöglicht. Zwei breitbandige integrierte Schaltungsbausteine werden in Silizium-Germanium-Bipolar-CMOS-(SiGe-BiCMOS-)Technologie realisiert: ein Verstärker sowie zwei Varianten eines Detektors. Der zweistufige, diskrete Verstärker wird auf einer kompakten Core-Fläche von $0.007\,\mathrm{mm}^2$ implementiert und erreicht eine 3 dB-Bandbreite von 60 GHz sowie eine gesättigte Ausgangsleistung von 10 dBm. Es werden ein diskreter Detektor sowie ein verteilter, zehnstufiger Detektor entwickelt. Im Vergleich zum diskreten Detektor weist der verteilte Detektor sowohl eine höhere Bandbreite als auch eine höhere Sensitivität auf. Der verteilte Detektor erreicht einen Eingangsreflexionskoeffizienten unter $-10\,\mathrm{dB}$ bis zu einer Frequenz von 110 GHz bei rauschäquivalenten Leistungen zwischen $1.8\,\mathrm{pW}/\sqrt{\mathrm{Hz}}$ und $4.8\,\mathrm{pW}/\sqrt{\mathrm{Hz}}$. Diese Ergebnisse übertreffen den kommerziellen diodenbasierten Detektor, der in dem oben beschriebenen TL-basierten EPR-Spektrometer verwendet wird, um Faktoren von 1.1 bis 2.6 innerhalb dessen Betriebsbandbreite von 50 GHz und erweitern die nutzbare Bandbreite um mehr als einen Faktor zwei. Der rauschäquivalente Modulationsindex wird als neue Kenngröße eingeführt, welche die Detektor-Performance direkt mit den Anforderungen der EPR-Detektion verknüpft.

Die in dieser Arbeit entwickelten Architekturen, Koppelstrukturen und integrierten Komponenten bilden die Grundlage für breitbandige On-Chip-EPR-Spektrometer. Das realisierte Spektrometer ergänzt bestehende resonatorbasierte Instrumente, indem es breitbandige EPR-Messungen ermöglicht und damit direkte Messungen der Nullfeldaufspaltung erlaubt. Darüber hinaus erlaubt der On-Chip-Ansatz Untersuchungen planarer Bauelemente wie Solarzellen und Batterien. Insgesamt leistet diese Arbeit einen wesentlichen Beitrag zur Realisierung kompakter und vielseitiger EPR-Spektrometer und erweitert das Anwendungsspektrum magnetresonanzbasierter Verfahren.

Abstract

Electron paramagnetic resonance (EPR) spectroscopy is a noninvasive technique for studying systems containing unpaired electrons. Its applications span biology, chemistry, physics, materials science, and medicine, enabling insights into spin defects in semiconductors, oxidative stress, and quantum memory. In EPR, unpaired electron spins absorb microwave radiation at resonance under an externally applied static magnetic field, providing spectroscopic access to their local magnetic environment. Conventional EPR spectrometers are narrowband resonator-based instruments operated in reflection mode at fixed frequencies, typically at 10 GHz, 35 GHz, and 94 GHz, while the magnetic field is swept across the resonance. For complex or unknown paramagnetic systems, single frequency measurements often provide an incomplete picture. Multifrequency EPR is required to disentangle field-dependent and field-independent interactions, but performing such measurements typically demands multiple bulky and expensive instruments. Moreover, certain interactions such as the zero-field splitting can be directly determined only when no external magnetic field is applied and the frequency is swept over a wide range, which is not possible with narrowband resonator-based spectrometers. Developing a compact and broadband on-chip spectrometer would make multi-frequency EPR more accessible and would extend the EPR technique to new applications and sample geometries.

This thesis investigates system- and component-level design strategies toward a broadband on-chip EPR spectrometer. Instead of a resonator, a transmission line (TL) microwave probe couples the excitation field into the sample, enabling operation across a continuous frequency range targeting up to 110 GHz. However, because it does not benefit from resonator-like magnetic field build-up, this approach generally exhibits reduced sensitivity compared to resonator-based spectrometers. In addition, the weak EPR response appears as a small variation superimposed on a large transmission signal. These challenges and the

broader requirements of broadband microwave system design are investigated and addressed throughout this thesis.

At the system level, three detection architectures are identified, analyzed and demonstrated: quadrature, interferometric, and lock-in detection. The interferometric approach suppresses the transmitted signal by destructive interference, while quadrature detection removes it in post-processing. For the interferometric setup, a new post-processing algorithm is developed that separates absorption and dispersion with fewer sampling points and shorter measurement time. The lock-in scheme separates the transmission and EPR signals in the frequency domain and directly detects absorption, combining conceptual simplicity with strong noise rejection and relaxed requirements for the millimeter-wave components. Based on this analysis, a complete TL-based EPR spectrometer employing lock-in detection is realized using commercial components and custom TL microwave probes. An automated post-processing scheme is developed to remove the effect of an unwanted interference path caused by magnetic field modulation. A subsequent noise analysis identifies amplitude noise from the signal generator and potentially flicker noise from the detector as the dominant contributions at higher input powers. Comparison with a high-end commercial resonator-based EPR spectrometer reveals the principal differences to the custom-developed TL-based approach. When operating both spectrometers shortly before the onset of saturation, the higher sensitivity of the resonator-based spectrometer is attributed primarily to differences in the effective noise contributions and to the spatial overlap between the microwave magnetic field and the sample volume. On-chip integration and advanced circuit architectures are expected to minimize losses and reduce noise, enhancing the sensitivity.

At the component level, TL microwave probes and integrated circuits are developed to enhance magnetic field strength, field homogeneity, and broadband signal amplification and detection. Electromagnetic simulations and experiments establish design guidelines for coplanar waveguide (CPW) and microstrip line (MSL) configurations aimed at maximizing the microwave magnetic field strength. Between the two configurations, the CPW geometry provides the higher field amplitude. In addition, an inverted microstrip line probe has been developed, offering a more homogeneous field distribution in the region accessible to the sample compared to both CPW and conventional MSL designs. Two integrated broadband building blocks are implemented in

silicon–germanium (SiGe) bipolar complementary metal-oxide-semiconductor (BiCMOS) technology: an amplifier and two detector architectures. The two-stage lumped amplifier is realized with a compact core area of 0.007 mm^2 and achieves a 3 dB bandwidth of 60 GHz as well as a saturated output power of 10 dBm. A lumped detector and a ten-stage distributed detector are designed. Compared to the lumped detector, the distributed implementation exhibits both a higher bandwidth and a higher sensitivity. The distributed detector achieves an input reflection coefficient below −10 dB up to 110 GHz, with noise-equivalent power values between 1.8 $pW/\sqrt{Hz}$ and 4.8 $pW/\sqrt{Hz}$. These results exceed those of the commercial diode-based detector employed in the TL-based EPR spectrometer by factors of 1.1 to 2.6 across its 50 GHz operating range and extend the operational bandwidth by more than a factor of two. The noise-equivalent modulation index is introduced as a new figure of merit that directly links device-level performance to EPR detection requirements.

The developed architectures, probe designs, and integrated components establish the conceptual and technological foundation for broadband on-chip EPR spectroscopy. The realized system complements existing resonator-based instruments and extends EPR capabilities to broadband operation, enabling direct zero-field splitting measurements and on-chip studies of flat, planar devices such as solar cells and batteries. By combining broadband performance with on-chip realization, this thesis takes a decisive step toward compact and versatile EPR spectrometers that enrich the magnetic resonance toolkit across disciplines.

Acknowledgment

During my PhD journey, I had the privilege of meeting remarkable people. This acknowledgment is for all of you who accompanied me and made these years unforgettable. I am sincerely grateful.

First and foremost, I would like to thank my professor and thesis advisor, Prof. Dr.-Ing. Ahmet Çağrı Ulusoy, for giving me the opportunity to pursue my PhD at IHE. I am grateful for the collegial nature of our discussions and for his valuable guidance. I deeply appreciate his continuous support for my endeavors and the flexibility he offered, which gave me room to grow into an independent researcher. I also thank Dr. Benno Meier for serving as my co-supervisor. His support was decisive at the very beginning of my magnetic resonance journey and again toward its end, providing valuable feedback on this manuscript.

Max, Daniel, Axel, David, Kateryna, and Matthias, thank you for your valuable feedback on this thesis. I especially appreciated your detailed and critical comments and the time you invested in understanding my work and pointing out where my arguments were unclear.

Matthias and Daniel, thank you for the great time establishing and teaching the exercise sessions for the electronic circuits lecture. It was a privilege working with you, and our mutual support went far beyond the course itself. Thomas H., Kateryna, Tsung-Ching, and Tai-Yu, thank you for the many inspiring discussions and for broadening my perspective, both technically and on a personal and societal level. Thank you, Christian, Joachim, and Marius, for getting me started in the mmW lab. Together with Alex Q., Luca, and Elizabeth you supported me with your expertise and many helpful discussions on circuit design and packaging related topics. Ibrahim, Alex H., Jerome, Binh, Zahra, and Hans thank you for sharing not just an office, but also the many moments along the way, filled with interesting conversations and many enjoyable times together. I also thank the entire circuit design group for the great atmosphere, the stimulating technical discussions, and the many fun moments at IHE and

outside. I would also like to thank Lina, Nikol, Jonas, Julian, Mathias T., and Matthias B. for their valuable support and contributions. Supervising you was highly rewarding and helped me see many topics with fresh clarity. Simone, Marion, and Angela, thank you for your patience with my urgent purchase requests and my sometimes complex travel arrangements, you made my daily work significantly easier. Finally, I would like to thank Thorsten, Andreas L., Andreas G., and Mirko for their hands-on support and their expertise in manufacturing and assembling components for my experimental work. Overall, IHE became a very special place to me because of its international spirit, its openness, and the genuine connections I was fortunate to build along the way.

Outside of IHE, I am grateful for the opportunities the CRC HyPERiON provided, especially the inspiring summer schools, the stimulating collaborations, and the supportive environment that enabled me to grow. I further want to express my gratitude to the international magnetic resonance community, where I felt genuinely welcomed by its openness and supportive atmosphere. I would especially like to thank the Britt lab at UC Davis and the Avalos lab at New York University for hosting me during my research stays. I learned a great deal about chemistry, spectroscopy, and the breadth of EPR experimentation. I also thank Daria from the Bittl lab at the Free University Berlin, Mirjam and Florian from the Corzilius lab at the University of Rostock, and Veronica from the National Institute of Standards and Technology for inviting me to their laboratories and for providing valuable feedback on my work.

Am Ende gilt mein Dank meiner Familie. Meine Eltern, ihr habt mir unzählige Möglichkeiten eröffnet und mich immer darin bestärkt, meinen eigenen Weg zu gehen. Mit eurer bedingungslosen Unterstützung, eurer Großzügigkeit und eurem Vertrauen habt ihr mir diesen Weg ermöglicht. Meinem Bruder Fabio, dir danke ich für deine ansteckende Leichtigkeit und dafür, dass du mich kritisch hinterfragst und gleichzeitig bestärkst. Meinem Mann David danke ich dafür, dass du mich durch alle Höhen und Tiefen dieser Zeit getragen und mir dabei immer wieder ein Lachen entlockt hast. Du inspirierst mich, lässt mich über mich hinauswachsen und bist die Quelle meiner Energie. Ich danke euch von Herzen für eure Liebe und euren Rückhalt. Ich bin unendlich dankbar, euch an meiner Seite zu haben.

Karlsruhe, April 2026

Selina Eckel

Contents

Acronyms and Symbols

Acronyms

AC	alternating current
AM	amplitude-modulated
BiCMOS	bipolar CMOS
BJT	bipolar junction transistor
BNC	Bayonet Neill–Concelman
CB	common-base
CE	common-emitter
CMOS	complementary metal-oxide-semiconductor
CPW	coplanar waveguide
CW	continuous wave
DC	direct current
DUT	device under test
EF	emitter follower
EM	electromagnetic
EPR	electron paramagnetic resonance
FMR	ferromagnetic resonance

FoM	figure of merit
FWHM	full-width at half-maximum
GaAs	gallium–arsenide
GPIB	general purpose interface bus
HBT	heterojunction bipolar transistor
IHE	Institute of Radio Frequency Engineering and Electronics
IQ	in-phase quadrature
IF	intermediate frequency
IHP	Leibniz Institute for High Performance Microelectronics
IMSL	inverted microstrip line
KIT	Karlsruhe Institute of Technology
LAN	local area network
LIA	lock-in amplifier
LNF	low noise filter
LO	local oscillator
MIM	metal-insulator-metal
mmW	millimeter-wave
MSL	microstrip line
MW	microwave
NEM	noise-equivalent modulation index
NEP	noise-equivalent power
PC	personal computer

PCB	printed circuit board
PSD	power spectral density
RF	radio frequency
RMS	root-mean square
SCPI	standard commands for programmable instruments
SG	signal generator
SiGe	silicon–germanium
SMB	SubMiniature version B
SMU	source measure unit
SNR	signal-to-noise ratio
TE	transverse electric
TEM	transverse electromagnetic
TL	transmission line
TM	transverse magnetic
VBIC	vertical bipolar intercompany
VCO	voltage controlled oscillator
VNA	vector network analyzer
ZFS	zero-field splitting

Constants

g_e	free electron g-factor: 2.002 319
h	Planck constant: $6.626\,070\,15 \times 10^{-34}$ Js

k_B	Boltzmann constant: $1.380\,649 \times 10^{-23}\,JK^{-1}$
μ_B	Bohr magneton: $9.274\,010\,078\,3 \times 10^{-24}\,JT^{-1}$
μ_0	vacuum permeability: $1.256\,637\,061\,3 \times 10^{-6}\,NA^{-2}$
π	pi: 3.14159 . . .

Frequently Used Latin Symbols

$\vec{B}_0$	external static magnetic field
$B_{0,r}$	EPR resonance magnetic field
$\vec{B}_1$	microwave magnetic field
B_m	modulated magnetic field strength
f_0	carrier frequency
$f_{0,r}$	EPR resonance frequency
f_m	modulation frequency
f_{max}	maximum oscillation frequency
f_T	unity current gain cut-off frequency
g_m	transconductance
$\hat{H}$	spin Hamiltonian
I_b	base current
I_c	collector current
k_A	effective magnetic field strength
L	inductance
m	modulation index
$\vec{M}$	magnetization

N_x	number of transistor fingers
P_0	input power
P_{abs}	total absorbed power
P_{dc}	DC power consumption
Q	quality factor
$\mathcal{R}$	detector responsivity
S_{xx}	scattering parameter
S	electron-spin quantum number
T	temperature
V_{be}	base emitter voltage
V_{ce}	collector emitter voltage
$v_{d,dc}$	detected output voltage at direct current
$v_{d,fm}$	detected output voltage at the modulation frequency
V_{EPR}	peak EPR voltage amplitude
v_n	noise voltage spectral density
V_n	RMS noise voltage
V_T	thermal voltage
Y	admittance parameter
Z_0	characteristic impedance

Frequently Used Greek Symbols

ε_r	dielectric constant
η	filling factor

μ_{m}	magnetic moment
μ	mean value
σ	variance
τ	time constant of lock-in amplifier
χ	complex magnetic susceptibility

1 Introduction

1.1 Motivation

Electron paramagnetic resonance (EPR) spectroscopy is a non-invasive technique that allows the study of samples containing unpaired electrons. Such paramagnetic species occur in many contexts, making EPR valuable across biology, chemistry, physics, material science, and medicine [CCM16].

EPR has played an important role in understanding fundamental biological processes. For example, it contributed to clarifying the mechanism of photosynthesis [WB07]. In medicine, EPR enables the direct detection of free radicals that are implicated in premature cell aging and a variety of diseases [AL19]. It has been applied to the diagnosis of melanoma, which is a specific type of skin cancer [ZCP19], to the study of oxidative stress [KCD+06], and to non-invasive oxygen monitoring relevant for radiation therapy and wound healing [MMS+05, VSZK00, JNL+96]. In material science, EPR provides insight into point defects in semiconductors such as silicon and silicon carbide [Lee76, IUM+08], and into defects in organic materials [Bar03]. Applications in studying chemical processes, such as catalysis, often involve systems containing metals in multiple oxidation states [EEBW10]. Industrial use cases include dosimetry for radiation-sterilized materials and quality control in food and pharmaceuticals, for example monitoring the shelf life stability of beer, the rancidity of vegetable oils, or the oxidation of drug excipients [EEBW10]. More recently, EPR has found applications in quantum information science, where it is used to manipulate and control spin qubits such as nitrogen-vacancy centers in diamond [OIH+23].

To enable all these applications, EPR spectroscopy exploits the absorption of microwave radiation by unpaired electron spins in an external magnetic field. This absorption originates from transitions between electron spin states, which are driven by the oscillating microwave magnetic field. In most spectrometers,

the microwave frequency is fixed to a single operating band while the magnetic field is swept to record an EPR spectrum. The most widely used instruments operate around 10 GHz, which falls within the X-band (8 GHz bis 12 GHz) as defined in IEEE Std 521-1984. However, for complex paramagnetic systems, measurements at a single frequency are often not sufficient. In such cases, multi-frequency EPR is required to gain a more complete and unambiguous picture of the underlying interactions [Mis11].

Often, at least three different frequencies are needed to extract full information about the interactions of a paramagnetic ion with its environment [Mis11]. The complementary advantages of low and high frequencies are the following: Low frequencies are suitable for probing field-independent parameters such as hyperfine coupling and zero-field splitting, while high frequencies enable accurate determination of field-dependent parameters such as the electron Zeeman tensor (g-tensor) [BC93]. Combining multiple frequency bands therefore helps to distinguish between the different contributions to the spectrum and enables a more reliable determination of spin-Hamiltonian parameters (see Section 1.2). Moreover, multi-frequency measurements can help to separate overlapping spectra of multiple paramagnetic species and to identify dominant relaxation mechanisms [Mis11].

To make use of the advantages of multi-frequency EPR, several single-frequency spectrometers, which are already commercially available, are needed. Their advantage is that they often achieve high sensitivity by employing resonant microwave probes that couple the microwave power efficiently into the sample. However, these spectrometers are typically bulky and expensive, and only a few research groups can afford to operate multiple systems across different frequency bands. Therefore, a single spectrometer capable of operating over multiple frequency ranges would make multi-frequency EPR spectroscopy far more accessible to the wider research community.

Even if multiple spectrometers are available, certain information cannot be obtained with conventional resonator-based approaches. A prominent example is the determination of zero-field splitting (ZFS) parameters in systems such as gadolinium, a paramagnetic compound widely used as a contrast agent in magnetic resonance imaging. Since the free ion is toxic, gadolinium must be chelated. However, limited chelate stability under certain conditions motivates ongoing safety investigations, which often employ EPR spectroscopy as an analytical tool [PDM+25]. ZFS denotes an interaction that is already present

in the absence of an applied external magnetic field (see Section 1.2). To directly measure it, the excitation frequency rather than the magnetic field must be swept. However, resonant narrowband spectrometers do not allow such frequency sweeps. A spectrometer with wide frequency tunability is therefore required [BS83].

Broadband EPR spectrometers are typically based on non-resonant microwave probes. Compared to resonators, their main disadvantage is the absence of magnetic field enhancement due to energy storage, such that achieving a given excitation field strength typically requires higher input power and generally results in reduced sensitivity. Resonator-based spectrometers, on the other hand, provide strong field enhancement but their physical dimensions scale with the operating frequency. At low frequencies, the resonator becomes larger, enabling the use of larger sample volumes, which can be advantageous for concentration-limited samples. At higher frequencies, the resonator volume decreases, which is generally better suited for mass-limited applications where only small sample amounts are available. At the same time, resonator-based spectrometers impose practical constraints, such as the need for different cavities and sample holders at different frequencies, and time-consuming cavity changes in cryogenic experiments [Mis11]. By contrast, non-resonant probes do not inherently suffer from these practical limitations and geometric constraints, making them attractive for broadband applications where a wide frequency range must be covered with a single probe.

To mitigate the sensitivity limitations of a non-resonant microwave probe approach, an integrated on-chip implementation offers additional opportunities for improvement. By co-designing all components on a single chip, conventional $50\,\Omega$ matching can be avoided, interconnect losses minimized, and overall power consumption reduced [AL19]. Integration also naturally leads to planar non-resonant microwave probes, which enable more straightforward studies of materials with flat geometries such as solar cells, batteries, or microfluidic systems. These types of samples are often difficult to investigate using conventional cavity-based EPR. The measurement typically requires the sample to be contained in a cylindrical glass or quartz tube that is inserted into the cavity, which is impractical for flat devices and planar geometries. In addition, non-resonant structures are not as restricted in size, since their properties do not depend directly on geometric dimensions as in on-chip resonant structures based on inductors and capacitors, where the inductor size must be adjusted

according to the operating frequency. This allows for more flexible microwave probe geometries that can be adapted to different sample shapes and volumes. Integration and planarization therefore not only promise more compact and affordable systems, but also extend the applicability of EPR to new classes of samples and experimental configurations.

Building on these considerations, this work investigates system- and component-level design approaches toward the realization of a broadband on-chip EPR spectrometer. A planar transmission line (TL) is employed as the non-resonant microwave probe, combining broadband operation with on-chip integrability. At the system level, the focus lies on identifying, comparing, and optimizing TL-based EPR architectures, improving signal processing, and analyzing the main noise limitations that determine overall sensitivity. At the component level, various TL types are explored as the microwave probes, focusing on maximizing coupling efficiency and achieving a uniform sample excitation. In addition, integrated circuit components are investigated to enhance sensitivity, support broadband operation, and further miniaturize the EPR spectrometer.

The next section introduces the fundamentals of EPR spectroscopy that form the basis for the concepts and design strategies developed in this thesis. Building on this foundation, the subsequent review places the present work into context by discussing advances in broadband spectrometers on the one hand, and integrated on-chip EPR spectrometers on the other.

1.2 Fundamentals of EPR Spectroscopy

In this section, the aim is to establish the theoretical background, outline the conventional measurement setup, and highlight the role of experimental parameters, thereby preparing the ground for developing broadband EPR spectrometers.

1.2.1 Theoretical Framework

EPR spectroscopy can be described from two complementary perspectives: a quantum mechanical view that focuses on the interactions of individual spins

and a classical view that treats the collective magnetization of an ensemble of spins. This section introduces both perspectives.

Quantum Mechanical Description of EPR

The objective of this section is to establish the quantum mechanical foundation of EPR spectroscopy. Understanding how magnetic interactions within a spin system give rise to discrete energy levels allows one to interpret EPR spectra, relate resonance conditions to physical parameters, and appreciate the advantages of broadband operation, where different interactions respond differently to magnetic field and frequency.

Throughout this section, matrices and vectors are denoted in **bold** font (e.g. $\mathbf{B_0}, \mathbf{g}, \mathbf{A}$), while operators are indicated by a hat symbol (e.g. $\hat{H}, \hat{S}, \hat{I}$). Scalar quantities are written in standard *italic* font.

A paramagnetic sample contains one or more unpaired electrons surrounded by atomic nuclei. Both electrons and nuclei possess a magnetic moment associated with the quantum mechanical property of spin. The combined system of interacting magnetic moments constitutes a spin system. Within this system, the spins interact with each other and are influenced by an external magnetic field, giving rise to a set of discrete energy levels that reflect the quantized nature of angular momentum in quantum mechanics [GS18].

These magnetic interactions can be described in a compact and general form by the spin Hamiltonian $\hat{H}$, which represents the total magnetic energy of the system. In a matrix representation, each matrix element corresponds to the interaction energy between spin states, and diagonalization of the Hamiltonian yields the energy eigenvalues corresponding to the quantized energy levels. These levels determine the conditions under which transitions between spin states can be induced by an oscillating magnetic field, giving rise to the EPR phenomenon [WB07].

For a general spin system consisting of one or more electron spins and surrounding nuclear spins, the spin Hamiltonian can be written as

$$\hat{H} = \hat{H}_{\mathrm{EZ}} + \hat{H}_{\mathrm{NZ}} + \hat{H}_{\mathrm{HF}} + \hat{H}_{\mathrm{NQ}} + \hat{H}_{\mathrm{NN}} + \hat{H}_{\mathrm{ZFS}}, \tag{1.1}$$

where the terms correspond to the electron Zeeman (EZ), nuclear Zeeman (NZ), hyperfine (HF), nuclear quadrupole (NQ), nuclear–nuclear (NN), and zero-filed splitting (ZFS) interactions, respectively [Poo96, RS18].

Each of these interactions contributes to the overall energy-level structure of the spin system and thus influences the position, intensity, and shape of the observed EPR spectra. Since not all interactions are relevant for every spin system, the focus is placed on the electron Zeeman, hyperfine and zero-field splitting interactions, which are common and provide a representative framework to illustrate the advantages of broadband EPR spectroscopy.

Electron Zeeman Interaction

The electron Zeeman interaction describes the coupling of one or more unpaired electron spins to an external magnetic field $\mathbf{B}$. Its Hamiltonian is written as

$$\hat{H}_{\mathrm{EZ}} = -\boldsymbol{\mu}_{\mathbf{m}} \cdot \mathbf{B} = \mu_{\mathrm{B}} \mathbf{B} \cdot \mathbf{g} \cdot \hat{\mathbf{S}}, \tag{1.2}$$

where $\boldsymbol{\mu}_{\mathbf{m}}$ is the magnetic moment of the electron spin, μ_{B} is the Bohr magneton, $\mathbf{g}$ is the $\mathbf{g}$-tensor, and $\hat{\mathbf{S}} = \left(\hat{S}_x, \hat{S}_y, \hat{S}_z\right)$ is the spin operator in units of $\hbar$. The $\mathbf{g}$-tensor relates the applied magnetic field to the electron's energy splitting and reflects how the local electronic structure modifies this splitting compared to an isolated electron ($g_e = 2.002319$). The spin operator corresponds to the quantum-mechanical representation of the spin angular momentum $\mathbf{S}$, whose magnitude is determined by the electron-spin quantum number $S = n/2$, with n being the number of unpaired electrons. Each spin state is specified by the spin projection quantum number m_S, which labels the possible orientations of $\hat{\mathbf{S}}$ along the external field axis. The allowed values of m_S range from $-S$ to $+S$ in integer steps, resulting in a total of $2S + 1$ distinct spin states [GS18].

For the analysis of the electron Zeeman interaction, the following simplifying assumptions are made:

- The system is restricted to a single unpaired electron: $S = 1/2$
- The external magnetic field is applied along the z-axis: $\mathbf{B} = (0, 0, B_0)$
- The electronic environment is assumed such that the electron Zeeman interaction is orientation-independent and the $\mathbf{g}$-tensor can be fully described by a scalar: g

Under these conditions, the Hamiltonian simplifies to

$$\hat{H}_{\mathrm{EZ}} = \mu_{\mathrm{B}} B_0 g \hat{S}_z. \tag{1.3}$$

To determine the corresponding energy levels, the Hamiltonian is represented in matrix form in the basis of the spin projection quantum numbers $m_S = \pm 1/2$. In this basis, the operator $\hat{S}_z$ is given by

$$\hat{S}_z = \frac{1}{2}\begin{pmatrix} 1 & 0 \\ 0 & -1 \end{pmatrix}, \tag{1.4}$$

Substituting this into the Hamiltonian yields

$$\hat{H}_{\mathrm{EZ}} = \begin{pmatrix} \frac{1}{2}\mu_{\mathrm{B}} g B_0 & 0 \\ 0 & -\frac{1}{2}\mu_{\mathrm{B}} g B_0 \end{pmatrix}. \tag{1.5}$$

Since the Hamiltonian is already diagonal, the eigenvalues can be read directly and correspond to the energy levels of the system [GS18]:

$$E = \pm\frac{1}{2}\mu_{\mathrm{B}} g B_0. \tag{1.6}$$

These levels are depicted in Fig. 1.1a, illustrating their linear dependence on the external magnetic field B_0.

The energy difference between the two spin states is

$$\Delta E = \mu_{\mathrm{B}} g B_0, \tag{1.7}$$

which defines the resonance condition in EPR spectroscopy [GS18]. To induce a transition between the spin states which leads to a measurable absorption, electromagnetic radiation can be applied. Two conditions have to be met so that a spin transition happens. First, the photon energy

$$E_{\mathrm{ph}} = h f_0, \tag{1.8}$$

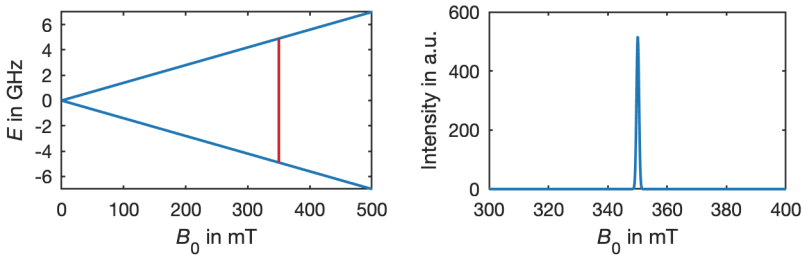

Figure 1.1: EPR simulations using EasySpin [SS06] illustrating the electron Zeeman interaction. (a) Energy-level diagram, with the red vertical line indicating the allowed transition for $f_{0,\mathrm{r}} = 9.8\,\mathrm{GHz}$ and $g = g_\mathrm{e}$. (b) Corresponding absorption spectrum.

where h is Planck's constant and f_0 is the microwave frequency, must be equal to the energy difference ΔE. This leads to the resonance condition

$$f_{0,\mathrm{r}} = \frac{\mu_\mathrm{B} g}{h} B_{0,\mathrm{r}}. \tag{1.9}$$

As follows from the Zeeman splitting, increasing B_0 increases ΔE and therefore the thermal population difference between the spin states, which typically leads to a stronger EPR signal at higher resonance frequencies.

The second condition is that the microwave magnetic field $\mathbf{B_1}$ must have a component perpendicular to the external field B_0, since only this component can induce transitions between the energy levels. If both conditions are met, an EPR signal can be observed [WB07].

As an example, for a resonance frequency of $f_{0,\mathrm{r}} = 9.8\,\mathrm{GHz}$ and the free electron g-factor g_e, the corresponding resonance field is $B_{0,\mathrm{r}} \approx 350\,\mathrm{mT}$. In a system containing only one unpaired electron, g_e corresponds to the intrinsic g-factor of a free electron, which is defined in the absence of interactions with its environment. In the energy level diagram shown in Fig. 1.1a, the allowed transition under this resonance condition is indicated by a red vertical line. The y-axis is expressed in frequency units, with the energy levels given by $E = \pm\frac{1}{2}\mu_\mathrm{B} g B_0/h$, which allows the resonance frequency to be directly extracted from the level splitting. The resulting absorption spectrum, displayed

in Fig. 1.1b, exhibits a single line at $B_{0,\mathrm{r}} \approx 350\,\mathrm{mT}$. The spectrum amplitude is given in arbitrary units, since the plotted intensity represents the simulated (relative) microwave absorption signal and its absolute scaling depends on factors such as sample amount as well as experimental and instrumental factors. Both the energy-level diagram and the corresponding spectrum are simulated using the software EasySpin [SS06].

In the general case, the **g**-tensor is a 3×3 matrix, and the electron Zeeman interaction depends on the orientation of the magnetic field **B** relative to the principal axes of **g**. This orientation dependence gives rise to anisotropy of the Zeeman splitting and therefore to direction-dependent resonance fields. In the principal axis frame **g** is diagonal and its principal values are denoted g_x, g_y, and g_z [CCM16].

Three symmetry cases of the **g**-tensor are commonly distinguished:

- Isotropic: $g_x = g_y = g_z = g_{\mathrm{iso}}$
- Axial: two principal values are equal, e.g., $g_x = g_y \neq g_z$
- Rhombic: all three values differ, $g_x \neq g_y \neq g_z$

The effects of g-anisotropy on EPR spectra for samples in the solid and liquid state are discussed below. In the isotropic case, the spectra of solid and liquid samples are identical and correspond to the absorption line already shown in Fig. 1.1b.

In the rhombic case, the spectrum of a solid is broadened, since different orientations contribute differently to the resonance field. For example, with $g_x = 1.8$, $g_y = 1.9$, and $g_z = 2.0$, the solid-state spectrum shown in Fig. 1.2a extends over a wider range of fields. Because the resonance field B_0 is inversely proportional to the g-factor, the smallest g-value corresponds to the high-field shoulder at approximately $B_0 = 390\,\mathrm{mT}$.

In liquid samples of small, rapidly tumbling molecules, molecular reorientation averages over all directions of the **g**-tensor on the timescale of the measurement. This leads to an effective isotropic g-value, calculated as

$$g_{\mathrm{iso}} = \frac{g_x + g_y + g_z}{3}, \tag{1.10}$$

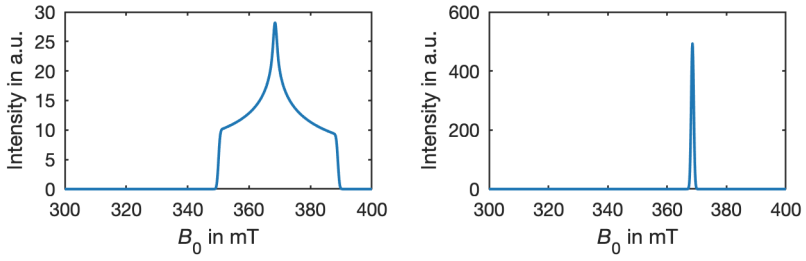

Figure 1.2: EPR simulations using EasySpin [SS06] illustrating the effect of a rhombic **g**-tensor of (a) a solid, and (b) a liquid.

which results in a single, sharp resonance line at the corresponding field position, as shown in Fig. 1.2b.

Hyperfine Interaction

The hyperfine interaction arises from the coupling between the magnetic dipole moment of unpaired electrons and that of nearby nuclei. Its contribution to the spin Hamiltonian is expressed as

$$\hat{H}_{\mathrm{HF}} = \hat{S}\mathbf{A}\hat{I}, \tag{1.11}$$

where $\hat{I}$ is the nuclear spin operator, and $\mathbf{A}$ is the hyperfine coupling tensor [RS18].

To illustrate, consider the previously described electron spin system extended by a single nucleus with $I = 1/2$ and an isotropic hyperfine constant of $A = 20\,\mathrm{mT}$. In this case, each electron spin state splits into two sublevels, resulting in four distinct energy levels, as shown in Fig. 1.3a. From highest to lowest energy, these correspond to the states $(m_S = +1/2, m_I = +1/2)$, $(m_S = +1/2, m_I = -1/2)$, $(m_S = -1/2, m_I = -1/2)$, and $(m_S = -1/2, m_I = +1/2)$. The resulting absorption spectrum is shown in Fig. 1.3b and exhibits two resonance lines separated by $A = 20\,\mathrm{mT}$. These lines are symmetrically positioned around $B_0 = 350\,\mathrm{mT}$ for a resonance frequency of $f_{0,\mathrm{r}} = 9.8\,\mathrm{GHz}$. The hyperfine interaction itself is independent of the external magnetic field. However, the

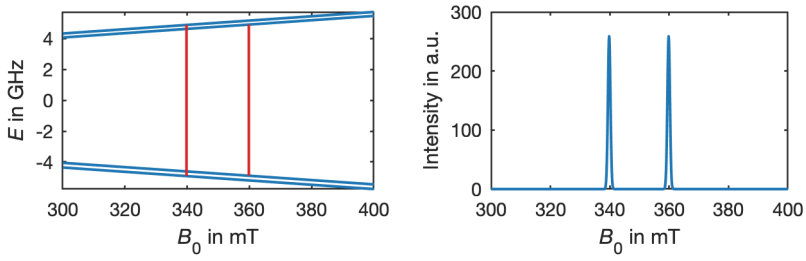

(a) (b)

Figure 1.3: EPR simulations using EasySpin [SS06] illustrating the hyperfine interaction. (a) Energy-level diagram, with the two red vertical lines indicating the allowed transitions for $f_{0,\mathrm{r}} = 9.8\,\mathrm{GHz}$ and $A = 20\,\mathrm{mT}$. (b) Corresponding absorption spectrum.

resulting energy levels vary with B_0 due to the additional field-dependent contribution from the electron Zeeman interaction.

Zero-field Splitting Interaction

The ZFS interaction occurs in systems with multiple strongly coupled unpaired electrons, i.e., for total spin quantum numbers $S > 1/2$. Its Hamiltonian is expressed as

$$\hat{H}_{\mathrm{ZFS}} = \hat{S}\mathbf{D}\hat{S}, \tag{1.12}$$

where $\mathbf{D}$ denotes the zero-field interaction tensor. As the name suggests, this interaction can lead to a splitting of spin states even in the absence of an external magnetic field [GS18]. The tensor is commonly parameterized by two constants: D, which reflects the average electron–electron spatial separation and determines the axial component of the splitting, and E, which quantifies the deviation from cubic symmetry [RS18].

To illustrate, the spin system of a single unpaired electron is extended by two additional unpaired electrons, resulting in a total spin of $S = 3/2$. Assuming axial symmetry with $D = 14\,\mathrm{mT}$ ($D = 392\,\mathrm{MHz}$ when converted to frequency using the Zeeman resonance condition of Eq. 1.9) and $E = 0$, the energy level diagram consists of four states corresponding to $m_S = +3/2, +1/2, -1/2$, and $-3/2$, as shown in Fig. 1.4a. At $B_0 = 0$, these states collapse into two distinct energy levels due to the ZFS. Upon application of an external field, three allowed

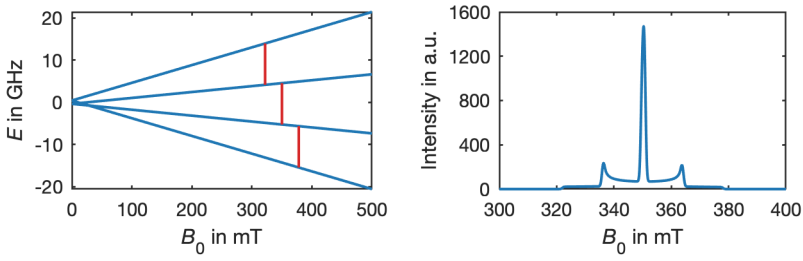

(a) (b)

Figure 1.4: EPR simulations using EasySpin [SS06] illustrating the zero-field interaction. (a) Energy-level diagram, with the three red vertical lines indicating the allowed transitions for $f_{0,\mathrm{r}} = 9.8\,\mathrm{GHz}$ and $D = 14\,\mathrm{mT}$. (b) Corresponding absorption spectrum.

transitions appear, leading to three resonance lines in the absorption spectrum. For this example, the central transition between $m_S = +1/2$ and $m_S = -1/2$ occurs at $B_0 \approx 350\,\mathrm{mT}$, while two additional peaks appear symmetrically displaced by $\pm D = 14\,\mathrm{mT}$, reflecting the influence of the ZFS parameter, as shown in Fig. 1.4b.

The ZFS is an intrinsic property of the spin–spin interaction and therefore independent of the external magnetic field. Consequently, it can be directly measured even in the absence of the external magnetic field, provided that the spectrometer allows sweeping over a sufficiently wide frequency range. In the given example, at zero magnetic field, the absorption spectrum as a function of frequency exhibits a single resonance at $f_{0,\mathrm{r}} = 2D \approx 0.8\,\mathrm{GHz}$. Depending on the sample, this resonance may occur at different frequencies, determined directly by the ZFS parameters. Conventional resonator-based spectrometers operate at fixed frequencies and can therefore determine the ZFS parameters only indirectly, by adjusting D and E in simulations to reproduce the experimental spectra.

Each interaction exhibits a distinct field and frequency dependence, making multi-frequency measurements necessary to disentangle their contributions. Direct measurement of the ZFS in particular requires a broadband spectrometer capable of sweeping the excitation frequency over a wide range.

Classical Description of EPR

The preceding discussion has focused on the energy levels and transitions of individual spin systems. In a macroscopic sample, however, the response arises from the collective behavior of an ensemble of spins. Instead of treating each spin separately, it is convenient to describe the spin ensemble in terms of its magnetization $\mathbf{M}$, which represents the net magnetic moment of N magnetic dipoles per unit volume V, expressed by

$$\mathbf{M} = \frac{1}{V} \sum_{i=1}^{N} \boldsymbol{\mu}_{\mathbf{m},i}. \tag{1.13}$$

When the ensemble is perturbed by an oscillating microwave magnetic field $\mathbf{B_1}$, the induced magnetization responds proportionally in the linear-response regime and can be written in terms of the magnetic susceptibility as

$$\mathbf{M} = \chi \mathbf{H_1} = \chi \kappa^{-1} \mu_0^{-1} \mathbf{B_1}, \tag{1.14}$$

where χ is the (possibly tensorial) complex magnetic susceptibility, μ_0 is the vacuum magnetic permeability, and $\kappa = 1 + \chi$ the relative permeability. In an isotropic sample, χ reduces to a scalar, and only the component of $\mathbf{M}$ along $\mathbf{B_1}$ contributes to the detected signal. In this case, the relation simplifies to

$$M = \chi \kappa^{-1} \mu_0^{-1} B_1. \tag{1.15}$$

The magnitude of the susceptibility is governed by the equilibrium spin polarization. In the high-temperature limit and for a dilute ensemble of non-interacting paramagnetic centers, the static susceptibility χ_0 follows Curie's law,

$$\chi_0 = \frac{N \mu_\mathrm{m}^2}{3 k_\mathrm{B} T} \mu_0 = \frac{C}{T}, \tag{1.16}$$

where k_B denotes the Boltzmann constant, T the temperature, and C the Curie constant. The squared magnetic moment of the paramagnetic center is given by $\mu_\mathrm{m}^2 = g^2 \mu_\mathrm{B}^2 S(S+1)$ [WB07].

In EPR, the spin ensemble is driven by an oscillating microwave field, such that its response is described by the complex dynamic susceptibility $\chi(\omega_0)$

at the excitation angular frequency $\omega_0 = 2\pi f_0$. This dynamic susceptibility represents the frequency-dependent extension of the static susceptibility and satisfies the low-frequency limit $\lim_{\omega\to 0}\chi(\omega) = \chi_0$. As a result, the Curie-law susceptibility χ_0 sets the overall magnitude of the EPR response, while the frequency dependence is governed by the spin dynamics. The magnetic susceptibility can therefore be expressed as

$$\chi(\omega_0) = \chi'(\omega_0) + \mathrm{j}\chi''(\omega_0). \tag{1.17}$$

The real part $\chi'(\omega_0)$ represents the in-phase component of the response, corresponding to dispersion, while the imaginary part $\chi''(\omega_0)$ represents the out-of-phase component, corresponding to the absorption of microwave energy. Both components are fundamentally linked through the Kramers–Kronig relations and together describe the complete dynamic response of the spin ensemble to the driving field. Consequently, the complex susceptibility directly determines the measurable signal in EPR experiments [WB07].

Fig. 1.5 illustrates the qualitative dependence of the susceptibility on the external magnetic field B_0. In conventional continuous wave (CW) EPR experiments, the microwave frequency is kept constant while the external magnetic field B_0 is swept through the resonance condition given by the Zeeman relation. The susceptibility is therefore expressed as $\chi(B_0)$ rather than $\chi(\omega_0)$. The absorptive component $\chi''(B_0)$ forms a symmetric peak centered at the resonance field $B_{0,\mathrm{r}}$, while the dispersive component $\chi'(B_0)$ exhibits an antisymmetric shape with a zero crossing at $B_{0,\mathrm{r}}$. The linewidth of the EPR resonance is characterized by $\Delta B_{1/2}$, defined as the full-width at half-maximum (FWHM) of the absorption signal. Together, these two components describe the characteristic EPR line shape [WB07, Poo96].

From this point onward, quantum mechanical operators are no longer used as they are not required for the experimental discussion, and vectors are denoted with an overhead arrow, replacing the earlier boldface notation used to avoid clashes with operator symbols. The external magnetic field B_0 is by default treated as a scalar, as is customary in EPR, but when its direction is relevant, the corresponding vector form is explicitly indicated.

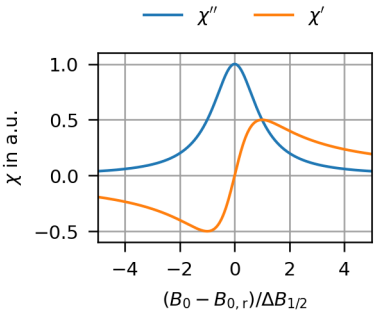

Figure 1.5: Qualitative shape of the absorptive (χ'') and dispersive (χ') components of the complex magnetic susceptibility as a function of the normalized external magnetic field B_0, with the resonance field $B_{0,\mathrm{r}}$ and the linewidth $\Delta B_{1/2}$. Based on [WB07, Poo96].

1.2.2 Conventional Measurement Setup

After outlining the fundamental principles of EPR, this section turns to the practical implementation of conventional EPR spectrometers. Since the main focus of this work is on a novel type of EPR hardware, the discussion of conventional spectrometers serves as an important basis for understanding the challenges, as well as the differences and similarities, compared to the envisioned broadband on-chip EPR spectrometer.

Two common techniques are used to perform EPR measurements. In CW EPR spectroscopy, the sample is continuously irradiated with low-intensity microwave radiation. Typically, the external magnetic field is swept while the microwave frequency remains fixed, so that different EPR transitions are brought into resonance and can be excited. In contrast, pulsed EPR spectroscopy employs short, high-intensity microwave pulses at a fixed magnetic field. The time-dependent spin response is recorded, and its Fourier transform yields the frequency-domain spectrum.

In most studies, CW EPR serves as the initial method of investigation because it is experimentally less demanding and well suited for obtaining an overview of unknown samples. Once the basic spectral features are identified, pulsed EPR and other advanced techniques are applied to study specific interactions

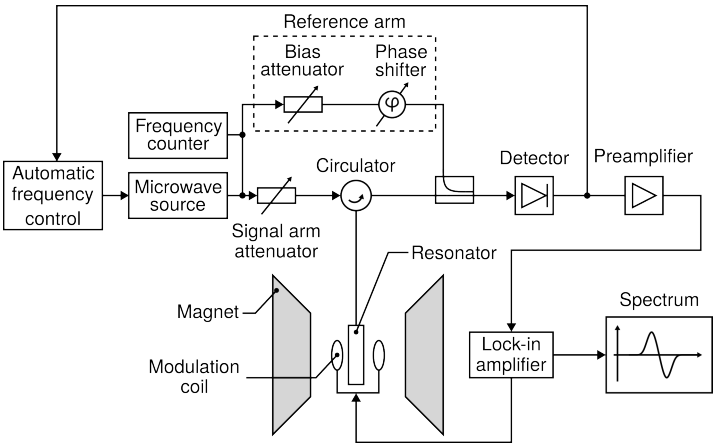

Figure 1.6: Block diagram of a typical continuous wave EPR spectrometer, based on [GS18, WB07].

in greater detail. Pulsed EPR is not as commonly employed as CW because the finite excitation bandwidth of microwave pulses can make it difficult to excite the entire spectrum, which is often broad due to the delocalized nature of the unpaired electrons. In addition, many paramagnetic systems exhibit short relaxation times that often require cryogenic operation, and the generation of short microwave pulses demands high power [GS18, RS18].

The development of conventional EPR spectrometers was strongly influenced by advances in microwave engineering during the Second World War, in particular in the context of radar technology. The frequency bands commonly used in EPR spectroscopy originated from the availability of radar components and waveguide standards. Today, the most widely used frequency bands are the X-band (around 10 GHz) and the Q-band (around 35 GHz), but spectrometers are also operated at the L-band (around 1 GHz), S-band (around 3 GHz), W-band (around 94 GHz), and even at higher frequencies up to 263 GHz. Although EPR measurements can, in principle, be performed at any frequency, these bands have become standard due to their historical development and component availability [Poo96].

Because CW EPR remains the most widely applied and experimentally accessible mode of operation, the present work focuses on this approach. A

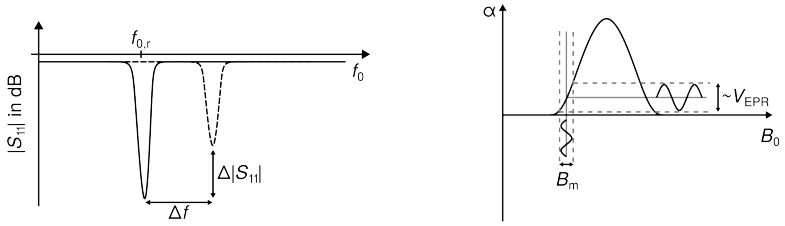

Figure 1.7: (a) Amplitude of S_{11} of the resonator. The solid curve shows the resonance peak tuned to the resonance frequency $f_{0,r}$ and the dashed curve indicates the behavior of the resonance curve at the EPR resonance condition. (b) EPR absorption α as a function of the external magnetic field and the effect of magnetic field modulation (adapted from [GS18]).

block diagram of a typical CW EPR spectrometer is shown in Fig. 1.6, adapted from [GS18, WB07]. The microwave source generates radiation at a frequency f_0, typically at a fixed output power. The power level delivered to the resonator is adjusted by a variable signal arm attenuator before the signal enters the circulator. The circulator directs the signal along the path indicated by the arrow and prevents reflections from traveling back toward the source. The signal is then coupled into a resonator that contains the EPR sample. The resonator itself is positioned between a modulation coil and an external magnet that provides the external magnetic field B_0.

Conventional CW EPR spectrometers mainly operate in reflection mode, i.e., the EPR response is detected as a change in the signal reflected from the resonator. In the off-resonance condition, i.e. $g\mu_B B_{0,r} \neq hf_{0,r}$, the resonator is critically coupled and, in the ideal case, no signal is reflected back to the circulator. This situation is illustrated by the solid resonance curve of the reflection coefficient S_{11} in Fig. 1.7a. Under resonance conditions, the sample absorbs microwave energy, the resonator is no longer critically coupled, and part of the signal is reflected back to the circulator, where it is detected as the EPR signal. The absorption corresponds to a decrease in the reflection coefficient, expressed as $\Delta|S_{11}|$.

As discussed in the previous section, spin transitions are driven by the oscillating microwave magnetic field $\vec{B}_1$. For efficient excitation, resonator designs therefore aim to maximize the strength and homogeneity of $\vec{B}_1$ at

the sample position, while ensuring that $\vec{B}_1$ is oriented perpendicular to B_0. It is also advantageous to spatially separate the maxima of the magnetic and electric fields inside the resonator, in order to minimize dielectric losses caused by electric-field absorption. A variety of resonator designs are used in EPR spectrometers. In the X-band, the most common general-purpose resonator is the TE_{102} rectangular cavity [GS18].

In addition to resonator design, sensitivity in EPR detection is further enhanced by the use of magnetic field modulation in combination with a lock-in amplifier (LIA). The modulation coils are driven by a sinusoidal signal at the modulation frequency f_m, generated by an internal oscillator of the LIA. As a result, the external magnetic field is modulated and the EPR response of the sample is modulated at the same frequency.

The modulated microwave signal is first demodulated by a detector, whose optimal operating point is adjusted by the bias attenuator in the reference arm. The resulting signal is then amplified and subsequently processed by the LIA. In this stage, the LIA mixes the signal with the reference modulation frequency f_m and applies a narrow low-pass filter. This procedure suppresses noise contributions at other frequencies and yields a very high signal-to-noise ratio (SNR).

Because the external field is slightly varied by the modulation, the detected signal corresponds to the first derivative of the absorption line rather than the absorption profile itself. This is illustrated in Fig. 1.7b. It shows the absorption peak and the effect of a modulated magnetic field B_m in addition to the external magnetic field B_0. A more detailed mathematical treatment of field modulation is shown in the next section and its implications for the detection chain is presented in Sections 2.5 and 3.1.1.

As absorption is always accompanied by dispersion, the resonance curve of the resonator is not only reduced in amplitude but also shifted in frequency when the Zeeman condition is met. This frequency shift, indicated as Δf in Fig. 1.7a, follows a dispersive line shape.

For most samples, it is sufficient to analyze only a single component of the response, and in practice the absorption signal is usually displayed. What is essential is that either the absorptive or the dispersive contribution is measured cleanly, without an uncontrolled mixture of both. Commercial EPR spectrometers therefore employ automatic frequency control together

with a frequency counter to stabilize the system and isolate the absorptive component. This keeps the microwave source frequency locked to the tuned resonance frequency $f_{0,\mathrm{r}}$ and suppresses the dispersive contribution so that a pure absorption spectrum is obtained. If the corrective frequency applied by the control loop is monitored the dispersive component can also be extracted.

Because the LIA selectively detects the signal component that is phase-correlated with the modulation, the described CW EPR measurement scheme is commonly referred to as phase-sensitive detection. Without automatic frequency control, however, the recorded spectrum would contain a varying admixture of absorption and dispersion, whereas frequency locking stabilizes the phase relation and ensures that the absorptive component can be isolated reliably [WB07].

For the purpose of this thesis, it is useful to distinguish between two largely orthogonal classification criteria for EPR spectrometers. First, spectrometers can be categorized by their measurement mode, namely reflection versus transmission. Second, they can be categorized by the type of microwave probe used to generate the excitation field, which in the context of this thesis refers to resonator-based versus TL-based implementations. As mentioned earlier, conventional CW spectrometers typically combine a resonant probe with reflection-mode detection, whereas this thesis focuses on TL probes operated in transmission mode.

1.2.3 Effect of Experimental Parameters

Several experimental parameters strongly influence the quality and appearance of the measured EPR spectra. In this section, emphasis is placed on the microwave input power, the amplitude and frequency of the magnetic-field modulation, and the time constant of the lock-in amplifier, since these parameters are central to the experiments described in this work. For each sample, they must be carefully optimized to record spectra accurately.

Input Power

The intensity of the EPR signal increases with the square root of the incident microwave power at low power levels. At higher power, however, the growth of the signal slows and eventually decreases, a phenomenon known as saturation [EEBW10]. Saturation occurs when the populations of the upper and lower spin states equalize, reducing the net absorption of microwave energy. Optimal input power therefore represents a compromise. It should be high enough to provide a strong SNR, but low enough to avoid saturation, which can also introduce distortions into the spectral line shape [CCM16].

Modulation Amplitude

In a second step, the effect of the magnetic-field modulation amplitude is examined in more detail, and a short derivation is provided to clarify the trade-off between signal enhancement and spectral distortion. During field modulation, the total magnetic field applied to the sample can be written as

$$B_0(t) = B_{0,\mathrm{s}}(t) + B_\mathrm{m}\cos(\omega_\mathrm{m} t), \tag{1.18}$$

with $\omega_\mathrm{m} = 2\pi f_\mathrm{m}$. Here, $B_{0,\mathrm{s}}(t)$ denotes the slowly swept external magnetic field, and B_m is the modulation amplitude. Since $B_{0,\mathrm{s}}(t)$ varies slowly compared to one modulation period $T_\mathrm{m} = 1/f_\mathrm{m}$, it can be treated as constant within one modulation cycle. Hence,

$$B_0(t) \approx B_{0,\mathrm{s}}^i + B_\mathrm{m}\cos(\omega_\mathrm{m} t), \tag{1.19}$$

where $B_{0,\mathrm{s}}^i$ denotes the instantaneous operating field [Poo96].

The absorptive response of the spin ensemble is described by $\alpha(B)$ (proportional to the imaginary part of the susceptibility), such that the time-dependent absorption becomes

$$\alpha(t) = \alpha(B_0(t)) = \alpha\left(B_{0,\mathrm{s}}^i + B_\mathrm{m}\cos(\omega_\mathrm{m} t)\right). \tag{1.20}$$

Because $\alpha(t)$ is periodic with period T_m, it can be represented by a Fourier series,

$$\alpha(t) = a_0 + \sum_{n=1}^{\infty} \left[a_n \cos(n\omega_\mathrm{m} t) + b_n \sin(n\omega_\mathrm{m} t) \right] . \tag{1.21}$$

The Fourier coefficients depend on the operating field $B^i_{0,\mathrm{s}}$, the modulation amplitude B_m, and the intrinsic linewidth $\Delta B_{1/2}$ (see Section 1.2.1), and are not written explicitly for clarity. The lock-in amplifier demodulates the detector signal at the reference frequency f_m. For appropriate phase adjustment, the in-phase lock-in output is proportional to the first-harmonic cosine coefficient a_1, while the quadrature channel is proportional to b_1 [Poo96].

For the following calculations, the small-modulation regime $B_\mathrm{m} \ll \Delta B_{1/2}$ is assumed, such that the absorption curve is approximately linear within the modulation interval around $B^i_{0,\mathrm{s}}$. Under this condition, the absorption can be expanded to first order around $B^i_{0,\mathrm{s}}$,

$$\alpha\left(B^i_{0,\mathrm{s}} + B_\mathrm{m} \cos(\omega_\mathrm{m} t)\right) \approx \alpha\left(B^i_{0,\mathrm{s}}\right) + \alpha'\left(B^i_{0,\mathrm{s}}\right) B_\mathrm{m} \cos(\omega_\mathrm{m} t). \tag{1.22}$$

The first term constitutes a static component, whereas the second term oscillates at f_m and therefore contributes to the first Fourier coefficient. Consequently, the in-phase demodulated CW-EPR signal becomes proportional to the first derivative of the absorption line

$$V_\mathrm{EPR}\left(B^i_{0,\mathrm{s}}\right) \propto B_\mathrm{m}\, \alpha'\left(B^i_{0,\mathrm{s}}\right) . \tag{1.23}$$

As long as the small-modulation approximation holds, the EPR signal amplitude therefore increases approximately linearly with B_m. For larger modulation amplitudes, higher-order Fourier components gain weight and the first Fourier coefficient a_1 no longer scales linearly with B_m, leading to overmodulation artefacts such as line broadening and distorted spectral line shapes, which ultimately reduce the peak-to-peak signal amplitude [EEBW10, GS18].

Modulation Frequency

The choice of the magnetic-field modulation frequency depends on both instrumental considerations and sample-specific spin dynamics. From an instrumentation perspective, increasing the modulation frequency shifts the detected signal away from low-frequency ($1/f$) noise contributions, thereby improving the achievable SNR. However, the modulation frequency must also be compatible with the dynamic response of the spin ensemble. In particular, f_m must be sufficiently low such that the magnetization can follow the periodic field variation quasi-statically within each modulation cycle. If the modulation is too fast compared to the characteristic relaxation times of the spin system, dynamic effects may occur and can manifest as line-shape distortions and phase shifts in the demodulated signal [EEBW10]. In general, additional considerations regarding the choice of f_m may become relevant when measuring very narrow EPR resonance lines. However, in the present work, only standard EPR samples with comparatively broad linewidths are investigated. Therefore, modulation-frequency–dependent effects associated with very narrow resonance lines are not expected to play a significant role and are not covered in detail.

In practice, the modulation frequency f_m is typically chosen in the range of several tens to a few hundreds of kilohertz. A commonly used standard value in CW-EPR spectroscopy is $f_\mathrm{m} = 100\,\mathrm{kHz}$.

Time Constant

The time constant τ of the low-pass filter in the LIA strongly influences both the noise level and the apparent line shape of CW-EPR spectra. Increasing τ reduces the contribution of random (white) noise, with the noise standard deviation decreasing approximately as $1/\sqrt{\tau}$ [EEBW10], such that longer time constants generally improve the SNR.

However, if τ becomes too long relative to the magnetic-field sweep, the signal cannot follow changes of the absorption intensity during the scan. As a result, narrow resonances may appear broadened, attenuated, or distorted, and in extreme cases spectral features can be partially filtered out [EEBW10]. The choice of τ must therefore be consistent with the sweep, i.e. short compared to the time required to traverse the narrowest line. A useful rule of thumb

is given by Eaton, who relates these parameters through the dimensionless inequality [EEBW10]

$$\frac{\text{spectrum width in T}}{\text{line width in T}} \times \frac{\text{time constant in s}}{\text{sweep time in s}} < 0.1. \tag{1.24}$$

This expression highlights that narrow lines, large scan ranges, or fast sweeps require shorter time constants, whereas longer time constants can be used without distortion only if the sweep time is increased accordingly.

1.3 State of the Art

EPR spectroscopy has been realized in a wide variety of architectures that differ in frequency coverage, level of integration, and detection principles. For the purpose of this work the literature review focuses on two areas, broadband spectrometers that aim to span large frequency ranges and integrated spectrometers that pursue compact on-chip implementations.

1.3.1 Broadband EPR Spectrometers

A wide variety of broadband solutions have been proposed in the literature. In this section the state-of-the-art is presented in two parts. Systems operating below 110 GHz, often referred to as classical microwave approaches, are particularly relevant in the context of this work. To provide a complete picture of the broadband landscape, systems operating above 110 GHz are also included, where quasi-optical approaches dominate.

Broadband Systems Below 110 GHz

Early examples of broadband operation used TL microwave probes. A shorted, non resonant microcoil operating from 0.1 GHz to 8.5 GHz is reported by Mahdjour et al. [MCB86]. The EPR response was detected in reflection mode using magnetic-field modulation and lock-in detection. Sample absorption perturbs the coil's complex impedance and is observed as a change in the

reflected signal. A limitation was the absence of a matched termination at the probe which produced standing waves.

Building on related principles, Hagen developed a sequence of broadband probes [Hag13, Hag19, Hag23]. In [Hag13], a non-resonant coaxial cable covering 0.8 GHz to 2.7 GHz was employed, where the sample formed part of the cable dielectric. The EPR response was read out in transmission mode using a vector network analyzer (VNA). In [Hag19], the coaxial cable was replaced by a wire microstrip line and operated as a multimode resonator by combining an electrically long transmission line with a tunable phase shifter in addition to the probe. Detection again relied on a VNA, but the EPR signal was extracted in reflection mode. In [Hag23], the wire microstrip probe was retained and integrated into a commercial Bruker spectrometer by replacing the bridge with a broadband version and adding a custom-built modulation coil, enabling classical reflection-mode detection with field modulation and lock-in readout. The circulator was the only component not covering the full bandwidth. Therefore, several units were used to span different frequency bands.

A related concept was introduced by Tsai et al., employing a three-dimensional wire-wound meander-line probe operating from 0.1 GHz to 20 GHz [TCC+09]. The spectrometer is based on transmission-mode detection with magnetic-field modulation and lock-in readout.

A second line of development used tunable cavities. A mechanically adjustable cavity covering frequencies from 1 GHz to 4.6 GHz was presented by Erickson, employing detection in transmission mode [Eri66]. Seck and Wyder extended this concept to the range of 40 GHz to 60 GHz using a tunable cylindrical cavity with classical reflection-type detection [SW98]. A tunable cavity operating in the TE_{011} mode and covering 4 GHz to 40 GHz was later reported by Schlegel et al., again using detection in transmission mode [SDS10]. In this mode, the end plates carry no surface currents, allowing mechanical adjustment for frequency tuning. Measurements were performed with a VNA, and dielectric loading was used to access lower frequencies.

Jang et al. demonstrated a dual antenna arrangement from 0.5 GHz to 9 GHz where one antenna transmitted and the other received [JSC+08]. This eliminated the need for a broadband circulator. Single-turn coupled loops and multi-turn coupled helix antennas were investigated. The response was read with a detector and a LIA.

Implementations based on planar transmission lines extend broadband EPR into the tens of gigahertz. Broadband coplanar waveguide (CPW) probes have been demonstrated in several publications [CBK+13, WSC+15, MDS20, JLS+19], while related microstrip line (MSL) implementations have been reported elsewhere [CSW17, SAA+19], reaching operating frequencies up to 67 GHz. In most designs the sample is placed on top of the line. There are also cases where the sample is embedded inside the dielectric. Johansson et al. realized a resonant microstrip line operating at 3.81 GHz, and the harmonic frequencies of the resonator were used for broadband operation with the sample placed inside the dielectric [JHPB74]. Shrestha et al. [SAA+19] likewise positioned the sample inside the microstrip dielectric but based their design on a transmission line rather than a resonator. With the exception of [JHPB74], these implementations mainly employ transmission-mode detection. Dual-mode operation in both transmission and reflection is demonstrated by Shrestha et al. [SAA+19].

Taken together, broadband systems below 110 GHz span non resonant coils, TL probes, tunable cavities, antenna based setups, and planar, coplanar or microstrip structures. An overview of the broadband EPR spectrometers is given in Tab. 1.1.

Quasi-Optical Systems at Higher Frequencies

At higher frequencies broadband EPR spectrometers are generally realized as quasi-optical systems where the radiation propagates as a Gaussian transverse electromagnetic $(TEM)_{00}$ beam and the optical components are comparable in size to the wavelength [MK25]. For the purpose of this overview the literature is presented according to the type of source technology that is employed.

Multiplier chain based systems are exemplified by Earle, Tipikin, and Freed which introduced a quasi-optical reflection bridge with a Fabry–Pérot resonator operating from 100 GHz to 300 GHz [ETF96]. Polarization transforming reflectors enabled separation of transmit and receive paths and conversion of linear to circular polarization which improved the detected signal. Corrugated waveguides were employed for low loss polarization preserving transmission. Later, this approach was extended to frequencies from 170 GHz to 1.1 THz using a computer controlled synthesizer with cascaded frequency multipliers by

Neugebauer et al. [NBM+18]. The quasi-optical bridge employed polarization analysis of the reflected signal from the sample or a mirror below the sample.

Backward wave oscillators have provided another source technology for broadband EPR. Tarasov and Shakurov demonstrated a setup spanning 79 GHz to 535 GHz that illuminated the sample directly through a quasi-optical lens system without a resonator and employed a liquid helium cooled n-InSb crystal detector [TS91]. The external magnetic field was limited to 1 T. The frequency range was extended to 30 GHz to 1.5 THz using a Mach–Zehnder interferometer for detection by Van Slageren et al. [SVG+03] while Ohmichi et al. employed backward wave oscillator excitation in combination with mechanically detected EPR, using microcantilevers or nanomembranes as probes and displacement measurement as the readout [OOTO21].

A third line of research has used synchrotron radiation as the broadband source. This approach has been demonstrated at the BESSY II synchrotron [SBL+09, NHBS17], operating from 150 GHz to 1.2 THz. This approach is known as frequency domain Fourier transform EPR. The radiation is guided by quasi-optical transmission lines into Michelson or Martin–Puplett interferometers and the time dependent intensity changes are recorded with a liquid helium cooled InSb bolometer as a function of mirror position. The transient signal is then Fourier transformed into the frequency domain. More recent work has also shown that multiplier chain sources can be combined with a double Martin–Puplett interferometer to achieve polarization control in the transmit and receive path [KFHF+23].

Commercial solutions have also been developed. One example was a reflection bridge offered by Bridge12 specified from 95 to 400 GHz. At present this system does not appear to be available any longer, possibly related to the company's acquisition by Bruker.

Table 1.1: Overview of broadband EPR spectrometers below 110 GHz.

Reference	Frequency range	Mode	Probe	Measurement setup
[MCB86]	0.1 – 8.5 GHz	reflection	non-resonant microcoil	lock-in with modulated field
[Hag13]	0.8 – 2.7 GHz	transmission	coaxial cable	VNA
[Hag19]	0.5 – 12 GHz	reflection	wire microstrip	VNA
[Hag23]	0.1 – 18 GHz	transmission	wire microstrip	modified Bruker spectrometer
[TCC+09]	0.1 – 20 GHz	transmission	3D wire-wound meander line	lock-in with modulated field
[Eri66]	1 – 4.6 GHz	transmission	mechanically tunable cavity	lock-in with modulated field
[SW98]	40 – 60 GHz	reflection	mechanically tunable cavity	lock-in with modulated field
[SDS10]	4 – 40 GHz	transmission	mechanically tunable cavity	VNA
[JSC+08]	0.5 – 9 GHz	transmission	antenna system	lock-in with modulated field
[CBK+13], [WSC+15], [JLS+19], [MDS20]	up to 67 GHz	transmission	CPW probes	VNA, interferometric or lock-in
[CSW17](1), [SAA+19](2)	up to 67 GHz	transmission(1), dual(2)	MSL probes	lock-in with modulated field
[JHPB74]	3.81 GHz + harm.	reflection	microstrip resonator	lock-in with modulated field

1.3.2 Integrated EPR Spectrometers

Over the past two decades, several research groups have pursued the miniaturization of EPR spectrometers in integrated semiconductor technology. For the purpose of this review the developments are grouped into three categories. The first adapts the conventional continuous wave architecture into an integrated platform. The second replaces the resonator by an oscillator, in which the frequency of the oscillator serves as the sensing parameter. The third employs a capacitively coupled LC tank to detect resonance. This section provides an overview of the advances made to date, summarized in Tab. 1.2 at the end of the section.

Miniaturization of Conventional EPR Architectures

One line of research on miniaturized EPR spectrometers was carried out at Rice University and focused on adapting the conventional continuous wave architecture into an integrated platform. All publications from this group employed 0.13 µm silicon–germanium (SiGe) bipolar CMOS (BiCMOS) technology and combined an on-chip transceiver with a resonator [YB15, CSB13, YB16]. In their first report, Yang and Babakhani presented an absorption-based spectrometer operating at approximately 1 GHz [YB15]. The transceiver was integrated on chip while the resonator was implemented on a printed circuit board and connected through an external circulator. A key difference to conventional architectures was the use of a mixer for direct conversion instead of a diode detector. This approach in principle allowed both continuous wave and pulsed operation, and the authors introduced a combined setup, although only continuous wave measurements were demonstrated.

In parallel, Chen et al. demonstrated pulsed operation at frequencies between 22 GHz and 26 GHz using an on-chip loop resonator [CSB13]. They introduced a switching mechanism at the buffer and power amplifier stage, which isolated the voltage controlled oscillator (VCO) output from the resonator. The switch enabled pulsed excitation and allowed one of the first pulsed measurements in an integrated spectrometer platform.

In a subsequent step, Yang and Babakhani focused on self interference cancellation in a spectrometer operating at 4.5 GHz [YB16]. In this case, the

transceiver was again realized on chip, while the resonator remained on a separate printed circuit board. The challenge of transmitter leakage into the receiver path due to limited isolation of the circulator and imperfect resonator matching was addressed by generating a cancellation signal. This method improved the SNR by about 25 dB compared to the earlier implementation and demonstrated the effectiveness of active cancellation techniques in integrated EPR spectrometers.

Oscillator-Based EPR Detection

A second line of development, initiated at the École Polytechnique Fédérale de Lausanne and later pursued in parallel at the University of Stuttgart, is based on the use of oscillators as sensing elements. In this approach the EPR phenomenon is detected through a variation of the oscillator frequency rather than through the voltage induced in a resonator. The magnetic resonance modifies the impedance of the integrated inductor, leading to a shift in the frequency of the LC oscillator that is proportional to the real part of the magnetic susceptibility. As a result, the recorded EPR spectrum resembles the dispersion signal obtained in conventional spectrometers [YB08].

Within this framework, Yalcin and Boero reported one of the first single-chip detectors based on LC oscillators [YB08]. They employed two oscillators operating at slightly different frequencies and combined their outputs in a subsequent mixer to generate an intermediate frequency. Continuous wave EPR measurements were demonstrated at 9 GHz in 350 nm complementary metal-oxide-semiconductor (CMOS). Building on this idea, Anders, Angerhofer, and Boero realized a spectrometer in 130 nm CMOS that operated at 27 GHz [AAB12]. The circuit was simplified to a single oscillator with a buffer and a frequency divider, replacing the earlier two-oscillator mixer scheme. This design also demonstrated measurements down to 77 K.

Subsequent developments extended the frequency range and pushed the operating temperature. Gualco et al. demonstrated measurements at cryogenic temperatures down to 4 K [GAS+14], while Matheoud et al. scaled the approach to 50 GHz, 92 GHz, and 146 GHz using 40 nm CMOS [MGJ+17]. Later, Matheoud et al. replaced CMOS by an indium gallium arsenide (InGaAs)

high-electron-mobility transistor (HEMT) device, which reduced the minimum $\vec{B}_1$ field and power consumption [MSB18].

Following these developments, further advances explored the potential of VCOs for tunability and system-level simplification. Handwerker et al. demonstrated that a VCO can be used to sweep the operating frequency electronically rather than sweeping the magnetic field [HSW+16]. This eliminated the need for a large electromagnet and enabled the use of a permanent magnet, opening the way toward portable spectrometer systems. The spectrometer, implemented in 130 nm CMOS and operating at 14 GHz, employed varactors controlled by a tuning voltage. This tuning voltage was further exploited for frequency modulation, which allowed lock-in detection without modulation coils and thereby reduced the overall power consumption of the setup.

Building on this concept, Chu et al. developed an injection-locked array of 8 VCOs operating at 13 GHz, which increased the sensitive volume and reduced phase noise [CSL+18]. In a later publication, the concept was scaled to 32 VCOs in a segmented-coil configuration, implemented in 130 nm BiCMOS, and demonstrated EPR measurements at 263 GHz [CKK+23]. In parallel, oscillator-based systems were also adapted for pulsed operation. Dead-time-free pulsed measurements at 30 GHz in 40 nm CMOS were reported by tuning the VCO frequency between on- and off-resonance [HKC+22]. Sun et al. introduced a CW and pulsed spectrometer in 65 nm CMOS with improved startup and ring-down dynamics through injection locking and active damping [SWQS24].

Capacitively Coupled LC Tank Approach

A third line of research has explored the use of a capacitively coupled LC tank as the sensing element [ZN21]. In this case, the inductance of the LC tank is modified by the EPR phenomenon, and the resulting change corresponds to the dispersion component of the susceptibility. This approach directly addresses two key limitations of oscillator-based detection, namely the sensitivity degradation caused by temperature drift and transistor flicker noise, both of which also affect the oscillator frequency.

The architecture employs a pulse-modulated injection signal that is coupled to the sensor through a wideband on-chip transformer. The sensor itself is realized as a capacitively coupled LC tank. At resonance, variations in

inductance manifest as a phase difference between the tank output and the injection signal. This phase difference is then converted to a voltage using a double-balanced voltage-commutative passive mixer. Measurements were demonstrated at 14 GHz in a 28 nm CMOS process, showing that the LC tank approach can combine high integration with reduced susceptibility to oscillator-related noise mechanisms [ZN21].

In summary, a wide range of challenges has already been addressed in the development of narrowband integrated EPR spectrometers, and substantial progress has been achieved across different architectures. However, broadband integrated circuits are fundamentally different from those structures and therefore require new design strategies. A central distinction is that narrowband circuits achieve impedance matching through resonant/reactive networks, which inherently operate only over a limited frequency range [Fan50]. This approach is not applicable to broadband operation, where alternative matching concepts must be employed. Beyond the design of individual components, the overall system architecture must also be reconsidered to accommodate broadband measurements and to fully exploit the potential of integrated solutions for broadband EPR.

Table 1.2: Overview of integrated EPR spectrometer implementations.

Reference	f_0 in GHz	Technology	Probe	Highlight
[YB15]	~1	130 nm BiCMOS	resonator	direct conversion with mixer
[CSB13]	22–26	130 nm BiCMOS	loop resonator	pulsed measurements
[YB16]	4.5	130 nm BiCMOS	resonator	active self-interference cancellation
[YB08]	9	350 nm CMOS	2 LC oscillators	first single-chip LC oscillator
[AAB12]	27	130 nm CMOS	LC oscillator	measurements down to 77 K
[GAS+14]	20	130 nm CMOS	2 LC oscillators	cryogenic operation at 4 K
[MGJ+17]	50, 92, 146	40 nm CMOS	2 LC oscillators	high-frequency operation
[MSB18]	11.2	InGaAs HEMT	LC oscillator	reduced B_1 and power consumption
[HSW+16]	14	130 nm CMOS	VCO	frequency instead of field sweeping
[CSL+18]	13	130 nm CMOS	array of 8 VCOs	increased sensitive volume, reduced phase noise
[CKK+23]	263	130 nm BiCMOS	array of 32 VCOs	high-frequency demonstration
[HKC+22]	30	40 nm CMOS	VCO	pulsed operation based on tuning VCO frequency on and off resonance
[SWQS24]	12.8–14.9	65 nm CMOS	VCO	pulsed operation based on injection-locked startup and active damping
[ZN21]	14	28 nm CMOS	capacitive coupled LC tank	reduced sensitivity to flicker noise and temperature drift

1.4 Thesis Organization and Goals

The literature review has shown that substantial progress has been made in extending EPR spectroscopy to broadband operation as well as in miniaturizing spectrometer architectures through integrated circuit technology. Spectrometers based on resonant microwave probes have already been implemented in integrated form. First attempts have also been made to miniaturize non-resonant microwave probes by realizing transmission line structures on printed circuit boards and on chip. However, no fully integrated broadband EPR spectrometer has been reported to date.

This thesis takes a step toward closing this gap by focusing on the frequency range below 110 GHz, where a broadband implementation is both technically feasible and scientifically valuable. This work investigates the potential of on-chip broadband spectrometers, analyzes their advantages and limitations, and focuses on identifying the sensitivity bottlenecks. These systems are not intended to replace conventional high-sensitivity resonator-based spectrometers, but rather to complement them as a versatile addition to the EPR toolbox.

The remainder of the thesis is organized as follows, proceeding step by step from system-level architecture analysis to the realization of a TL-based measurement setup, the development of optimized non-resonant microwave probes, and finally the design of integrated circuit components.

Chapter 2: System Architectures for TL-based EPR

In contrast to conventional resonator-based EPR, a TL microwave probe operated in transmission mode is used to realize a broadband spectrometer architecture. The challenges associated with TL-based EPR are discussed, three possible system architectures to address these challenges are identified, and proof-of-concept measurements are presented and compared.

Chapter 3: TL-based EPR Measurement Setup

Based on the analysis of the system architecture, the lock-in principle combined with a modulated magnetic field is chosen as the most suitable approach. This concept is implemented as a measurement setup using commercial components together with a custom-built TL microwave probe, which is introduced in the

next chapter. Emphasis is placed on the signal chain and the challenges that arise in its realization. A detailed noise analysis is carried out to identify the main bottleneck. Finally, the performance of the custom-built TL-based spectrometer is compared to that of a commercial resonator-based spectrometer.

Chapter 4: TL Microwave Probes

The use of TL microwave probes is explored as a route towards broadband systems instead of narrowband resonators. The optimization of transmission lines for high microwave magnetic field strength is discussed, since continuous wave EPR is the main focus of this work. Microstrip and coplanar waveguide probes are compared, design guidelines are derived for both, and the results are validated through electromagnetic simulations and EPR measurements. In addition, an inverted microstrip line is introduced as a proof-of-concept to achieve a more homogeneous magnetic field strength, which can be beneficial for certain sample types.

Chapter 5: Integrated Circuit Components

This chapter introduces circuit-level building blocks for integrated broadband EPR spectrometers. The design of a broadband lumped single-ended amplifier and a broadband distributed detector, both implemented in a SiGe BiCMOS process, is presented. Special design considerations are highlighted and the achieved performance is compared to the state-of-the-art.

Chapter 6: Conclusions and Outlook

The main findings of this work are summarized, and perspectives for future research are outlined. The developed concepts demonstrate the feasibility of broadband TL-based EPR, bridging the gap between system-level design and component-level realization. Building on these results, directions for future research are outlined, focusing on enhancing the level of integration and expanding the application range of the proposed broadband architecture to other magnetic resonance spectroscopies.

2 System Architectures for TL-based EPR

Parts of this chapter include material previously published in [3].

In a first step, various system architectures are identified and analyzed to realize a broadband TL-based EPR spectrometer. The following research questions are addressed in this chapter:

- What are the challenges of TL-based EPR?
- What are possible system architectures for implementing a TL-based EPR spectrometer?
- How are the absorption and dispersion signals measured?
- What are the trade-offs for each system architecture?
- Which system architecture is most feasible for a first prototype?

2.1 State of the Art and Motivation

One of the primary limitations to bandwidth in commercial narrowband spectrometers is the use of a resonator as the microwave probe. As previously discussed, a TL can serve as an alternative. However, from a system design perspective, the use of a TL microwave probe poses some challenges.

Compared to resonator-based probes, a TL does not provide magnetic-field enhancement through energy storage. Consequently, for a given input power the achievable excitation strength at the sample is typically lower, or, equivalently, higher input power is required to reach a comparable excitation level. This reduced excitation efficiency can translate into a smaller detected

EPR response and may therefore limit sensitivity. This is discussed in more detail in Section 3.3.1. A second challenge is that the EPR response appears as a small perturbation superimposed on a large transmitted carrier signal, requiring efficient carrier suppression or separation. In contrast, resonator-based spectrometers can suppress the carrier signal through critical coupling, thereby improving signal isolation.

From the literature, three principle system architectures are identified: quadrature detection, interferometric detection and lock-in detection combined with a modulated external magnetic field.

Quadrature detection is demonstrated by [CBK+13, WSC+15], both from the same research group. [CSW17] presents EPR measurements using an interferometric detection scheme and compares it to quadrature detection. Lock-in detection combined with a modulated external magnetic field is used by [MDS20, JLS+19, SAA+19], with [MDS20] omitting a reference arm and benchmarking against quadrature detection. In contrast, [JLS+19] incorporates a reference arm and demonstrates both magnetic field sweep with field modulation and frequency sweep with frequency modulation. [SAA+19] combines elements of both lock-in detection and interferometric detection.

While prior works often compare only two detection schemes, this chapter juxtaposes all three architectures in a unified framework, highlighting their operational principles and comparative advantages. A key focus lies on the methods each setup uses for frequency separation, as well as the detection of dispersion and absorption signals, thereby clarifying to which physical quantities they are proportional. Proof-of-concept measurements are presented for all three detection schemes. Furthermore, the fundamental working principles of resonator-based and TL-based detection approaches are compared and the system architecture, which most closely mimics the behavior of a resonator-based system, is identified. Finally, this chapter shifts attention toward on-chip realization, which has not yet been addressed in the cited literature.

Before discussing the individual system architectures in detail, the following section provides an overview of the general measurement methodology employed in this work, including the TL microwave probe, the sample preparation, and the measurement instruments used for all proof-of-concept experiments.

2.2 Measurement Methodology

The meandered coplanar waveguide microwave probe used for all presented measurements is shown in Fig. 2.1. The probe represents one of the first prototypes developed during the course of this work and is primarily optimized for achieving a flat transmission coefficient S_{21} over the studied bandwidth rather than for maximizing the microwave magnetic field strength. More detailed probe design considerations and later optimized TL implementations are discussed in Chapter 4. For the system-level comparison of the detection architectures, the specific TL implementation is not critical.

The coplanar waveguide has a line width of $w = 50\,\mu\text{m}$ and a gap of $s = 25\,\mu\text{m}$ between the signal conductor and the ground planes. Gold is used as the conductor material, and the substrate is made of alumina with a dielectric constant of $\varepsilon_\text{r} = 9.9$ and a thickness of $h = 500\,\mu\text{m}$. These parameters result in a characteristic impedance of $Z_0 = 50\,\Omega$. The transmission (S_{21}) and reflection (S_{11}) coefficients, measured from 0.01 GHz to 26.5 GHz, are shown in Fig. 2.1b. The effective area of the transmission line contributing to the EPR signal is $3.7\,\text{mm} \times 1.9\,\text{mm}$, corresponding to the rectangular outline of the meandered structure. For the signal interfacing, 3.5 mm end-launch connectors are used.

For each measurement, a droplet of an aqueous solution of 4-hydroxy-2,2,6,6-tetramethylpiperidine-1-oxyl (TEMPOL) with a concentration of $C = 10\,\text{mM}$ was applied to the effective area of the TL microwave probe. The sample was subsequently dried under ambient conditions, forming very thin disk-like residues, as visible in the center of the microwave probe in Fig. 2.1.

TEMPOL is a nitroxide radical containing a single unpaired electron that is predominantly localized on the nitroxide group. The nitrogen nucleus (^{14}N) has a nuclear spin quantum number of $I = 1$, which gives rise to three possible nuclear spin states. Through hyperfine interaction with the unpaired electron, the EPR resonance is split into three distinct lines [ATL23]. In the absence of anisotropy in the **g**-tensor and hyperfine **A**-tensor, this three-line pattern would be observed both in the liquid and in the solid state. In practice, however, TEMPOL exhibits anisotropic **g**- and **A**-tensors. In the solid (dried) state, the molecules are randomly oriented, and the spectrum represents an average over all molecular orientations, leading to a powder-type line shape and substantial broadening. As the TEMPOL sample dries, additional broadening is expected

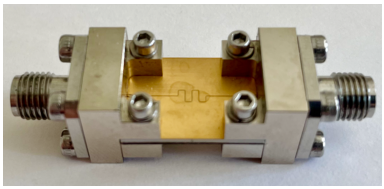

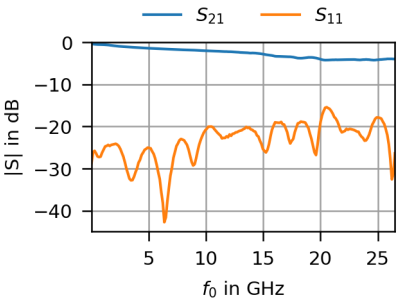

(a) (b)

Figure 2.1: a) Photograph of the coplanar meandered TL microwave probe with the dried TEMPOL droplet in the center and b) S-Parameter measurements of the TL microwave probe. Adapted from [3], ©IEEE.

to be dominated by strong dipolar spin–spin interactions arising from the close proximity of the radicals. Further line broadening may also arise from magnetic-field inhomogeneities and relaxation effects. Consequently, the measured EPR spectra of dried TEMPOL appear as a single broad peak in which the three hyperfine lines are no longer resolved.

The measurements presented here are not intended for quantitative comparison between the different system architectures, but rather serve as proof-of-concept demonstrations. During transitions between measurement setups, the sample was removed and reapplied, resulting in slight variations in sample volume and mass. A rough estimate of the sample mass is determined as follows. The approximate diameter of the droplet is $D = 1\,\text{mm}$. Assuming a sphere with a radius $R = D/2$, the volume of the droplet is

$$V = \frac{4}{3}\pi\left(\frac{D}{2}\right)^3 = 523 \times 10^{-9}\,\text{l}. \tag{2.1}$$

The number of particles is calculated as

$$N = C \cdot V = 5.23 \times 10^{-9}\,\text{Mol}. \tag{2.2}$$

With a molar mass of $M = 172.248\,\mathrm{g/Mol}$, this leads to a mass of

$$m = M \cdot N \approx 0.9\,\mu\mathrm{g}. \tag{2.3}$$

To demonstrate the broadband capabilities of the system architectures, the measurements are performed at a resonance frequency of $f_{0,\mathrm{r}} = 9.86\,\mathrm{GHz}$ and $f_{0,\mathrm{r}} = 19.72\,\mathrm{GHz}$ which correspond to a resonance magnetic field of $B_{0,\mathrm{r}} = 352.2\,\mathrm{mT}$ and $B_{0,\mathrm{r}} = 704.5\,\mathrm{mT}$, respectively, assuming a g-factor of $g = 2$. The specific instruments used for the measurement setups are listed in Tab. 2.1.

Table 2.1: Measurement instruments used in the three proof-of-concept setups: L (lock-in detection), Q (quadrature detection), and I (interferometric detection).

Setup	Instrument	Name (company)
all	electromagnet	3474-70 Electromagnet (GMW Associates)
all	power supply	AMETEK SGA (Sorensen)
all	teslameter	HGM09s (MAGSYS)
L	signal generator	8350A + 83595A Sweep Oscillator (Hewlett-Packard)
L	lock-in amplifier	HF2LI 50 MHz Lock-In Amplifier (Zurich Instruments)
L	high-voltage amplifier	2100HF (Trek)
L	diode detector	R451 533 000 (Radiall)
Q, I	vector network analyzer	PNA-X N5242B (Keysight)
I	power divider	11667B (Hewlett-Packard)

2.3 Quadrature Detection

Quadrature detection is a direct detection architecture that enables EPR measurements via the complex transmission coefficient of the microwave probe.

2.3.1 Concept

The system architecture is illustrated in Fig. 2.2a. In this setup, the microwave (MW) signal is first amplified and then fed into the TL microwave probe. The EPR sample is positioned on top of the probe, which is placed within an external magnetic field. The transmitted signal at the output of the microwave probe is downconverted using an in-phase quadrature (IQ) mixer driven by a local oscillator (LO). The resulting signal is then measured at a fixed intermediate frequency (IF). This configuration follows a superheterodyne architecture, a common approach in VNAs. The complex output signal corresponds to the transmission coefficient S_{21}, which can be expressed as

$$S_{21} = s_{21} e^{\mathrm{j}\varphi_{21}}, \tag{2.4}$$

where $s_{21} = |S_{21}|$ denotes the magnitude and φ_{21} the phase of the transmission coefficient. At the EPR resonance condition, the magnetic moments of the unpaired electrons undergo transitions between spin states, leading to microwave energy absorption. This results in a change in the transmitted power through the TL microwave probe. Consequently, a change in the magnitude s_{21} corresponds to the absorptive component of the EPR response. The dispersive component is in quadrature with the absorptive component and therefore appears in the transmission phase φ_{21}. To link the absorption and dispersion to the measured S_{21} parameter, a mathematical formalism is developed in the following section.

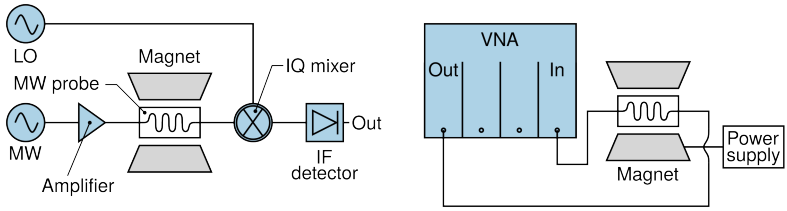

(a) (b)

Figure 2.2: (a) System architecture and (b) proof-of-concept measurement setup for the quadrature detection.

2.3.2 Mapping Absorption and Dispersion to S_{21}

To quantify the relationship between the EPR response and the measured transmission coefficient, the absorption and dispersion are modeled as α and β, respectively. The normalized EPR signal can be expressed as

$$\frac{E_t}{E_0} = (1-\alpha)\cdot\cos(\omega_0 t) + \beta\cdot\sin(\omega_0 t), \tag{2.5}$$

where E_t denotes the transmission signal containing the EPR signal, E_0 the input signal, and ω_0 the measured angular frequency. The quadrature relationship between absorption and dispersion is represented by the cosine and sine terms. The magnitude of the transmission coefficient is then

$$s_{21} = \sqrt{(1-\alpha)^2+\beta^2} = \sqrt{1-2\alpha+\alpha^2+\beta^2}. \tag{2.6}$$

Since the population difference between the lower and upper spin states in thermal equilibrium is small [WB07], the overall EPR effect is weak compared to the transmitted microwave signal. Consequently, the parameters α and β are much smaller than one, i.e. $\alpha, \beta \ll 1$. Under this condition, second-order terms α^2 and β^2 can be neglected, and the Taylor series expansion yields

$$s_{21} \approx \sqrt{1-2\alpha} \approx 1-\alpha, \tag{2.7}$$

confirming that the magnitude s_{21} approximately represents the absorptive component of the EPR signal.

The phase of the transmission coefficient is

$$\varphi_{21} = \arctan\left(\frac{\beta}{1-\alpha}\right) \approx \arctan(\beta)\,, \tag{2.8}$$

demonstrating that φ_{21} corresponds approximately to the dispersive component of the signal. Given that α is much smaller than one, it can be neglected in the first-order approximation.

2.3.3 Proof-of-Concept Measurements

The quadrature system architecture and the derived relations between the absorption and dispersion with respect to S_{21} are verified through proof-of-concept measurements. The setup shown in Fig. 2.2b is employed for this purpose. The components highlighted in blue in the block diagram (Fig. 2.2a) are all internally integrated into the VNA.

Raw Measurement Data

Fig. 2.3 shows the raw measurement results of the transmission coefficient. During the measurement, the magnetic field is swept while the microwave frequency is fixed at $f_{0,\mathrm{r}} = 19.72\,\mathrm{GHz}$. According to the Zeeman resonance condition, the resonance peak is expected at $B_{0,\mathrm{r}} = 704.5\,\mathrm{mT}$. The measured resonance peak is slightly shifted from this theoretically predicted magnetic field value. This shift is most likely caused by imperfect synchronization between the start of the magnetic field sweep and the VNA frequency sweep, which are manually triggered.

The VNA is configured to record 2001 points with an IF bandwidth of 200 Hz, resulting in a total measurement time of 42 s. The output power of the VNA is set to $P_0 = 12\,\mathrm{dBm}$, and the magnetic field step size is $0.02\,\mathrm{mT/point}$. The raw measurement confirms that the magnitude s_{21} reflects the absorptive response, while the phase φ_{21} represents the dispersive response of the sample (see the characteristic shapes of both components in Fig. 1.5 in Section 1.2.1).

Fig. 2.4 shows the raw measurement data in the complex plane, including an overview and a zoomed-in view of the trajectory. This representation plays a

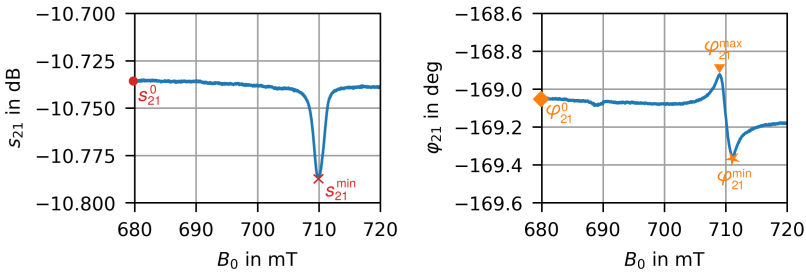

(a) (b)

Figure 2.3: Raw measurement data of the quadrature detection setup showing (a) the magnitude s_{21} and (b) the phase φ_{21} at the fixed frequency $f_{0,r} = 19.72\,\text{GHz}$. According to the Zeeman resonance condition, the resonance peak is expected at $B_{0,r} = 704.5\,\text{mT}$, but appears slightly shifted due to timing inaccuracies in the manual triggering of the measurements. Adapted from [3], ©IEEE.

key role in analyzing the interferometric detection and is therefore examined in detail to serve as the basis for understanding the interferometric behavior. The zoomed-in view shows that the trajectory traces an elliptical-like shape, which contains the full variation of both s_{21} and φ_{21}. To aid interpretation, several representative points are marked: for the magnitude, s_{21}^0 denotes the initial measurement point where no EPR effect occurs and s_{21}^{min} indicates the minimum magnitude, corresponding to the point of maximum EPR absorption. For the phase, φ_{21}^0 corresponds to the initial measurement value, while φ_{21}^{min} and φ_{21}^{max} represent the minimum and maximum phase values, respectively. These reference points are also highlighted in Fig. 2.3.

In the overview plot of Fig. 2.4, the data are plotted relative to the origin. The arrow tip indicates the position of each data point at a given magnetic field step, while the arrow length represents the magnitude s_{21}, and its angle corresponds to φ_{21}. The absolute values of magnitude and phase at the first measurement point are arbitrary and depend on the measurement setup. However, the elliptical-like shape remains invariant, and its short axis (connection from s_{21}^0 and s_{21}^{min}) consistently points toward the origin. Consequently, the magnitude s_{21} always represents the absorptive component, and φ_{21} the dispersive component, independent of the initial magnitude s_{21}^0. Note that the extent of φ_{21}^{min} and φ_{21}^{max} depends on the initial magnitude s_{21}^0 and does not convey quantitative

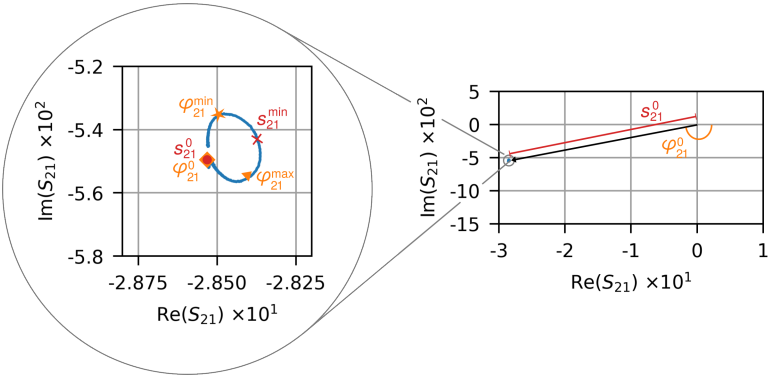

Figure 2.4: Raw measurement data of the quadrature detection setup of S_{21} at $f_{0,\mathrm{r}} = 19.72\,\mathrm{GHz}$ in the complex plane. Adapted from [3], ©IEEE.

information. However, the absolute values are typically not required in standard EPR measurements.

Post-Processed Measurement Data

The large background transmission signal can be removed by performing a reference measurement. The simplest approach is to repeat the measurement with the magnetic field set to a fixed off-resonance value (without sweeping), yielding a reference signal $s_{21,\mathrm{ref}}$ to subtract from the raw EPR data s_{21}:

$$\Delta s_{21} = s_{21} - s_{21,\mathrm{ref}} \tag{2.9}$$

For the raw measurement result in Fig. 2.3, the reference magnetic field is set to $B_0 = 630\,\mathrm{mT}$, which is far away from the resonance peak at $B_{0,\mathrm{r}} = 704.5\,\mathrm{mT}$. This post-processing step eliminates the static background transmission of the setup, including losses and phase offsets, and therefore eliminates the need for prior calibration. The corrected EPR measurement results are shown as blue curves in Fig. 2.5, while the purple curves correspond to measurements taken without a sample. For the data presented here, a reference measurement is not strictly required, as the background signal is nearly flat and the EPR feature can be directly identified. However, a small residual background remains visible

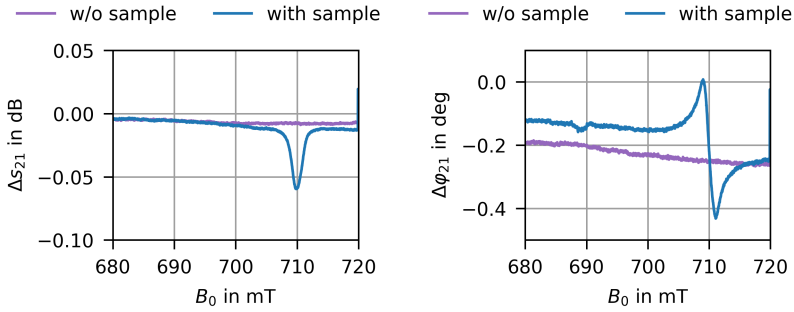

(a) (b)

Figure 2.5: Post-processed proof-of-concept measurements for the quadrature detection setup at $f_{0,\mathrm{r}} = 19.72\,\mathrm{GHz}$ for (a) the magnitude of S_{21} and (b) the phase of S_{21}.

in the post-processed data. To further suppress this residual, an alternative reference can be acquired at an off-resonance microwave frequency while sweeping the magnetic field, instead of using a fixed field and frequency. In this case, to correct for frequency-dependent variations introduced by dielectric losses and impedance mismatches, the entire VNA system, including the TL microwave probe, must be properly calibrated.

The measurements can also be performed by sweeping the frequency while keeping the magnetic field constant. In this case, a reference measurement is typically necessary to account for frequency-dependent variations in S_{21} which are often much larger than the EPR signal itself.

To enable a qualitative comparison of the three system architectures, a rough SNR estimate is derived for each measurement. Since the sample is removed and reapplied when changing setups and the measurement times differ slightly between the systems, the resulting SNR values must not be interpreted quantitatively, but only as approximate reference values for comparing the different approaches. The EPR signal strength is extracted from the post-processed trace Δs_{21} as the peak depth, defined as the difference between the signal value at $B_0 = 705\,\mathrm{mT}$ and the minimum value of the resonance dip. The root-mean square (RMS) noise level is estimated as the standard deviation of the measurement fluctuations in an off-resonance magnetic-field interval

($B_0 = 680\,\mathrm{GHz} - 700\,\mathrm{mT}$), where no EPR contribution is expected. Since the measured transmission data exhibits slow residual baseline variations, a baseline estimate is obtained in this interval using a Savitzky–Golay filter (window size 100 points, 5th-order polynomial) and subtracted before computing the standard deviation, such that the residual noise is centered around zero. A Savitzky–Golay filter smooths the data by fitting a low-order polynomial to a moving window of points, which reduces noise while preserving the shape of the signal [SG51]. For the quadrature-detection dataset at 19.72 GHz, this yields a signal depth of 5.5×10^{-3} (linear units) and a noise standard deviation of 3×10^{-5}, resulting in SNR ≈ 182.

Broadband Capabilities and On-Chip Consideration

To demonstrate the system's multi-frequency capabilities, the measurements are repeated at a lower microwave frequency of $f_{0,\mathrm{r}} = 9.86\,\mathrm{GHz}$, resulting in an EPR resonance at $B_{0,\mathrm{r}} = 352\,\mathrm{mT}$. The magnetic-field sweep range is adjusted accordingly to cover this resonance position. The corresponding results are shown in Fig. 2.6. Again, the resonance peak is slightly shifted due to

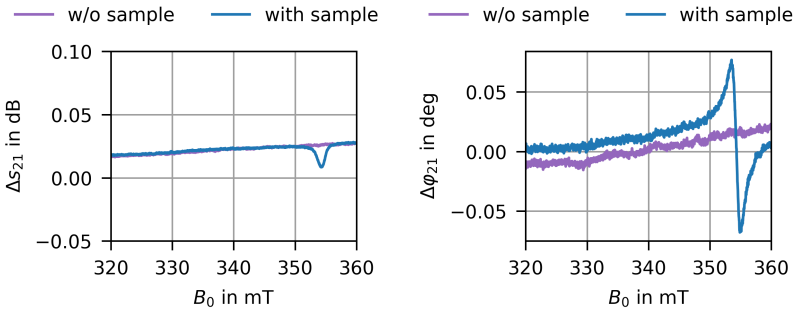

Figure 2.6: Post-processed proof-of-concept measurement data for the quadrature detection setup at $f_{0,\mathrm{r}} = 9.86\,\mathrm{GHz}$, obtained after subtraction of the large transmission signal. (a) Magnitude Δs_{21} and (b) the phase $\Delta\varphi_{21}$. According to the Zeeman resonance condition, the resonance peak is expected at $B_{0,\mathrm{r}} = 352\,\mathrm{mT}$, but appears slightly shifted due to timing inaccuracies in the manual triggering of the measurements.

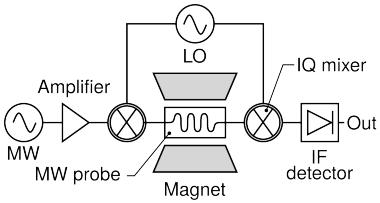

Figure 2.7: Optimized system architecture for quadrature detection to reduce the influence of the LO's phase noise.

timing inaccuracies in the manual triggering of the measurements. The reference measurement is recorded at an off-resonance magnetic field of $B_0 = 270\,\mathrm{mT}$. As expected from the smaller Zeeman splitting and thus reduced spin population difference (see Eq. 1.7), the EPR peak amplitude decreases compared to the measurements at $f_{0,\mathrm{r}} = 19.72\,\mathrm{GHz}$.

When considering an on-chip implementation of the quadrature detection system, the modified architecture shown in Fig. 2.7 is proposed. In this configuration, the microwave source operates at a lower base frequency, which is upconverted using a mixer driven by a LO. This approach relaxes the design and performance requirements for the on-chip microwave source. The same LO is also employed for downconversion after the microwave probe, ensuring that both mixers share a common reference. As a result, any phase noise introduced by the LO is effectively canceled. In addition, integrating a low-noise amplifier before the downconversion mixer can further improve the overall sensitivity by reducing the effective noise figure of the system.

2.4 Interferometric Detection

2.4.1 Concept

For interferometric detection, a reference arm is added to the quadrature measurement setup to enable destructive interference at the resonance frequency $f_{0,\mathrm{r}}$. This configuration effectively cancels out the dominant transmission signal that does not contain any EPR information. As a result, only the small

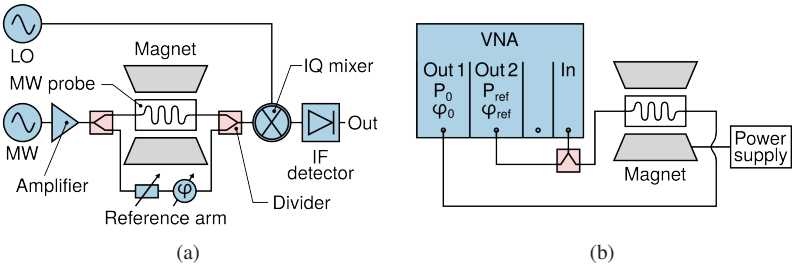

Figure 2.8: (a) System architecture and (b) proof-of-concept measurement setup for the interferometric detection. Adapted from [3], ©IEEE.

EPR-induced signal variation remains at the output. The corresponding block diagram is shown in Fig. 2.8. The reference arm comprises a variable attenuator and a phase shifter, while the input signal is divided by a power splitter and recombined at the output using another power splitter.

This selective suppression results in a key advantage in that the analog-to-digital converter no longer needs to allocate dynamic range to digitize large, irrelevant background signals. Consequently, a higher effective resolution can be dedicated to the informative part of the signal without increasing the total bit depth, potentially improving the sensitivity of the detection system.

2.4.2 Proof-of-Concept Measurements

To perform the proof-of-concept measurements for the interferometric detection, the setup shown in Fig. 2.8b is employed. Instead of realizing the reference arm with a discrete phase shifter and attenuator, a four port VNA is used. Commercial phase shifters that operate over several tens of GHz with fine resolution are not readily available, making the VNA a practical and flexible alternative. In addition, this allows to automate the whole measurement procedure.

The Keysight PNA-X N5242B features two coherent microwave sources. Using the *Differential I/Q Mode* software option, the phase and amplitude of one source can be precisely controlled relative to the other, thereby reproducing the interferometric setup. In this configuration, source 1 provides the main

excitation signal, while source 2 acts as the reference arm, its amplitude and phase being defined relative to source 1.

The interferometric detection proceeds in two main stages: (1) tuning the system to achieve optimal destructive interference, and (2) performing the actual EPR measurement under the optimized conditions. The full measurement procedure is partially automated and consists of the following four steps:

1. Initialization: Both sources are set to $P = 12\,\mathrm{dBm}$, $\varphi = 0°$ and the resonance frequency $f_{0,\mathrm{r}}$ is defined.

2. Coarse Tuning: Destructive interference is achieved by minimizing $|S_{21}(f_{0,\mathrm{r}})|$ through sweeping the reference phase φ_{ref} and power P_{ref}. First, φ_{ref} is varied from 0° to 360° in 0.1° steps to identify $\varphi_{\mathrm{ref,min}}$. Then, with this phase fixed, P_{ref} is swept from −20 dBm to 12 dBm in 0.1 dB steps to find $P_{\mathrm{ref,min}}$.

3. Fine Tuning: With $P_{\mathrm{ref,min}}$ fixed, a high-resolution phase sweep from $\varphi_{\mathrm{ref,min}} - 3°$ to $\varphi_{\mathrm{ref,min}} + 3°$ in 0.005° steps is conducted to refine $\varphi_{\mathrm{ref,min}}$. Subsequently, a fine power sweep around $P_{\mathrm{ref,min}}$ (from $P_{\mathrm{ref,min}} - 1\,\mathrm{dB}$ to $P_{\mathrm{ref,min}} + 1\,\mathrm{dB}$ in 0.01 dB steps) is performed.

4. EPR measurement: Using the optimized values $\varphi_{\mathrm{ref,min}}$ and $P_{\mathrm{ref,min}}$ for source 2, the magnetic field is swept to acquire the EPR signal. The measurement is performed at fixed frequency $f_{0,\mathrm{r}}$, using the same number of points and IF bandwidth as in the quadrature detection.

Similar to the quadrature detection, a reference measurement at an off-resonance magnetic field can be performed to eliminate any background signal.

Fig. 2.9 shows the results obtained at $f_{0,\mathrm{r}} = 19.72\,\mathrm{GHz}$, resulting again in a resonance peak near $B_{0,\mathrm{r}} = 704.5\,\mathrm{mT}$. Source 1 is configured as described above with $P_0 = 12\,\mathrm{dBm}$ and $\varphi_0 = 0°$. Destructive interference is achieved at $P_{\mathrm{ref,min}} = 3.12\,\mathrm{dBm}$ and $\varphi_{\mathrm{ref,min}} = 178.980°$. Compared to the quadrature detection in Fig. 2.3a, the transmission signal is suppressed by approximately 41.6 dB.

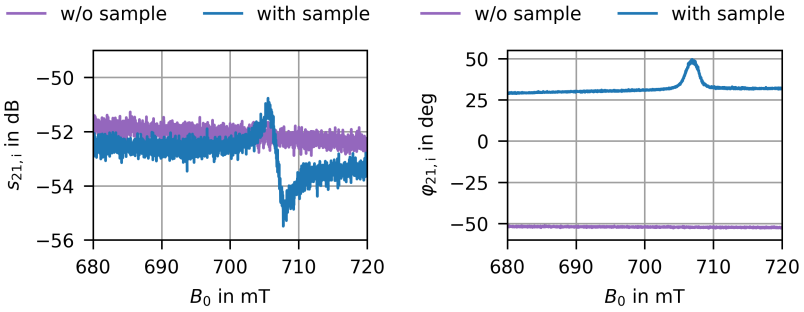

(a) (b)

Figure 2.9: (a) Magnitude $s_{21,\mathrm{i}}$ and (b) phase $\varphi_{21,\mathrm{i}}$ of the raw measurement results for the interferometric detection at $f_{0,\mathrm{r}} = 19.72\,\mathrm{GHz}$. According to the Zeeman resonance condition, the resonance peak is expected at $B_{0,\mathrm{r}} = 704.5\,\mathrm{mT}$, but appears slightly shifted due to timing inaccuracies in the manual triggering of the measurements. Adapted from [3], ©IEEE.

In the interferometric measurement results, the magnitude $s_{21,\mathrm{i}}$ exhibits an apparently dispersive line shape, while the phase $\varphi_{21,\mathrm{i}}$ resembles an absorptive response, which is opposite to what is typically observed in quadrature detection. It will be shown that this behavior is specific to the measurement configuration used here. In general, depending on the interference conditions, a superposition of the absorptive and dispersive components can appear in both the magnitude $s_{21,\mathrm{i}}$ and the phase $\varphi_{21,\mathrm{i}}$. To resolve these mixed contributions, a dedicated post-processing method is introduced, ensuring that the pure absorptive signal is represented in the magnitude $s_{21,\mathrm{i}}$, while the dispersive component is contained in the phase $\varphi_{21,\mathrm{i}}$.

2.4.3 Post-Processing Scheme

The underlying reason for the apparent inversion of absorption and dispersion becomes evident when the measurement data are analyzed in the complex plane. The results of Fig. 2.9 are represented in Fig. 2.10a. The initial measurement point of the magnitude $s^0_{21,\mathrm{i}}$ is slightly offset from the origin due to non-ideal destructive interference. Given the very small amplitude of the EPR

response, the remaining imbalance is of comparable size and therefore non-negligible. While the signal still traces an elliptical-like trajectory, the short axis of the ellipse does not point toward the origin. This rotation results from the combination of the global arbitrary phase offset φ_{21}^{0}, which was already discussed in the context of quadrature detection, and residual phase and amplitude imbalances caused by imperfect destructive interference in the interferometric setup. Together, these effects result in an arbitrary shift of both the real and imaginary components of the measured signal.

To recover a pure absorptive response in the magnitude $s_{21,\mathrm{i}}$ and a pure dispersive response in the phase $\varphi_{21,\mathrm{i}}$, the raw data in the complex plane are rotated around their initial value by a correction phase φ_{c} such that the short axis of the ellipse aligns with the origin. Geometrically, this step corresponds to a rotation of $\mathbf{r}'$ around $\mathbf{r_0}$ by the angle φ_{c} [BHL+12]

$$\vec{r} = \vec{r}_0 + \begin{pmatrix} \cos\varphi_{\mathrm{c}} & -\sin\varphi_{\mathrm{c}} \\ \sin\varphi_{\mathrm{c}} & \cos\varphi_{\mathrm{c}} \end{pmatrix} (\vec{r'} - \vec{r}_0), \tag{2.10}$$

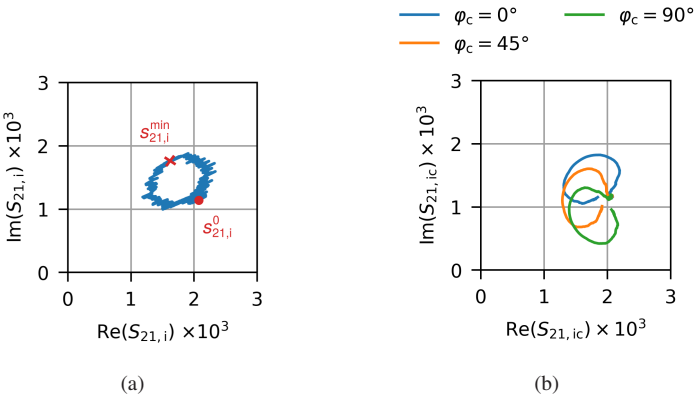

(a) (b)

Figure 2.10: (a) Raw and (b) post-processed measurement results for the interferometric detection at $f_{0,\mathrm{r}} = 19.72\,\mathrm{GHz}$. Adapted from [3], ©IEEE.

with

$$\vec{r_0} = \begin{pmatrix} \mathrm{Re}\, S^0_{21,\mathrm{i}} \\ \mathrm{Im}\, S^0_{21,\mathrm{i}} \end{pmatrix}, \quad \vec{r'} = \begin{pmatrix} \mathrm{Re}\, S_{21,\mathrm{i}} \\ \mathrm{Im}\, S_{21,\mathrm{i}} \end{pmatrix}. \tag{2.11}$$

The equivalent complex expression is

$$S_{21,\mathrm{ic}} = S^0_{21,\mathrm{i}} + e^{\mathrm{j}\varphi_\mathrm{c}} \left(S_{21,\mathrm{i}} - S^0_{21,\mathrm{i}} \right). \tag{2.12}$$

Fig. 2.10b illustrates the rotated transmission coefficient $S_{21,\mathrm{ic}}$ for three different correction angles. A Savitzky-Golay filter is applied to the data in order to reduce the noise and better reveal the underlying signal trend. A window size of 100 points and a polynomial order of five are used. The corresponding magnitude and phase of the corrected signal are shown in Fig. 2.11.

For the data shown, applying a correction phase of approximately $\varphi_\mathrm{c} = 90°$ aligns the magnitude $s_{21,\mathrm{ic}}$ with the absorptive response and the phase $\varphi_{21,\mathrm{ic}}$ with the dispersive response. This correction phase of about 90° also explains why the absorption and dispersive signals appeared reversed in the unprocessed data.

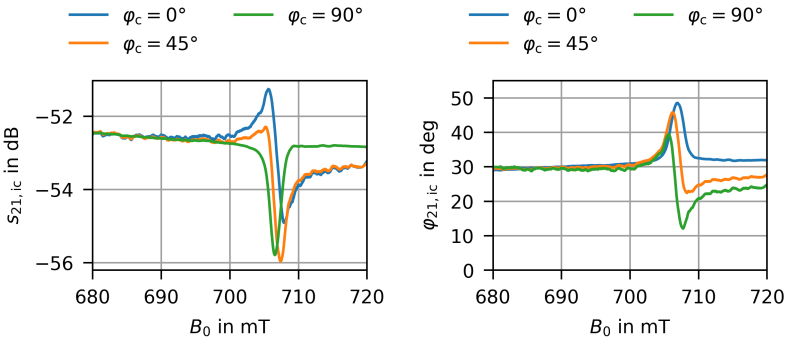

(a) (b)

Figure 2.11: Post-processed data of the interferometric detection setup at $f_{0,\mathrm{r}} = 19.72\,\mathrm{GHz}$. Savitzky–Golay–filtered results are shown for three different correction angles φ_c: (a) the magnitude $s_{21,\mathrm{ic}}$ and (b) the phase $\varphi_{21,\mathrm{ic}}$. Adapted from [3], ©IEEE.

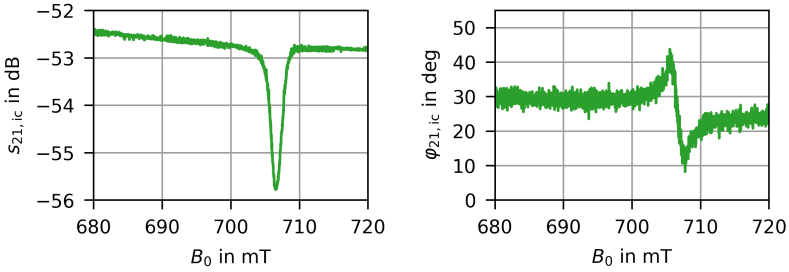

(a) (b)

Figure 2.12: Post-processed data of the interferometric detection setup at $f_{0,\mathrm{r}} = 19.72\,\mathrm{GHz}$. Unfiltered results are shown for the correction angle $\varphi_{\mathrm{c}} = 90°$.

The final unfiltered post-processed data for $\varphi_{\mathrm{c}} = 90°$ are shown in Fig. 2.12. The SNR is determined analogously to Section 2.3.3. The signal depth is extracted relative to $B_0 = 700\,\mathrm{mT}$. This yields a signal depth of 6.8×10^{-4} and a noise standard deviation of 6.9×10^{-6}, resulting in SNR ≈ 100.

Under ideal conditions, i.e., when realizing the interferometric detection according to Fig. 2.8 using a dedicated passive reference arm driven by a single microwave source, approximately the same SNR would be expected for interferometric and quadrature detection, assuming that the receiver dynamic range is not limiting (as is typically the case when using a high-end VNA). In the presented proof-of-concept measurements, however, the interferometric setup exhibits a lower SNR compared to the quadrature detection. The most likely cause is the use of two coherent VNA sources to synthesize the reference arm, which introduces additional noise, effectively increasing the measurement noise level.

2.4.4 Comparison to the Resonator-based Approach

The working principle of the interferometric setup shares key similarities with the resonator-based EPR spectrometer. In both approaches, the first step is to suppress the large transmission signal. In the resonator-based method, this is done by tuning the resonator so that the magnitude of the reflection

coefficient s_{11} reaches a minimum at the resonance frequency $f_{0,\mathrm{r}}$. In the interferometric setup, suppression is achieved by adjusting the reference arm to create destructive interference. Since this interference occurs only within a narrow frequency band around $f_{0,\mathrm{r}}$, the tuning curves of the magnitudes s_{11} and s_{21} appear nearly identical. Unlike the resonator-based method, however, the interferometric setup remains broadband, as the reference arm can be reconfigured for each resonance frequency $f_{0,\mathrm{r}}$ without relying on a narrowband structure.

Instead of measuring the magnitude and phase of the transmission coefficient at a fixed frequency, one could alternatively sweep the frequency for each magnetic-field step and extract the magnitude s_{21} as a function of frequency. Similar to the resonator-based approach, absorption manifests as an increase in the minimum magnitude s_{21}^{min}, while dispersion results in a shift of the frequency at which this minimum occurs [CSW17]. By tracking these minima for each magnetic-field step, the absorption signal can be directly reconstructed. However, this method requires significantly more data points per magnetic step and therefore results in longer overall acquisition times compared to fixed-frequency measurements.

While the resonator-based spectrometer also uses a reference arm, its purpose is fundamentally different from that in the interferometric setup. It is mainly used to set the optimal operating point of the detector. In the interferometric setup, a second reference arm could be introduced to control the global phase φ_{21}^{0} such that the absorption signal is directly mapped to the magnitude $s_{21,\mathrm{i}}$ [SAA+19]. Alternatively, an automatic frequency-control scheme, similar to that used in resonator-based spectrometers, could be implemented to lock the source frequency to the EPR resonance.

2.4.5 Proposed On-Chip System Architecture

From a circuit design perspective, it is particularly challenging to realize a broadband phase shifter and attenuator with high resolution. To address this, the modified system architecture shown in Fig. 2.13 is proposed as a concept for potential on-chip realization.

In this configuration, the design requirements of the reference arm are relaxed by shifting its functionality into the IF frequency domain. Both the phase shifter and the attenuator can then be designed to operate at a fixed IF frequency, rather than

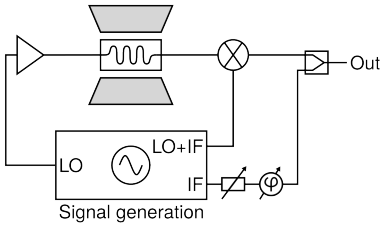

Figure 2.13: Optimized system architecture for the interferometric setup to relax the design requirements of the phase shifter and attenuator in the reference arm.

across the entire system bandwidth. This modification significantly simplifies circuit implementation and illustrates how the interferometric detection scheme could be adapted for an integrated on-chip EPR spectrometer.

2.5 Lock-In Detection

2.5.1 Concept

The lock-in approach is based on external magnetic field modulation combined with a LIA and is illustrated in Fig. 2.14a. By modulating the external magnetic field, the strength of the EPR effect in the sample varies periodically, which results in an amplitude-modulated (AM) signal at the input of the detector. An AM signal consists of three frequency components in the frequency domain. These are the carrier frequency f_0 and the two sidebands at $f_0 \pm f_\mathrm{m}$, where f_m denotes the modulation frequency. The carrier component at f_0 contains the unmodulated background transmission. The sidebands at $f_0 \pm f_\mathrm{m}$ carry both the transmission signal and the EPR signal.

Using a detector as a demodulator, the output signal contains all possible sums and differences of the three input frequency components. Among these, the EPR signal specifically appears at the modulation frequency f_m, spectrally separated from the dominant background at zero frequency. Therefore, the EPR signal becomes accessible in the frequency domain as an isolated tone at f_m, where it is no longer masked by the strong unmodulated transmission background. The LIA then downconverts this signal using a LO at f_m, which is also used to

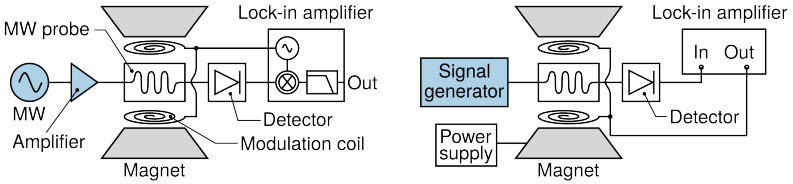

Figure 2.14: (a) System architecture and (b) proof-of-concept measurement setup for the lock-in detection combined with a modulated magnetic field.

drive the external magnetic-field modulation. After downconversion, the EPR signal appears at direct current (DC), allowing a very narrow low-pass filter to be applied to maximize sensitivity. A detailed analysis of the complete setup is presented in Section 3.1.1.

2.5.2 Mapping Absorption to V_{EPR}

To describe how absorption and dispersion manifest in the lock-in detection approach, the mathematical model developed in Section 2.3.2 is adapted accordingly. Compared to the quadrature approach, where absorption and dispersion are measured as steady responses to a slowly swept magnetic field, both components are here periodically modulated in time by the external magnetic-field modulation introduced in Chapter 1.2.3. In the small-modulation regime, the resulting first-order Taylor approximation yields a sinusoidal modulation of the absorptive and dispersive response coefficients, which can be expressed using the amplitude-modulation formalism [Poz21]

$$\alpha(t) = \alpha_0 \left(1 - m_\mathrm{B} \cos(\omega_\mathrm{m} t)\right) \tag{2.13}$$

$$\beta(t) = \beta_0 \left(1 - m_\mathrm{B} \cos(\omega_\mathrm{m} t)\right), \tag{2.14}$$

where m_B denotes the magnetic-field modulation index. It represents the normalized modulation depth of the EPR response and is proportional to the

modulation amplitude and the local slope of the resonance (see Eq. 1.23). For the absorptive response, this relationship can be written as

$$m_{\mathrm{B}} = -\frac{B_{\mathrm{m}}}{\alpha_0}\alpha'\left(B^i_{0,\mathrm{s}}\right), \tag{2.15}$$

with an analogous definition for $\beta(B)$.

Substituting $\alpha(t)$ and $\beta(t)$ into Eq. 2.5 gives

$$\begin{aligned}\frac{E_{\mathrm{t}}}{E_0} = {} & 1 \cdot \cos(\omega_0 t) - \alpha_0 \cdot \cos(\omega_0 t)\,(1 - m_{\mathrm{B}}\cos(\omega_{\mathrm{m}} t)) \\ & + \beta_0 \cdot \sin(\omega_0 t)\,(1 - m_{\mathrm{B}}\cos(\omega_{\mathrm{m}} t))\,.\end{aligned} \tag{2.16}$$

By using the following addition theorems [BHL+12]:

$$\cos(A)\cdot\cos(B) = \frac{1}{2}\left(\cos(A+B) + \cos(A-B)\right) \tag{2.17}$$

$$\sin(A)\cdot\cos(B) = \frac{1}{2}\left(\sin(A-B) + \sin(A+B)\right) \tag{2.18}$$

Eq. 2.16 can be rewritten as

$$\begin{aligned}\frac{E_{\mathrm{t}}}{E_0} = {} & (1-\alpha_0)\cos(\omega_0 t) + \beta_0 \sin(\omega_0 t) \\ & + \left(\alpha_0 \frac{m_{\mathrm{B}}}{2}\right)\cdot\cos((\omega_0+\omega_{\mathrm{m}})t) - \left(\beta_0\frac{m_{\mathrm{B}}}{2}\right)\cdot\sin((\omega_0+\omega_{\mathrm{m}})t) \\ & + \left(\alpha_0 \frac{m_{\mathrm{B}}}{2}\right)\cdot\cos((\omega_0-\omega_{\mathrm{m}})t) - \left(\beta_0\frac{m_{\mathrm{B}}}{2}\right)\cdot\sin((\omega_0-\omega_{\mathrm{m}})t).\end{aligned} \tag{2.19}$$

At the carrier frequency ω_0, the signal components are identical to those observed in the quadrature detection scheme. Both the absorptive and dispersive responses of the EPR signal are present and superimposed in the same manner. The amplitudes at the sidebands are described by the last four terms in Eq. 2.19.

This modulated signal is present at the input of the detector diode. The diode acts as a nonlinear device that demodulates the AM signal and translates the high-

frequency components into baseband. The diode current can be approximated by its Taylor series [Poz21]

$$I_{\mathrm{D}}(v) = I_{\mathrm{S}} \cdot \exp\left(\frac{v}{V_{\mathrm{T}}}\right) = I_0 + v \cdot G_{\mathrm{D}} + \frac{v^2}{2} \cdot G'_{\mathrm{D}} + O(v^3), \tag{2.20}$$

where I_{S} is the reverse-bias saturation current, V_{T} is the thermal voltage, and G_{D} denotes the dynamic conductance of the diode and G'_{D} its derivative. By multiplying Eq. 2.19 by E_0, the transmitted field E_{t} is obtained and can be substituted for v. Terms with orders higher than two are neglected because their contribution to the signal at f_{m} scale with the higher powers of the modulation index m_{B} and are therefore much smaller than the dominant quadratic term, which scales linearly with m_{B}. Collecting the terms according to their order, the diode current at f_{m} becomes

$$I_{\mathrm{D},f_{\mathrm{m}}}(v) = \frac{G'_{\mathrm{D}}}{2}\left(\left(\alpha_0 m_{\mathrm{B}} - \alpha_0^2 m_{\mathrm{B}} - \beta_0^2 m_{\mathrm{B}}\right) \cdot \cos(\omega_{\mathrm{m}} t) + 0 \cdot \sin(\omega_{\mathrm{m}} t)\right) E_0^2 \tag{2.21}$$

$$= \frac{1}{2} G'_{\mathrm{D}} \alpha_0 m_{\mathrm{B}} \cos(\omega_{\mathrm{m}} t) E_0^2. \tag{2.22}$$

Analogous to the quadrature detection, the second-order terms α_0^2 and β_0^2 can be neglected in a first-order approximation. Since only the squared terms lead to a frequency translation at f_{m}, the sine components cancel out, and only the absorption signal remains at the output of the detector.

2.5.3 Proof-of-Concept Measurements

To validate the system concept, proof-of-concept measurements are performed at the resonance frequencies of $f_{0,\mathrm{r}} = 9.86\,\mathrm{GHz}$ and $f_{0,\mathrm{r}} = 19.72\,\mathrm{GHz}$. The corresponding results are shown in Fig. 2.15, measured using the setup illustrated in Fig. 2.14b. An input power of $P_0 = 12\,\mathrm{dBm}$ is used. The parameters of the LIA are set to a modulation amplitude of 10 V and a modulation frequency of $f_{\mathrm{m}} = 30\,\mathrm{kHz}$. 512 points are acquired over a measurement time of 30 s. The magnetic field steps are 0.08 mT/points. Due to magnetic field modulation, the measured EPR spectrum exhibits a first-derivative line shape of the absorption

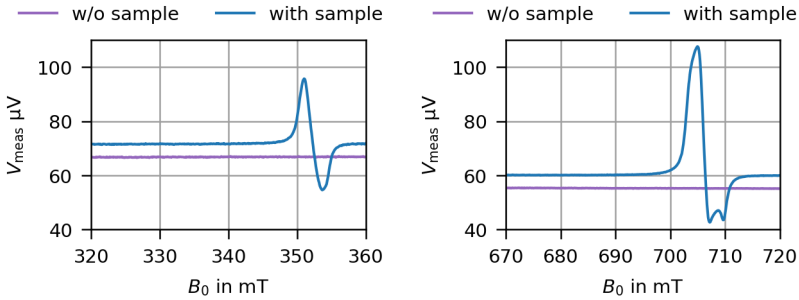

Figure 2.15: Proof of concept measurements for the lock-in detection setup at (a) $f_{0,r} = 9.86\,\text{GHz}$, and (b) $f_{0,r} = 19.72\,\text{GHz}$.

signal. The y-axis shows the voltage amplitude directly acquired by the LIA and is denoted as V_{meas}.

Both measurement results demonstrate that the EPR signal is clearly distinguishable. However, an offset is visible, and in particular, the response at $f_{0,r} = 19.72\,\text{GHz}$ appears distorted. As will be discussed in detail in Chapter 3, these effects originate from an unwanted interference path. Nonetheless, the EPR signal can be recovered using an appropriate post-processing scheme which will be introduced. For the results shown in this section, only amplitude data were recorded. However, to enable the post-processing scheme, full information about the signal, including phase, is required.

For the measurement data at 19.72 GHz in Fig. 2.15b, the SNR is determined as follows. The EPR signal amplitude is extracted from the lock-in output as the peak-to-peak voltage of the derivative-shaped resonance, defined as the voltage difference between the minimum and maximum peak. Since the response is slightly distorted, the smaller of the two minima is used, resulting in a conservative estimate of the signal amplitude. The noise is evaluated in the off-resonance magnetic-field range $B_0 = 680\,\text{mT} - 690\,\text{mT}$. The mean value in this interval is subtracted to remove the DC offset before calculating the standard deviation, such that the noise fluctuations are centered around zero as required for an RMS estimate. This yields a signal amplitude of $6.5 \times 10^{-5}\,\text{V}$ and a noise standard deviation of $3.6 \times 10^{-8}\,\text{V}$, resulting in SNR ≈ 1800. Interpreting

this value in the context of measurement bandwidth, the effective integration time of 60 ms per point corresponds to an equivalent noise bandwidth on the order of 17 Hz. This is roughly one order of magnitude smaller than the 200 Hz IF bandwidth used in the quadrature approach, which provides a plausible explanation for the observed factor-of-ten difference in SNR.

2.5.4 Comparison to the Resonator-based Approach

In both cases, magnetic field modulation transfers the EPR response to sidebands at $f_0 \pm f_m$ and, after the detector, the EPR signal appears at the modulation frequency f_m, which is demodulated and filtered by the LIA to improve the SNR. The principal difference is how the large carrier background at f_0 is handled.

In the resonator-based approach, the resonator is critically coupled in the off-resonance condition, ideally suppressing the reflected carrier. As a consequence, the signal at the detector input is largely dominated by the modulation-related components rather than by a strong unmodulated background. The reference arm is therefore required to set its operating point. In contrast, for the TL-based approach, a large carrier transmission is inherently present at the detector input. This carrier provides a sufficiently strong background level to bias the detector without requiring an additional reference arm.

Finally, an additional mechanism to separate absorption and dispersion is not required in the TL-based lock-in architecture. Since only the absorptive component contributes to the detected tone at f_m after square-law demodulation, the lock-in signal directly corresponds to the field-derivative of the absorption line shape.

2.6 Summary and Discussion

In this chapter, three system architectures for TL-based EPR were analyzed and compared, each addressing the central challenges of this approach: the inherently lower sensitivity caused by the use of nonresonant microwave probes and the need to separate the strong transmission signal from the much weaker EPR response.

The lock-in, quadrature, and interferometric detection schemes were introduced and evaluated in detail. Proof-of-concept measurements were carried out for all three systems, supported by analytical models describing how dispersion and absorption manifest in each setup.

Quadrature detection represents the most straightforward method for extracting the absorption signal generated by the EPR sample. Both the transmission and EPR signals are measured at the intermediate frequency, and the transmission component is subsequently removed during post-processing. In this scheme, the absorption signal is proportional to the magnitude of the transmission coefficient s_{21}, while the dispersion is proportional to its phase φ_{21}.

Interferometric detection most closely resembles the resonator-based approach, as both suppress the dominant transmission signal. In a resonator-based system, suppression is achieved by critical coupling of the resonator, whereas in the interferometric setup it results from destructive interference between the signal path and a tunable reference arm. The interference produces a distinct dip in the transmitted signal when both paths have equal amplitude and a phase difference of 180°, effectively canceling the signal. When an EPR sample is introduced, the absorption and dispersion components modify the amplitude and phase of the signal path, which in turn alter the depth and frequency position of this interference dip. The absorption is therefore proportional to the change in signal amplitude at the point of destructive interference $\Delta s_{21}^{\min}$, while the dispersion corresponds to the frequency shift of the dip $\Delta f\left(s_{21}^{\min}\right)$. For the proof-of-concept demonstration, a four port VNA was employed to realize automatic tuning to the condition of destructive interference, eliminating the need for manually adjusted components in the reference arm at the cost of a higher noise level.

The lock-in detection scheme achieves signal separation in the frequency domain by modulating the magnetic field and thereby modulating the EPR response at the modulation frequency f_{m}. After detection, this modulation is translated to an isolated tone at f_{m}, which can be selectively recovered using the lock-in amplifier. To first order, the absorption signal is obtained directly at the lock-in amplifier output.

Enhancements were proposed for both the quadrature and interferometric detection setups. For quadrature detection, the focus was on noise reduction to improve the SNR. In the case of interferometric detection, the improvements targeted continuous operation over a broad frequency range, suitable for

integration into an on-chip solution. Furthermore, a dedicated post-processing algorithm was developed to isolate the pure absorption signal. In contrast to the approach proposed by Chen et al. [CSW17], this method reduces measurement time without compromising accuracy.

From a circuit design perspective, quadrature detection requires fewer components and simpler signal processing than the interferometric system. However, the interferometric approach is not limited by the dynamic range of the receiver components. The lock-in detection setup imposes the lowest millimeter-wave (mmW) design requirements on the individual components for broadband operation and benefits from the inherently high signal-to-noise ratio provided by the filtering characteristics of the lock-in amplifier. Given these advantages, the lock-in scheme was selected for further implementation. Moreover, its architecture allows potential extension by incorporating interferometric detection, thereby combining the strengths of both approaches.

A detailed comparison of how each architecture separates the EPR signal, captures absorption and dispersion, and their respective advantages is summarized in Tab. 2.2.

Table 2.2: Comparison of the three broadband TL-based system architectures.

	Lock-in	Quadrature	Interferometric
Frequency of the measured EPR signal	DC	f_{IF}	f_{IF}
Signal separation	transmission and EPR signals are separated in the frequency domain	transmission signal is eliminated in a post-processing step	transmission signal is eliminated by destructive interference
Absorption	V_{meas}	magnitude s_{21}	$\Delta s_{21}^{\mathrm{min}}$
Dispersion	not available	phase φ_{21}	$\Delta f\left(s_{21}^{\mathrm{min}}\right)$
Advantages	- lowest design requirements for mmW components	- less components necessary than for interfer. detection	- not limited by the dynamic range of receiver components
	- high SNR due to the inherent good filter capabilities of the lock-in principle	- simpler signal processing than for interfer. detection	

3 TL-based EPR Measurement Setup

This chapter provides a detailed analysis of the implemented broadband TL-based measurement setup based on lock-in detection combined with magnetic field modulation. Different aspects of the setup are examined to identify key challenges and to establish design specifications for the on-chip components. The following research questions are addressed:

- How is the EPR response encoded into the microwave signal by magnetic-field modulation, and what is its spectral content along the measurement signal chain?
- Why is the EPR spectrum distorted when using a planar microwave probe, and how can it be corrected?
- What are the main noise contributors in the setup?
- What are the main differences between TL- and resonator-based EPR setups, and how does the SNR of the TL-based approach compare quantitatively to that of the resonator-based approach?

3.1 Signal Chain of the Measurement Setup

3.1.1 System Overview

Parts of this section include material previously published in [1, 4].

In Section 2.5, the lock-in detection scheme was introduced and analyzed with a focus on the physical modeling of EPR absorption and dispersion. This analysis established that magnetic-field modulation encodes the EPR response into an amplitude-modulated microwave signal, in which the EPR contribution

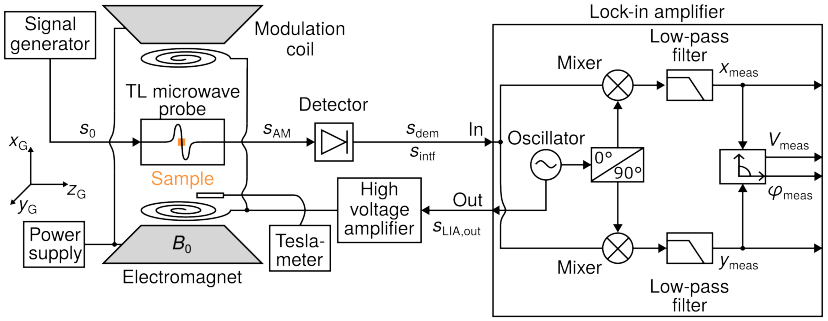

Figure 3.1: Block diagram of the TL-based EPR measurement setup. The signals present at each stage are annotated. Adapted from [1], under CC BY 4.0 license.

is contained in the modulation sidebands and can be downconverted to the modulation frequency by demodulating the AM signal with a detector.

Building on this foundation, the present section embeds this physical signal model into the context of a complete, experimentally realized measurement system. Rather than focusing on the physical origin of the EPR signal itself, the following analysis addresses how the relevant signals are generated, routed, and combined within the setup, and how the resulting modulated microwave signal propagates through the entire measurement signal chain.

This system-level perspective is essential to identify non-ideal effects that are not captured by the physical model alone. Furthermore, it provides the necessary framework for the detailed detector analysis presented in Section 5.2, where modeling the detector input as an AM signal is crucial.

Fig. 3.1 shows the block diagram of the implemented TL-based measurement setup. It is based on commercial measurement instruments and the TL microwave probe which will be discussed in detail in Chapter 4.

A stage-by-stage analysis of the signal chain is presented, starting at the microwave source and proceeding stage by stage through the probe, detector, and lock-in amplifier. Accordingly, the analysis begins with the microwave excitation generated by the signal generator (SG),

$$s_0(t) = V_0 \cos(\omega_0 t) \tag{3.1}$$

with the microwave frequency $f_0 = \omega_0/(2\pi)$ and the amplitude V_0. This signal is fed into the TL microwave probe, on top of which the sample is positioned.

The TL probe is placed inside a 3D-printed pair of Helmholtz coils, which is located inside an electromagnet. The electromagnet generates the external magnetic field B_0 and is driven by a 10 kW power supply. The external magnetic field B_0 is modulated by the modulation coils. The two coils of the Helmholtz pair have a radius R and are separated from each other by a distance $d = R = 16.8$ mm. Each coil has 100 turns. The modulation coil is driven by the output of the LIA

$$s_{\mathrm{LIA,out}}(t) = V_{\mathrm{m}} \cos(\omega_{\mathrm{m}} t), \tag{3.2}$$

with the modulation drive voltage V_{m} and the modulation frequency $f_{\mathrm{m}} = \omega_{\mathrm{m}}/(2\pi)$. The signal $s_{\mathrm{LIA,out}}(t)$ is amplified by a factor of 50 by a high-voltage amplifier. In combination with the modulation coil geometry, the corresponding magnetic-field modulation amplitude B_{m} is obtained by scaling V_{m} with the conversion factor 0.4 mT/V. For all subsequent analyses, the modulation amplitude is specified in terms of V_{m}, as this is the experimentally controlled quantity.

To describe the AM signal s_{AM} at the output of the TL microwave probe, the physically motivated description of the EPR-induced modulation derived in Section 2.5 is reformulated in terms of the standard AM representation in order to facilitate a system-level analysis of the measurement setup.

At a given microwave frequency ω_0, this reformulation shows that the EPR effect can be modeled as a standard AM signal at a single carrier frequency with a small effective modulation index. This modulation index captures the combined influence of the EPR response, the probe, and the magnetic-field modulation, thereby providing a compact signal-level representation of the EPR effect. As a result, the EPR-induced signal can be represented as a well-defined test signal directly at the signal-generator level. This abstraction is particularly useful for the detector analysis presented in Section 5.2.6, where the detector input can be emulated by a controlled AM signal generated by a SG, without requiring the full EPR measurement setup.

This abstraction is formalized below by reformulating the physically motivated expression for the transmitted signal into the standard mathematical representation of an amplitude-modulated waveform.

As shown in Section 2.5, the dispersive component of the EPR response is not detected in the TL-based lock-in configuration considered here. Accordingly, the dispersion coefficient is set to $\beta_0 = 0$ in the signal model, which simplifies the expression for the transmitted signal derived previously in Eq. 2.16 to

$$E_\mathrm{t} = E_0 \left(1 - \alpha_0 + \alpha_0 m_\mathrm{B} \cos(\omega_\mathrm{m} t)\right) \cos(\omega_0 t). \tag{3.3}$$

In this form, the signal is expressed in terms of the absorption coefficient α_0 and the magnetic-field modulation index m_B, which directly reflect the physical EPR response. To obtain a representation that is suitable for system-level modeling, the expression is rearranged as

$$E_\mathrm{t} = E_0(1 - \alpha_0) \left(1 + \frac{\alpha_0}{1 - \alpha_0} m_\mathrm{B} \cos(\omega_\mathrm{m} t)\right) \cos(\omega_0 t). \tag{3.4}$$

By defining $V_0 = E_0 \cdot (1 - \alpha_0)$ and introducing an equivalent modulation index

$$m = \frac{\alpha_0}{1 - \alpha_0} m_\mathrm{B}, \tag{3.5}$$

the transmitted signal can be written in the standard form of an AM signal,

$$\begin{aligned} s_\mathrm{AM}(t) = E_\mathrm{t} &= V_0 \left(1 + m \cos(\omega_\mathrm{m} t)\right) \cos(\omega_0 t) \\ &= V_0 \cos(\omega_0 t) + \frac{m V_0}{2} \cos\left((\omega_0 + \omega_\mathrm{m}) t\right) \\ &+ \frac{m V_0}{2} \cos((\omega_0 - \omega_\mathrm{m}) t), \end{aligned} \tag{3.6}$$

which explicitly reveals the carrier at ω_0 and the two modulation sidebands at $\omega_0 \pm \omega_\mathrm{m}$.

The effective modulation index m is directly proportional to both the absorptive EPR response and the modulation amplitude V_m (see Eq. 2.15). Owing to its nonlinear current–voltage characteristic, the diode detector demodulates this AM signal, as discussed in Section 2.5. As a result, the EPR information is

translated to the modulation frequency ω_m, where it is entirely contained in the corresponding signal component, which can be expressed as

$$s_\mathrm{dem}(t) = \frac{V_0^2 G'_\mathrm{d} m}{2} \cos(\omega_\mathrm{m} t + \varphi_0) + (\ldots), \tag{3.7}$$

where G'_d denotes the effective transconductance of the detector and φ_0 accounts for phase offsets and propagation delays introduced by the system components [TS13].

The LIA downconverts the demodulated signal $s_\mathrm{dem}(t)$ with the modulation frequency f_m of the oscillator which leads to a downconversion of the EPR signal to DC. This allows the use of a narrowband adjustable low-pass filter with a low cut-off frequency leading to a high SNR [Ins23]. Note that the lock-in principle is ultimately enabled by the modulated external magnetic field. The signal at the output of the lock-in amplifier can be described in its complex representation as

$$s_\mathrm{meas}(f_0) = V_\mathrm{meas}(f_0) \cdot \exp(\mathrm{j}\varphi_\mathrm{meas}(f_0)). \tag{3.8}$$

The results can be extracted either in polar coordinates with the amplitude V_meas and the phase φ_meas, or in Cartesian coordinates, where x_meas denotes the real part (in-phase component) and y_meas denotes the imaginary part (quadrature component).

3.1.2 Implemented Measurement Setup

A photograph of the implemented EPR measurement setup is shown in Fig. 3.2. The instruments are labeled with numbers which correspond to the instrument descriptions listed in Tab. 3.1. Fig. 3.3 shows a close-up view of the components located between the poles of the electromagnet (8), where the external magnetic field B_0 is applied along the x_G direction. Fixed between the pole faces are the modulation coils (9), which generate the magnetic-field modulation. The TL microwave probe (11) is positioned centrally between the modulation coils. A 3D-printed stamp (10) is used to press the sample, here Trityl (12), onto the surface of the TL microwave probe.

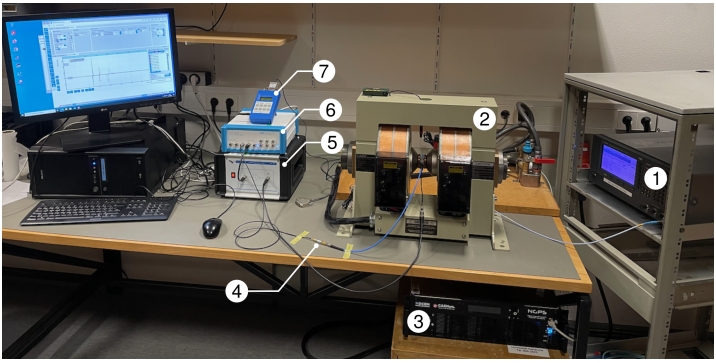

Figure 3.2: Picture of the TL-based EPR measurement setup. Instruments are labeled with numbers which correspond to the instrument descriptions listed in Tab. 3.1.

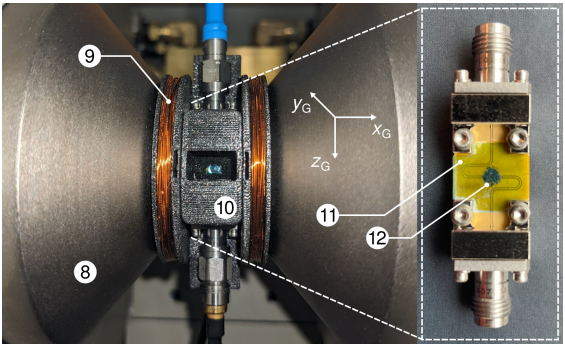

Figure 3.3: Picture of the TL microwave probe (11) placed inside the 3D-printed modulation coil (9) which is fixed between the poles of the electromagnet (8). The sample (12) is pressed on to the TL microwave probe with a 3D-printed stamp (10). Adapted from [1], under CC BY 4.0 license.

All instruments of the measurement setup are selected to achieve a wide operating bandwidth. The SG operates up to 67 GHz, and this frequency range can in principle be extended by employing frequency multipliers, albeit at the expense of reduced output power. The electromagnet generates magnetic fields up to 2 T, corresponding to a resonance frequency of approximately 56 GHz according to Eq. 1.9 with $g = 2$. A tabletop electromagnet is chosen as it provides a favorable trade-off between achievable field strength, weight, and cost. The teslameter probe operates up to 30 kHz and is selected for its ability

Table 3.1: Overview of the instruments used in the EPR measurement setup.

Fig. 3.2	Instrument	Name (company)
1	signal generator	E8257D PSG Analog Signal Generator (Keysight Technologies)
2	electromagnet	5405 Electromagnet (GMW Associates)
3	power supply	NGPS-100-100 (CAEN ELS s.r.l.)
4	diode detector	33330C Coaxial Detector (Keysight Technologies)
5	high-voltage amplifier	WMA-300 (Falco Systems)
6	lock-in amplifier	MFLI 5 MHz Lock-In Amplifier (Zurich Instruments)
7	teslameter	Teslameter FM 302 (Projekt Elektronik GmbH)

to accurately measure both the DC and alternating current (AC) components of the magnetic field. Among commercially available teslameter probes, it offers the largest measurable AC magnetic field amplitude. A modulation frequency of $f_\mathrm{m} = 20\,\mathrm{kHz}$ is used for all EPR measurements to ensure accurate determination of the field modulation strength, which is slightly below the upper frequency limit of the teslameter probe. The maximum usable frequency of the setup is limited to 50 GHz by the diode detector, which represents the best commercially available option compatible with the system. The detector is a planar-doped barrier gallium–arsenide (GaAs) diode. To enable repeatable measurements with powder samples, a custom sample holder was designed, consisting of a 12.5 µm thin Kapton foil (yellow) and an adhesion foil (blue). The powder sample is sandwiched between these two foils. To ensure consistent positioning in the x_G- and z_G-directions, the foils are cut using an in-house manufactured cutter to fit precisely between the connectors (see Fig. 3.4a). A 3D-model of the stamp, labeled as number 10 in Fig. 3.3, is shown in Fig. 3.4b and is used to press the sample onto the TL microwave probe, ensuring reproducible

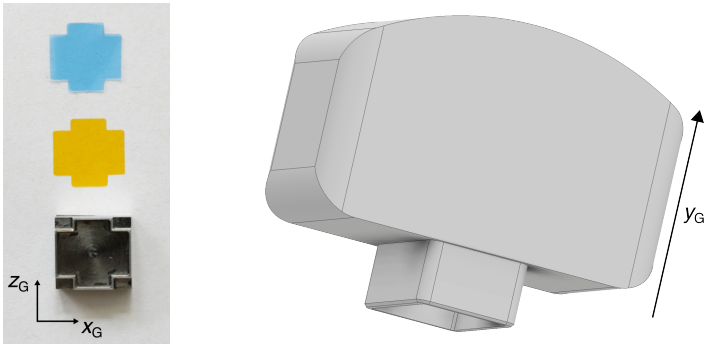

(a) (b)

Figure 3.4: (a) Components of the sample holder which ensure reproducible sample positioning in $x_G z_G$-direction. The sample is placed between a 12.5 µm thin Kapton foil (yellow) and an adhesion foil (blue). The two foils are cut out with a cutter shown at the bottom of the picture. (b) 3D-model of the stamp which ensures reproducible sample positioning in y_G-direction. Adapted from [1], under CC BY 4.0 license.

placement in the y_G-direction. The bottom of the stamp features a hollow rectangular outline that serves as the only contact point with the sample holder, preventing compression of the powder sample.

The EPR measurements are fully automated. The SG is connected to the control personal computer (PC) via general purpose interface bus (GPIB) and operated using standard commands for programmable instruments (SCPI). The power supply of the magnet is connected via local area network (LAN), uses the Transmission Control Protocol/Internet Protocol (TCP/IP) and is operated by a CAEN ELS specific command set. The LIA is connected via USB and the communication is handled by a Zurich Instruments proprietary LabOne Data Server which also uses TCP/IP.

3.1.3 Interference Path and Post-Processing Scheme

During characterization of the TL-based EPR measurement setup, systematic offsets and distortions are observed in the measured signal that cannot be

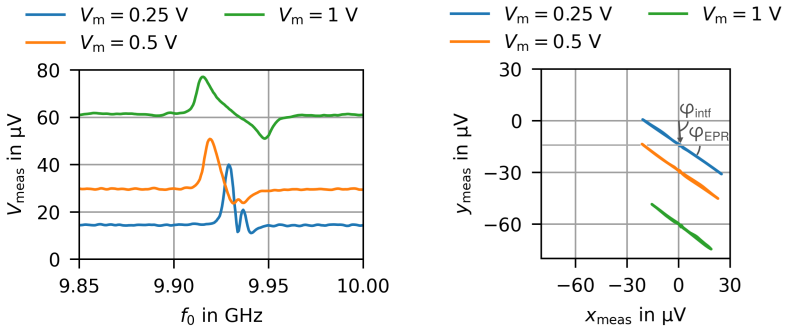

(a) (b)

Figure 3.5: EPR measurements of the BDPA sample for different modulation amplitudes. The external magnetic field is set to $B_{0,r} = 354.7\,\text{mT}$ ($f_{0,r} = 9.93\,\text{GHz}$). (a) Amplitude of the complex measurement signal as a function of the microwave frequency. (b) Representation of the complex signal in Cartesian coordinates with equal scaling of both axes, yielding an angle-preserving display in which phase angles can be extracted directly. Adapted from [4], ©IEEE.

attributed to the EPR response itself. These effects are traced back to an undesired interference path within the measurement chain, shown as s_{intf} at the input of the LIA in Fig. 3.1.The experimental manifestation and origin of this interference are analyzed, followed by the introduction of a post-processing scheme to recover the undistorted EPR signal.

Experimental Manifestation of the Interference Path

The performance of the EPR measurement setup is evaluated by analyzing the measured amplitude V_{meas}, obtained directly at the output of the LIA, for different modulation amplitudes. The data shown in Fig. 3.5a are obtained using a 1,3-bisdiphenylene-2-phenylallyl (BDPA) powder sample. BDPA is a radical commonly used as an EPR standard because it has a high spin concentration ($1.57 \times 10^{27}\,\text{spins/m}^3$ [ZN21]) and exhibits a single sharp resonance line. The external magnetic field strength is fixed at $B_{0,r} = 354.7\,\text{mT}$ which corresponds to a resonance microwave frequency of $f_{0,r} = 9.93\,\text{GHz}$.

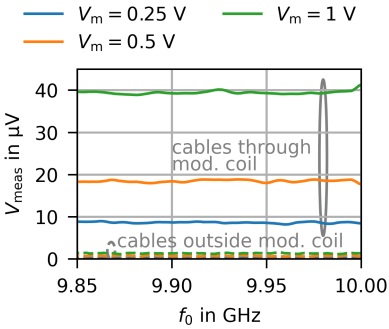

Figure 3.6: The measured signal amplitude for different modulation amplitudes when the cables in Fig. 3.2 are directly connected. The connected cables were placed through the modulation coil for the solid curves and were placed outside the modulation coil for the dashed curves. Adapted from [4], ©IEEE.

As discussed in Section 1.2.3, the modulation amplitude needs to be chosen carefully for each sample to maximize the EPR signal amplitude while avoiding overmodulation. This behavior is reflected in Fig. 3.5a, where increasing modulation amplitude leads to a progressive broadening of the EPR line. In addition to this expected effect, a modulation-dependent baseline offset is present in all measured curves. The magnitude of this offset increases with modulation amplitude and deviates from the behavior expected if only the EPR signal were present at the input of the LIA. Moreover, the curves corresponding to $V_m = 0.25\,V$ and $V_m = 0.5\,V$ deviate from the expected shape of an ideal derivative of an absorption spectrum.

For these measurements, the microstrip line rotated by 90°, which will be introduced in Section 4.1.2 and is shown in Fig. 4.8a, is used as the microwave probe. The observed baseline offset and line-shape distortion, however, are not specific to this particular probe geometry. The developed post-processing scheme used to recover the correct EPR signal, introduced later in this section, is applicable to all planar microwave probes.

Origin of Interference Path

The origin of the offset can be traced to an undesired interference path. The signal generated by the modulation coil inductively couples into the measurement chain, resulting in an additional component s_{intf} at the input of the LIA (see Fig. 3.1). Since the modulation frequency f_{m} is relatively low, it can readily couple via magnetic induction into nearby conductors, including the TL microwave probe and the associated cabling. The magnitude of the EPR signal itself is typically in the microvolt range, which is comparable to the amplitude of the interference-induced offset observed in Fig. 3.5a.

To isolate and characterize this interference mechanism experimentally, the TL microwave probe is removed from the setup shown in Fig. 3.1. The SG and detector are instead connected directly using the measurement cables, thereby eliminating contributions from the TL probe itself. In the first measurement configuration, the cables are routed through the modulation coil. The resulting signal amplitudes for various modulation voltages are shown as solid lines in Fig. 3.6. A pronounced offset is observed that increases with modulation amplitude, consistent with inductive coupling of the modulation signal into the cables.

In a second measurement configuration, the same cables are placed outside the region influenced by the modulation coil. The corresponding results, shown as dashed curves in Fig. 3.6, exhibit only a minimal offset, indicating a strong reduction of the interference contribution.

This interference-induced offset can significantly distort both the amplitude and shape of the measured EPR signal. As such, careful consideration and mitigation of this effect are essential for accurate interpretation of the measurement results.

On the experimental side, a high-pass filter placed before the detector is found to partially suppress the interference component. However, because of the magnetic coupling mechanism, a residual common-mode contribution is expected to remain on the cable and could not be completely eliminated by filtering.

Post-Processing Scheme

To accurately remove the effect of the interference path from the measurements and thus eliminate the artifacts shown in Fig. 3.5, a dedicated post-processing approach is developed. The measured signal s_{meas} at the output of the LIA is represented in complex form as $s_{\mathrm{meas}}(f_0) = V_{\mathrm{meas}}(f_0) \cdot \exp(\mathrm{j}\varphi_{\mathrm{meas}}(f_0))$, as introduced in Eq. 3.8. In the presence of an interference path, this signal consists of two contributions

$$s_{\mathrm{meas}}(f_0) = V_{\mathrm{intf}} \cdot \exp(\mathrm{j}\varphi_{\mathrm{intf}}) + V_{\mathrm{EPR}}(f_0) \cdot \exp(\mathrm{j}\varphi_{\mathrm{EPR}}), \tag{3.9}$$

where V_{EPR} is the amplitude of the desired EPR signal and is directly proportional to the effective modulation index m defined in Eq. 3.7. The interference signal is characterized by amplitude V_{intf} and phase φ_{intf}, while φ_{EPR} denotes the phase of the EPR signal. Across the measured frequency range, V_{intf}, φ_{intf}, and φ_{EPR} are frequency-independent.

When measuring only the magnitude V_{meas} of the complex signal, direct extraction of the EPR amplitude V_{EPR} becomes problematic unless the interference and EPR signals are in phase. In the special case where $\varphi_{\mathrm{intf}} = \varphi_{\mathrm{EPR}}$, the EPR amplitude can be obtained by simple subtraction

$$V_{\mathrm{EPR}} = V_{\mathrm{meas}} - V_{\mathrm{intf}}. \tag{3.10}$$

However, if $\varphi_{\mathrm{intf}} \neq \varphi_{\mathrm{EPR}}$, this relationship no longer holds. In such cases, extracting V_{EPR} from V_{meas} using Eq. 3.10 results in amplitude errors and distortion of the signal shape.

To illustrate this, Fig. 3.5b presents the measured data in Cartesian form

$$s_{\mathrm{meas}} = x_{\mathrm{meas}} + \mathrm{j}y_{\mathrm{meas}}. \tag{3.11}$$

In this representation, the center of each measured curve corresponds to the interference component, indicated by the arrow in Fig. 3.5b, and its amplitude is given by

$$V_{\mathrm{intf}} = \sqrt{x_{\mathrm{intf}}^2 + y_{\mathrm{intf}}^2}. \tag{3.12}$$

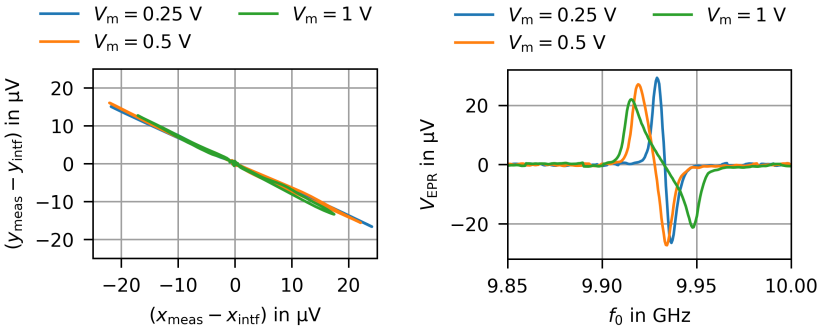

(a) (b)

Figure 3.7: EPR measurements after applying the post-processing scheme. (a) shows the corrected results in Cartesian coordinates, and (b) the amplitude of the EPR signal calculated using Eq. 3.14 as a function of the microwave frequency. The external magnetic field is set to $B_{0,r} = 354.7$ mT ($f_{0,r} = 9.93$ GHz). Adapted from [4], ©IEEE.

The EPR contribution appears as the amplitude variation around this center, and is calculated as

$$V_{EPR} = \sqrt{x_{EPR}^2 + y_{EPR}^2}. \tag{3.13}$$

In the example shown in Fig. 3.5b, the interference and EPR signals have different phases: $\varphi_{intf} = 89°$ and $\varphi_{EPR} = 40°$. Under these conditions, using Eq. 3.10 would yield incorrect results, misrepresenting both the amplitude and shape of the EPR signal. The extent of this distortion depends on the relative amplitudes and phases of the interference and EPR contributions. To accurately extract the amplitude of the EPR signal, the interference component must first be subtracted from the measured signal before calculating the magnitude. The interference components are obtained by computing the mean values of x_{meas} and y_{meas}. Because the EPR signal is antisymmetric about its center, it averages to zero, leaving only the interference contribution. After this correction, illustrated in Fig. 3.7a, the amplitude of the EPR signal is computed as

$$V_{EPR} = \text{sign}(x_{meas}) \cdot \sqrt{(x_{meas} - x_{intf})^2 + (y_{meas} - y_{intf})^2}. \tag{3.14}$$

The sign of the I- or Q-component is reintroduced after computing the absolute value in order to recover the correct shape of the derivative spectrum.

As shown in Fig. 3.7b, the corrected EPR curves are free from distortion, exhibit the expected amplitude, and match the characteristic shape of a derivative absorption spectrum.

3.1.4 Demonstration on More Complex Spin Systems

The implemented post-processing scheme enables the measurement of spectra of more complex spin systems. Fig. 3.8a presents the EPR spectrum of TEMPOL. In contrast to the measurements shown in Chapter 2, TEMPOL is now measured in its liquid state. The anisotropy is motionally averaged, such that the characteristic three-line spectrum caused by hyperfine coupling to the $(^{14}\mathrm{N})$ nucleus is visible. The prepared sample had a concentration of 100 mM, with water, deuterated water, and glycerol used as the solvent components. The measurement is performed using the following experimental parameters: $B_{0,\mathrm{r}} = 645\,\mathrm{mT}$, $V_\mathrm{m} = 0.5\,\mathrm{V}$, $f_\mathrm{m} = 20\,\mathrm{kHz}$, $\tau = 70\,\mathrm{ms}$, and $P_0 = 8.2\,\mathrm{dBm}$.

Fig. 3.8b displays the spectrum of Mn:$CaCO_3$, i.e. calcium carbonate doped with manganese. In this system, Mn^{2+} is a high-spin ion with five unpaired electrons ($S = 5/2$), corresponding to six electron-spin Zeeman energy levels. Since the naturally abundant isotope ^{55}Mn has a nuclear spin of $I = 5/2$, hyperfine coupling splits each allowed electron-spin transition into $2I+1 = 6$ components, giving rise to the characteristic six-line pattern in the EPR spectrum. Additional peaks can occur due to zero-field splitting, which further perturbs the level structure and can make additional transitions or splittings observable [GM06]. The sample was prepared by mixing $MnCl_2$ and $NaHCO_3$ in aqueous solution, followed by precipitation of $MnCO_3$ and $CaCO_3$ and evaporation of the solvent. The resulting material contained approximately one Mn ion per 75 Ca ions. Such a relatively high dopant concentration can lead to line broadening in the spectrum due to Mn–Mn dipolar interactions. The following experimental parameters are used: $B_{0,\mathrm{r}} = 628\,\mathrm{mT}$, $V_\mathrm{m} = 3\,\mathrm{V}$, $f_\mathrm{m} = 20\,\mathrm{kHz}$, $\tau = 10\,\mathrm{ms}$, and $P_0 = 7.2\,\mathrm{dBm}$. All six major peaks arising from the hyperfine splitting are clearly visible.

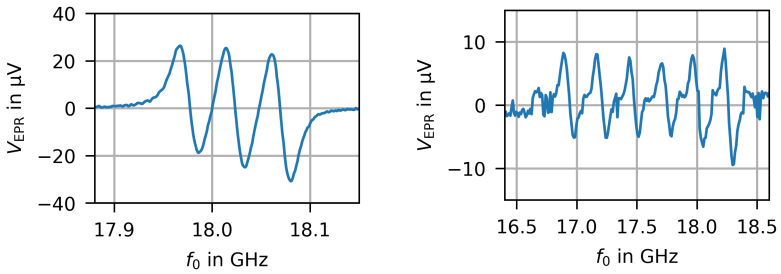

(a) (b)

Figure 3.8: EPR spectra of (a) TEMPOL measured at $B_{0,r} = 645\,\text{mT}$ and (b) Mn:$CaCO_3$ measured at $B_{0,r} = 628\,\text{mT}$.

3.1.5 Mapping EPR Signal Strength to Modulation Index

As established in Section 3.1.1, the EPR effect at a given microwave frequency can be represented as a standard AM signal with a small effective modulation index m. In this representation, m captures the strength of the EPR-induced absorption and directly determines the amplitude of the EPR signal V_{EPR} measured at the output of the LIA. This abstraction allows the EPR response to be emulated by a well-defined test signal generated by a signal source and applied directly to the detector.

The purpose of this section is to estimate the order of magnitude of the effective modulation index m encountered in EPR measurements. This estimate defines the range of modulation indices that the detector must be able to resolve in order to reliably detect EPR signals and therefore provides a quantitative basis for the detector design and performance evaluation presented in Section 5.2.

The EPR measurements used for this purpose, which are presented in the next chapter in Section 4.1.3, are chosen because they cover a broad microwave frequency range and therefore provide a representative overview of the achievable EPR signal amplitudes. In these measurements, microwave frequencies between 5 and 45 GHz are investigated. Across this frequency range, the measured peak EPR voltages range approximately from 3 µV to 100 µV.

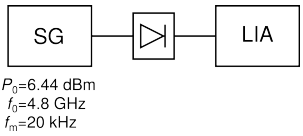

(a)

m	V in µV
2×10^{-3}	420
4×10^{-3}	836
10×10^{-3}	2032
20×10^{-3}	4119

(b)

Figure 3.9: (a) Measurement setup used to determine the LIA's output voltage at the modulation frequency $f_m = 20\,\text{kHz}$ for various modulation indices m. (b) Resulting output voltage values corresponding to the different modulation indices.

To reproduce these signal levels under well-defined conditions, the setup shown in Fig. 3.9a is employed. A SG produces an AM signal with a carrier frequency of $f_0 = 4.8\,\text{GHz}$ and a modulation frequency of $f_m = 20\,\text{kHz}$. The input power is set to $P_0 = 6.44\,\text{dBm}$, resulting in a power level of 3 dBm at the detector input. The time constant of the LIA low-pass filter is set to 75 ms, corresponding to an equivalent bandwidth of 1.06 Hz. These parameters are chosen to match the operating conditions used in the EPR measurements described in Section 4.1.3. The output voltage is then measured with the LIA for different modulation indices m.

The measured relationship between modulation index and output voltage is summarized in Tab. 3.9b. From these measurements, an EPR peak voltage amplitude of 1 µV corresponds approximately to a modulation index of $m \approx 4.8 \times 10^{-6}$. Applying this conversion to the EPR measurements shown in Section 4.1.3 yields effective modulation indices m on the order of 1.5×10^{-7} to 5×10^{-6}. These values are subsequently used in Section 5.2.6 to evaluate the noise performance and sensitivity limits of the designed integrated detector circuits.

3.2 Noise Analysis of the Measurement Setup

In this section, the noise floor of various parts of the measurement setup in Fig. 3.1 is analyzed. The noise measurements are performed with the LIA. The underlying theory of measuring the noise with the LIA is summarized by [Ale21] and is revisited here.

3.2.1 Theoretical Foundation

For a complex (IQ) noise model $v(t) = x(t) + \mathrm{j}y(t)$, the time averaged noise power at frequency ω can be calculated as

$$P_\omega = V^2 = X^2 + Y^2. \tag{3.15}$$

Here, the noise power is expressed in normalized form by assuming an equivalent noise resistance of $R_\mathrm{n} = 1\,\Omega$. The quantities in this expression represent time-averaged values at frequency ω, with V denoting the RMS noise amplitude, and X and Y the corresponding RMS values of the in-phase and quadrature components, respectively. For the analysis it is assumed that the in-phase and quadrature noise components are independent Gaussian random processes.

The quantities which are measured by the LIA correspond to ensemble averages, which can be expressed using the expectation value $\mathbb{E}\{\cdot\}$ as

$$P_\mathrm{n} = \mathbb{E}\{P_\omega\} = \mathbb{E}\left\{V^2\right\} = \mathbb{E}\left\{X^2\right\} + \mathbb{E}\left\{Y^2\right\}. \tag{3.16}$$

These terms can be expressed in terms of mean μ and variance σ. For a discrete random variable z with N equally likely values z_i, the mean value is given by

$$\mu_z = \frac{1}{N}\sum_{i=1}^{N} z_i \tag{3.17}$$

and the variance as

$$\sigma_z^2 = \frac{1}{N}\sum_{i=1}^{N}(z_i - \mu_z)^2. \tag{3.18}$$

Since the mean of the in-phase and quadrature components is zero, while the amplitude V has a non-zero mean, the following relationship holds

$$P_\mathrm{n} = \mu_V^2 + \sigma_V^2 = \sigma_X^2 + \sigma_Y^2 \tag{3.19}$$

The noise power P_n is contained in the bandwidth W of the filter of the LIA, so the noise power density is

$$S_\mathrm{n} = \frac{P_\mathrm{n}}{W}. \tag{3.20}$$

In the lock-in detection scheme, noise components in both sidebands around the frequency ω are translated to baseband during demodulation. As a result, the effective noise bandwidth W of the bandpass around ω is twice the bandwidth B of the low-pass filter used in the LIA, so $W = 2B$ [PS08]. This yields

$$S_\mathrm{n} = \frac{\sigma_X^2 + \sigma_Y^2}{2B} = \frac{1}{2}\left(\frac{\sigma_X^2}{B} + \frac{\sigma_Y^2}{B}\right) = \frac{1}{2}(S_X + S_Y). \tag{3.21}$$

In the EPR measurements, the voltage rather than the power is measured. Therefore, the noise voltage spectral density v_n in $\mathrm{V}/\sqrt{\mathrm{Hz}}$ is used for the noise analysis and is calculated to

$$v_\mathrm{n} = \sqrt{S_\mathrm{n}}. \tag{3.22}$$

The measured noise power spectral density $S_\mathrm{n,meas}$ needs to be corrected by the noise floor of the lock-in amplifier $S_\mathrm{n,LIA}$ to obtain the device under test (DUT) inherent noise contribution

$$v_\mathrm{n,DUT} = \sqrt{S_\mathrm{n,meas} - S_\mathrm{n,LIA}}. \tag{3.23}$$

The input range of the LIA can be adjusted, and for the highest accuracy the smallest suitable range should be chosen. With larger input ranges, the noise

floor of the LIA increases. Within the Zurich Instrument Labview software, the noise voltage spectral density can be directly measured with the *frequency sweeper tool*. The oscillator frequency is swept and the noise spectrum is recorded. The noise spectrum is directly divided by the measurement bandwidth to obtain the values in $\mathrm{nV}/\sqrt{\mathrm{Hz}}$ [Ale21].

3.2.2 Verification of Noise Measurement Setup

To verify the noise measurement setup with the LIA, the thermal noise of three surface mount resistors soldered to a Bayonet Neill–Concelman (BNC) connector is measured and compared to their theoretical value.

The theoretical values are calculated based on

$$v_\mathrm{n} = \sqrt{4k_\mathrm{B}TR}, \tag{3.24}$$

where R denotes the resistance and $T = 295\,\mathrm{K}$ the temperature. The corresponding predictions are shown as dashed curves in Fig. 3.10.

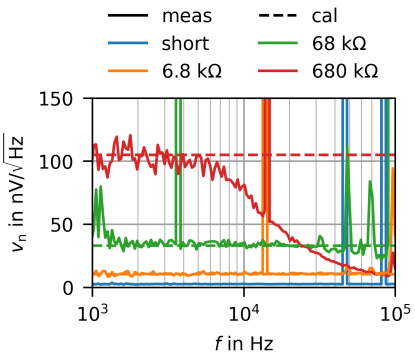

Figure 3.10: Noise voltage spectral density of various surface mount resistors. The measured values are shown as solid lines, whereas the calculated values are shown as dashed lines. The noise floor of the LIA is measured by presenting a short at its input.

The noise measurements of the resistors are shown in Fig. 3.10 as solid curves. As a reference, the noise floor of the LIA, measured with a short at its input, is also shown. The input voltage range of the LIA is chosen to be 1 mV. The spikes are assumed to be spurious signal from the lab environment.

For the lower resistor values 6.8 kΩ and 68 kΩ, the measured and calculated values fit quite well. For the resistor $R = 680\,\mathrm{k\Omega}$ a low pass characteristic can be observed in the measured data. The input impedance of the LIA is $Z_{\mathrm{LIA,in}} = 10\,\mathrm{M\Omega} \parallel 27\,\mathrm{pF}$. The input impedance in parallel with the measured resistor results in a cut-off frequency of

$$f_{\mathrm{c}} = \frac{1}{2\pi\,(R \parallel R_{\mathrm{LIA}})\,C_{\mathrm{LIA}}} \approx 9.26\,\mathrm{kHz}. \tag{3.25}$$

Considering the tolerances of the surface-mount resistor, this aligns with the observed measurement results.

3.2.3 Noise Contributions by Component

The noise contribution of each component is measured, starting at the end of the signal chain with the LIA. The input impedance of the LIA is set to $R_{\mathrm{LIA,in}} = 10\,\mathrm{M\Omega}$, the input range is set to 100 mV, and v_{n} is measured from 10 kHz to 1 MHz.

LIA and Detector

In a first step, v_{n} of the LIA is determined by terminating its input with a short, as described in [Ale21] (see Fig. 3.11a). The noise voltage spectral density is shown in Fig. 3.12a. All further shown results are corrected by this noise voltage spectral density of the LIA according to Eq. 3.23.

The noise voltage spectral density of the detector is also shown in Fig. 3.12a and is approximately $v_{\mathrm{n}} = 5\,\mathrm{nV}/\sqrt{\mathrm{Hz}}$ up to 300 kHz. The input of the detector is terminated by 50 Ω, as can be seen in Fig. 3.11b. As the detector is terminated by 50 Ω, the main noise source is thermal noise.

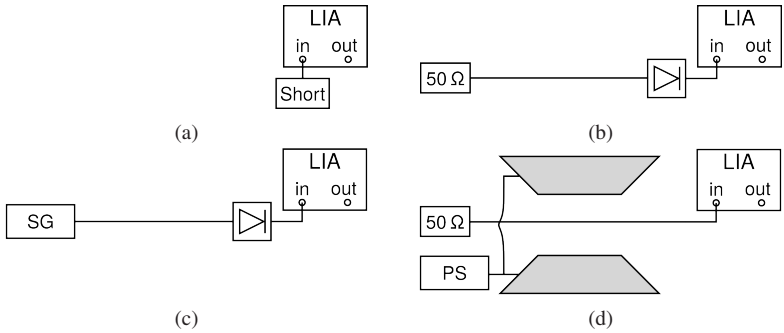

Figure 3.11: Measurement setups to analyze the noise voltage spectral density along the signal chain. (a) is used to determine the noise floor of the LIA, (b) to determine v_n of the detector, (c) to analyze the influence of the SG, and d) to analyze if the magnetic field has an influence on the noise floor.

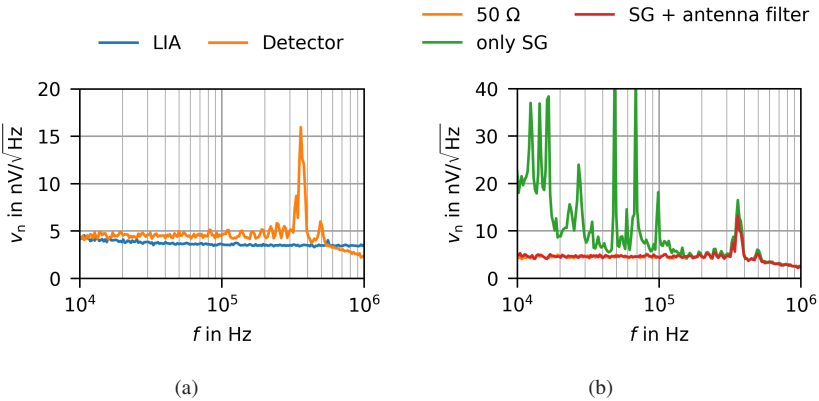

Figure 3.12: Noise voltage spectral density of (a) the LIA and the detector, and (b) the detector with various input terminations.

Signal Generator

In the subsequent step, the 50 Ω termination is replaced by the SG, as illustrated in Fig. 3.11c. The output current of the SG can be written as [Ell07]

$$i(t) = (I + \Delta I) \cdot \cos(\omega_0 t + \Delta\phi), \tag{3.26}$$

where ΔI denotes the amplitude noise and $\Delta\varphi$ the phase noise.

Because of the field modulation and the use of a LIA, noise components at the modulation frequency are of particular interest. In the AM signal at the detector input, both the carrier and its modulation sidebands originate from the same source and therefore share identical phase fluctuations. When the detector, operating as a self-mixer, demodulates the signal, the common phase noise of these components is effectively canceled. Consequently, the signal generator's phase noise contributes negligibly to the overall noise performance [Kel25], leaving amplitude noise as the dominant term.

The green curve in Fig. 3.12b shows the measured noise voltage spectral density using the setup illustrated in Fig. 3.11c, with a carrier frequency of $f_0 = 25\,\text{GHz}$ and a calibrated input power of $P_0 = -33\,\text{dBm}$. The noise floor increases at frequencies below 100 kHz. To identify the origin of the elevated noise level, a bandpass filter is introduced into the signal path between the SG and the diode detector. The bandpass is realized using a transmit and receive antenna. Horn antennas (LB-34-15-C-KF), operating over a frequency range from 22 to 33 GHz with a nominal gain of 15 dB, are employed. A subsequent measurement of v_n shows the same noise level as when the SG is replaced by a 50 Ω termination. This indicates that, at low input powers, the increased noise floor originates from baseband noise.

Fig. 3.13 shows the noise voltage spectral density for input powers ranging from −33 dBm to 9 dBm. The setup is calibrated up to the detector input. Input powers above −15 dBm result in a noticeable increase in the noise voltage spectral density. This trend is observed in both measurement setups, without the antenna filter (Fig. 3.13a) and with it (Fig. 3.13b). The only difference between the results of the two setups is that the setup with antenna filters exhibits fewer spectral ripples, as already shown in Fig. 3.12b. At higher input power levels, the elevated noise floor is attributed to increased in-band noise components, which are most likely dominated by amplitude noise.

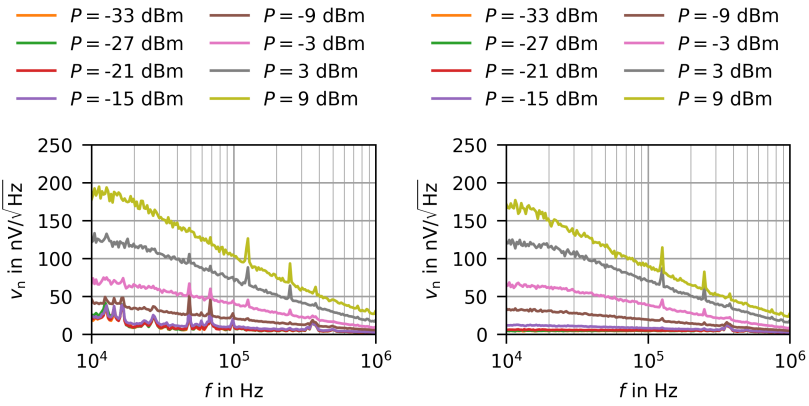

Figure 3.13: Noise voltage spectral density of the setup shown in Fig 3.11c for various input powers. (a) Setup with the SG directly connected to the detector. (b) Setup with the antenna filter inserted between the SG and the detector.

To better assess the measured values, they are compared with the data provided in the signal generator's datasheet. However, the datasheet specifies only phase noise values. The SG used in the measurement setup corresponds to the standard configuration of the instrument. According to the datasheet, the single-sideband phase noise at 20 GHz and a 20 kHz offset from the carrier is $-108\,\text{dBc/Hz}$. The manufacturer also offers a low phase noise hardware option that achieves $-121\,\text{dBc/Hz}$ under the same conditions. For this enhanced configuration, additional amplitude noise data provided by the manufacturer indicate a value of $-140\,\text{dBc/Hz}$ at the same settings. No amplitude noise data are available for the standard configuration. Assuming the same relationship between phase and amplitude noise as described by [Ell07], where amplitude noise is typically about 20 dB lower than phase noise due to oscillator saturation, an amplitude noise of $-128\,\text{dBc/Hz}$ can be estimated for the standard configuration. At an input power of 3 dBm, this corresponds to a noise voltage spectral density of $125\,\text{nV}/\sqrt{\text{Hz}}$, which agrees well with the measured values.

In addition to the amplitude noise originating from the SG, the detector itself introduces additional noise contributions when an RF signal is

applied [GZV+16]. Beyond the thermal noise discussed earlier, flicker noise also arises under radio frequency (RF) excitation. Flicker noise, caused by trapping and de-trapping of carriers in the semiconductor [Hoo94], increases with input power due to self-biasing of the detector, which raises the DC output current [She13], and can become the dominant noise source at higher power levels [HC07]. As previously mentioned, the detector used in the EPR measurement setup is a planar-doped GaAs device. Dale et al. [DNC+90] report that such detectors exhibit significantly lower 1/f noise than Schottky diodes due to the superior material quality of their epitaxial structure and report corner frequencies below 10 kHz. Since the measurement setup does not allow separation of amplitude noise and detector flicker noise, the observed spectral density can reflect a combination of both. Whether flicker noise contributes significantly above 10 kHz depends on the actual corner frequency. Given that the estimated amplitude noise aligns well with the measured data, it is assumed to be the dominant contribution, though this cannot be conclusively verified without further analysis.

Control Mechanism of Signal Generator

Another potential source for sub-1 MHz noise is the digital communication with the SG. Three methods of controlling the SG are investigated: manual operation, remote control via LAN, and remote control via a GPIB interface. The noise voltage spectral density is measured under the condition that the RF output of the SG is turned off to eliminate all influences of the active components of the SG. However, the same results are obtained when the SG is operated at low input powers. The results are shown in Fig. 3.14a.

Control via GPIB was originally implemented in the setup because it provided a more stable connection with the SG. However, a pronounced increase in noise voltage spectral density is observed in the range between 10 kHz and 30 kHz when the system is remotely controlled through a GPIB cable. This frequency range coincides with that used in the EPR experiments. In contrast, manual operation and remote control via LAN produced nearly identical noise spectra. The higher noise level associated with GPIB control is likely caused by the inferior shielding of GPIB cables, which are more susceptible to electromagnetic interference than LAN cables that use twisted-pair conductors for improved noise rejection. When the setup included the antenna filter, no

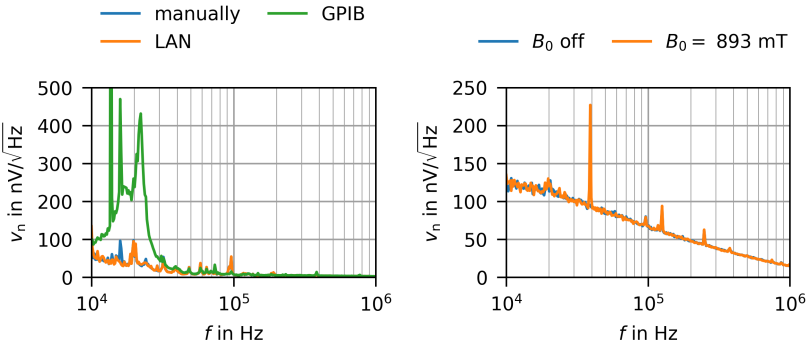

Figure 3.14: Influence on the noise voltage spectral density of (a) various methods of controlling the SG and (b) the external magnetic field.

difference in the noise voltage spectral density was observed between LAN and GPIB control. Unless stated otherwise, all other noise spectra presented in this work were measured using LAN remote control.

External Magnetic Field

Lastly, the effect of the external magnetic field on the noise floor is analyzed. The RF measurement cables connecting the SG with the detector are routed through the poles of the magnet. The SG is operated at $f_0 = 25\,\text{GHz}$ and $P_0 = 3\,\text{dBm}$ and the external magnetic field is set to the resonance magnetic field of $B_{0,\text{r}} = 893\,\text{mT}$. As can be seen from Fig. 3.14b, v_n remains largely unchanged. This is reasonable, as the electromagnet is powered by a supply connected to the 50 Hz mains grid, which is well below the modulation frequency so it does not contribute significantly to the noise floor.

Summary

The noise voltage spectral densities at the modulation frequency $f_m = 20\,\text{kHz}$ used for the EPR measurements are summarized in Tab. 3.2. The noise floor is dominated by the noise generated by the SG, particularly at higher input powers. Especially for modulation frequencies between 10 kHz and 30 kHz, the SG should be controlled via LAN.

Table 3.2: Noise voltage spectral density at 20 kHz.

DUT	P_0 in dBm	Remote control	v_n in $\text{nV}/\sqrt{\text{Hz}}$
LIA	–	–	3.8
Detector	–	–	4.7
SG	−33	GPIB	210.5
SG	−33	LAN	8.9
SG	−27	LAN	8.7
SG	−21	LAN	9.5
SG	−15	LAN	13.4
SG	−9	LAN	34.6
SG	−3	LAN	65.8
SG	3	LAN	119.3
SG	9	LAN	178.4

3.3 Comparison of TL- and Resonator-based EPR Spectrometers

In this section, the custom-built TL-based EPR spectrometer operated in transmission mode is compared with a high-end commercial resonator-based system operated in reflection mode. While several aspects of both approaches have been discussed in the preceding chapters, their principal differences are consolidated in Tab. 3.3 for clarity and completeness and are discussed in more detail here.

Table 3.3: Main differences between TL-based and resonator-based approach.

	TL-based	Resonator-based
Sweep parameter	magnetic field and frequency	magnetic field only
Reference arm	not necessary; transmission signal is used to set operating point of detector	necessary to set optimal operating point of detector
Separation of E- and H-field	not possible	possible; tailored resonator design can lead to different locations for the maximum E- and H-field
Bandwidth	broadband	narrowband
Sensitivity to phase noise	low	rises for higher Q resonators
Absorption	directly acquired	frequency locking necessary

The TL-based approach provides broadband operation with wide frequency tunability, whereas the resonator-based spectrometer offers higher sensitivity and stronger field confinement at the cost of limited bandwidth. Owing to its broadband characteristics, the TL-based setup allows sweeping not only the magnetic field but also the microwave frequency, which is not possible in resonator-based configurations. This capability is particularly advantageous for rapid-scan experiments [EE12], as the microwave frequency can be varied

much faster than the magnetic field, and it further enables direct measurements of the ZFS interaction (see Section 1.2). In the TL-based setup, the large transmitted carrier is inherently present at the detector input and can be used to set the detector operating point. In contrast, in the resonator-based approach the carrier component is largely suppressed by critical coupling of the resonator, and a reference arm is used to set the detector operating point. Moreover, it enables effective separation of the electric and magnetic fields, which is particularly important for liquid or high-permittivity samples, as a large electric field in the sample volume can lead to increased dielectric losses. The TL-based spectrometer, however, measures the absorptive response directly without requiring a reference arm or additional detection stages. Furthermore, TL probes are inherently less affected by the phase noise of the SG, whereas in high-Q resonators, small frequency fluctuations of the source translate into amplitude modulation at the detector [Kel25].

To understand the sensitivity difference between the custom-built broadband TL-based EPR spectrometer and a conventional resonator-based system, both the underlying signal generation mechanisms and experimental results are compared. The discussion begins with a qualitative physical background identifying the parameters that govern the generated EPR signal, followed by experiments performed under comparable conditions. Although a fully quantitative calibration is not attempted, this comparison provides a first-order assessment of the main factors determining the achievable SNR in both setups.

3.3.1 Signal Models

The following signal model focuses on the microwave signal formation in the respective structures (resonator versus transmission line) and is therefore independent of the specific detection principle used to extract the signal. For a resonator-based spectrometer, the unsaturated EPR signal can be expressed as [EEBW10]

$$V_{\mathrm{EPR}}^{\mathrm{R}} = \chi'' \eta Q_{\mathrm{L}} \sqrt{P_0 Z_0}, \tag{3.27}$$

where η is the magnetic filling factor, Q_L is the loaded quality factor, P_0 denotes the incident microwave power at the resonator input and Z_0 the line impedance. The filling factor is defined as

$$\eta = \frac{\int_{V_\mathrm{s}} \vec{H}_1{}^2 \mathrm{d}V}{\int_{V_\mathrm{c}} \vec{H}_1{}^2 \mathrm{d}V}, \tag{3.28}$$

where V_s is the sample volume and V_c is the cavity volume. The filling factor η quantifies the fraction of the total microwave magnetic field energy stored in the cavity that is located within the sample volume V_s.

The quality factor is formally defined as

$$Q = \omega \frac{\text{energy stored}}{\text{average power dissipated per cycle}}. \tag{3.29}$$

In a resonator, the electromagnetic field forms a standing wave, allowing energy to build up and leading to a well-defined Q-factor [Poz21]. In contrast, in a transmission line the microwave field corresponds to a traveling wave that continuously transports energy rather than storing it. Therefore, the quality factor is not a meaningful figure of merit for a TL structure. To enable a direct comparison between resonator-based and TL-based EPR spectroscopy, both signal models are therefore reformulated in terms of the microwave magnetic field $\vec{H}_1$ in the sample volume. The Q-factor in Eq. 3.29 for a cavity filled with a paramagnetic sample can be expressed as [Feh56]:

$$Q = \omega \frac{\frac{1}{8\pi} \int_{V_\mathrm{c}} \vec{H}_1{}^2 \mathrm{d}V}{P_1 + P_\mathrm{abs}} \tag{3.30}$$

Here, P_1 denotes the microwave power dissipated in the resonator in the absence of paramagnetic absorption, and P_abs is the additional power absorbed by the paramagnetic sample. The absorbed power is given by [Feh56, Poo96]

$$P_\mathrm{abs} = \frac{1}{2}\omega \int_{V_\mathrm{s}} \vec{H}_1{}^2 \chi'' \mathrm{d}V. \tag{3.31}$$

Based on Eq. 3.30, the Q-factor in the absence of paramagnetic losses is

$$Q_0 = \frac{\omega}{8\pi P_1} \int_{V_c} \vec{H}_1{}^2 \mathrm{d}V. \tag{3.32}$$

Under critical coupling, the loaded quality factor Q_L, defined as the Q-factor of the resonator coupled to an external load [EEBW10], is approximately $Q_L = Q_0/2$. Moreover, in the ideal case, the incident microwave power P_0 is fully absorbed by the resonator, such that $P_1 = P_0$. Substituting Q_L and η into Eq. 3.27 yields the signal model for the resonator-based approach

$$V_{EPR}^{R} = \sqrt{P_0 Z_0}\chi'' \frac{\omega}{4\pi P_0} \int_{V_s} \vec{H}_1{}^2 \mathrm{d}V. \tag{3.33}$$

For the TL-based EPR spectrometer operated in transmission mode, an analogous model is derived based on the transmitted microwave power. The voltage at the output of the TL is proportional to the transmitted power after absorption

$$V_{det} = \sqrt{Z_0 \left(P_0 - P_{abs}\right)} = \sqrt{Z_0 P_0}\sqrt{1 - \frac{P_{abs}}{P_0}}. \tag{3.34}$$

With the approximation $P_{abs} \ll P_0$ [Feh56], a Taylor expansion yields

$$V_{det} \approx \sqrt{Z_0 P_0} \cdot \left(1 - \frac{1}{2P_0} P_{abs} + \mathcal{O}\left(\frac{P_{abs}}{P_0}^2\right)\right). \tag{3.35}$$

Subtracting the baseline voltage $V_0 = \sqrt{Z_0 P_0}$ and inserting Eq. 3.31 results in the pure EPR contribution

$$V_{EPR}^{TL} = V_0 - V_{det} = \sqrt{P_0 Z_0}\chi'' \frac{\omega}{4P_0} \int_{V_s} \vec{H}_1{}^2 \mathrm{d}V. \tag{3.36}$$

Comparing V_{EPR}^{R} and V_{EPR}^{TL} shows that both approaches have very similar dependencies: the EPR signal is proportional to χ'' and to the microwave magnetic field within the sample. Therefore, the principal difference between resonator-based and TL-based EPR does not lie in the functional form of the signal expression but in the achievable magnitude and spatial distribution of $\vec{H}_1$ for a given incident power in the effective interaction volume. In general,

resonators enable stronger $\vec{H}_1$ at lower input powers due to energy build-up, whereas TL-based structures offer broadband operation at the expense of reduced field enhancement.

3.3.2 Experimental Comparison

To experimentally compare both spectrometers, measurements are carried out under individually optimized conditions. For the resonator-based measurement, Bruker's high-performance X-band ElexSys-II E500 CW EPR spectrometer is employed. The input power of the Bruker spectrometer can be adjusted between 2 nW and 200 mW (equivalent to −57 dBm to 23 dBm), with a modulation amplitude of up to 2 mT. It is equipped with the ER4122SHQE cavity which operates between 9.2 GHz and 9.9 GHz and has an unloaded quality factor of $Q_0 = 5000$ [Bre].

For the TL-based measurement, the CPW 90°-rotated TL probe shown in Fig. 4.8b (Section 4.1.2) is used. Among the TL probes designed in this thesis, this geometry provides the highest effective microwave magnetic field strength within the sample volume. The SG is remote controlled with the LAN interface.

For both measurements, the same BDPA sample is used. First, the BDPA powder is fixed between the sample holder in Fig. 3.4a and EPR measurements are performed with the TL-based spectrometer. The Bruker spectrometer uses a glass tube as the sample holder. The BDPA powder combined with the two foils is inserted into the glass tube and pressed together at the bottom like a paper crumble. This ensures that both spectrometers probe the same sample amount and thus the absorptive susceptibility χ'' appearing in $V_{\mathrm{EPR}}^{\mathrm{R}}$ (Eq. 3.27) and $V_{\mathrm{EPR}}^{\mathrm{TL}}$ (Eq. 3.36) is identical.

All measurements are performed in the X-band at room temperature. In the Bruker spectrometer, the external magnetic field is swept from 343.42 mT to 348.78 mT at a fixed frequency of 9.71 GHz, whereas in the TL-based spectrometer a frequency sweep from 9.725 GHz to 9.875 GHz is performed at a constant magnetic field of 350 mT. This frequency range of 150 MHz corresponds to a magnetic-field range of approximately 5.35 mT, allowing direct comparison between the two sweep modes assuming a g-factor close to $g_{\mathrm{e}} = 2.002319$. Note that a magnetic field of 350 mT corresponds to a resonance frequency of $f_{0,\mathrm{r}} = 9.81$ GHz. This slightly higher value in resonance

frequency is not expected to significantly affect the final SNR comparison. The modulation frequency is set to 20 kHz and each scan lasts 10 s. For the Bruker spectrometer, 1024 points are recorded at 0 dB receiver gain and for the custom-built spectrometer 512 points are recorded.

Choice of Optimal Experimental Parameters

From the viewpoint of experimentally adjustable measurement parameters, the signal amplitude is primarily determined by the input power P_0 and the modulation amplitude B_m (see Section 1.2.3). To determine the optimal values of these parameters, the peak-to-peak EPR voltage $V_\mathrm{pp,EPR}$ is extracted and plotted as a function of the parameter under investigation. The measurement results are presented in Fig. 3.15 for the Bruker spectrometer and in Fig. 3.16 for the custom-built system. The vertical axis of the Bruker data is given in arbitrary units and labeled $A_\mathrm{EPR,pp}$, denoting the peak-to-peak EPR signal amplitude.

For the Bruker spectrometer the input power is adjusted by setting the attenuation of the microwave source. The set attenuation values are converted to corresponding power levels, where 0 dB corresponds to an input power of 23 dBm. For the custom-built spectrometer, the shown input power levels correspond to the uncalibrated values set at the SG.

The parameters are selected to avoid sample saturation and overmodulation. To identify the onset of these effects, the dashed curves represent the expected linear response in the absence of saturation and overmodulation. As described in Section 1.2.3, within the linear region the EPR signal scales with the square root of the incident power and linearly with the modulation amplitude. The final parameter settings are chosen near the upper limit of the linear region, ensuring optimal SNR under unsaturated conditions. The values of the experimental parameters are summarized in Tab. 3.4.

Because the input power in each setup is adjusted such that both systems operate just below saturation, it is assumed that, neglecting microwave magnetic field inhomogeneities, both spectrometers generate comparable microwave magnetic field strengths $\vec{H}_1$ in $V_\mathrm{EPR}^\mathrm{R}$ (Eq. 3.27) and $V_\mathrm{EPR}^\mathrm{TL}$ (Eq. 3.36).

A direct comparison of the power levels at the sample is challenging because the signal-chain losses in the Bruker spectrometer are not specified. However,

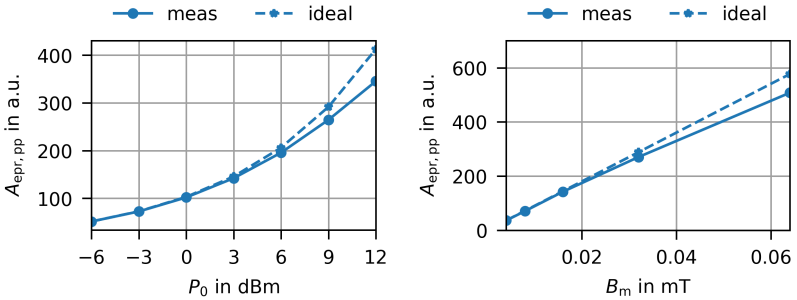

(a) (b)

Figure 3.15: Measured peak-to-peak amplitude with the Bruker spectrometer for an (a) input power and (b) modulation amplitude sweep. The dashed curves represent the ideal response in the absence of saturation and overmodulation.

Table 3.4: Parameters for EPR spectrometer comparison.

Parameter	TL-based	Resonator-based
P_0	6 dBm	3 dBm
B_m	0.016 mT	0.016 mT
f_m	20 kHz	20 kHz
τ	10 ms	10 ms

it is assumed that the power indicated by the instrument corresponds to the calibrated power delivered to the sample, as this is the quantity most relevant to the user. In the custom-built spectrometer operating at 10 GHz, the transmit path exhibits approximately 3 dB of loss up to the sample, with an additional 3 dB loss in the receive path up to the detector, primarily due to the cables and the TL probe. The input power values listed in Tab. 3.3 for the TL-based setup are calibrated at the sample position, and the same assumption is applied to the Bruker spectrometer. As expected, the resonator-based system requires less input power to generate the $\vec{H}_1$ field required to operate just below saturation, owing to its higher Q-factor. However, the power required at the sample is only about 3 dB lower than for the TL-based setup, suggesting that part of the

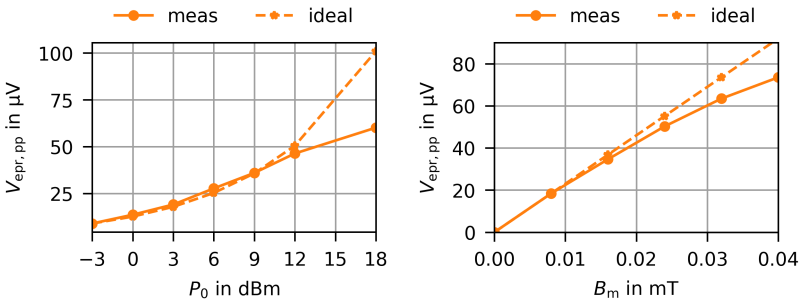

(a) (b)

Figure 3.16: Measured peak-to-peak amplitude with the broadband custom-built spectrometer for an (a) input power calibrated up to the sample position and (b) modulation amplitude sweep. The dashed curves represent the ideal response in the absence of saturation and overmodulation.

resonator energy is not effectively used for sample excitation because only a small fraction of the resonator mode volume overlaps with the small sample.

The noise measured by the spectrometers can mainly be influenced by the time constant of the low-pass filter of the LIA. For the broadband custom-built EPR spectrometer, the low-pass filter bandwidth is set to $B = 7.959\,\text{Hz}$ which results in a time constant of $\tau = 10.19\,\text{ms}$. In the *xEPR* Bruker software, the time constant is configured under *Acquisition Parameter* → *Setup Scan* and is set to $\tau = 10.24\,\text{ms}$. Similar to Chapter 2, the RMS noise voltage is estimated from the measurement data as the standard deviation of the measured magnetic-field or frequency interval where no EPR response occurs.

SNR Comparison

Finally, the SNR is calculated as

$$\text{SNR} = \frac{V_{\text{pp,EPR}}}{V_{\text{n}}},$$

where $V_{\text{pp,EPR}}$ denotes the peak-to-peak EPR voltage and V_{n} the RMS

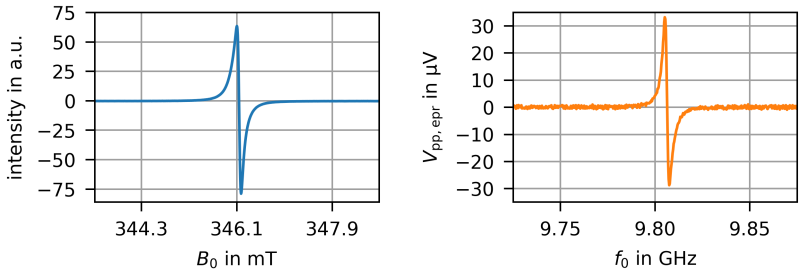

(a) (b)

Figure 3.17: EPR measurements of a powder BDPA sample with (a) the Bruker and (b) the custom-built spectrometer.

noise voltage. The EPR measurements of both spectrometers are shown in Fig. 3.17. The Bruker spectrometer achieves a signal peak-to-peak amplitude of $A_{\mathrm{pp,EPR}} = 142.3$. The noise floor is extracted in the interval from 343.42 mT to 344.49 mT. A small offset is present in the EPR data, which is presumed to be deterministic and likely arises from non-ideal parameter settings. This offset is subtracted prior to variance calculation. It should be noted that if a non-zero mean is present in the noise, it cannot be identified, as it is indistinguishable from the deterministic offset. The RMS noise amplitude in arbitrary units is $A_{\mathrm{n}} = 0.023$ which results in an SNR of 6207.

The broadband custom-built EPR spectrometer has a peak-to-peak amplitude of $V_{\mathrm{pp,EPR}} = 61.9\,\mu\mathrm{V}$. The RMS noise voltage is $V_{\mathrm{n}} = 0.41\,\mu\mathrm{V}$ for the noise floor from 9.725 GHz to 9.76 GHz which leads to an SNR of 151. Hence, the Bruker spectrometer achieves a 41 SNR improvement for the given experimental settings and the specific sample.

The experimentally observed SNR advantage of the resonator-based spectrometer is attributed primarily to differences in the effective noise contributions and in the spatial overlap between the microwave magnetic field and the sample volume. It is assumed that the dominant limitation of the TL-based setup is a higher amplitude noise at the receiver input. This is likely caused by the use of a broadband microwave source and by the requirement of higher input power to reach the $\vec{H}_1$ field necessary to operate just below saturation. In contrast, the Bruker system operates in a comparatively narrow frequency band

and employs a source architecture that can be optimized specifically for low phase and amplitude noise, resulting in a lower effective noise floor.

From the signal perspective, although both spectrometers are operated close to the onset of saturation, the resulting $\vec{H}_1$ field can be assumed to irradiate the entire sample volume more uniformly in the resonator. In the TL-based approach, the planar field distribution decays rapidly with distance from the signal line and therefore only a fraction of the sample may experience the field strength required for saturation, reducing the effective interaction volume.

For the TL-based approach, reducing the noise floor of the overall system architecture is expected to move the achievable SNR closer to that of the resonator-based spectrometer. In addition, for samples with lower spin numbers, corresponding to smaller χ'' and thus reduced coupling, it becomes increasingly beneficial to reduce power consumption and losses, for example by implementing the transceiver electronics on-chip instead of using discrete instruments connected via cables. For mass-limited samples, the transmission-line length can be further reduced to match the small sample extent and thereby minimize losses. In contrast, for concentration-limited samples, increasing the effective transmission-line interaction area can improve coupling by increasing the effective sample volume exposed to $\vec{H}_1$.

Note that the SNR values obtained in this chapter are not directly comparable to the proof-of-concept SNR estimates in Chapter 2. In Chapter 2, the lock-in measurements were performed under substantially different experimental conditions, including a dried and highly concentrated TEMPOL residue covering a larger area of the TL probe, which increases the effective interaction volume and thus the signal amplitude. In addition, the linewidth in the data presented in Chapter 2 is significantly broader, allowing the use of a larger magnetic-field modulation amplitude without excessive line-shape distortion, thereby increasing the detected lock-in signal. Moreover, the RF configuration differs. In particular, much longer cables were used in Chapter 2, such that the actual power delivered to the TL probe cannot be directly compared. Further differences arise from the use of a narrower-band SG and a higher operating frequency, which increases the resonance field and can lead to a larger EPR-induced transmission change, while simultaneously affecting losses and the effective receiver noise floor. Finally, the achievable noise suppression depends on the lock-in amplifier filter settings.

3.4 Summary and Discussion

In this chapter, the design and characterization of various aspects of the TL-based EPR measurement setup realized with lock-in detection and magnetic field modulation were presented. The setup employs a TL as the microwave probe and is operated in transmission mode. In contrast to most conventional mmW transceivers, the TL-based EPR setup utilizes amplitude modulation resulting from the interaction of a modulated magnetic field with the sample's absorption characteristics. This produces an AM microwave signal, which is subsequently demodulated by a detector and further processed using a lock-in amplifier for enhanced signal isolation.

When using planar microwave probes, an unwanted coupling path is present in the setup. It was shown that it is necessary to remove the introduced offset before calculating the absolute value of the data, which leads to the correct amplitude of the EPR measurement data. Another approach would be to choose the phase of the oscillator such that the EPR signal is only present in one of the quadrature components. In this case, the offset does not affect the shape of the EPR signal, but the correct phase would need to be determined for each measurement. A high-pass filter before the detector partially attenuates the interference signal, but due to the nature of the magnetic coupling, a common mode component is also expected to be present on the cable.

The order of the effective modulation index was mapped to the measured EPR signal amplitude V_{EPR}, providing a quantitative link between the two quantities. An EPR peak amplitude of $V_{\mathrm{EPR}} = 1\,\mu\mathrm{V}$ is approximately equivalent to an effective modulation index of $m = 4.8 \times 10^{-6}$ in the presented measurement setup. This approximation is applied in Section 5.2 to design and evaluate the performance of the integrated detector.

A detailed noise analysis was carried out to evaluate the influence of various system components and control interfaces. At higher input powers, amplitude noise from the SG and potentially flicker noise from the detector were identified as the dominant noise contributors. Phase noise is assumed to be largely suppressed, as the detector operates as a demodulator or self-mixer and ideally cancels out correlated phase fluctuations. Remote control of the SG via GPIB and LAN was compared, revealing that the GPIB interface introduces significantly higher noise precisely within the modulation frequency range used

in the EPR setup, between 10 kHz and 30 kHz. Therefore, remote control via LAN is better suited for operation in this frequency range.

In comparison to resonator-based EPR spectrometers operated in reflection mode, the TL-based setup in transmission mode exhibits a difference in how the detector operating point is established. In the transmission configuration, a large carrier signal is inherently present at the detector input and can be used to set the detector operating point directly. In contrast, in resonator-based reflection-mode spectrometers the carrier component is largely suppressed by critical coupling of the resonator, such that a reference arm is used to set the detector operating point. In both approaches, lock-in detection is employed to improve the SNR.

To quantify the performance difference between a high-end resonator-based EPR spectrometer and the custom-built TL-based system, measurements were performed using the same sample and with both setups operated close to the onset of saturation. Under these conditions, the resonator-based setup achieves an SNR approximately 41 times higher than the TL-based system. The observed difference was attributed primarily to two factors: first, the effective noise performance of the respective excitation and receive chains, and second, the spatial overlap between the microwave magnetic field and the sample volume. Notably, the latter aspect is not unique to transmission-line probes and is expected to apply similarly when using planar resonators, since their microwave magnetic field also decays rapidly away from the conductor structure. Future improvements to the TL-based architecture, such as on-chip integration of the transceiver electronics to reduce interconnect losses, optimization of the TL geometry to the intended sample dimensions, and reduction of the overall system noise floor, are expected to increase the achievable SNR and further narrow the sensitivity gap to resonator-based spectrometers. Despite its lower SNR, the TL-based configuration offers a much broader operational bandwidth, enabling applications such as direct zero-field EPR measurements and broadband multi-frequency spectroscopy using a single instrument. It therefore represents a complementary and versatile alternative to conventional resonator-based systems, particularly for experiments requiring broadband capability or frequency-domain flexibility.

In addition to the improvements already made to the TL-based measurement setup, several further enhancements are possible. First, the 3D-printed modulation coil could be redesigned to support higher modulation frequencies.

Increasing the modulation frequency would reduce the influence of $1/f$ noise, thereby improving signal quality. To enable higher modulation frequencies, the inductive nature of the coils must be compensated by a carefully tuned capacitance. However, as the frequency increases, electromagnetic effects such as skin depth reduction and mutual coupling between coil windings lead to a sharp rise in effective impedance, ultimately limiting practical operation to below a few hundred kilohertz [Kel25].

Second, implementing a rail system to mount the TL microwave probe would allow precise positioning and alignment within the magnet. This system would ensure that the probe remains fixed and can be smoothly inserted or retracted, reducing positional variability. Currently, without the support of the 3D-printed holder, the probe tends to shift slightly outside the magnet, and minor movements within the modulation coil can adversely affect EPR measurements. A rail system would effectively eliminate this issue.

Furthermore, the amplitude noise of the SG can be reduced by a factor of $\sqrt{10}$ in terms of voltages by upgrading the SG to the low-noise hardware option.

Finally, implementing long-term signal averaging, as commonly employed in commercial spectrometers to detect weak EPR signals, would be a valuable enhancement to the custom-built system. Such averaging, sometimes conducted over several hours, could significantly enhance sensitivity and SNR.

4 TL Microwave Probes

Parts of this chapter include material previously published in [1, 2].

The key quantity determining the performance of a microwave probe in EPR spectroscopy is the microwave magnetic field, denoted as $\vec{H}_1$. Two aspects of this field are of particular importance: its effective strength within the sample volume and its spatial homogeneity. The effective $\vec{H}_1$ field strength determines the achievable signal amplitude, while its homogeneity affects the accuracy and reproducibility of quantitative measurements.

A strong effective $\vec{H}_1$ field in the sample region is essential because, in the absence of saturation, the EPR signal intensity is directly proportional to the effective microwave excitation strength. Consequently, microwave probe designs aim to maximize the effective $\vec{H}_1$ excitation strength at the sample for a given incident microwave power P_0, thereby improving the attainable SNR and enabling the detection of samples with low spin concentrations. For many CW EPR experiments, where the number, spacing, and relative intensities of the resonance lines provide information about the structure and properties of the sample, a high effective $\vec{H}_1$ field alone is sufficient. In such cases, variations in field homogeneity mainly cause a reduction in signal intensity, which is already reflected in the evaluation of the effective $\vec{H}_1$ excitation strength, and do not significantly alter the spectral shape [HSM19]. Therefore, maximizing the magnetic field strength is often the primary design objective for microwave probes in CW EPR.

However, for certain applications, the homogeneity of the $\vec{H}_1$ field becomes equally critical. In quantitative CW measurements, such as spin counting, an inhomogeneous field distribution can introduce systematic errors, as regions with higher $\vec{H}_1$ contribute disproportionately and lead to sample-shape-dependent results [SMV+20]. In saturation-type CW experiments, $\vec{H}_1$ inhomogeneities affect the accuracy of relaxation time determinations [FM82]. For pulsed EPR experiments, field uniformity is even more important,

since the excitation flip angle is directly determined by the local $\vec{H}_1$ field strength [HSM19].

As briefly introduced in Section 1.3, several TL–based microwave probe designs have been reported in the literature. Tab. 4.1 summarizes these probes, including their geometries, substrates, and sample placements. CPW probes are presented in several works [CBK+13, WSC+15, MDS20, JLS+19], with similar dimensions in the first three works, likely reflecting their origin in the same research group. MSL probes have also been implemented in other works [CSW17, SAA+19]. Alternative approaches include wire-based conductors wound around a sample compartment [Hag19, Hag23]. However, these studies primarily employ TLs as components within complete TL-based EPR spectrometers rather than focusing on their detailed design. As a result, no consistent design rules have been established, and guidelines for systematic optimization of TL microwave probes for EPR remain limited.

The focus on $\vec{H}_1$-field homogeneity in TL microwave probe designs reported in the literature has been relatively scarce. Only the work by Shreshta et al. specifically addresses field uniformity by positioning the sample inside a cavity within the substrate to improve homogeneity [SAA+19].

Against this background, the analysis in the present chapter is guided by the following research questions:

- Which of the two common TL types, MSL or CPW, is more suitable as a microwave probe for EPR spectroscopy?
- Which simulation parameter provides the most meaningful basis for comparing different TL designs in the EPR context?
- What are the optimal geometrical and material parameters for MSL and CPW to maximize the magnetic field strength at the sample?
- To what extent is the EPR signal amplitude reduced if only one component of the microwave magnetic field $\vec{H}_1$ of the CPW and MSL is oriented perpendicular to the external magnetic field B_0?
- Can the inverted microstrip line (IMSL) be employed as a viable probe concept for EPR spectroscopy, providing a more homogeneous $\vec{H}_1$ field?

Table 4.1: Overview of published TL microwave probes for EPR spectroscopy. Adapted from [1] under CC BY 4.0 license.

Reference	Transmission line		Substrate			Dimensions		Frequency range	
	Type	Orientation	Material	ε_r	h	w	s	f_{min}	f_{max}
					mm	µm	µm	GHz	GHz
[CBK+13]	CPW	meander	sapphire	10	0.33	60	25	0.5	40
[WSC+15]	CPW	meander	sapphire	10	0.43	100	41	0.1	67
[MDS20]	CPW	meander	sapphire	10	0.43	100	42	0.1	25
[CSW17]	MSL	meander	silica	3.8	1.52	100	–	8.0	13
[JLS+19]	CPW	straight	RO4350	3.34	1.00	150	100	1.0	15
[SAA+19]*	MSL	straight	n.a.	2	0.75	1920	–	n.a.	n.a.
[Hag23]	wire MSL	meander	acrylic tape	3.15	0.15	250	–	0.1	18

*values extracted from supplementary material

4.1 Magnetic Field Strength Optimization

In this section, two common TL types, the CPW and the MSL, are investigated, optimized, and compared as microwave probes, with the objective of achieving a high microwave magnetic field strength.

4.1.1 Optimized Geometries for CPW and MSL

To determine the optimal designs for the CPW and MSL probes, this subsection uses the signal model introduced in Section 3.3.1 to derive an appropriate optimization metric for TL probes. Based on this metric, design guidelines for both structures are formulated, and the resulting optimized geometries are compared using simulation results.

Signal Metric and Modeling Approach

As shown in Eq. 3.31 in Section 3.3.1, in the absence of sample saturation, the EPR signal is proportional to the microwave power absorbed by the spin system, which is itself proportional to the microwave magnetic-field intensity within the sample [Poo96]. Since only the component of the oscillating magnetic field perpendicular ($\vec{H}_1^{\perp}$) to the external field B_0 drives spin transitions, this yields

$$V_{\mathrm{EPR}} \propto P_{\mathrm{abs}} \propto \iiint_{V_s} \left|\vec{H}_1^{\perp}(\vec{r})\right|^2 \mathrm{d}V. \tag{4.1}$$

For a linearly polarized excitation, only one of the two counter-rotating circular components of $\vec{H}_1$ couples efficiently to the spin system and contributes to microwave absorption [GS18]. For TLs, the field distribution is approximately invariant along the propagation direction over the relevant interaction length, so the volume integral can be reduced to an integral over the sample cross-section A_s

$$\iint_{A_s} \left|\vec{H}_1^{\perp}(\vec{r})\right|^2 \mathrm{d}A =: k_A. \tag{4.2}$$

The parameter k_A represents an effective measure of the microwave magnetic field excitation within the sample cross-section that directly relates to the EPR signal amplitude. Owing to the cross-sectional integration, k_A has units of A^2. The non-normalized form is used because the detected signal depends on the total integrated field strength, see Eq. 4.2, assuming the field is entirely confined within the sample region. A normalized/average field would strongly depend on the arbitrarily chosen integration domain, which is why the non-normalized form is used here.

In general, the electromagnetic fields of planar TLs are hybrids of transverse magnetic (TM) and transverse electric (TE) modes. For substrates that are electrically thin (thickness much smaller than the wavelength), the fields are quasi-TEM and are consequently very close to the solution of the electrostatic problem of two charged conductors [Poz21]. However, analytical descriptions of the exact field distributions of planar TLs are not straightforward and no general closed-form solutions exist [Col07].

For MSL structures,Wiesbeck derived approximate field expressions under the TEM assumption by modeling the conductor as an array of line charges, from which the electrical potential is obtained [Wie72]. The electric field is then calculated from this potential, and the magnetic field is subsequently derived using the Cauchy–Riemann relations. For CPW structures, Simons and Arora approached the coupled slotline problem by transforming it into an equivalent rectangular waveguide problem with suitable boundary conditions, thereby enabling field calculation [SA82].

Although these derivations provide valuable theoretical insight, the resulting equations remain complex, and the dependence of magnetic field strength on geometric design parameters is not immediately apparent. For this reason, a 3D finite-element electromagnetic solver (CST Microwave Studio) is employed in this work to directly optimize the TL geometry.

The cross-sections of the MSL and CPW structures together with their respective design parameters are shown in Fig. 4.1. In addition to the global coordinate system introduced in the EPR measurement setup in Fig. 3.1, a local coordinate system (denoted by the subscript “L”) is defined where the propagation direction of the TL always coincides with the z_L-axis. Owing to the quasi-TEM character of the guided mode, the longitudinal magnetic field component $\vec{H}_{1,z}$ can be neglected. Depending on how the TL is oriented relative

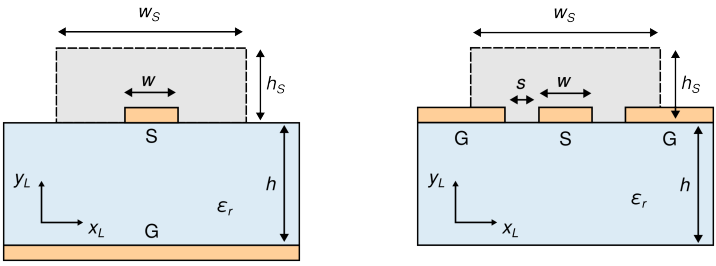

(a) (b)

Figure 4.1: Cross-sections of (a) the MSL, and (b) the CPW in the $x_\mathrm{L}y_\mathrm{L}$-plane showing conductor width w, gap s, substrate height h, and dielectric constant ε_r. The gray region marks the sample cross-section with w_s and h_s. Adapted from [1] under CC BY 4.0 license.

to the external field $\vec{B}_0$, two extreme configurations can be distinguished, both of which are realized and analyzed in this chapter. Here, $\vec{e}_{i,\mathrm{L}}$ denotes the unit vector along the i-axis of the local TL coordinate system.

1. $\vec{B}_0 \parallel \vec{e}_{z,\mathrm{L}}$: The external magnetic field is pointing in the direction of propagation. In this case, both $H_{1,x}$ and $H_{1,y}$ contribute to the EPR signal and the magnitude of the magnetic field strength can be calculated as

$$\left|\vec{H}_1^{\perp}\right| = \sqrt{H_{1,x}^2 + H_{1,y}^2}. \tag{4.3}$$

   This case is relevant for the manufactured 90°-rotated structures (MSL90 and CPW90, see Fig. 4.8) as discussed in Section 4.1.2.

2. $\vec{B}_0 \parallel \vec{e}_{x,\mathrm{L}}$: The external magnetic field is oriented perpendicular to the direction of propagation, which results in the contribution of only $H_{1,y}$ to the EPR signal:

$$\left|\vec{H}_1^{\perp}\right| = \sqrt{H_{1,y}^2} \tag{4.4}$$

   This case is relevant for the manufactured straight structures (MSL0 and CPW0, see Fig. 4.8) as discussed in Section 4.1.2.

Note that in Eq. 4.3 and 4.4, the explicit dependence of the magnetic fields on the position $\vec{r}$ is omitted for clarity. This convention is adopted throughout the remainder of the text. The spatial distributions of $H_{1,x}^2$ and $H_{1,y}^2$ are very similar, as will be shown graphically in Fig. 4.5a and 4.6a. In both cases, the regions of strong and weak magnetic field intensities coincide, differing only in their vector orientation. Additional simulations further confirm that optimizing the geometric parameters for the first orientation yields the same optimal configurations as for the second case. Consequently, the parameters that maximize k_A in one case are also optimal for the other. For the subsequent parameter optimization, the analysis shows the results for the first orientation case.

In the CST simulations, the sample cross-section is approximated by a rectangle of width $w_\mathrm{s} = 2500\,\mu\mathrm{m}$ and height $h_\mathrm{s} = 300\,\mu\mathrm{m}$ in the $x_\mathrm{L}y_\mathrm{L}$-plane, indicated by the dashed gray box in Fig. 4.1. These dimensions are chosen sufficiently large to ensure that the magnetic field is fully confined within the integration region across the entire design space. Consequently, the optimized TL parameters are independent of the exact sample size as long as the sample is not substantially smaller than the assumed dimensions. For completeness, the impact of very small sample sizes is discussed separately in Section 4.3.

In the $x_\mathrm{L}z_\mathrm{L}$-plane, the sample shape is intermediate between a circle and a rectangle, so its cross-section in the $x_\mathrm{L}y_\mathrm{L}$-plane is not perfectly uniform along the z-axis. However, the chosen dimensions ensure that the regions where the sample deviates from uniformity occur where the microwave magnetic fields are negligible, and therefore their influence on the simulation results is minimal.

Because the underlying electromagnetic model is linear, variations in the applied input power result only in proportional scaling of the absolute field amplitudes. Therefore, the relative differences between configurations considered in the optimization are independent of the input power. Throughout this work, the numerical values of the simulated effective magnetic field strengths are shown for an input power of $P_0 = 0.5\,\mathrm{W}$. The boundary conditions are set as follows: all structures are simulated with open boundaries in the x_L- and z_L-directions, while in the positive y_L-direction an open boundary is applied with an extended free-space region between the structure and the boundary. For the MSL configuration, the boundary in the negative y_L-direction is defined as a perfect electric conductor, whereas for the CPW configuration it is set as open. A

hexahedral mesh with local refinement in the sample region is used to achieve high spatial resolution of the magnetic field distribution.

Microstrip Transmission Line

A MSL is primarily defined by the substrate height h, the dielectric constant ε_r, and the conductor width w, as shown in Fig. 4.1a. The signal conductor is located on the top surface of the substrate, while the ground plane lies on the bottom.

Fig. 4.2a shows the simulated dependence of k_A on the substrate height h for $\varepsilon_r = 9.9$ and $w = 235\,\mu m$. The results indicate that h has only a weak influence on k_A, with slightly higher values at smaller h for increasing frequency. A possible explanation for the latter effect is the excitation of higher-order modes, particular at higher frequencies [Poz21].

The influence of substrate modes can be understood by approximating the MSL as a grounded dielectric substrate. In such a structure, the TM_0 surface-wave mode has a zero cutoff frequency. Since part of its field distribution is aligned with the quasi-TEM mode of the MSL, coupling can occur between the guided mode and the surface-wave mode, leading to additional power loss. At DC, the electromagnetic fields vanish. However, the frequency at which this coupling becomes significant is inversely proportional to the substrate height. The same dependence holds for the cutoff frequencies of the TE_1 and TM1 modes. The chosen relatively high dielectric constant ε_r further decreases the cutoff frequencies of these modes. Consequently, increasing the substrate height lowers the frequency at which higher-order surface modes can be excited [Poz21]. Therefore, to achieve a high effective magnetic field strength, a substrate height of 250 µm or less is preferable.

To evaluate the role of the substrate permittivity, three commonly available dielectric constants are analyzed while keeping $h = 250\,\mu m$ and $w = 235\,\mu m$ constant. The chosen materials, Rogers 4003C ($\varepsilon_r = 3.38$), Rogers 3006 ($\varepsilon_r = 6.15$), and alumina ($\varepsilon_r = 9.9$) represent typical substrate options.

As shown in Fig. 4.2b, increasing ε_r results in a higher effective magnetic field strength. An explanation for this behavior is that a higher dielectric constant leads to stronger confinement of the electric field within the substrate. For a

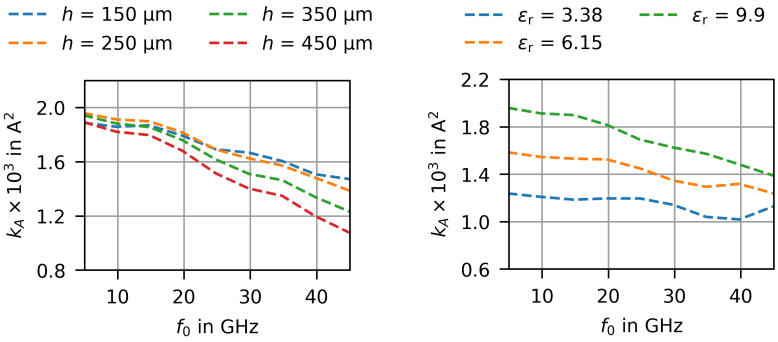

Figure 4.2: MSL simulation results showing (a) the influence of the substrate height h for $w = 235$ µm and $\varepsilon_r = 9.9$ and (b) the effect of dielectric constant ε_r for $w = 235$ µm and $h = 250$ µm. Adapted from [1] under CC BY 4.0 license.

given excitation, this results in a higher surface current density on the signal conductor [Poz21]. This increased current density can contribute to an enhanced magnetic field strength. Therefore, among the materials considered here, the highest dielectric constant of $\varepsilon_r = 9.9$ is favorable for achieving a high k_A.

To explain the observed frequency dependence of k_A, the effective dielectric constant ε_e is considered. The effective dielectric constant ε_e depends on the relative permittivity of the substrate ε_r as well as on the conductor width w and substrate height h, and accounts for the fact that the electromagnetic fields are distributed partly in the dielectric substrate and partly in the surrounding air. It may be interpreted as the permittivity of an equivalent homogeneous medium that reproduces the propagation behavior of the MSL. As the MSL does not support a true TEM mode, its propagation constant is not a linear function of frequency. As a consequence, the effective dielectric constant becomes frequency dependent, leading to a dispersive behavior of the guided mode. With increasing frequency, this dispersion can result in a reduction of the effective magnetic field strength [Poz21].

The effect of varying the conductor width is shown in Fig. 4.3, with $\varepsilon_r = 9.9$ and $h = 250$ µm. Here, k_A increases as w decreases. This trend can be attributed

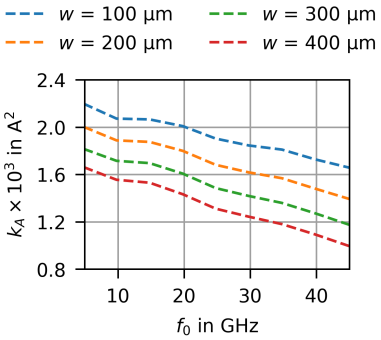

Figure 4.3: MSL simulation results showing the effect of varying the conductor width w with $\varepsilon_r = 9.9$ and $h = 250\,\mu m$. Adapted from [1] under CC BY 4.0 license.

to the increased surface current density associated with narrower signal conductors [Poz21], which in turn can enhance the magnetic field generated by the MSL. Consequently, selecting a smaller conductor width is beneficial for obtaining a high effective magnetic field strength.

In the measurements, the TLs are driven by a commercial 50 Ω signal generator and connected using standard 50 Ω connectors. To guarantee efficient power transfer over a broad frequency range, the characteristic impedance of the TLs is fixed at $Z_0 = 50\,\Omega$, reducing the number of free design parameters from three to two [Poz21]. Under this constraint, a larger dielectric constant ε_r results in a smaller conductor width w, which both contribute to an increased effective magnetic field strength. Due to fabrication limits in the context of this work, the smallest available substrate thickness for $\varepsilon_r = 9.9$ is $h = 250\,\mu m$, which fixes the conductor width at $w = 235\,\mu m$.

Coplanar Waveguide Transmission Line

The cross-section of a CPW transmission line is shown in Fig. 4.1b. In contrast to the MSL, both the signal and ground conductors are located on the same side of the substrate. A CPW structure is characterized by the substrate dielectric constant ε_r, the conductor width w, and the gap s between signal and ground.

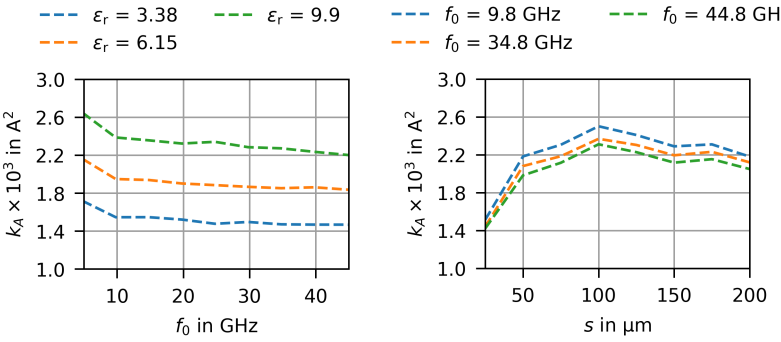

(a) (b)

Figure 4.4: CPW transmission line simulation results showing (a) the effect of dielectric constant ε_r with $s = 110\,\mu m$, $w = 235\,\mu m$, and $h = 250\,\mu m$ and (b) the effect of gap size s with w adjusted for $Z_0 = 50\,\Omega$, $\varepsilon_r = 9.9$, and $h = 250\,\mu m$. Adapted from [1] under CC BY 4.0 license.

To first order, the CPW transmission mode is not influenced by the substrate thickness h.

Fig. 4.4a shows the dependence of the effective magnetic field strength on the dielectric constant. In these simulations, the conductor width is fixed at $w = 235\,\mu m$ and the gap at $s = 110\,\mu m$. Similar to the behavior observed for MSLs, an increase in ε_r leads to an enhancement of the effective microwave magnetic field strength. This trend can be attributed to comparable field-confinement and current-distribution effects in the coplanar waveguide geometry. Consequently, among the materials investigated, the substrate with the highest dielectric constant of $\varepsilon_r = 9.9$ is most suitable for maximizing the effective magnetic field strength.

The dependence of k_A on the gap size s and the conductor width w is shown in Fig. 4.4b. In view of the targeted characteristic impedance of $Z_0 = 50\,\Omega$ for the final design, only combinations of s and w that yield this impedance are considered and directly compared. Since the conductor width w has only a minor influence on k_A compared to the gap size s, the observed results predominantly reflect the influence of s on the effective magnetic field strength. For a substrate

permittivity of $\varepsilon_r = 9.9$, the condition $Z_0 = 50\,\Omega$ is approximately fulfilled when $w \approx 2s$.

The results are shown for $f_0 = 9.8\,\text{GHz}$, $f_0 = 34.8\,\text{GHz}$, and $f_0 = 44.8\,\text{GHz}$, while the same qualitative behavior is observed across the entire frequency range considered. The data reveal a maximum in k_A for the gap size s (and the corresponding width w) at around $s = 100\,\mu\text{m}$. For larger gap sizes, k_A decreases slightly. For smaller gap sizes, the electric field between the signal and ground conductors becomes more strongly concentrated, which leads to an increased surface current density along the conductor edges. As a result, the magnetic field intensity at the edges of the signal and ground conductors increases. At the same time, the spatial extent of the magnetic field distribution is reduced, as the fields become more localized near the conductor edges [Poz21]. This trade-off between local field enhancement and spatial confinement explains the existence of an optimum gap size for maximizing the effective magnetic field strength. Consequently, the maximum effective magnetic field strength is achieved for a gap size of about $s = 100\,\mu\text{m}$.

In contrast to MSLs, the conductor width w in CPW structures can be chosen independently of the substrate thickness while maintaining $Z_0 = 50\,\Omega$, since the characteristic impedance is only weakly dependent on h. To ensure manufacturability with the available in-house equipment, the dimensions $w = 235\,\mu\text{m}$ and $s = 110\,\mu\text{m}$ are selected in this work. To suppress substrate modes at higher frequencies [Poz21], the smallest available substrate thickness of $h = 250\,\mu\text{m}$ is used for the final CPW design.

Comparison

After optimizing the MSL and CPW individually, their performance is compared in this section. The chosen dimensions for both TL types are summarized in Tab. 4.2 and are used for the following simulations. Fig. 4.5 shows the simulated magnetic field of the MSL in the $x_L y_L$-plane at $f_0 = 9.8\,\text{GHz}$ for case one, where both field components, $H_{1,y}$ and $H_{1,x}$, are considered. The magnetic field magnitude distribution and the corresponding field lines are illustrated. The maximum field amplitude for the CPW is 870 A/m and occurs at the edges of the signal line.

Table 4.2: Dimensions of the TL structures.

TL type	Substrate	w µm	s µm	h µm
CPW	alumina, $\varepsilon_r = 9.9$	235	110	250
MSL	alumina, $\varepsilon_r = 9.9$	235	-	250

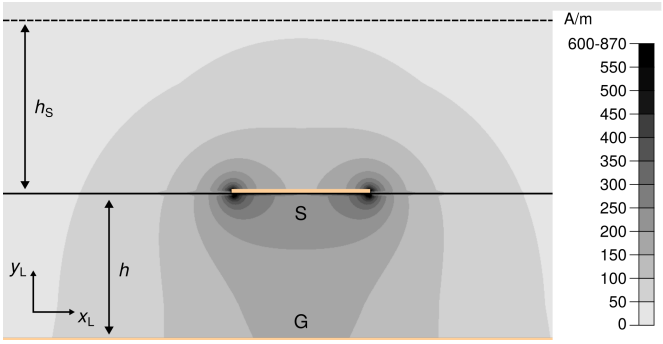

(a)

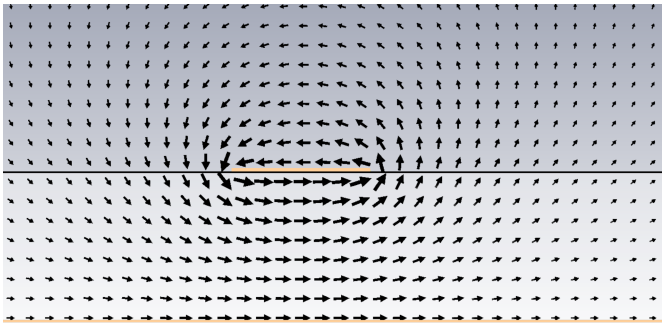

(b)

Figure 4.5: Simulated magnetic field of the MSL for case 1 ($H_{1,y}$ and $H_{1,x}$) in the $x_L y_L$-plane at $f_0 = 9.8$ GHz. The field reaches a maximum of 870 A/m at the edges of the signal and ground lines. (a) Field magnitude. (b) Magnetic field lines. Adapted from [1] under CC BY 4.0 license.

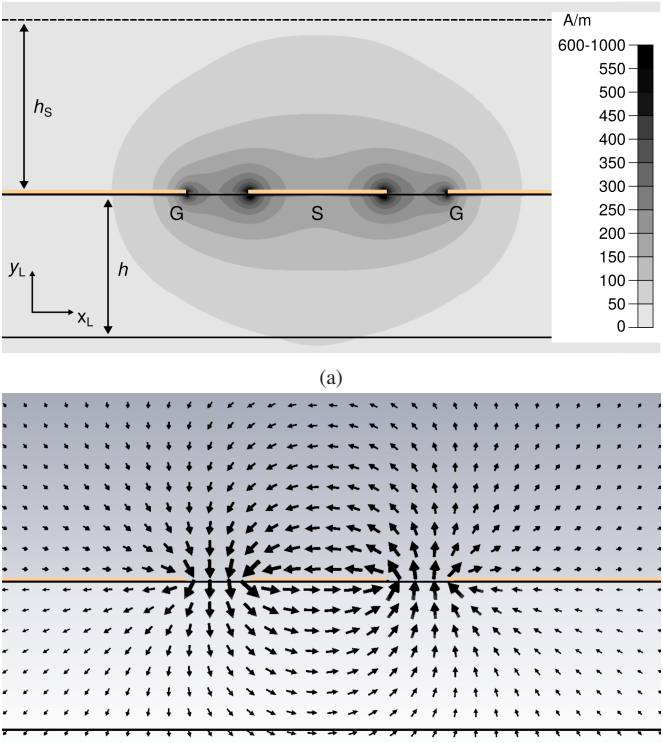

(a)

(b)

Figure 4.6: Simulated magnetic field of the CPW for case 1 ($H_{1,y}$ and $H_{1,x}$) in the $x_L y_L$-plane at $f_0 = 9.8\,\mathrm{GHz}$. The field reaches a maximum of $1000\,\mathrm{A/m}$ at the edges of the signal line. (a) Field magnitude. (b) Magnetic field lines. Adapted from [1] under CC BY 4.0 license.

Fig. 4.6 shows the equivalent representation for the CPW. The maximum field amplitude is $1000\,\mathrm{A/m}$, occurring at the edges of the conductors.

To emphasize the differences, Fig. 4.7a shows the lateral distribution of the magnetic field strength along the x_L-axis for both TL types. This distribution is obtained by integrating the magnetic field over the sample height $h_s = 300\,\mu\mathrm{m}$ from Fig. 4.5 and 4.6, respectively. For both TLs, the maximum magnetic field occurs at the edges of the signal conductor ($x_L \approx \pm 0.12\,\mathrm{mm}$), with the CPW

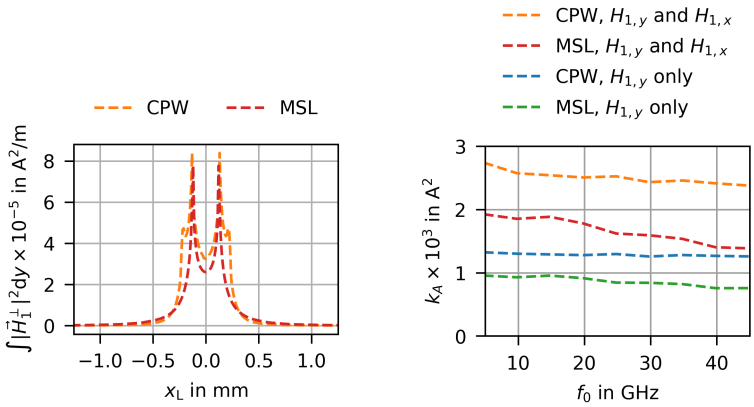

Figure 4.7: (a) Simulated lateral distribution of the effective magnetic field strength for case 1 ($H_{1,y}$ and $H_{1,x}$) at $f_0 = 9.8$ GHz for the CPW and MSL and (b) a comparison of the effective magnetic field strength k_A for the two lines in their two orientations. Adapted from [1] under CC BY 4.0 license.

showing a slightly higher peak. Additionally, the CPW exhibits a secondary peak at the edge of the ground line ($x_L \approx \pm 0.17$ mm). Along the x_L-axis, the magnetic-field strength of the CPW exceeds that of the MSL up to approximately ± 0.3 mm.

Integrating the lateral distribution along the x_L-axis yields the effective magnetic field strength k_A. Fig. 4.7b shows the effective magnetic field strength k_A for the MSL and CPW in both orientations relative to B_0, as discussed in Eq. 4.3 and Eq. 4.4, corresponding to the four designs that were fabricated and characterized in Section 4.1.2.

For both orientations, k_A is higher for the CPW transmission line than for the MSL. Notably, the MSL shows a higher effective magnetic field when both $H_{1,y}$ and $H_{1,x}$ contribute than the CPW line does when only $H_{1,y}$ contributes. When only the $H_{1,y}$ component contributes to the EPR signal, k_A is reduced by approximately a factor of two for both line types.

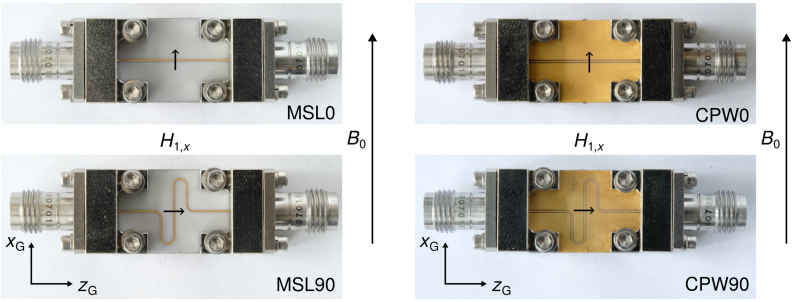

(a) (b)

Figure 4.8: Pictures of (a) the MSL and (b) the CPW microwave probes manufactured from gold-laminated alumina. The upper pictures show the straight TLs (MSL0 and CPW0) and the lower pictures show the 90°-rotated TLs (MSL90 and CPW90). The arrows in the center of the structure indicate the direction of the microwave magnetic field $H_{1,x}$ (defined in the local coordinate system) at the sample position. Adapted from [1] under CC BY 4.0 license.

4.1.2 Assembly and Electrical Characterization

To validate the simulated results from Fig. 4.7b, four TL structures are fabricated and assembled. A top-view of the structures is shown in Fig. 4.8. The global coordinate system (subscript “G") is used to define the orientations of the TLs and the external magnetic field B_0. The sample is positioned at the center of each line, and the arrows indicate the direction of the microwave magnetic field component along the x_L axis, which is defined in the local coordinate system rather than the global coordinate system.

For the 90°-rotated lines in the lower half of the figure (MSL90, CPW90), both $H_{1,y}$ and $H_{1,x}$ contribute to the EPR signal, corresponding to the first case described in Eq. 4.3. For the straight lines in the upper half (MSL0, CPW0), only $H_{1,y}$ contributes to the EPR signal. In all cases, the optimized parameters listed in Tab. 4.2 are applied.

All TL probes are based on an alumina substrate with a dielectric constant of $\varepsilon_r = 9.9$. For the MSL, the substrate is gold-laminated on both sides, whereas for the CPW, only one side is gold-laminated. The gold layer thickness is approximately 3 µm. All structures have overall dimensions of $W = 12.7$ mm

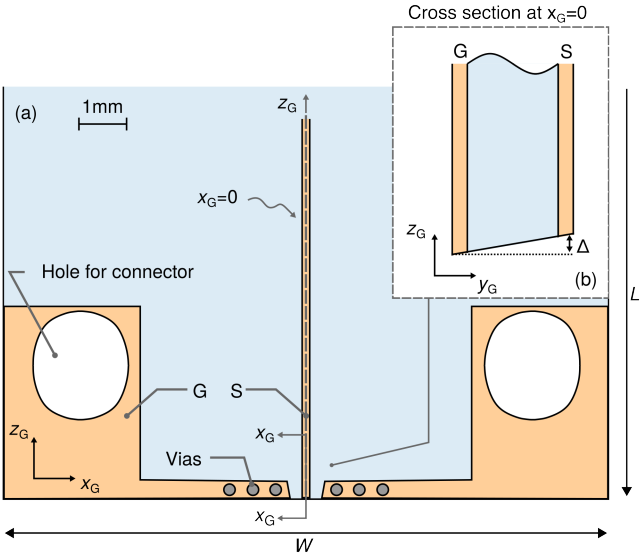

Figure 4.9: In the main figure (a), the designed microstrip–to–connector transition in the $x_G z_G$-plane is shown. The inset (b) shows the structure in the $y_G z_G$-plane at position $x_G = 0$ to visualize the inclined edge of the board outline caused by laser cutting. Adapted from [1] under CC BY 4.0 license.

and $L = 17.8\,\text{mm}$ (see Fig. 4.9) and are fabricated in-house using a LPKF ProtoLaser R4. The TLs are assembled with 1.85 mm end-launch connectors featuring a pin diameter of 0.13 mm, covering the frequency range up to 67 GHz.

Connectors introduce unavoidable losses and ripples in the transmission coefficient S_{21}. To minimize these effects, a transition structure is designed for the MSL to convert the connector's coplanar/coaxial mode to the desired microstrip mode, see Fig. 4.9. The signal line width is maintained at $w = 235\,\mu\text{m}$, while the gap between the signal line and the ground plane gradually increases in the positive z_G-direction. To reduce impedance mismatch, the first via of the transition structure is positioned as close as possible to the edge of the ground plane parallel to the signal line. For the CPW transmission line, the connector is attached directly without a dedicated transition structure. Tapering the signal or ground line to compensate for impedance mismatch did not result in any observable improvement.

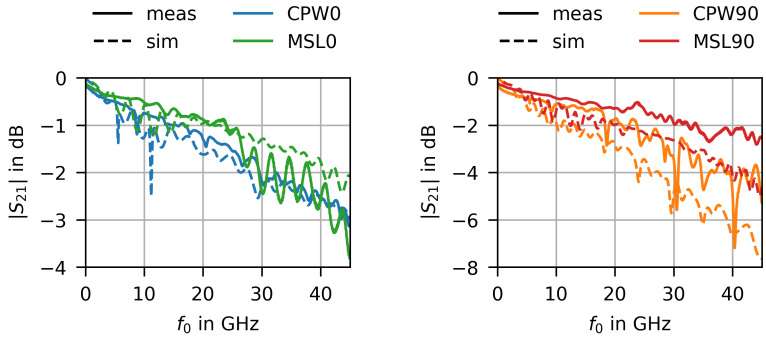

(a) (b)

Figure 4.10: Comparison of measured (solid lines) and simulated (dashed lines) transmission magnitudes $|S_{21}|$ for (a) the straight TLs and (b) the TLs rotated by 90°. Note the different scales of the y-axes. Adapted from [1] under CC BY 4.0 license.

To suppress undesired propagation modes, a 0.5 mm thick FR4 substrate is placed beneath the alumina substrate of the CPW, increasing the separation between the bottom of the alumina and the connector, which acts as ground. A 0.5 mm thick FR4 substrate is also installed under the MSL to provide mechanical stability. This configuration results in the MSL ground connecting to the connector ground only via the vias and at the sidewalls of the TL.

The measured magnitude of the transmission coefficient $|S_{21}|$ for all four structures is shown in Fig. 4.10 (solid curves). The TLs rotated by 90° are longer than the straight lines, resulting in higher losses. Due to the laser cutting of the alumina substrate, the outer edge is slightly inclined, resulting in a small gap Δ between the connector and the alumina board (see inset of Fig. 4.9). Modeling this effect in the CST simulations indicates that a presence of a gap increases losses, particularly at higher frequencies. Incorporating a 100 µm gap, along with the connectors, FR4 substrates, and a metal roughness of 2 µm, yields the simulated transmission coefficient $|S_{21}|$ shown as dashed curves in Fig. 4.10. Overall, the simulated results are in reasonable agreement with the measurements, reproducing the loss trends as well as comparable standing-wave patterns in $|S_{21}|$.

4.1.3 EPR Performance Evaluation

To evaluate the performance of the different TL microwave probes, Trityl powder is used as a test sample. Trityl contains a single unpaired electron that interacts predominantly with the external magnetic field B_0, producing a single, well-defined resonance line in the EPR spectrum [EEBW10].

EPR measurements are carried out across a wide frequency range, with resonance frequencies between 4.8 GHz and 44.8 GHz in steps of 5 GHz. For each measurement, the microwave frequency f_0 is swept while the external magnetic field B_0 is fixed.

For a fair comparison, both signal and noise contributions must be considered. In the measurements presented in this chapter, the signal generator is remotely controlled via a GPIB interface. As discussed in Section 3.2, switching to LAN control would lower the noise floor, an aspect that was only identified after the measurements in this chapter had been conducted.

To assess probe-specific noise contributions, a separate noise analysis is performed following the procedure described in Section 3.2. The probe inputs are terminated with 50 Ω loads, while the outputs are connected identically to the EPR measurements, including the detector and lock-in amplifier. Under these conditions, the measured baseband noise represents the contribution of the TLs to the noise observed in the final EPR measurements after demodulation by the detector. The resulting spectra, shown in Fig. 4.11, demonstrate that the TL probes do not introduce additional noise. Consequently, relative SNR comparisons can be made directly based on the measured signal amplitudes.

As outlined in Section 1.2.3, a number of experimental parameters must be chosen carefully for each measurement. The input power P_0 is adjusted such that, when the TL probe is replaced by a direct connection, the power at the detector input is constant at 3 dBm, thereby compensating for cable losses. The modulation amplitude is set to $V_\mathrm{m} = 0.4\,\mathrm{V}$, chosen to maximize signal intensity while avoiding distortion. A modulation frequency of $f_\mathrm{m} = 20\,\mathrm{kHz}$ is used so that the corresponding modulation field B_m can still be reliably detected with the teslameter. The lock-in amplifier time constant is set to $\tau = 75\,\mathrm{ms}$, ensuring an optimal balance between distortion suppression and SNR.

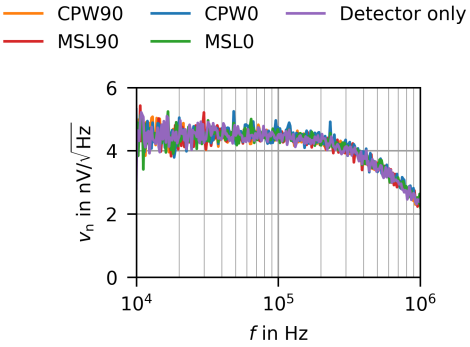

Figure 4.11: Noise voltage spectral density measurements for the different TL microwave probes. As a reference, the noise floor of the 50 Ω-terminated detector is also shown.

To allow direct comparison between the TL microwave probes, the measured EPR amplitude V_{EPR} is normalized by the corresponding transmission losses

$$V_{\text{EPR,norm}} = \frac{V_{\text{EPR}}}{|S_{21}|}, \tag{4.5}$$

where $|S_{21}|$ is obtained from the data in Fig. 4.10. This normalization removes the influence of impedance mismatches and connector losses, isolating the probe losses from the EPR-induced absorption. However, since repeated mounting of the probes can slightly shift the measured $|S_{21}|$ along the frequency axis, the normalization primarily compensates for the overall trend of the losses but may not fully account for frequency-localized effects.

Normalized EPR spectra are shown in Fig. 4.12 for two commonly used frequency bands, X-band and Q-band. In Fig. 4.12a, the field is set to $B_{0,\text{r}} = 350\,\text{mT}$, resulting in an EPR resonance at the expected frequency $f_{0,\text{r}} = 9.8\,\text{GHz}$, as given by Eq. 1.9. Similarly, Fig. 4.12b shows a resonance at $f_{0,\text{r}} = 34.8\,\text{GHz}$ with the external field set to $B_{0,\text{r}} = 1243.2\,\text{mT}$. Each spectrum consists of 512 data points.

In EPR spectroscopy, a quantity of particular interest is the signal intensity which is proportional to the number of unpaired spins [EEBW10]. The signal

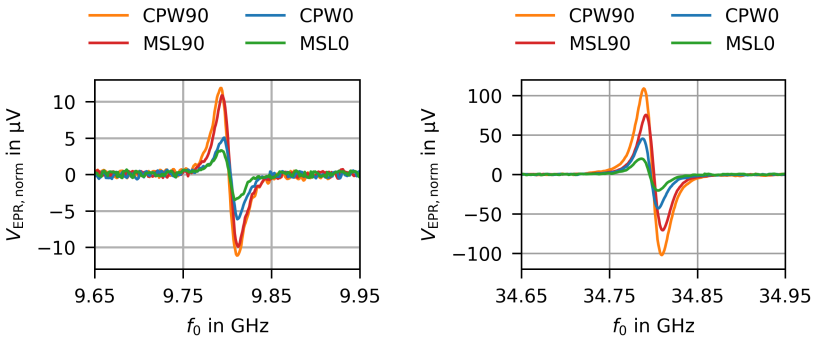

Figure 4.12: Measured EPR curves for (a) an external magnetic field strength of $B_{0,r} = 350\,\mathrm{mT}$ ($f_{0,r} = 9.8\,\mathrm{GHz}$) and (b) an external magnetic field strength of $B_{0,r} = 1243.2\,\mathrm{mT}$ ($f_{0,r} = 34.8\,\mathrm{GHz}$) for the microwave TLs shown in Fig. 4.8. The microwave frequency f_0 is swept and the external magnetic field B_0 is kept constant. Adapted from [1] under CC BY 4.0 license.

intensity is determined by calculating the double integral of the normalized signal amplitude $V_{\mathrm{EPR,norm}}$

$$\text{Signal intensity} = \iint V_{\mathrm{EPR,norm}} \mathrm{d}f_0 \mathrm{d}f_0. \tag{4.6}$$

which corresponds to the area under the absorption curve. If the line shape is preserved, comparisons may also be based on the peak-to-peak derivative amplitude $V_{\mathrm{EPR,norm,pp}}$ [CCM16].

Control experiments were also conducted to rule out spurious EPR signals from the probes or the sample holder. Neither the bare probes nor the empty sample holder produced any detectable EPR response across the investigated frequency range.

Fig. 4.13a summarizes the frequency dependence of $V_{\mathrm{EPR,norm,pp}}$ for the four probe designs. The trends follow the simulated effective magnetic field strengths k_A in Fig. 4.7b. The CPW90 probe, where both $H_{1,y}$ and $H_{1,x}$ contribute, consistently yields the strongest EPR response, whereas the straight CPW shows a reduction by a factor of approximately two to three and the straight MSL by

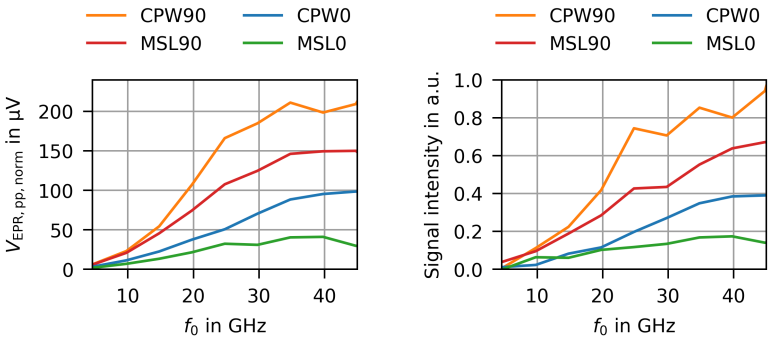

Figure 4.13: Comparison of the different TL microwave probes of (a) the normalized EPR peak-to-peak amplitude and (b) the signal intensity (double integral of the EPR curves). Adapted from [1] under CC BY 4.0 license.

at least a factor of three relative to their 90°-rotated counterparts. For both straight lines, the measured reduction is slightly larger than predicted by the simulations.

This deviation may be related to uncertainties in the measurement setup. One possibility is that the sample, when positioned on the center conductor of the 90°-rotated structures, also overlaps slightly with the adjacent parallel conductors. These conductors could contribute weakly to the EPR response, which might explain why the rotated structures appear partly stronger in the measurements than in the simulations. Another factor could be a slight misalignment of the external magnetic field B_0, which may not have been perfectly confined to the $x_G z_G$-plane. Since the poles of the magnet can be adjusted in all three spatial directions, small alignment inaccuracies cannot be ruled out.

As predicted by Eq. 1.6, the normalized peak-to-peak amplitude increases with frequency/magnetic field strength due to the larger spin-state energy splitting. However, this increase becomes less pronounced above 25 GHz, which may indicate the onset of additional relaxation- or saturation-related effects at higher excitation frequencies. The normalization by $|S_{21}|$ mainly compensates the

higher intrinsic losses of the CPW90 probe at high frequencies and the slightly increased loss of the MSL0 probe near $f_0 = 29.8\,\text{GHz}$ (Fig. 4.10a).

A comparison based on signal intensity, obtained from the double integral of the normalized signals (Fig. 4.12), is shown in Fig. 4.13b. The same overall trends are observed, with the CPW90 design producing the highest values.

Two deviations from the general trend are noteworthy. First, at 9.8 GHz, the MSL0 probe yields a higher signal intensity than the CPW0 probe. This deviation may be attributed to a local anomaly in the measured response at this frequency. A denser sampling of measurement frequencies could help to better resolve this behavior and clarify its origin. Second, the CPW90 probe exhibits dips near 30 GHz and 40 GHz. These anomalies may arise from non-ideal baseline corrections in the raw EPR data. While commercial spectrometers often employ semi-manual baseline correction methods [EEBW10], no such processing is applied here. Additionally, the transmission coefficient $|S_{21}|$ of the CPW90 design exhibits minima close to 29.8 GHz and 39.8 GHz, which, depending on small shifts in the frequency response due to repeated mounting, could also influence the observed EPR signals.

4.2 Magnetic Field Homogeneity Optimization

In the previous sections, the optimization of the CPW and MSL probes was primarily aimed at maximizing the microwave magnetic field strength $\vec{H}_1$ in the sample area. As discussed in the introduction, however, $\vec{H}_1$ field homogeneity becomes critical in applications requiring quantitative accuracy.

A previously reported approach to improve field uniformity was proposed by Shrestha et al., who introduced a MSL design with a cavity etched into the substrate [SAA+19]. Since the $\vec{H}_1$ field is more homogeneous inside the dielectric than above it, positioning the sample within such a cavity enhances field uniformity. Nevertheless, this concept requires lithographic fabrication and access to specialized facilities, making it technically demanding and less suitable for straightforward implementation.

An alternative approach is the IMSL, in which the signal conductor is positioned beneath the substrate, while the ground plane is separated from it by an air gap. This configuration inherently leaves space to place the sample in the most

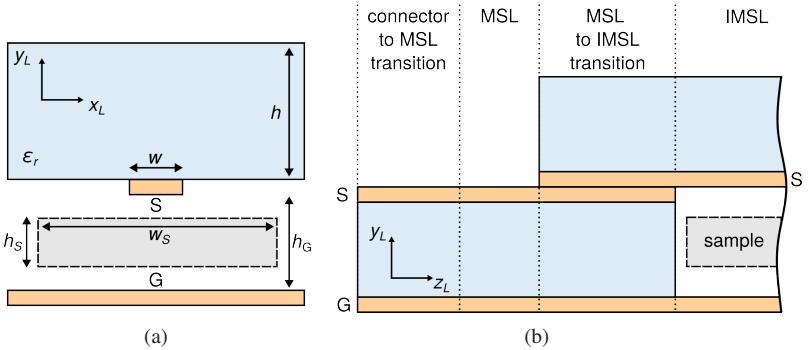

Figure 4.14: Cross-sections of the IMSL in (a) the $x_L y_L$ plane, showing the general structure of the line, and (b) the $z_L y_L$ plane, illustrating the transition from the connector to the IMSL. Adapted from [2], under CC BY 4.0 license.

homogeneous $\vec{H}_1$ region as the magnetic and electric field between the signal and ground conductor remain similar to a microstrip line. The cross-section of the IMSL structure is shown in Fig. 4.14a, where the parameter h_G denotes the distance between the signal and ground line.

Although not as widely adopted as conventional microstrip structures, the IMSL has nevertheless been applied across a range of different areas. In combination with liquid crystals, IMSLs are used to realize tunable devices such as phase shifters, resonators, and antennas [ZFB19, DBK+24, WPTJ22, JGW20]. They also serve as a platform for characterizing liquid materials, enabling precise measurements of dielectric properties [PZZ+22, RSM+24]. Beyond liquid-crystal applications, IMSL resonators have been proposed for human head imaging [ZUSC05], while IMSL-based gap waveguides have been developed for high-frequency signal guidance [LZK16, SWYGG24].

4.2.1 Design and Implementation of an IMSL

For the initial IMSL microwave probe prototype, the air gap is chosen as $h_G = 200\,\mu m$, as a trade-off between providing sufficient sample space and maintaining a strong microwave magnetic field. The signal conductor has a width of $w = 925\,\mu m$, and Rogers 4003C is used as the substrate material

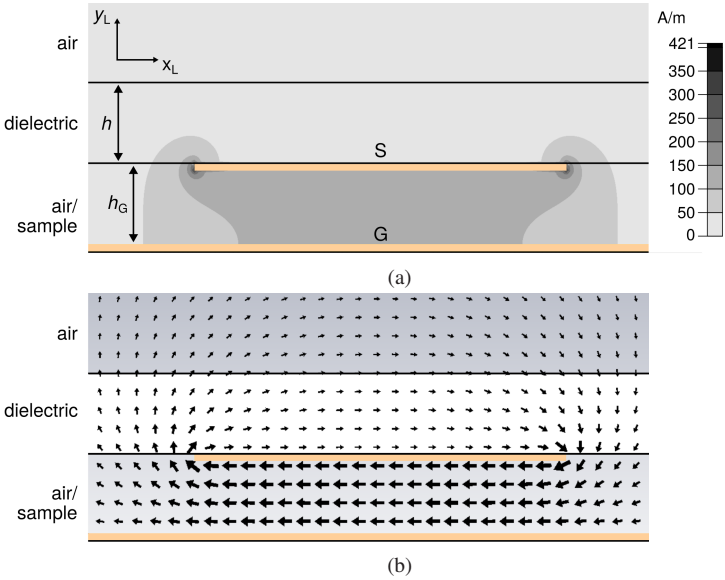

Figure 4.15: Simulated magnetic field distribution of the IMSL in the $x_L y_L$-plane at $f_0 = 9.8\,\text{GHz}$. Adapted from [2], under CC BY 4.0 license.

with a dielectric constant of $\varepsilon_r = 3.43$. This material is chosen because it is softer and less brittle than alumina, making it easier to drill and handle during assembly and the EPR experiments without breaking. The substrate thickness is $h = 200\,\mu\text{m}$. The IMSL is designed such that the characteristic impedance is approximately $Z_0 = 50\,\Omega$.

The simulated magnetic field of the IMSL design is shown in Fig. 4.15, considering both magnetic field components, $H_{1,y}$ and $H_{1,x}$. The magnetic field magnitude distribution and the corresponding field lines are illustrated. As expected, the field in the sample region between the signal and ground plane is considerably more homogeneous than in the corresponding regions above the MSL and CPW, shown in Fig. 4.5 and 4.6, respectively. In the sample area, the magnetic field is predominantly oriented along the x_L-axis ($H_{1,x}$).

The design of the IMSL is composed of four main parts: the two connector–to–MSL transitions at both ends, the IMSL line itself, and the

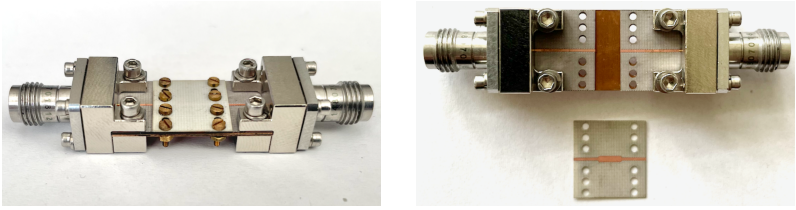

(a) (b)

Figure 4.16: Photograph of the IMSL microwave probe showing (a) the fully assembled structure and (b) the unfolded configuration. Adapted from [2], under CC BY 4.0 license.

ground plane. Fig. 4.14b shows the cross-section in the $x_L y_L$ plane. The connector–to–MSL transition is employed analogous to Fig. 4.9. The transition from the MSL to the IMSL is the most critical aspect of the design, and several approaches are reported in literature. In the prototype, designed in this work, the IMSL is positioned above the MSL over a 4 mm transition region. The initial width of the MSL, $w_{\mathrm{MSL}} = 410\,\mu\mathrm{m}$, is tapered to the width of the IMSL ($w = 925\,\mu\mathrm{m}$), as part of the transition. This taper ensures that the characteristic impedance Z_0 remains approximately constant while the substrate height h and the air gap height h_G are kept unchanged. The total length of the IMSL section is 4 mm. The ground plane for both the MSL and IMSL is provided by a 200 µm thick copper plate that also serves as mechanical support.

The transition takes advantage of the fact that the substrate thickness of the MSL, $h = 200\,\mu\mathrm{m}$, is chosen to match the required air gap of the IMSL used to accommodate the sample. As a result, when the MSL and its substrate terminate, the structure continues seamlessly into the IMSL region. This inherently avoids the need for additional support structures or complex design features to overcome a height mismatch.

A photograph of the fully assembled and unfolded IMSL microwave probe is shown in Fig. 4.16. The IMSL is secured on top of the MSL using four screws on each side. A soldering paste between the transition from the MSL and IMSL is also tested, to investigate its effect on the losses of the structure. However, no improvement is observed when comparing the transmission coefficient S_{21}. The structure without the connectors has a length of $L = 28$ mm and a width of $W = 12.8$ mm.

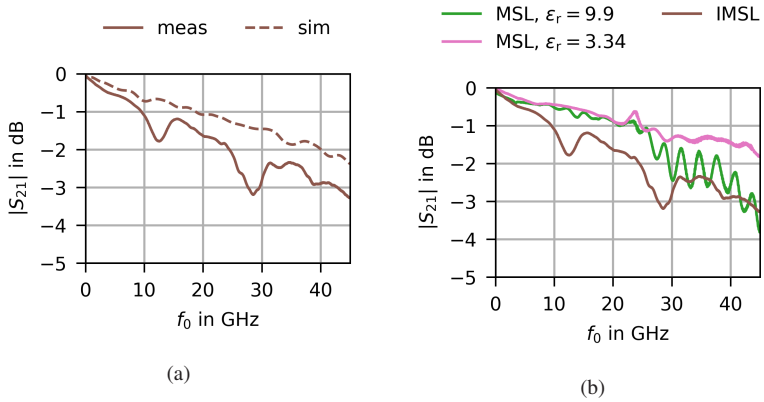

Figure 4.17: (a) Measured and simulated magnitude of the transmission coefficient of the IMSL. (b) Comparison of the measured results with the alumina-based and Rogers-based MSLs. Adapted from [2], under CC BY 4.0 license.

To evaluate the electrical performance, the simulated and measured magnitude of the transmission coefficient $|S_{21}|$ is presented in Fig. 4.17a. As for the MSL and CPW structures, the simulations account for a connector offset of 100 µm and a metal surface roughness of 2 µm. Overall, the simulated and measured trend of $|S_{21}|$ show good agreement. Two distinct dips, however, appear in the measurement results around 12 GHz and 29 GHz, which may originate from reflections caused by non-idealities in the assembly. These effects predominantly affect the transmission efficiency, while the underlying $\vec{H}_1$ field distribution in the sample region remains largely unchanged. Consequently, they are not expected to significantly influence the EPR response within the narrow resonance bandwidth.

4.2.2 EPR Performance Evaluation

For the EPR measurements, a strip of regular 80 g/mm^2 copy paper with a height of 100 µm is coated with 2,2-diphenyl-1-picrylhydrazyl (DPPH) by dipping it into a DPPH–acetone solution, following the procedure in [SAA+19]. DPPH contains a single unpaired electron, which gives rise to a single sharp

line in the EPR spectrum, similar to BDPA [EEBW10] and has a g-factor of $g = 2.0037$ [WB07]. After the acetone evaporates, a thin film of DPPH remains on the surface of the paper. Since one side of the strip is in direct contact with the bottom of the mixing vessel during drying, this side is only lightly coated with DPPH, whereas the opposite side exhibited a more uniform coverage. The prepared DPPH strip has a length of 2.5 mm and a width of 12.8 mm, matching the width of the TL structures.

For comparison, two straight MSLs are used: the alumina-based design from Fig. 4.8a with $\varepsilon_\mathrm{r} = 9.9$, and a second MSL fabricated on the same substrate material as the IMSL (Rogers 4003C, $\varepsilon_\mathrm{r} = 3.43$). The Rogers-based MSL is designed with a substrate thickness of $h = 200\,\mu\mathrm{m}$ and a conductor width of $w = 440\,\mu\mathrm{m}$, resulting in a characteristic impedance of $50\,\Omega$. The overall dimensions of the Rogers-based MSL are the same as the alumina-based MSL.

This comparison serves two purposes: First, to evaluate the MSL and IMSL on the same substrate, and second, to compare the IMSL with the alumina-based MSL, which represents the MSL design with the highest magnetic field strength, but is not optimized for homogeneity. Simulations for the IMSL indicate only slight improvements when using an alumina substrate, as the air gap between signal and ground dominates the magnetic field, making substrate differences less significant.

The magnitude of the transmission coefficient of all three structures is compared in Fig. 4.17b to provide a reference for losses. The subsequent EPR measurements are performed with the EPR resonance condition set to $f_{0,\mathrm{r}} = 34.8\,\mathrm{GHz}$. At this frequency, the differences between the three structures remain within 1.5 dB.

Next, the influence of the orientation of the TLs within the modulation coils is analyzed. Fig. 4.18a presents the EPR measurement results when the TL microwave probes are positioned such that $\vec{B}_0 \perp H_{1,y}$, corresponding to the same orientation used for all previous measurements, where the microwave probes are positioned horizontally inside the modulation coil. The TL microwave probes are then rotated by 90°, positioning them vertically on the edge of the connectors such that $\vec{B}_0 \perp H_{1,x}$. The corresponding EPR results are shown in Fig. 4.18b, with the external magnetic field set to $B_{0,\mathrm{r}} = 1241\,\mathrm{mT}$.

Both MSL structures exhibit similar peak-to-peak EPR amplitudes in either orientation. This behavior is consistent with the magnetic field lines shown in

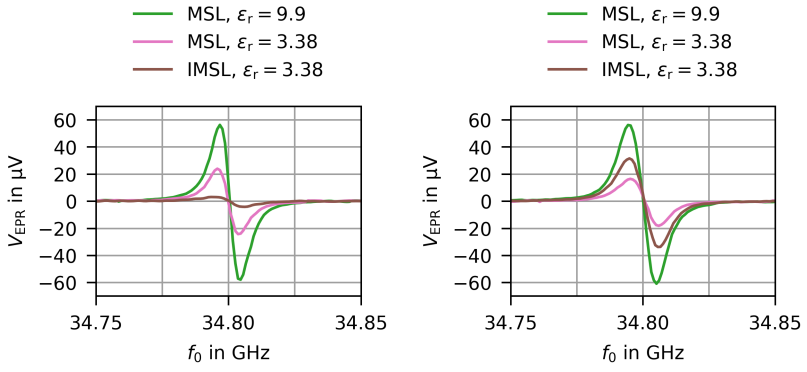

Figure 4.18: EPR measurements of the three compared TL microwave probes, with the probes positioned inside the modulation coil such that (a) $\vec{B}_0 \perp H_{1,y}$ and (b) $\vec{B}_0 \perp H_{1,x}$. The external magnetic field is set to $B_{0,r} = 1241$ mT.

Fig. 4.5b (see Section 4.1.1), where the magnetic field components along the x_L- and y_L-axes display similar spatial distributions. In contrast, the IMSL structure yields a substantially higher peak-to-peak EPR amplitude when oriented such that $\vec{B}_0 \perp H_{1,x}$. This observation agrees with the field-line pattern of the IMSL (see Fig. 4.15b), where the magnetic field in the region between the signal and ground conductors, where the sample is located, is predominantly oriented along the x_L-axis.

To evaluate the main advantage of the IMSL in providing a more uniform $\vec{H}_1$ field, the sample is measured in two orientations. In the reference position, corresponding to the previously shown results, the side of the copy paper with the higher DPPH coating faces the signal conductor. In the second orientation, the sample is flipped so that this side is closer to the ground plane. If the magnetic field is homogeneous across the sample region, the measured EPR signals should be largely independent of the sample orientation.

Fig. 4.19a compares the two sample orientations for the alumina MSL, while Fig. 4.19b presents the comparison for the IMSL. Both structures are measured in their orientation such that $\vec{B}_0 \perp H_{1,x}$. For the IMSL, the EPR curves remain nearly identical between the two positions. In contrast, for the alumina MSL, the

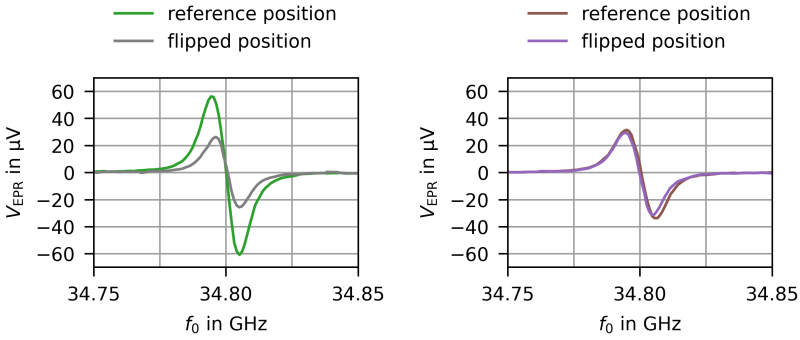

Figure 4.19: EPR measurements evaluating the $\vec{H}_1$ field homogeneity for (a) the alumina-based MSL ($\varepsilon_r = 9.9$) and (b) the IMSL ($\varepsilon_r = 3.38$). Both TL microwave probes are positioned such that $\vec{B}_0 \perp H_{1,x}$. In the reference sample position, the side with the higher DPPH coating faces the signal line, while in the other position the sample is flipped. Adapted from [2], under CC BY 4.0 license.

peak-to-peak amplitude decreases by a factor of approximately three when the sample is flipped. Measurements were also performed at 9.8 GHz and 19.8 GHz to verify the broadband capabilities of the IMSL, and similar results were observed, which are therefore not shown. These results clearly demonstrate the improved field homogeneity of the IMSL.

4.3 Summary and Discussion

In the first part of this chapter, the CPW and MSL were examined with the objective of achieving a high effective microwave magnetic field strength in the sample area. Design guidelines were established for both types of TLs. For both CPW and MSL, increasing the dielectric constant enhances the effective magnetic field strength. In the case of MSL, reducing the conductor width results in a stronger effective magnetic field, whereas the substrate height has only a minor effect. For CPWs, the gap size exerts a greater influence on the

effective magnetic field than the conductor width, with the field strength initially increasing with the gap size before reaching a maximum.

When using samples much smaller than the sample area specified in Section 4.1.1, it is important to ensure that the peaks of the magnetic field, which occur at the edges of the conductor, fall within the sample area. For MSLs, the previously determined conductor width also provides an optimal effective magnetic field strength for smaller samples. In the case of CPWs, the maximum magnetic field strength increases for smaller gap sizes, which can be advantageous for very small samples. Here, precise sample placement becomes even more critical, as the sample must be positioned directly at the edge of the conductor to exploit the peak field.

Each optimized TL type was fabricated in two orientations. For the MSL90 and CPW90 structures, both microwave magnetic field components $H_{1,y}$ and $H_{1,x}$ are perpendicular to the external magnetic field B_0, whereas for the MSL0 and CPW0 structures, only $H_{1,y}$ is perpendicular to B_0. The CPWs exhibit higher measured EPR peak-to-peak amplitudes and greater signal intensity than their MSL counterparts. The 90°-rotated structures (MSL90 and CPW90) generate a stronger effective magnetic field than the straight structures (MSL0 and CPW0). The MSL90 structure produces a higher effective magnetic field than the CPW0 structure. A straight TL with a smaller connector may still be advantageous in setups where the space between the poles of the electromagnet is constrained.

Although the CPW90 transmission line produces a higher effective magnetic field strength, it exhibits more pronounced ripples in $|S_{21}|$. For EPR samples with multiple spin states, which generate several EPR peaks, a broad frequency sweep with a relatively flat $|S_{21}|$ response is required to capture all peaks accurately, typically in the range of single-digit gigahertz rather than megahertz. Under these conditions, the MSL90 transmission line may be a more suitable choice than the CPW90 structure.

In the second part, the focus shifted to achieving a more uniform magnetic field distribution. The standard MSL exhibits a more homogeneous field within the substrate between the signal and ground planes compared to the region above the signal line. However, placing the sample inside this area, for example by providing a cavity within the substrate, requires specialized and costly fabrication steps. An alternative approach is the inverted microstrip line, which was designed and assembled as an EPR microwave probe. In this configuration,

the microwave magnetic field is predominantly oriented along the x_{L}-axis. This orientation was experimentally verified by EPR measurements with the IMSL positioned vertically, i.e. on its edge, for which only the $H_{1,x}$ component contributes and a clear EPR signal is observed. In contrast, when the IMSL is positioned horizontally, only the $H_{1,y}$ component contributes, resulting in a strongly reduced EPR peak.

The IMSL achieves a higher magnetic field strength than the corresponding MSL, when using the same substrate with a dielectric constant of $\varepsilon_{\mathrm{r}} = 3.43$. Compared to the alumina MSL, however, the IMSL exhibits a lower magnetic field strength. Changing the substrate for the IMSL to alumina results in only a slight increase in microwave magnetic field strength and would not be sufficient to surpass the performance of the alumina MSL. The main advantage of the IMSL is its more uniform magnetic field, which was demonstrated by measuring the sample in different positions relative to the signal line. For the MSLs, moving the sample further from the signal conductor causes a significant drop in the EPR peak-to-peak amplitude, whereas the IMSL shows minimal variation.

The findings of this chapter indicate that for a broadband on-chip EPR spectrometer, a CPW transmission line is preferred for standard qualitative EPR measurements, as it delivers the highest EPR peak-to-peak amplitude. In contrast, for quantitative experiments where a more uniform magnetic field is desirable, the IMSL provides improved field homogeneity, making it better suited for such specialized applications.

5 Integrated Circuit Components

After selecting a suitable system architecture, evaluating and optimizing key aspects of the EPR measurement setup, and designing the TL microwave probe, this chapter focuses on the development of integrated circuits in the transmit and receive paths. As illustrated in the envisioned system architecture in Fig. 2.14a of Chapter 2, the last component in the transmit chain before the microwave probe is an amplifier, while the first component in the receive chain after the probe is a detector. The design of both components, with the primary objective of achieving a wide bandwidth, is presented in this chapter. The main emphasis is placed on the detector, as it represents the element that currently limits the bandwidth of the EPR measurement setup. Implementing these components as integrated circuits not only paves the way toward a fully miniaturized spectrometer but also offers the potential for improved overall system performance through reduced interconnect losses and enhanced signal integrity enabled by on-chip integration.

Both circuits are implemented using the SG13G2 0.13 µm SiGe BiCMOS process from the Leibniz Institute for High Performance Microelectronics (IHP). The bipolar junction transistor (BJT) in this process is a heterojunction bipolar transistor (HBT) with a unity current gain cut-off frequency of $f_T = 300\,\text{GHz}$ and a maximum oscillation frequency of $f_{max} = 500\,\text{GHz}$. The emitter area of one transistor finger is $70\,\text{nm} \times 900\,\text{nm}$. The aluminum metal stack includes five lower metal layers and two thick top metal layers. The process also provides metal-insulator-metal (MIM) capacitors and polysilicon resistors [RHF12].

5.1 Broadband Amplifier

Parts of this chapter include material previously published in [5].

The amplifier presented in this chapter serves as a driver for the EPR microwave probe, providing sufficient power for its operation. As discussed in Section 1.2.3, higher microwave power leads to a higher microwave excitation field $\vec{H}_1$ in the microwave probe, which increases the EPR-induced absorption signal and, consequently, improves the EPR signal strength. Beyond a certain level, however, the sample becomes saturated, and further power increase no longer enhances the signal. This saturation behavior depends on the number of unpaired electrons (spin density), the applied magnetic field strength, and the spin relaxation mechanisms of the sample [EEBW10, GS18]. Especially for samples with a low spin density and thus weak EPR response, amplifiers for EPR spectrometers must provide high saturated output power to ensure sufficient excitation at the probe, while maintaining wide bandwidth.

This section addresses the following research question: What bandwidth and saturated output power can be achieved using a compact amplifier based on a lumped-element design?

5.1.1 State of the Art

Broadband amplifier architectures can generally be divided into two categories: lumped-element and distributed designs. For the purposes of a compact on-chip EPR spectrometer, this work explores the limits of a lumped-element approach. Numerous circuit-level techniques exist to extend amplifier bandwidth by reducing effective time constants in the signal path [Raz12a]. Fig. 5.1 illustrates several representative bandwidth extension techniques, which will be discussed in this subsection.

One common method used in single-stage transistor amplifiers is inductive peaking. By introducing an inductive element into the signal path, an additional pole and zero are introduced, where the zero is primarily responsible for increasing the bandwidth. Depending on the circuit topology, the peaking element may be implemented as a series inductor, a shunt inductor, or as a T-coil network, which represents a coupled-inductor implementation of inductive

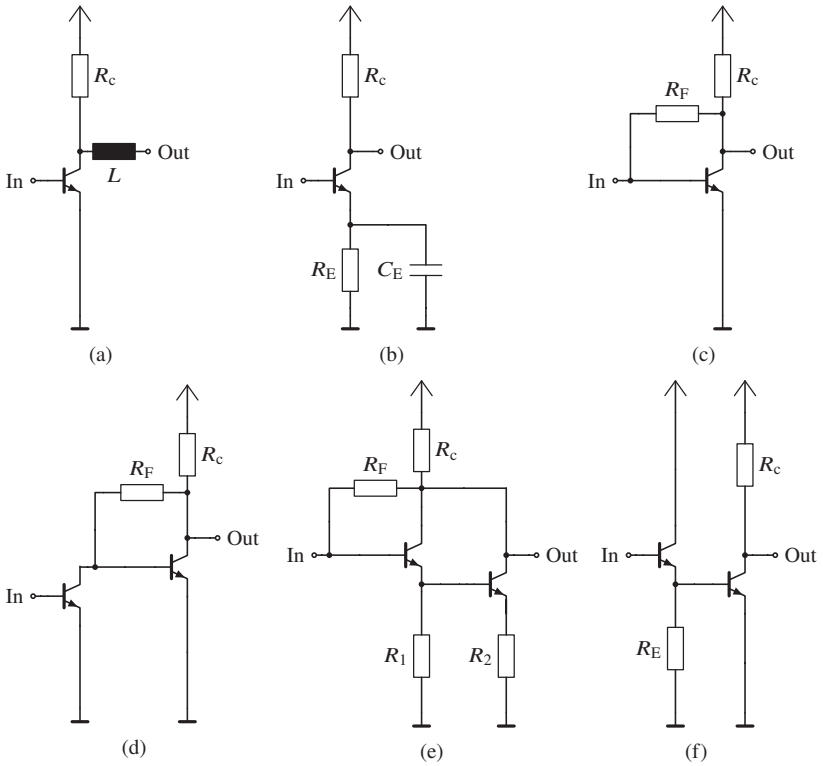

Figure 5.1: Various bandwidth enhancement lumped circuits. (a) Series inductive peaking, (b) emitter degeneration, (c) resistive feedback, (d) Cherry–Hooper, (e) Darlington feedback, (f) emitter-follower combined with a CE stage. Adapted from [Raz12a,Lee04].

peaking [KSE11]. Fig. 5.1a shows an example of series inductive peaking. For transistors operating in a common-emitter (CE) configuration, bandwidth enhancement can also be achieved through emitter degeneration [AFAS15, PWK+04, TKA+07] (see Fig. 5.1b) and resistive feedback [GFWK12] (see Fig. 5.1c) from the collector to the base. The former introduces a zero that compensates for the dominant low-frequency pole, while the latter lowers input resistance, contributing to increased bandwidth [Raz12a].

In two-stage broadband amplifier designs, low-impedance nodes at the output of the first stage are often used to facilitate wideband operation. For example, cascode and Cherry–Hooper amplifiers [HHL04, Raz12a] achieve this by using either a common-base (CB) stage or a CE stage with local feedback in the collector as the second stage, respectively. The Cherry–Hooper topology is illustrated in Fig. 5.1d. Another approach is the Darlington feedback amplifier [KB09, VLG14], shown in Fig. 5.1e, which employs cascaded transistors with local feedback to achieve high gain and extended bandwidth through reduced effective input resistance and improved high-frequency response [Lee04]. An emitter follower (EF) at the input can further improve bandwidth by presenting a low impedance to the next stage, which may be a CE or cascode amplifier [TKA+07, PWK+04]. The combination of an EF input stage and a CE stage is shown in Fig. 5.1f.

5.1.2 Circuit Design

The schematic of the designed amplifier is shown in Fig. 5.2a. A two-stage topology consisting of an EF and a cascode stage is selected. Inductive peaking elements TL_1 and TL_2 are included at the input and output to further enhance the bandwidth. Because the TL microwave probe in the envisioned on-chip EPR spectrometer is single-ended, the amplifier is also implemented as a single-ended design to eliminate the need for a balun. The subsequent sections describe the incremental improvements in performance when each bandwidth extension method is added to the basic gain cell.

The cascode configuration is selected over a CE topology for the gain cell to mitigate the Miller effect, which would otherwise limit the bandwidth [SSCG21]. To achieve broadband resistive matching at the output, a collector resistor of $R_c = 50\,\Omega$ is used. The supply voltage V_{cc2} is set to 4.2 V. Transistor Q_2, operating in CE configuration, is biased at $V_{Q2,be} = 0.86\,V$ and $V_{Q2,ce} = 1.55\,V$. Transistor Q_3, which functions as the CB device in the cascode, operates at $V_{Q3,be} = 0.85\,V$ and $V_{Q3,ce} = 2.05\,V$. This biasing results in a collector current of 12.36 mA flowing through both Q_2 and Q_3. Each transistor uses 14 fingers to strike a balance between gain and bandwidth. The electromagnetically simulated $|S_{21}|$ of the cascode stage is shown as the blue curve in Fig. 5.3a. A $50\,\Omega$ resistor is included at the input during simulation

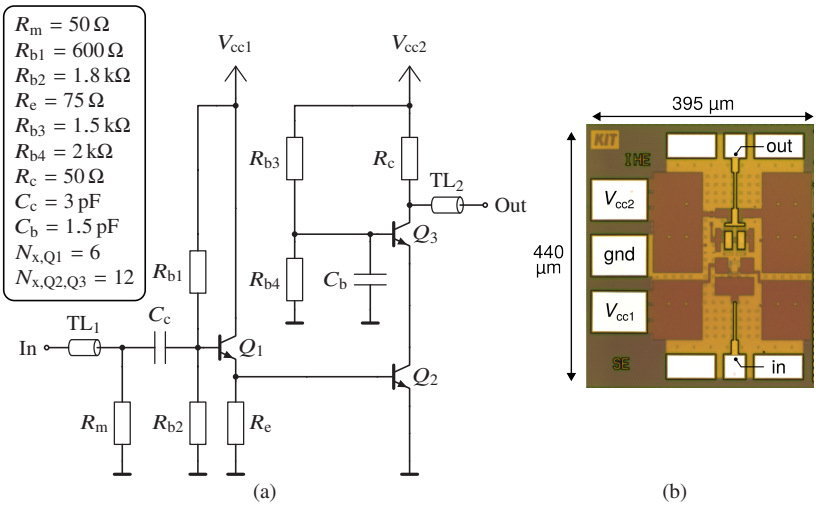

Figure 5.2: (a) Schematic of the designed amplifier. The decoupling capacitors along the supply lines are not shown. The emitter area of a transistor finger N_x is 70 nm × 900 nm. (b) Microphotograph of the fabricated amplifier with a core area of 0.007 mm^2 including the peaking inductors. Adapted from [5], ©IEEE.

to provide a fair comparison with the full amplifier design. The cascode alone achieves a low-frequency gain of 13 dB and a 3 dB bandwidth of 29 GHz.

One limitation of the cascode topology is the relatively high input impedance, which restricts the achievable bandwidth. To address this, an EF is added before the cascode to present a low impedance at the input. The small-signal output resistance of the EF stage is approximately $r_o = 1/g_m$, where g_m is the transconductance [SSCG21]. A higher transconductance is desirable for bandwidth extension, which in turn requires a higher collector current. A transistor with six fingers and a collector supply current of I_{cc1} = 12.4 mA is selected to maximize bandwidth while ensuring the small-signal stability factor K remains above one. The EF is supplied with V_{cc1} = 2.35 V, and its biasing results in $V_{Q1,be}$ = 0.91 V and $V_{Q1,ce}$ = 1.5 V. With the EF added, the amplifier bandwidth increases by 20 GHz, while the low-frequency gain is reduced by approximately 1 dB, as shown in the orange curve in Fig. 5.3a.

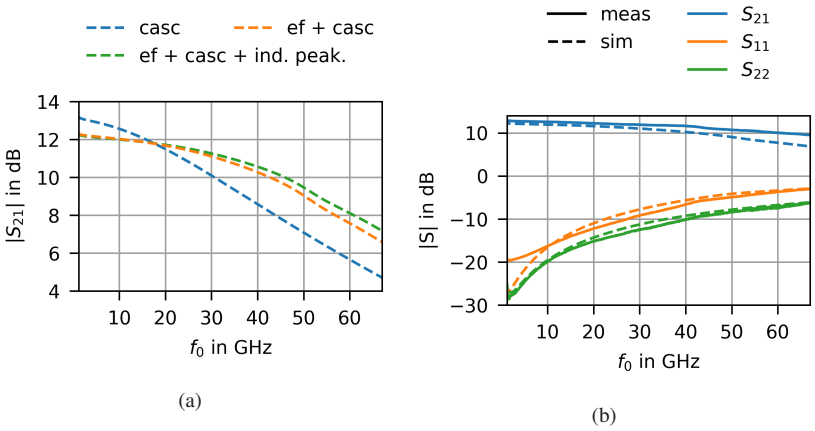

Figure 5.3: (a) Simulated magnitude of the transmission coefficient for the different bandwidth extension methods. (b) Simulated and measured magnitude of the S-parameter results of the fabricated circuit. Adapted from [5], ©IEEE.

The inductive peaking elements TL_1 and TL_2 have a length of 64 µm and a width of 2 µm. These lines introduce an inductance of approximately 40 pH, resulting in a modest bandwidth increase of about 3 GHz. As sufficient space was available between the pads, this area was used to implement the inductive line sections, making effective use of the available layout space. The combined result of all enhancements is shown as the green curve in Fig. 5.3a.

All simulation results are based on full electromagnetic (EM) simulations and include the supply lines. The EM simulations are performed using the Cadence EMX Planar 3D Solver. The simulations include a model for the DC probes, and each transistor's substrate connection is represented by a 1 Ω resistor to ground to capture realistic layout effects.

A microphotograph of the fabricated amplifier is provided in Fig. 5.2b. The total chip area including pads is 395 µm × 440 µm, while the active core, including inductive peaking structures, occupies only 0.007 mm^2. The ground-signal-ground RF input and output pads are located at the bottom and top of the chip, respectively. Power-ground-power pads for the supply voltages V_{cc1} and V_{cc2} are positioned on the left. The area between the active circuit and the pads is filled with decoupling capacitors, which are not shown in the schematic. A total

of 27.9 pF and 45.5 pF of decoupling capacitance is placed along the V_{cc1} and V_{cc2} lines, respectively. Small resistors are added between the capacitors and ground to suppress resonances caused by the inductance of the DC probes at low frequencies.

5.1.3 Measurement Results

Small-signal characterization of the amplifier is carried out using a Keysight N5247B Power Network Analyzer, which supports measurements up to 67 GHz. The test setup includes two Infinity ground-signal-ground probes with a pitch of 100 µm for RF probing. DC biasing is supplied by a Keysight M9614A source measure unit (SMU). Prior to measurement, the setup is calibrated up to the probe tips using a standard calibration substrate to ensure accurate de-embedding of the measurement setup itself. The amplifier is characterized using an input signal power of −20 dBm. A comparison between small-signal measurement and electromagnetic simulation results is shown in Fig. 5.3b. The measured low-frequency gain reaches 13 dB, and the amplifier exhibits a 3 dB bandwidth of 60 GHz. To match the collector current I_{cc2} used in simulations, the supply voltage V_{cc1} is set to 2.35 V during measurement. The applied supply voltages of $V_{cc1} = 2.35$ V and $V_{cc2} = 4.2$ V, together with the corresponding supply currents of $I_{cc1} = 11.8$ mA and $I_{cc2} = 12.5$ mA, result in a total DC power consumption of 80.2 mW.

Large-signal measurements are carried out using a Keysight E8257D PSG Analog Signal Generator up to 67 GHz, in combination with the network analyzer operating in spectrum analyzer mode. The spectrum analyzer is configured with a frequency span of 100 kHz and a resolution bandwidth of 1 kHz. Measurements are performed from 5 GHz to 65 GHz in 5 GHz increments, with additional data points at 1 GHz and 67 GHz. Frequency-dependent power calibration is carried out in three steps. First, the input path loss is measured by replacing the DUT with a power meter. Second, the output path loss is determined by connecting the input and output paths through an adapter and measuring the loss directly using the spectrum analyzer. Third, the RF probe losses are extracted by probing a thru calibration standard. These steps ensure that the measured power levels reflect the actual amplifier performance.

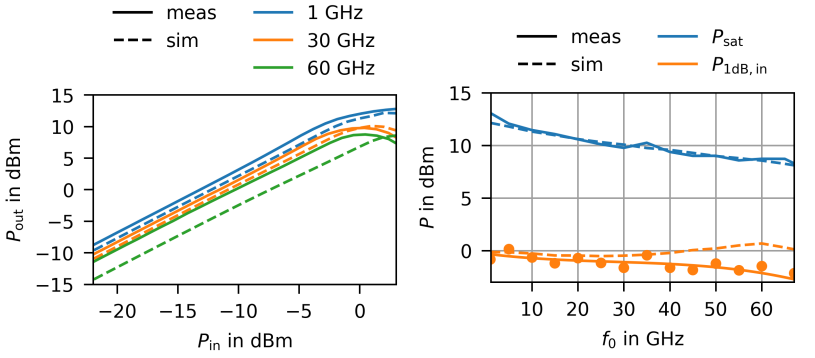

Figure 5.4: Measured and simulated results for (a) the output power as a function of the input power for three different frequencies and (b) saturated output power and input-referred 1 dB-compression point. Adapted from [5], ©IEEE.

In Fig. 5.4a, the measured and simulated output power P_{out} as a function of input power P_{in} is shown at three frequencies. The input power is swept from −24 dBm to −3 dBm in 3 dB steps, and then from −3 dBm to 3 dBm in finer 1 dB steps. The simulation and measurement results align well at lower frequencies, although deviations become more noticeable at higher frequencies.

The measured data generally exhibit slightly higher output power and small-signal gain than predicted by the simulations. Deviations of this type have been reported previously for broadband circuit designs implemented in the same technology when using the vertical bipolar intercompany (VBIC) model for the BJTs. One possible reason is an underestimation of the transconductance g_{m} at a given operating point in the VBIC model [Boh24].

The input-referred 1 dB-compression point $P_{\text{1dB,in}}$ is shown in orange in Fig. 5.4b, with a polynomial fit applied to the measured data. At the center of the amplifier's bandwidth, $P_{\text{1dB,in}}$ is approximately −1.5 dBm. The corresponding saturated output power results are illustrated by the blue curves in the same figure. A peak output power of 10 dBm is achieved at a frequency of 30 GHz.

5.1.4 Performance Comparison and Summary

A comparison of published broadband amplifiers with a focus on lumped and single-ended designs is shown in Tab. 5.1, where GBW denotes the gain bandwidth product and G_{LF} the low-frequency gain. Multiple works report lumped amplifier designs [HHL04, KB09, VLG14, TKA+07, PWK+04, KSE11], whereas multiple other works deploy a distributed design [TBP+15, FLB16, EAR19]. The highest GBW and saturated output power are reported by El-Aassar and Rebeiz [EAR19].

The amplifier presented in this work has a very small core area of only $0.007\,\mathrm{mm}^2$, has a 3 dB bandwidth of 60 GHz, and achieves a saturated output power of $P_{\mathrm{sat}} = 10\,\mathrm{dBm}$ at 30 GHz. This saturated output power leads to a sufficiently large EPR signal amplitude for standard EPR samples like BDPA, DPPH and Trityl. To achieve a large bandwidth, several EF stages can be implemented similar to the work by Trotta et al. [TKA+07] or a distributed amplifier design based on the proposed unit cell can be employed. Enhancing saturated output power commonly involves power combining techniques [Lee04], typically using resonant matching structures such as Wilkinson power combiners [Wil60]. However, Wilkinson combiners rely on $\lambda/4$ transmission lines, which inherently constrain the operational bandwidth [Lee04]. For broadband applications, active power combining can instead be realized through a distributed architecture [TCE16].

Table 5.1: Comparison of published broadband amplifiers. Adapted from [5], ©IEEE.

Reference	Technology	G_{LF} dB	BW GHz	GBW GHz	P_{sat} dBm	P_{dc} mW	Core area mm^2	Total area mm^2
[TBP+15]	130 nm SiGe BiCMOS	10	170	537	9.4	108	n.a.	0.38
[FLB16]	90 nm SiGe BiCMOS	12	91	362	17	297	n.a.	1.51
[EAR19]	45 nm CMOS RFSOI	23	108	1525	21.5	890	0.31	n.a.
[HHL04]	47 GHz f_T SiGe BiCMOS	19.7	13.7	132	n.a.	34	n.a.	0.49
[KB09]	120 nm SiGe BiCMOS	10	102	323	n.a.	73	0.02	0.29
[VLG14]	90 nm SiGe BiCMOS	12	123(2)	492(2)	n.a.	48	0.003	0.197
[TKA+07](3)	180 nm SiGe bipolar	14	84.6	990	n.a.	990	0.055	0.63
[PWK+04](3)	200 GHz f_T SiGe bipolar	10	62	196(1)	n.a.	775	n.a.	0.303
[KSE11]	250 nm SiGe BiCMOS	10.5	69	231(1)	n.a.	74	n.a.	0.36
This work	130 nm SiGe BiCMOS	13	60	268	10	188	0.007	0.17

(1) calculated based on given values, (2) simulated, (3) differential design, single-ended gain reported

5.2 Broadband Detectors

Detectors are used in a wide range of microwave-frequency applications. In microwave systems, the detection of a specific input signal is typically accomplished by frequency conversion, which enables subsequent signal processing in the baseband [Poz21]. Fig. 5.5 shows two common frequency conversion operations.

When operated in rectifier mode, the detector downconverts a sinusoidal input signal at frequency f_0 to a DC output. Detectors used in this mode are commonly found in power sensors for test and measurement equipment [Bru07], in RF energy-harvesting front ends [NCG+23], as well as in built-in self-test systems and automatic gain control loops within transceivers for automotive and communication systems [WMI24].

When used as a demodulator, the detector retrieves the modulation envelope from an AM input signal, yielding an output at the modulation frequency f_m. In passive imaging applications, Dicke-switched radiometers operate as demodulators to measure signals above the $1/f$ noise corner frequency, thereby

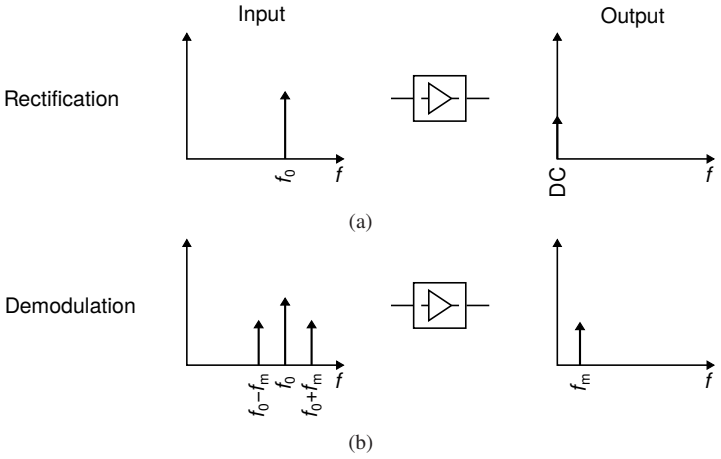

Figure 5.5: Two common frequency conversion operations of a detector. (a) Rectification: A sinusoidal input signal with the microwave frequency f_0 is downconverted to DC. (b) Demodulation: An amplitude modulated input signal is downconverted to the modulation frequency f_m. Adapted from [Poz21].

enhancing sensitivity. This is achieved by rapidly switching the input between the receive antenna and a reference load, which modulates the measurement at the switching frequency and thereby suppresses low-frequency noise [Dic46]. As discussed in Chapter 3, the detector in the EPR measurement setup also functions as a demodulator. However, in contrast to passive imaging systems, where the input power P_0 is the parameter of interest, the relevant quantity in EPR measurements is the modulation index m.

In this section, the following research questions are addressed:

- Which figure of merit is suitable for characterizing the detector in the context of EPR?
- Which circuit topology leads to a broadband operation and a high sensitivity? What is the optimal design space for each component in the circuit diagram?
- How does the performance of a distributed design compare to that of a lumped design?
- What are the dominant noise contributors in the design and how can the circuit be optimized to achieve a low output noise?

5.2.1 Figures of Merit for Detector Sensitivity

If the quantity of interest is the input power, the usual figure of merit (FoM) for detectors is the noise-equivalent power (NEP) [Bro03]. It is defined as

$$\mathrm{NEP} = \frac{v_\mathrm{n}}{\mathcal{R}_\mathrm{p}}, \tag{5.1}$$

given in $W/\sqrt{\mathrm{Hz}}$ with the detector output noise voltage spectral density v_n and the responsivity $\mathcal{R}_\mathrm{p}$. The responsivity $\mathcal{R}_\mathrm{p}$ is defined as

$$\mathcal{R}_\mathrm{p} = \frac{v_\mathrm{d,dc}}{P_0}, \tag{5.2}$$

where $v_\mathrm{d,dc}$ denotes the detected output voltage at DC and P_0 is the microwave input power. The NEP can be interpreted as the minimum detectable input power

per square root of bandwidth. In other words, it is the minimum input power that results in an output-referred SNR of one in a 1 Hz bandwidth [MR10].

To evaluate the detector's capability in measuring the modulation index m (which corresponds to the EPR signal, see Section 3.1.1), the noise-equivalent modulation index (NEM) is developed as a FoM. It can be interpreted as the minimum detectable modulation index per square root of bandwidth and is calculated as

$$\mathrm{NEM} = \frac{v_\mathrm{n}}{\mathcal{R}_\mathrm{m}}, \tag{5.3}$$

with the unit of $1/\sqrt{\mathrm{Hz}}$. The responsivity $\mathcal{R}_\mathrm{m}$ related to m can be defined as

$$\mathcal{R}_\mathrm{m} = \frac{v_\mathrm{d,fm}}{m}, \tag{5.4}$$

with m being dimensionless. The detected output voltage $v_\mathrm{d,fm}$ is measured at the modulation frequency f_m.

5.2.2 Device Choice

As discussed in Chapters 2 and 3, frequency conversion in detectors is achieved using nonlinear devices. Typical implementations employ diodes or transistors as the nonlinear elements. In both rectification and demodulation modes, the underlying physical mechanism is the second-order nonlinearity of the current–voltage characteristic, which enables frequency translation [Poz21].

Because both modes rely on the same physical principle, optimization of the detector in one mode is directly applicable to the other. As most publications report the NEP, the optimization presented in this work is likewise based on NEP, ensuring applicability in a broader context. The final characterization of the detectors includes both modes of operation.

When measuring the output power as a function of the input power, a diode detector has two distinct areas of operations. For low input powers, the detector operates in the square-law region where the output voltage is proportional to the input power. Small signal conditions apply in this case. For large input powers, the output saturates and the voltage is first proportional and then constant as a

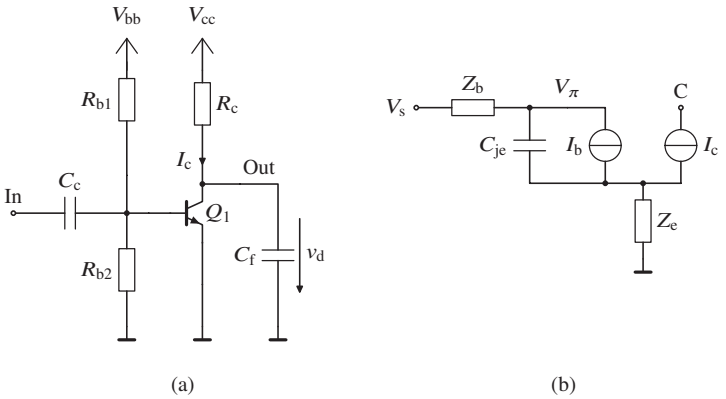

Figure 5.6: (a) Circuit diagram of a transistor-based detector in CE configuration and (b) the large-signal model of transistor Q_1.

function of the input voltage [Poz21]. This region is often called linear/peak or saturation. A transistor-based detector can operate in either one or both regions, depending on its configuration [WMI24].

With a bipolar technology, a diode can be implemented by connecting the collector and the base terminals. Since a bipolar transistor is a vertical device, the collector has a very large area which can lead to capacitive coupling to the substrate. The injected microwave power can be partially dissipated in the substrate leading to a reduced NEP [HGHP13]. A transistor-based detector can be implemented in all its basic configurations. Published results indicate that a CE configuration has a higher responsivity than a CB configuration for broadband operations from 1 GHz to 67 GHz [MS16] and for a frequency below f_T and f_{max} where the transistor can still provide gain [HGHP13]. Therefore, a transistor Q_1 in CE configuration is chosen and the circuit in Fig. 5.6a is used as a starting point of the design. R_{b1} and R_{b2} serve as biasing and input matching resistors, R_c is the collector resistor and C_c and C_f are the coupling capacitor and filter capacitor, respectively.

5.2.3 Theory of the Common-Emitter Configuration

To understand the parameters influencing the detector performance, the following section revisits the theory of nonlinear signal behavior and low-frequency noise characteristics of a CE stage.

Nonlinear Signal Behavior

To describe the nonlinear, frequency-dependent behavior of a CE stage under large-signal excitation, Volterra-series-based modeling approaches have been employed [FM98, MR10]. Fong and Meyer developed a general Volterra-series formulation for nonlinear mixers and amplifiers [FM98], which was later applied by May and Rebeiz to the analysis of square-law detector circuits in the context of passive millimeter-wave imaging [MR10]. The results derived in [MR10] are used here to analyze the nonlinear detector behavior of the circuit shown in Fig. 5.6a.

A simplified large-signal model of transistor Q_1 is shown in Fig. 5.6b. The nonlinear behavior of the transistor can be described in the frequency domain based on its dynamic characteristics, including charge-storage effects associated with the base–emitter junction capacitance and the finite forward transit time. A Volterra-series-based analysis can then be employed to analyze the resulting nonlinear detector behavior [MR10].

For detector operation in the square-law region, the rectified DC response is dominated by the second-order Volterra contribution, which describes the conversion of the applied RF signal into a DC component [Poz21, MR10]. The nonlinear detector behavior can be characterized by the collector signal current

$$I_{c,s} = I_{c,RF} - I_{c,bias}, \tag{5.5}$$

where $I_{c,RF}$ denotes the additional collector current resulting from the applied RF input signal, and $I_{c,bias}$ is the collector current in the absence of an RF excitation.

Based on the large-signal analysis presented by May and Rebeiz [MR10], a closed-form expression for the collector signal current is used directly in this work and is given by

$$I_{\mathrm{c,s}} = \frac{V_{\mathrm{s}}^2}{2V_{\mathrm{T}}\left[(1+g_{\mathrm{m}}Z_{\mathrm{e}})^2 + Z^2\omega^2\left(\frac{g_{\mathrm{m}}}{\omega_{\mathrm{T}}} + C_{\mathrm{je}}\right)^2\right]} \cdot \frac{g_{\mathrm{m}}}{1+g_{\mathrm{m}}Z_{\mathrm{e}}}, \tag{5.6}$$

where g_{m} is the transconductance, V_{T} the thermal voltage, ω_{T} the unity current-gain cut-off frequency in angular units, and C_{je} the base–emitter junction capacitance. The total small-signal impedance seen at the base–emitter junction is given by $Z = Z_{\mathrm{b}} + Z_{\mathrm{e}}$, where Z_{b} and Z_{e} denote the impedances at the base and emitter, respectively.

The detected DC output voltage can be expressed as

$$v_{\mathrm{d,dc}} = R_{\mathrm{c}} I_{\mathrm{c,s}}, \tag{5.7}$$

which directly relates the rectified collector signal current to the output voltage and, consequently, to the detector responsivity.

For the design of a detector, several conclusions for achieving a high responsivity can be drawn from the preceding analysis. Equation 5.7 shows that the responsivity $\mathcal{R}_{\mathrm{p}}$ increases linearly with the collector resistance R_{c}. Furthermore, Eq. 5.6 indicates that a larger collector signal current $I_{\mathrm{c,s}}$, and thus a higher responsivity, can be obtained by reducing the effective resistance at the base–emitter junction Z, the emitter impedance Z_{e}, and the base–emitter junction capacitance C_{je}.

The collector signal current $I_{\mathrm{c,s}}$ depends on the transconductance g_{m} through both the numerator and the denominator. For small values of g_{m}, the terms proportional to g_{m} in the denominator are negligible, and $I_{\mathrm{c,s}}$ increases approximately linearly with g_{m}. As g_{m} increases, however, the g_{m}-dependent terms in the denominator become significant and increasingly counteract the growth of the numerator. Consequently, the ratio no longer increases monotonically with g_{m}, but instead reaches a maximum and decreases for sufficiently large g_{m}. This leads to the existence of an optimum value of g_{m} for maximizing the responsivity, which must be determined as part of the design process.

Low Frequency Noise

The low frequency noise at the output of the detector determines the limit for the smallest detectable output voltage which can still be measured. In a circuit, noise appears as a voltage or current that fluctuates randomly and is modeled as a stationary stochastic process [Voi13]. The power spectral density (PSD) characterizes the average noise power within a 1 Hz bandwidth and is represented by $\overline{v_\mathrm{n}^2}$ with units of V^2/Hz. The PSD given in terms of current is denoted as $\overline{i_\mathrm{n}^2}$ with units of A^2/Hz [Raz12b].

The main noise contributors in a bipolar semiconductor process are [Voi13]:

Thermal noise: caused by random fluctuation of charges in lossy components, and is calculated as

$$\overline{i_{\mathrm{n,th}}^2} = 4k_\mathrm{B}T/R \tag{5.8}$$

Shot noise: caused by random fluctuation of charges traversing potential barriers in pn junctions, and is calculated as

$$\overline{i_{\mathrm{n,s}}^2} = 2qI \tag{5.9}$$

Flicker $(1/f)$ noise: caused by trapping and de-trapping of carriers in the semiconductors [Hoo94], and is modeled for SiGe polysilicon resistors as

$$\overline{i_{\mathrm{n,f}}^2} = \frac{K_\mathrm{fn} I^{A_\mathrm{fn}}}{f^{B_\mathrm{fn}}} \frac{1}{WL}, \tag{5.10}$$

and for SiGe BJTs as

$$\overline{i_{\mathrm{n,f}}^2} = \frac{K_\mathrm{fn} I^{A_\mathrm{fn}}}{f^{B_\mathrm{fn}}} \tag{5.11}$$

where q denotes the elementary charge. K_fn, A_fn and B_fn are technology specific parameters, W the physical width and L the physical length in µm.

From a circuit design perspective, these noise mechanisms lead to several important considerations. Thermal noise is proportional to the resistance value and can therefore be reduced by minimizing resistive elements. Shot noise scales with the DC current flowing through pn junctions, indicating that lower bias currents reduce this noise contribution. Flicker noise similarly increases with current in both SiGe BJTs and SiGe polysilicon resistors, such that operating at lower current levels is beneficial for suppressing low-frequency noise. In the case of the polysilicon resistors, the flicker noise contribution also depends on the physical device dimensions, with larger resistor areas resulting in reduced $1/f$ noise.

The PSD of each component in Fig. 5.6 at the output can be calculated as

$$\overline{v_{\mathrm{n,i}}^2} = G_{\mathrm{n,i}}^2 \cdot \overline{i_{\mathrm{n,i}}^2}, \tag{5.12}$$

where $G_{\mathrm{n,i}}$ in V/A denotes the noise gain. For N stochastically independent noise processes, the total output-referred PSD is calculated as

$$\overline{v_{\mathrm{n,tot}}^2} = \sum_{i=1}^{N} \overline{v_{\mathrm{n,i}}^2}. \tag{5.13}$$

The NEP is defined in terms of the noise voltage spectral density v_{n}, rather than of the PSD (see Eq. 5.1). Therefore, v_{n} is used throughout this chapter to characterize the noise. For improved readability, the overbar, denoting the average value of the noise variables, is omitted.

5.2.4 Design of Lumped and Distributed Detectors

In this section, the design considerations for both lumped and distributed detector implementations are discussed. As outlined in the preceding theoretical analysis, the detector responsivity and noise performance depend on several interrelated parameters, which can impose competing design requirements. These considerations are examined in detail with the primary objectives of achieving a low NEP, broadband operation extending ideally up to 110 GHz, and low power consumption.

First, the lumped detector shown in Fig. 5.6 is analyzed, with the design focus placed on the selection of the transistor size and the corresponding optimal operating point. Building on this design, a distributed detector is subsequently developed, in which the core circuit of the lumped detector serves as the unit cell of the distributed architecture. For the distributed design, particular emphasis is placed on the choice of the number of stages and the optimization of the transmission line geometries connecting the stages. The layouts of both detector implementations are then presented. In addition, the optimal value of the collector resistor R_c is evaluated. While most design decisions are based on schematic-level simulations, the optimization of R_c is carried out using fully EM-simulated circuits. This distinction is motivated by the fact that variations in the core device sizing of the lumped and distributed detectors significantly affect the layout, rendering full EM simulations impractical at this stage. By comparison, changes in R_c only have a minor impact on the layout, allowing EM simulations to be used efficiently to obtain more realistic results.

For all NEP simulation results presented below, harmonic-balance simulations are used to evaluate the signal component, while small-signal noise simulations are used to determine the noise contribution. Unless stated otherwise, an input power of $P_0 = -30\,\mathrm{dBm}$ at a frequency of $f_0 = 10\,\mathrm{GHz}$ is assumed.

Sizing of the Lumped Detector

In this section, the sizing of the lumped detector shown in Fig. 5.6 is examined with respect to the achievable NEP. The bias resistors are chosen as $R_{b1} = R_{b2} = 100\,\Omega$, providing resistive input matching to $50\,\Omega$ and the collector resistor is chosen as $R_c = 500\,\Omega$. Its choice will be analyzed at the end of this section.

Fig. 5.7a presents the simulated NEP as a function of the collector bias current $I_{c,bias}$ for different numbers of transistor fingers N_x, thereby illustrating the influence of both parameters on detector performance. Owing to limitations of the process design kit, a maximum of 10 fingers per transistor is supported. The case $N_x = 12$ is therefore realized by connecting two six-finger transistors in parallel, resulting in an equivalent effective finger count.

For clarity, the analysis is structured such that the key trends observed in the simulation results are first described, followed by a discussion of their

underlying origin, which is traced back to the nonlinear signal model and the noise behavior introduced in the preceding theoretical section.

The following trends for the NEP are observed:

- Dependence on collector bias current $I_{c,bias}$: The NEP decreases with increasing collector bias current, reaches a minimum, and then rises again at higher current levels.
- Dependence on number of transistor fingers N_x: The NEP decreases with larger transistor size and then saturates.

The collector-emitter voltage is kept constant at $V_{ce} = 1.4\,\text{V}$, while the base emitter voltage V_{be} is adjusted for each $I_{c,bias}$. A collector resistor of $R_c = 500\,\Omega$ is used.

To explain the observed NEP behavior, the responsivity and the noise voltage spectral density are analyzed separately. Unless stated otherwise, v_n is simulated at 100 kHz, while the input signal frequency is set to 10 GHz.

Responsivity $\mathcal{R}_p$

Fig. 5.7b shows the responsivity $\mathcal{R}_p$ as a function of $I_{c,bias}$. In addition to the simulated results, the calculated results are also shown. The procedure used to obtain these values is described below.

The responsivity is calculated as the ratio of the output voltage $v_{d,dc}$, given in Eq. 5.7, to the input power $P_0 = 1\,\mu\text{W}$. The voltage $v_{d,dc}$ is calculated from the collector signal current according to Eq. 5.6.

The constant parameters in Eq. 5.6 are set to: $V_s = 7.07\,\text{mV}$, $V_T = 25\,\text{mV}$, and $f_T = 300\,\text{GHz}$. The transistor-finger-dependent variables $Z_b = r_b$, $Z_c = r_c$, and C_{je} are calculated using the expressions provided in the IHP technology file, and are shown in Fig. 5.7c. The VBIC large-signal model is employed, in which r_b and r_c denote the base and collector resistances, respectively. The base resistance r_b is further divided into internal ($r_{b,i}$) and external ($r_{b,x}$) components. The transconductance is given by

$$g_m = \frac{I_{c,bias}}{V_T}. \tag{5.14}$$

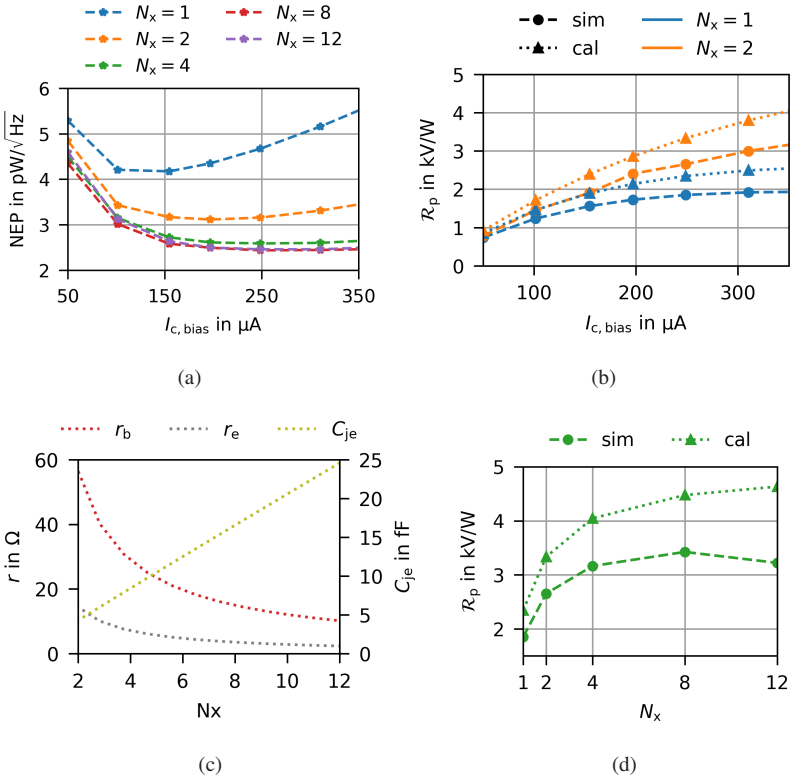

Figure 5.7: (a) Simulated NEP. (b) Calculated and simulated responsivity $\mathcal{R}_p$ as a function of collector bias current for one and two transistor fingers. Only two cases are shown for clarity. (c) Transistor-finger-dependent model parameters derived from the IHP technology file. (d) Calculated and simulated $\mathcal{R}_p$ as a function of the number of fingers at a fixed collector bias current of $I_{c,bias} = 250\,\mu A$. Higher finger counts ($N_x \geq 4$) are shown only at this bias point to illustrate the scaling trend.

Using these parameters, the calculated curves reproduce the overall trend of the simulated data but yield slightly higher responsivity values, which are likely attributable to the simplifications inherent in the expression for the calculated collector signal current given in Eq. 5.6. Given the close agreement, the calculated results are suitable for attributing specific effects to individual components in the large-signal model shown in Fig. 5.6b and are subsequently assigned to the various effects observed in the responsivity.

Figure 5.7b shows that increasing the collector bias current $I_{\mathrm{c,bias}}$ leads to an initial increase in the collector signal current $I_{\mathrm{c,s}}$ and, consequently, in the responsivity $\mathcal{R}_{\mathrm{p}}$, followed by a saturation at higher bias currents.

This behavior can be understood by examining which parameters in Eq. 5.6 governing $I_{\mathrm{c,s}}$ depend on the collector bias current. Among these parameters, only the transconductance g_{m} is a function of $I_{\mathrm{c,bias}}$ (see Eq. 5.14). As discussed in Section 5.2.3, g_{m} appears in both the numerator and the denominator of the expression for $I_{\mathrm{c,s}}$. For small values of g_{m}, the g_{m}-dependent terms in the denominator can be neglected. This includes both the quadratic terms and the linear term $g_{\mathrm{m}}Z_{\mathrm{e}}$, provided that $g_{\mathrm{m}}Z_{\mathrm{e}} \ll 1$. In this regime, the responsivity increases approximately linearly with g_{m}. As g_{m} increases further, the denominator terms become increasingly significant, which limits the growth of $I_{\mathrm{c,s}}$ and ultimately leads to a saturation of the responsivity $\mathcal{R}_{\mathrm{p}}$.

Fig. 5.7d shows the responsivity $\mathcal{R}_{\mathrm{p}}$ as a function of the number of transistor fingers N_{x} for a fixed collector bias current of $I_{\mathrm{c,bias}} = 250\,\mu\mathrm{A}$. The responsivity initially increases with increasing N_{x}, reaches a maximum, and subsequently decreases for larger transistor sizes. An increase in the number of transistor fingers corresponds directly to an increase in the effective transistor area.

The behavior of $\mathcal{R}_{\mathrm{p}}$ can be explained by identifying the parameters in the expression for the collector signal current $I_{\mathrm{c,s}}$ that depend on the number of transistor fingers. These parameters are the base resistance r_{b}, the emitter resistance r_{e}, and the base–emitter junction capacitance C_{je}. As discussed in the theoretical analysis, a reduction of the resistive terms and the junction capacitance generally leads to an increase in responsivity. However, as can be seen from Fig. 5.7c, these parameters exhibit opposing trends as a function of N_{x}. The resistances r_{b} and r_{e} decrease with approximately $1/N_{\mathrm{x}}$ due to parallel operation of the individual fingers, while the junction capacitance C_{je} increases approximately linearly with the total transistor area.

For small values of N_x, the reduction of the parasitic resistances dominates over the increase in junction capacitance, resulting in an increase in responsivity. As N_x increases further, the resistances approach their minimum values, whereas the junction capacitance continues to grow. In this regime, the capacitive term becomes dominant, leading to a decrease in the responsivity $\mathcal{R}_p$.

Noise Voltage Spectral Density v_n

Fig. 5.8a shows the noise voltage spectral density v_n as a function of the collector bias current for different numbers of transistor fingers. The noise voltage spectral density increases with increasing $I_{c,bias}$. This behavior can be attributed to the rise in shot noise and flicker noise at higher bias currents, as discussed in the preceding noise analysis.

The dependence of v_n on the number of transistor fingers N_x is comparatively weak. Variations in N_x primarily affect the thermal noise contribution through changes in the resistances. As discussed previously, increasing the effective transistor area reduces these resistances and thus lowers the associated thermal noise. However, as will be shown in Section 5.2.5, the overall noise performance is dominated by shot noise, such that the influence of thermal noise remains minor.

Noise Equivalent Power NEP

Combining the behaviors of $\mathcal{R}_p$ and v_n explains the trends of the NEP observed in Fig. 5.7a and is subsequently explained.

- Dependence on collector bias current $I_{c,bias}$: The NEP is governed by the interplay between the nonlinear saturation of the responsivity $\mathcal{R}_p$, resulting from the increasing transconductance g_m, and the approximately linear increase of the noise voltage spectral density v_n with higher $I_{c,bias}$ due to increased shot noise. At low bias currents, the rise in $\mathcal{R}_p$ dominates, leading to a reduction in the NEP. As the bias current increases further and the responsivity begins to saturate, the continued increase in noise causes the NEP to reach a minimum and then rise slightly again.
- Dependence on number of transistor fingers N_x: Since the noise voltage spectral density v_n is nearly independent of N_x due to the minor contribution of thermal noise compared to shot noise, the behavior of the NEP is primarily governed by the responsivity $\mathcal{R}_p$. For small values

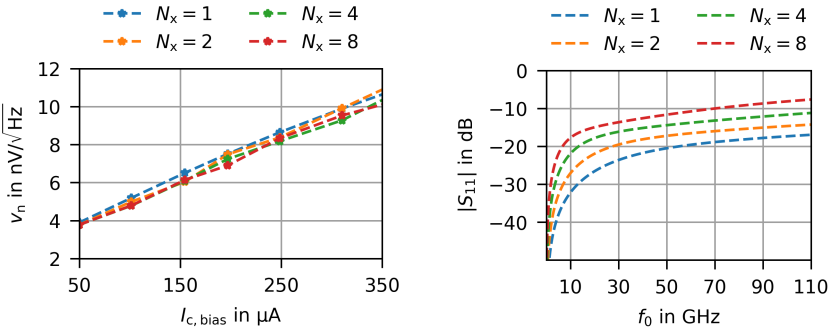

(a) (b)

Figure 5.8: (a) Simulated v_n for varying numbers of transistor fingers N_x. The common-emitter voltage is held constants at $V_{ce} = 1.4\,V$, while V_{be} is adjusted for each $I_{c,bias}$. (b) Simulated $|S_{11}|$ for different numbers of transistor fingers N_x.

of N_x, the reduction of parasitic base and emitter resistances leads to an increase in $\mathcal{R}_p$ and thus to a decrease in the NEP. As the number of transistor fingers increases further, the growing base–emitter junction capacitance C_{je} limits further improvements in responsivity, leading to saturation with a slight reduction. As a result, the NEP reaches a plateau and increases only marginally.

Broadband Capabilities

The previous analysis was limited to a single frequency ($f_0 = 10\,GHz$). To evaluate the broadband capabilities of the different transistor sizes, Fig. 5.8b shows the magnitude of the input reflection coefficient $|S_{11}|$ for the targeted frequency range. For each N_x, the bias point corresponding to the minimum NEP is chosen (see Tab. A.1 in Appendix A). The input matching degrades with increasing transistor size due to the larger parasitic capacitances, which are further increased by layout-related parasitics.

In summary, the minimum NEP is achieved for transistor finger numbers equal to or greater than $N_x = 8$. However, for the broadband EPR spectrometer, wide bandwidth is the most critical design requirement. As can be seen from Fig. 5.8b, a configuration with $N_x = 8$ does not achieve an input matching better

than −10 dB across the entire frequency range of interest, primarily due to the increased parasitic capacitance at the detector input associated with the larger transistor size. In contrast, the simulation results for $N_x = 4$ remain close to this matching criterion over a broader bandwidth. To also account for layout-related parasitics and deviations from idealized simulations, a two-finger transistor configuration is selected for the lumped detector, to ensure input matching over the entire bandwidth. This transistor core subsequently serves as the unit cell for the distributed detector design discussed in the following section and as the reference design for comparison with the distributed detector.

Sizing of the Distributed Detector

To combine the low NEP associated with larger transistor sizes with broadband input matching, a distributed detector architecture is employed. Figure 5.9 shows the complete circuit schematic of the distributed detector. In this approach, the parasitic input capacitances of the individual transistor cores are compensated by inserting inductive transmission-line sections between successive stages. This distributed arrangement enables the use of a larger effective number of transistor fingers while maintaining good input matching over a wide frequency range.

The biasing and load components, including R_c, R_{b1}, and R_{b2}, are chosen identical to those used for the lumped detector in the previous section. Each stage X_s consists of two transistor fingers.

Subsequently, the choice of the number of stages X_S and the length of the transmission lines are discussed. Fig. 5.10a shows the simulated NEP and the DC power consumption P_{dc} as a function of X_s. As X_s increases, the NEP initially decreases significantly, then saturates, and shows a slight increase for larger number of stages.

The collector-emitter voltage is again kept constant to $V_{ce} = 1.4\,\text{V}$ for each stage. For a number of stages larger than one, the minimum NEP is achieved for a collector supply current of $I_{cc,bias} = 250\,\mu\text{A}$. For a single stage, the minimum NEP is achieved for a collector supply current of $I_{cc,bias} = 200\,\mu\text{A}$ (see Fig. 5.7a). Here, the total collector supply current is given by $I_{cc,bias} = I_{c,bias} \cdot X_s$, where $I_{c,bias}$ denotes the collector bias current per stage. The base-emitter voltage V_{be}

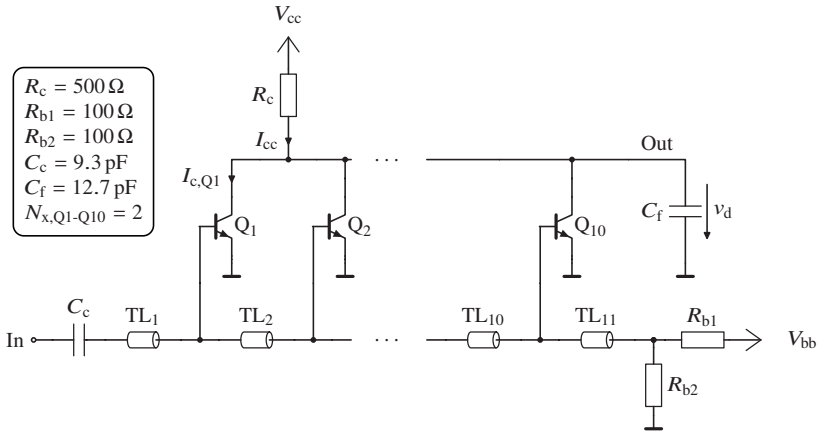

Figure 5.9: Circuit diagram of the 10-stage distributed detector. Each transistor consists of two transistor fingers. The decoupling capacitors along the supply voltage lines are omitted.

is again adjusted for each number of stages. The exact values for the supply voltages can be found in Tab. A.2 in Appendix A.

The observed NEP behavior can be understood by considering the responsivity $\mathcal{R}_p$ and the noise voltage spectral density v_n shown in Fig. 5.10b. The responsivity increases with the number of stages and reaches a maximum for four stages, corresponding to an effective transistor size of eight fingers, before decreasing slightly for larger X_s. This behavior is consistent with the trends observed for the lumped detector when increasing the number of transistor fingers. Since increasing the number of stages also increases the total effective transistor area, the same underlying mechanism applies.

The decrease in both P_{dc} and v_n with increasing X_s can be attributed to the lower base supply voltage required to achieve the optimum collector bias current of $I_{cc,bias} = 250\,\mu A$ per stage. A reduced base supply voltage V_{bb} leads to a lower base bias current I_{bb} and consequently to a reduced contribution of flicker noise from the biasing resistors.

For a number of stages $X_s \geq 4$, the combined saturation and slight reduction of both the responsivity $\mathcal{R}_p$ and the noise voltage spectral density v_n account for the observed saturation behavior of the NEP. As the NEP increases only

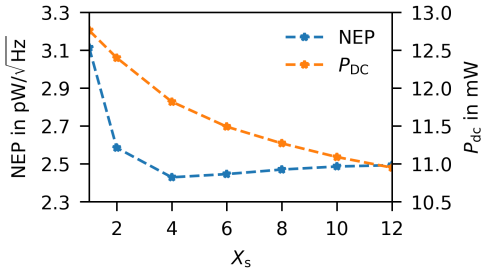

(a)

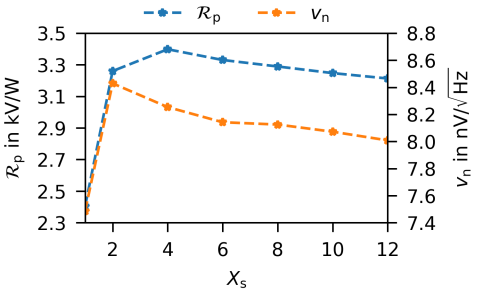

(b)

Figure 5.10: The number of stages is varied for (a) the simulated NEP and the power consumption P_{dc}, and (b) the responsivity $\mathcal{R}_p$ and the noise voltage spectral density v_n. The optimal collector supply current is $I_{cc,bias} = 200\,\mu A$ for one stage and $I_{cc,bias} = 250\,\mu A$ for a stage number larger than one. The collector-emitter voltage is $V_{ce} = 1.4\,V$ and V_{be} is adjusted for each number of stages.

slightly and shows little dependence on X_s for $X_s \geq 4$, the number of stages can be selected primarily based on DC power consumption considerations. For the final design, ten stages are chosen as a compromise between achieving a low NEP and maintaining moderate DC power consumption.

On the schematic level, each stage is biased at a collector current of $I_{c,bias} = 25\,\mu A$, resulting in a total collector supply current of $I_{cc,bias} = 250\,\mu A$ for the ten-stage configuration. The corresponding base current is $I_{b,bias} = 24\,nA$, with a base–emitter voltage of $V_{be} = 0.73\,V$, and a collector–

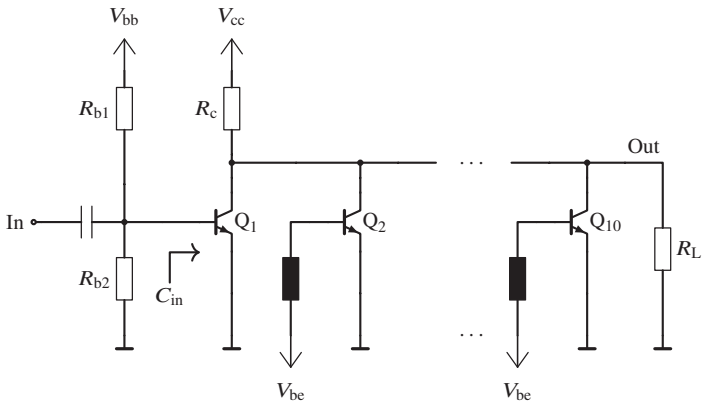

Figure 5.11: Circuit diagram used to simulate the input capacitance of the transistors.

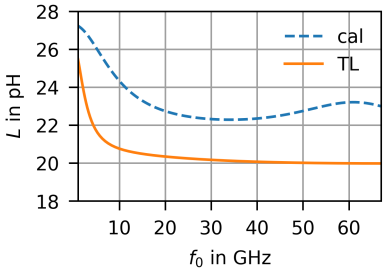

Figure 5.12: Calculated inductance according to Eq. 5.16 and simulated inductance of the implemented 40 µm long transmission line.

emitter voltage of $V_{ce} = 1.4\,\text{V}$. A collector supply voltage of $V_{cc} = 1.525\,\text{V}$ and a base supply voltage of $V_{bb} = 1.465\,\text{V}$ are used to set the operating point.

The circuit shown in Fig. 5.11 is used to determine the input capacitance that must be compensated by the transmission line. Transistors Q_2 to Q_{10} are included because they influence the input impedance of transistor Q_1. They are biased ideally by a DC feed at $V_{be} = 0.73\,\text{V}$. At the output, a load resistor of

$R_L = 10\,M\Omega$ is included. With 1-Port S-Parameter simulations, the admittance parameter Y_{11} can be extracted, and the input capacitance is determined to

$$C_{in} = \frac{\mathrm{Im}(Y_{11})}{2\pi f_0} \tag{5.15}$$

The input capacitance ranges between 9 fF and 11 fF. To achieve an input matching of $Z_{in} = 50\,\Omega$, the inductance of the transmission line can be calculated as

$$L = Z_{in}^2 C_{in}, \tag{5.16}$$

which is shown in Fig. 5.12. Since the input capacitance exhibits the same trend as the calculated inductance in Fig. 5.12, it is not shown separately.

For the transmission lines, a microstrip line is chosen. The signal line is implemented on the upper most metal layer and the ground plane is distributed on the first three metal layers. To achieve the necessary inductance with a TL, the width of the signal line is chosen to $w = 2\,\mu m$ which is the smallest allowed width according to the design rules. The smallest width leads to the shortest possible length to achieve a certain inductance. A length of $l = 40\,\mu m$ leads to the inductance shown in Fig. 5.12. This length is chosen for TL_2 to TL_{10} by simulating the transmission lines with the whole layout. TL_1 has a length of $l = 120\,\mu m$ to compensate for the parasitic capacitances introduced by the layout of the coupling capacitance at the input of the circuit.

Layout and Optimal Operating Point

The microphotograph of the lumped detector is shown in Fig. 5.13a [6]. The total chip area measures $480\,\mu m \times 398\,\mu m$ and is primarily determined by the pad dimensions, while the active core occupies only $24\,\mu m \times 32\,\mu m$. The coupling capacitor has a value of $C_c = 5\,pF$, and the output filter capacitance is $C_f = 52.5\,pF$. Decoupling of the supply voltages is provided by capacitors of $C_{d,cc} = 12.5\,pF$ and $C_{d,bb} = 15.3\,pF$ [6]. Low-frequency resonances may arise from the interaction between these decoupling capacitors and the parasitic inductances of the DC probes or bond wires. To suppress such resonances, small series resistors are inserted between $C_{d,bb}$ and ground.

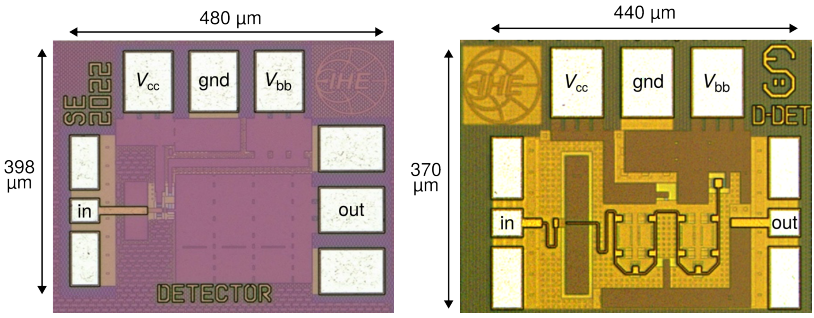

Figure 5.13: Microphotograph of (a) the lumped detector with an active core area of 770 µm^2, adapted from [6], ©IEEE, and (b) the distributed detector with an active core area of 0.025 mm^2.

The microphotograph of the distributed detector is shown in Fig. 5.13b. The overall chip dimensions, including pads, are 440 µm × 370 µm, while the core area occupies 180 µm × 141 µm. In the distributed design, the transistors are arranged in a meandered layout to achieve a space-efficient implementation. The remaining area is utilized for decoupling capacitors along the base and collector supply voltage lines, with values of $C_{d,bb}$ = 19 pF and $C_{d,cc}$ = 6.2 pF, respectively, to ensure proper AC grounding. As in the lumped design, small series resistors are included between $C_{d,bb}$ and ground to damp low-frequency resonances. At the output, a filter capacitor of C_f = 12.7 pF is employed, while the input is coupled through a capacitor of C_c = 9.3 pF. The ground plane is distributed across the first three metal layers. To achieve an input return loss below −10 dB, the spacing between the upper plate of the MIM coupling capacitor C_c, located in the fifth metal layer, and the surrounding ground plane is carefully optimized, and additional U-shaped input TLs are introduced. The ground plane beneath C_c is completely removed to further improve the input matching.

Both detector circuits are fully EM simulated, excluding the pads. A pad capacitance of 10 fF and a DC-probe model consisting of piecewise inductors with intermediate shunt capacitors to ground are included in the simulations. To compensate for layout-induced EM effects, the operating point of both circuits is further optimized by adjusting the collector bias current $I_{c,bias}$ to

Table 5.2: Operating point and supply voltages of the designed detectors in Fig 5.13.

Det. type	V_{be} V	V_{ce} V	$I_{b,bias}$ nA	$I_{c,bias}$ µA	V_{bb} V	V_{cc} V	$I_{bb,bias}$ mA	$I_{cc,bias}$ µA
Lumped	0.771	1.4	100	100	1.542	1.45	7.66	100
Distributed	0.743	1.4	34	35	1.485	1.575	7.392	350

minimize the NEP. The corresponding optimal operating points are summarized in Tab. 5.2. In all cases, the collector–emitter voltage is fixed at $V_{ce} = 1.4\,\text{V}$. The lumped detector achieves its minimum NEP at a collector supply current of $I_{cc,bias} = 100\,\mu\text{A}$, while the distributed detector reaches its optimum performance at $I_{cc,bias} = 350\,\mu\text{A}$.

Optimal Collector Resistor

The influence of the collector resistor R_c is investigated in this section and the results shown are based on the EM simulated distributed detector. The collector supply voltage is adapted for each resistor value according to

$$V_{cc} = V_{ce} + I_{cc} R_c, \tag{5.17}$$

so that $V_{ce} = 1.4\,\text{V}$ and $I_{cc,bias} = 350\,\text{mA}$. The NEP and the DC power consumption are shown in Fig. 5.14a and the responsivity and the noise voltage spectral density are shown in Fig. 5.14b. As the resistor value increases, the detected output voltage (see Eq. 5.7) and consequently the responsivity $\mathcal{R}_p$ also increase. The noise voltage spectral density v_n increases due to the higher thermal noise. Since v_n increases more slowly, the NEP decreases with larger resistors but the DC power consumption increases due to a higher V_{cc} to achieve the same collector current.

As a compromise between power consumption and minimum NEP, a collector resistor value of $R_c = 500\,\Omega$ is selected. The same trade-off applies to the lumped detector, and therefore the same resistor value is used. In applications where power consumption is of lesser importance, a larger collector resistor value may be chosen to further reduce the NEP.

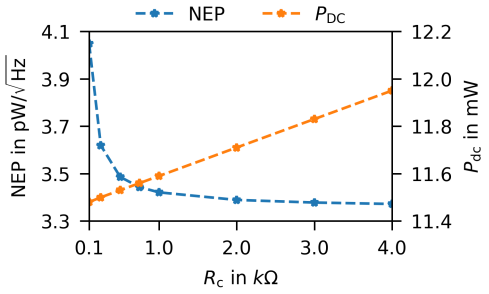

(a)

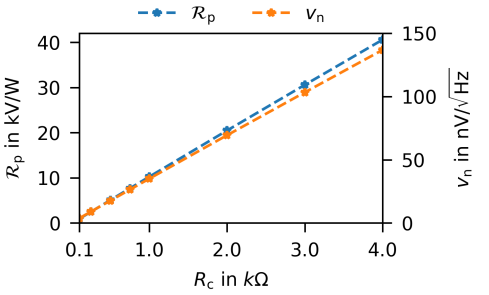

(b)

Figure 5.14: (a) NEP and DC power consumption, and (b) responsivity $\mathcal{R}_p$ and noise voltage spectral density v_n as functions of the collector resistor R_c. For each value of R_c, the collector supply voltage V_{cc} is adjusted to maintain the same operating point.

5.2.5 Noise Analysis

In this section, the noise behavior of the distributed detector is analyzed in more detail. The noise simulations are focused on the distributed design, as it represents the higher-performing architecture, as will be shown in the subsequent sections. For this reason, the distributed detector serves as the reference for the detailed simulation-based noise analysis. In contrast, noise measurements are presented for both the lumped and distributed detectors to

experimentally validate the simulation results and to enable a direct comparison between the two designs.

Simulation Results

Depending on the mode of operation, different types of noise simulations are chosen. The NEP is evaluated for small input powers, making a small-signal noise simulation sufficient. On the other hand, the NEM is determined across a range of input powers. At higher input powers, non-linear frequency translation effects lead to increased DC currents and, consequently, higher values of v_n (see Eqs. 5.9, 5.10, and 5.11 for the different noise sources). Therefore, a harmonic balance noise simulation is required to accurately capture these effects.

To identify the dominant noise source in the distributed detector shown in Fig. 5.9, a small-signal noise simulation is conducted. Although the harmonic balance simulation yields higher overall values of v_n, the qualitative trend remains consistent.

Fig. 5.15a shows v_n for each component. The operating point of the distributed detector from Tab. 5.2 is used. The noise contribution of the ten distributed BJTs are summed up according to Eq. 5.13. R_{b1} and R_{b2} produce identical noise voltage densities, leading to overlapping curves. The input matching resistors, which also serve as bias resistors, dominate v_n up to approximately 910 kHz. For frequencies above, the BJTs are the dominant noise source.

The main noise sources of one of the bias resistors is shown in Fig. 5.15b. The flicker noise is the dominant noise source up to approximately 650 kHz due to the high bias current $I_{bb} = 7.392\,\text{mA}$ flowing through the resistor, see Eq. 5.10.

The noise separation of a single BJT can be seen in Fig. 5.15c. The dominant noise source in the BJTs is the collector current shot noise. Due to the physical resistors at the base (r_b), emitter (r_e) and collector (r_c), BJTs also generate thermal noise. For a two finger transistor in the SG13G2 IHP technology, the following resistor values are extracted: $r_{bx} = 13.4\,\Omega$, $r_{bi} = 36.71\,\Omega$ and $r_e = 14.25\,\Omega$. The internal base resistor r_{bi} is the largest resistor and thus generates the highest thermal noise.

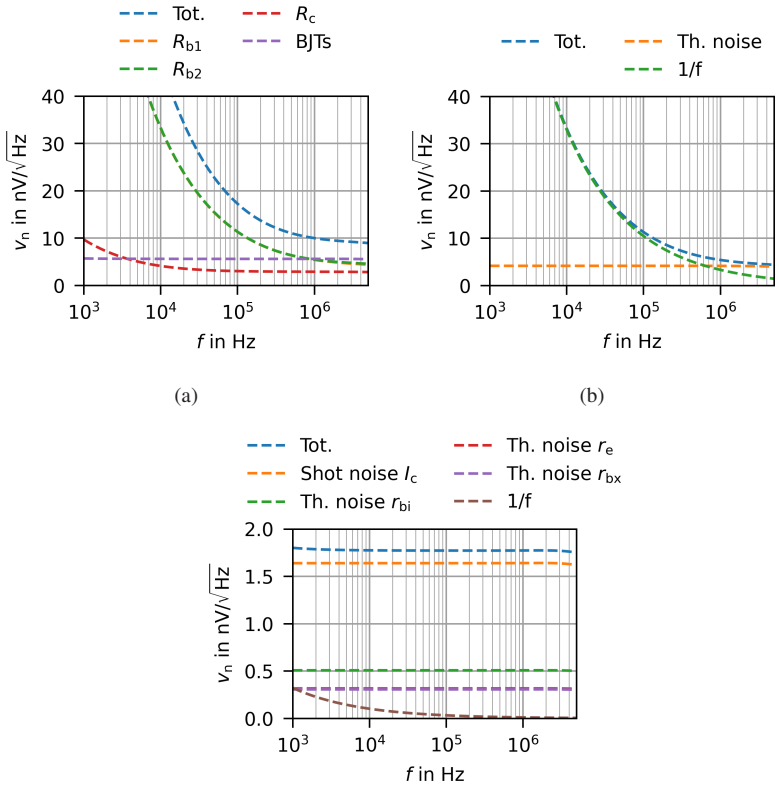

Figure 5.15: (a) Simulated v_n for each component of the circuit diagram in Fig. 5.9. The noise contributions of transistor Q_1 to Q_{10} are summed up according to Eq. 5.13. The dominant noise contributors of one of the bias resistors are shown in (b) and of a single BJT in (c). All curves are simulated and the dashed blue lines show the total v_n for each shown plot.

Measurement Results

The noise voltage spectral density is measured with the setup shown in Fig. 5.16a. The input probe is terminated with a 50 Ω resistor and v_n is measured

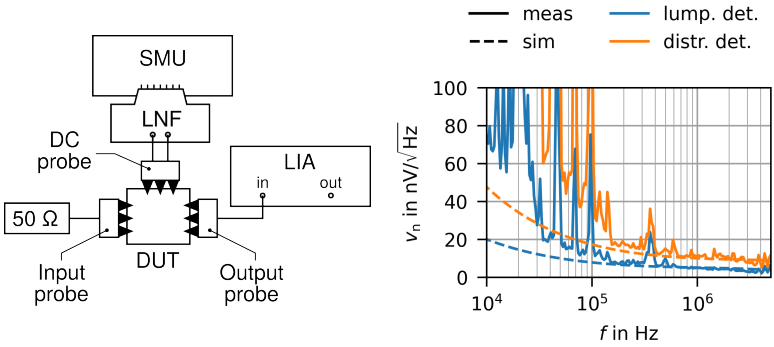

(a) (b)

Figure 5.16: (a) Noise measurement setup to determine the noise voltage spectral density v_n and (b) measurement and simulation results for the lumped and the distributed detector.

with the lock-in amplifier from Tab. 3.1. The Keysight PX0107A low noise filter (LNF) is used at the output of the SMU to reduce the noise caused by the DC path. It has a low noise filtering capability down to 25 μV_{rms} in a bandwidth of 20 MHz which results in $v_n = 5.6\,nV/\sqrt{Hz}$. The low noise filter is connected with a SubMiniature version B (SMB) to BNC cable. The BNC connector is connected to the DC probe.

In Fig. 5.16b, the simulated and measured noise results of the lumped and the distributed detector are compared. The same operating points used for the subsequent signal measurements are applied for both circuits. These operating points are listed in Tab. 5.3 and are discussed in the next section. The noise measurements are corrected by the noise floor of the LIA. The simulation and measurement results align well for frequencies above 200 kHz. The origin of the higher noise level of the measurement results for lower frequencies is examined in Fig. 5.17a.

As a reference measurement, a short is presented at the input of the LIA. The input voltage range is set to 100 mV. In a second measurement, the distributed detector is probed at the RF input and output, without connecting the DC probes. Both probes are connected according to Fig. 5.16a. It can be seen that v_n is elevated below 100 kHz and shows the typical $1/f$ noise characteristics. For

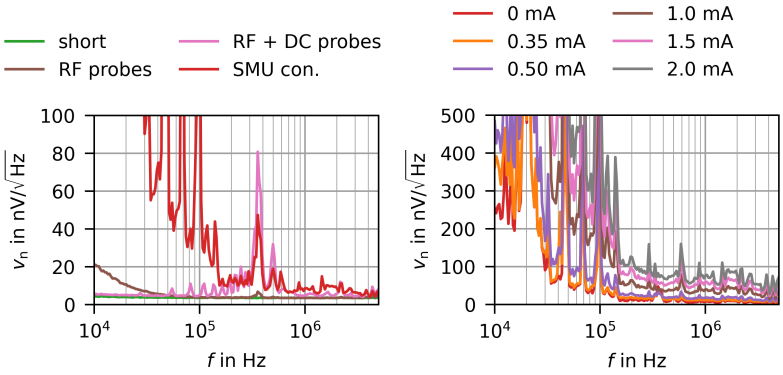

(a) (b)

Figure 5.17: Noise measurements of the distributed detector for a detailed noise analysis of the setup. (a) Influence of various components in the setup, and (b) influence of the collector supply current $I_{\text{cc,bias}}$.

higher frequencies the noise floor is very similar to the reference measurement with the exception of a small peak appearing at 350 kHz.

In the next measurement, the DC probe is also contacting the DUT. The BNC to SMB cables are already attached to the DC probe but are left open at the other end. Due to the large decoupling capacitances incorporated in the DC probe, the $1/f$ noise is reduced, but spikes are appearing for higher frequencies. Finally, the BNC to SMB cables are connected to the SMU. The supply voltages are set to $V_{\text{bb}} = V_{\text{cc}} = 0\,\text{V}$. Especially for low frequencies, the noise voltage spectral density rises significantly. A possible explanation is that noise couples from the SMU chassis into the measurement setup through the ground connection. Since the LIA is controlled by a PC, which often introduces a connection between protective and electrical ground, ground loops may form, potentially increasing v_{n}. Various ferrite rings were tested on the DC cables to suppress ground line noise. However, no significant improvement was observed. Note that for better comparison, the curves in Fig. 5.17a are not corrected for the noise voltage spectral density of the LIA.

All scenarios shown in Fig. 5.17a should ideally yield identical noise results, as the DUT is turned off. In particular, the influence of the SMU on the noise floor at lower frequencies is the primary reason for the deviation between simulation and measurement results observed in Fig. 5.16b.

As a final check of the circuit's noise behavior, the distributed detector is operated at different collector supply currents $I_{\mathrm{cc,bias}}$. The corresponding results are presented in Fig. 5.17b. An increase in $I_{\mathrm{cc,bias}}$ leads to a higher v_{n}, which is consistent with the expected rise in shot noise at higher bias currents. Notably, the noise voltage spectral density at the ideal operating point of $I_{\mathrm{cc,bias}} = 350\,\mu\mathrm{A}$ is only slightly higher than that measured at $I_{\mathrm{cc,bias}} = 0\,\mathrm{A}$, i.e. in the off-state.

5.2.6 Measured and Simulated Detector Characteristics

After analyzing the noise behavior of the distributed detector through simulations and confirming the results experimentally, the small and large signal behavior is examined. In combination with the noise analysis, this allows the calculation of the NEP and NEM.

Small-Signal Results

To verify the input matching of the lumped and the distributed detector, the magnitude of the reflection coefficient $|S_{11}|$ is measured with the N5242B Keysight VNA combined with the N5295AX02 extensions modules. A 1-mm Infinity RF probe is used to contact the input pads. The output pad is probed and connected to the LIA. The input impedance of the LIA is set to $10\,\mathrm{M\Omega}$ to present the same load as for the large signal measurements. The input path is calibrated up to the probe with a standard open, short, and load calibration algorithm.

Fig. 5.18 shows the comparison between the measured and simulated results for $|S_{11}|$. For the simulation results, the operating point given in Tab. 5.2 is used. To obtain the same bias point in the measurements as in the simulation (i.e., matching V_{ce} and $I_{\mathrm{cc,bias}}$), the base supply voltage V_{bb} had to be adjusted slightly for each circuit. The difference can be attributed to process variations. The exact values for the supply voltages and currents are listed in Tab. 5.3.

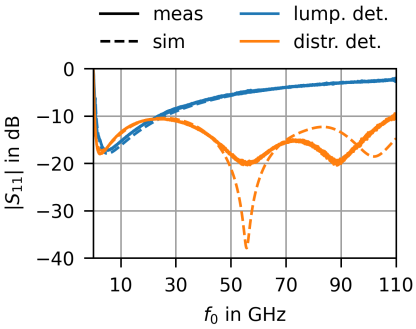

Figure 5.18: Measurement and simulation results for the magnitude of the input reflection coefficient of the lumped and the distributed detector.

The measurement and simulation results are in good agreement, although the measurement results for the distributed detector deviate slightly above 70 GHz. As expected from its distributed architecture, the distributed detector achieves a substantially wider input-matching bandwidth, remaining well matched over the entire frequency range, whereas the lumped detector maintains $|S_{11}| < -10\,\mathrm{dB}$ only up to 25 GHz. This significantly extended bandwidth represents a key advantage of the distributed detector topology. The DC power consumption for the lumped design is $P_{\mathrm{dc}} = 11.3\,\mathrm{mW}$ and for the distributed design $P_{\mathrm{dc}} = 11.1\,\mathrm{mW}$.

Table 5.3: Supply voltages of the designed detectors for the measured $|S_{11}|$ in Fig. 5.18.

Detector type	V_{bb} V	V_{cc} V	$I_{\mathrm{bb,bias}}$ mA	$I_{\mathrm{cc,bias}}$ µA
Lumped	1.525	1.45	7.32	100
Distributed	1.482	1.575	7.15	350

Noise-Equivalent Power

The NEP is determined as the ratio of the responsivity $\mathcal{R}_\mathrm{p}$ to the noise voltage spectral density v_n, as defined in Eq. 5.1. To determine the responsivity, which is defined as the ratio of the DC output voltage v_DC to the input power P_0, the measurement setup shown in Fig. 5.19 is used. The microwave input signal is generated using the SG listed in Tab. 3.1. The setup is calibrated at the input up to the probe tips. The supply voltages are provided by the SMU, which is equipped with the LNF. The DC output voltage is measured using an Agilent Technologies DSO-X 3014A oscilloscope. The noise voltage spectral density is extracted from the measurements shown in Fig. 5.16b.

The responsivity $\mathcal{R}_\mathrm{p}$ and the NEP are compared for both detectors in Fig. 5.20 for an input power of $P_0 = -21\,\mathrm{dBm}$. The noise voltage spectral density v_n is extracted at 1 MHz, where the noise floor is not dominated by the noise of the SMU, allowing the noise values to be extracted directly. The noise voltage spectral density of the lumped detector is $v_\mathrm{n} = 5.1\,\mathrm{nV}/\sqrt{\mathrm{Hz}}$ in simulation and $v_\mathrm{n} = 5.2\,\mathrm{nV}/\sqrt{\mathrm{Hz}}$ in measurement. For the distributed detector, the simulation yields $v_\mathrm{n} = 9.9\,\mathrm{nV}/\sqrt{\mathrm{Hz}}$ and the measurement yields $v_\mathrm{n} = 11.4\,\mathrm{nV}/\sqrt{\mathrm{Hz}}$.

Simulation and measurement results show good agreement. The lumped detector achieves a NEP between $3.5\,\mathrm{pW}/\sqrt{\mathrm{Hz}}$ and $5.7\,\mathrm{pW}/\sqrt{\mathrm{Hz}}$ up to 67 GHz, and $9.7\,\mathrm{pW}/\sqrt{\mathrm{Hz}}$ up to 110 GHz. The distributed detector achieves a NEP between $1.8\,\mathrm{pW}/\sqrt{\mathrm{Hz}}$ and $3.8\,\mathrm{pW}/\sqrt{\mathrm{Hz}}$ up to 67 GHz, and $4.8\,\mathrm{pW}/\sqrt{\mathrm{Hz}}$ up to 110 GHz, corresponding to an improvement factor of 1.3 – 2.4 relative to

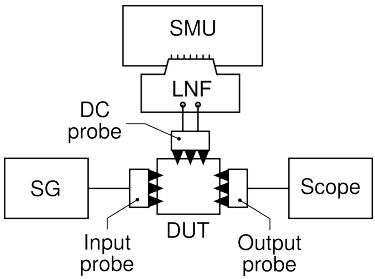

Figure 5.19: Setup to characterize the responsivity $\mathcal{R}_\mathrm{p}$ of the detectors to subsequently determine the NEP. The SG generates a sinusoidal input signal and the DC voltage is measured at the output.

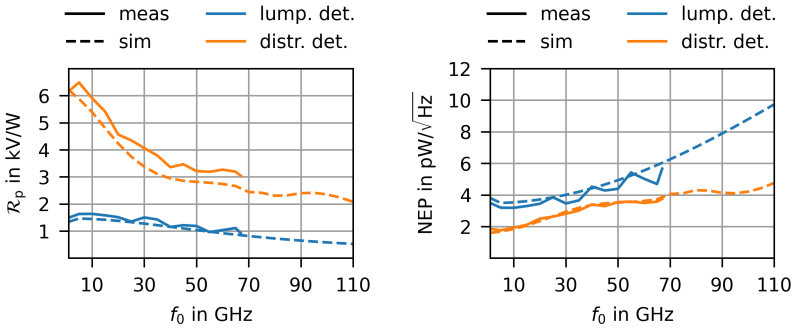

(a) (b)

Figure 5.20: Measurement and simulation results for both detector designs operated as rectifiers. (a) Responsivity $\mathcal{R}_p$ at $P_0 = -21$ dBm and (b) corresponding NEP.

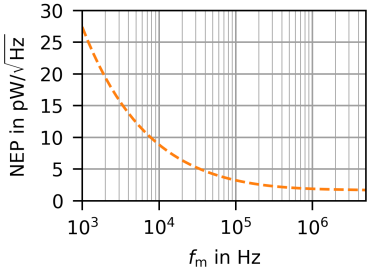

Figure 5.21: Simulated NEP as a function of the modulation frequency f_m.

the lumped detector. This advantage becomes more pronounced at frequencies above 50 GHz. Due to the available measurement setup, the characterization could only be performed up to 67 GHz.

Various modulation frequencies have been used in the literature to extract v_n. For a consistent comparison between the designed distributed detector and state-of-the-art detectors, the simulated NEP as a function of f_m is presented in Fig. 5.21. As f_m increases, the NEP decreases, which is attributed to the reduction in flicker noise at higher frequencies.

Noise-Equivalent Modulation Index

As mentioned at the beginning of this chapter, when the detector is used in an EPR spectrometer, the quantity of interest is the modulation index m, and the detector operates as a demodulator. Compared to the rectification operation, the input power P_0 and the frequency f_0 are known quantities. To measure the voltage at the modulation frequency f_m to determine the responsivity $\mathcal{R}_\mathrm{m}$ (see Eq. 5.4), the setup shown in Fig. 5.16a is used, with the 50 Ω input termination replaced by the signal generator from Fig. 5.19. Since the EPR response can be represented as an AM signal with a small effective modulation index (see Section 3.1.5), the modulation index m is chosen to be as small as possible and is limited here by the minimum modulation depth achievable with the signal generator. Accordingly, the input signal is amplitude modulated with a modulation index of $m = 2 \times 10^{-3}$.

For the simulation results, a harmonic-balance simulation is used, in which the AM input signal is represented in the frequency domain by three discrete input tones. The corresponding tone amplitudes are extracted from the time-domain expression of the AM signal given in Eq. 3.6 as

$$v(f_0) = V_0 \tag{5.18}$$

$$v(f_0 \pm f_\mathrm{m}) = \frac{mV_0}{2}, \tag{5.19}$$

with

$$V_0 = \sqrt{P_{0,\mathrm{lin}} R_\mathrm{in}}, \tag{5.20}$$

where $P_{0,\mathrm{lin}}$ denotes the input power in linear units and $R_\mathrm{in} = 50\,\Omega$ the input resistance.

Due to the non-linear frequency translation behavior of the detector, not only the desired output signal at the modulation frequency f_m is present, but also a DC component. The DC component shifts the operating point depending on the specific input power and carrier frequency. To keep the detector at its optimal collector current and collector-emitter voltage (see Tab. 5.2), the base supply voltage V_bb is adapted for each combination of input power and frequency while the collector supply voltage is kept constant. For larger input powers, a lower V_bb is sufficient to achieve the optimal collector current. For higher carrier

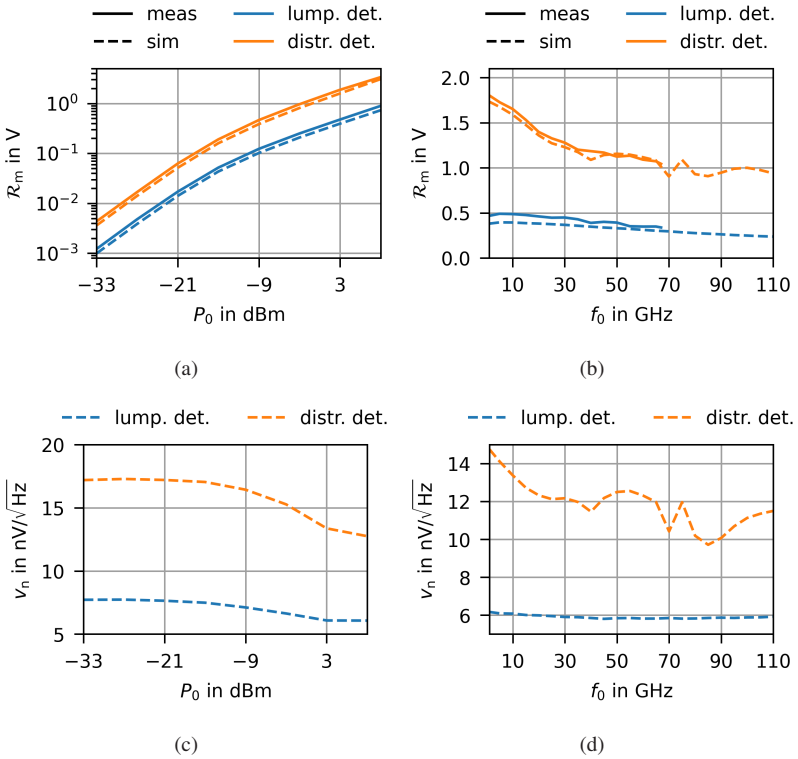

Figure 5.22: Measurement and simulation results for both designed detectors operating as demodulators. (a) and (b) show the responsivity $\mathcal{R}_m$, calculated as the output voltage at the modulation frequency $f_m = 100\,\text{kHz}$ divided by the modulation index $m = 2 \times 10^{-3}$. (c) and (d) display the simulated noise voltage amplitude at the same modulation frequency. Results in (a) and (c) are obtained at the carrier frequency of $f_0 = 10\,\text{GHz}$, while (b) and (d) correspond to an input power of $P_0 = 3\,\text{dBm}$.

frequencies, a higher V_{bb} is necessary to compensate for the higher losses. The exact values for V_{bb} for an input power sweep and for a carrier frequency sweep are listed in Appendix A in Tab. A.3 and Tab. A.4, respectively.

The simulated and measured responsivity $\mathcal{R}_m$ is shown in Fig. 5.22a and 5.22b. It is calculated as the output voltage at the modulation frequency divided by

the modulation index $m = 2 \times 10^{-3}$. For the input power sweep in Fig. 5.22a, the carrier frequency is fixed at $f_0 = 10\,\text{GHz}$ and the power is varied in 6 dB steps. At low input powers, $\mathcal{R}_\text{m}$ increases proportionally to the input power and saturates at higher input powers, similar to the detector's behavior when operated as a rectifier. For the frequency sweep in Fig. 5.22b, the input power is set to 3 dBm, and the carrier frequency is swept in 5 GHz steps. $\mathcal{R}_\text{m}$ decreases with increasing frequency due to higher losses. The simulation and measurements align well, with the measurement values being slightly higher.

The responsivity is ideally independent of the specific modulation frequency. For the measurements, a modulation frequency of $f_\text{m} = 10\,\text{kHz}$ is selected. As the modulation frequency of the SG approaches its maximum value of 80 kHz, the quality of the AM signal appears to degrade, motivating the choice of a comparatively low modulation frequency.

The simulated noise voltage spectral density v_n is shown for the input power and carrier frequency sweep in Fig. 5.22c and 5.22d, respectively. v_n decreases at higher input powers, as a lower V_bb is required to achieve the optimum collector current. This leads to a decrease in I_bb and in the thermal noise voltage generated by R_b1 and R_b2. For the frequency sweep, v_n shows a similar trend as the responsivity $\mathcal{R}_\text{m}$. Due to increased losses at higher frequencies, the gain is reduced, leading to a decrease in both the signal and the noise.

Reproducing the simulated noise behavior as a function of input power and frequency is not feasible in measurement. In the simulations, the operating point is adjusted for each input power and carrier frequency to maintain the optimal collector current. Achieving this experimentally would require performing noise measurements while driving the detector with the signal generator at the corresponding input powers. However, the intrinsic noise of the signal generator is much higher than that of the detector and dominates the measured noise, which prevents an accurate characterization of the detector's intrinsic noise.

When the detector noise is measured with a 50 Ω termination and no input signal, only a single operating point can be set, which corresponds to low input power because the operating point is not shifted by a rectified component. At higher input powers, the simulated operating points cannot be reproduced because the collector current cannot be maintained while independently varying the base bias current. The operating points used during the responsivity measurements

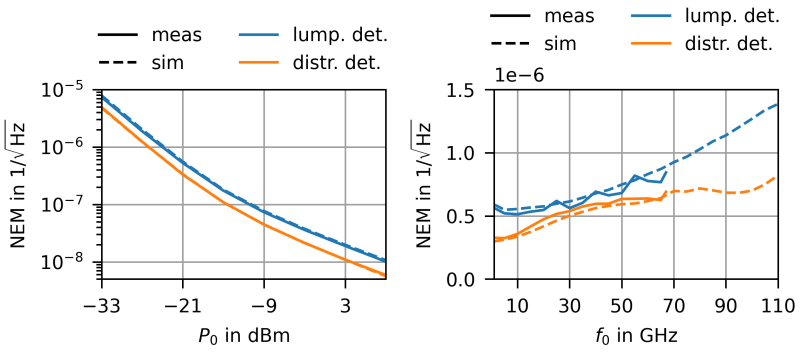

Figure 5.23: Measured and simulated NEM as a function of (a) the input power and (b) the frequency. The values are obtained based on the responsivity $\mathcal{R}_\mathrm{m}$ and the noise voltage spectral density v_n of Fig. 5.22.

at higher input powers are only achievable in the presence of an input signal, since the rectified DC component adds bias that is absent under noise-only conditions.

For the noise measurements, an input power of $P_0 = -21\,\mathrm{dBm}$ is chosen. A modulation frequency of 100 kHz is used, as this value is common in commercial EPR spectrometers. Since the noise contribution of the SMU already affects the measurements at 100 kHz, the noise data is interpolated. This yields the following noise voltage spectral densities: For the lumped detector, the simulated value is $v_\mathrm{n} = 7.8\,\mathrm{nV}/\sqrt{\mathrm{Hz}}$ and the measurement gives $v_\mathrm{n} = 9\,\mathrm{nV}/\sqrt{\mathrm{Hz}}$. For the distributed detector, the simulation gives $v_\mathrm{n} = 17.3\,\mathrm{nV}/\sqrt{\mathrm{Hz}}$ and the measurement gives $v_\mathrm{n} = 20.3\,\mathrm{nV}/\sqrt{\mathrm{Hz}}$.

The NEM as a function of input power is shown in Fig. 5.23a. A constant v_n, as reported above, is used for all input power levels. Due to the logarithmic scale of the plot, the variation in noise with input power has a negligible impact on the overall trend. As the input power increases, a lower NEM is achieved, enabling the detection of smaller modulation indices.

The NEM as a function of frequency is shown in Fig. 5.23b. Similar to the rectifier mode of operation, the measurements show good agreement with the

simulations. At $P_0 = -21\,\mathrm{dBm}$, the lumped detector achieves a NEM between $5.6\times10^{-7}\ 1/\sqrt{\mathrm{Hz}}$ and $8.4\times10^{-7}\ 1/\sqrt{\mathrm{Hz}}$ up to 67 GHz, and $1.4\times10^{-6}\ 1/\sqrt{\mathrm{Hz}}$ up to 110 GHz. The distributed detector achieves a NEM between $3.2\times10^{-7}\ 1/\sqrt{\mathrm{Hz}}$ and $6.9\times10^{-7}\ 1/\sqrt{\mathrm{Hz}}$ up to 67 GHz, and $8.2\times10^{-7}\ 1/\sqrt{\mathrm{Hz}}$ up to 110 GHz.

The performance of the distributed detector at higher input powers is evaluated using simulations, since the noise behavior at the corresponding operating points cannot be reproduced experimentally for the reasons discussed previously. Figure 5.24a shows the simulated NEM for $P_0 = 3\,\mathrm{dBm}$. At this input power, the adapted operating point reduces the noise, and the advantage of the distributed architecture becomes more pronounced. Under these conditions, the distributed detector achieves a lower NEM in the range of $9\times10^{-9}\ 1/\sqrt{\mathrm{Hz}}$ to $1.2\times10^{-8}\ 1/\sqrt{\mathrm{Hz}}$.

As discussed in Section 3.1.5, the EPR measurements presented in Chapter 4 require modulation indices between 1.5×10^{-7} and 5×10^{-6} at an input power of 3 dBm and a lock-in bandwidth of 1.06 Hz. Normalizing the modulation index m by the square root of the lock-in bandwidth yields a required NEM in the range of $1.4\times10^{-7}\ 1/\sqrt{\mathrm{Hz}}$ to $4.9\times10^{-7}\ 1/\sqrt{\mathrm{Hz}}$. Consequently, the simulated NEM of the distributed detector is at least one order of magnitude lower than the required values, confirming its suitability for highly sensitive EPR measurements across the entire frequency range.

To evaluate the benefit of adapting the supply voltage V_{bb}, Fig. 5.24b compares the NEM of the distributed detector obtained using a frequency-optimized V_{bb} with that obtained using a fixed base supply voltage of $V_{\mathrm{bb}} = 0.968\,\mathrm{V}$, which corresponds to the optimal value at the center frequency $f_0 = 50\,\mathrm{GHz}$. A fixed supply voltage of $V_{\mathrm{bb}} = 0.968\,\mathrm{V}$ yields results comparable to those of the frequency-optimized V_{bb} within the 15 GHz to 95 GHz bandwidth. However, at the band edges, the NEM increases slightly. This indicates that adapting V_{bb} across frequency is not strictly necessary for EPR measurements, thereby reducing system complexity. In contrast, as shown earlier, adapting the base supply voltage for varying input powers provides a significant performance benefit.

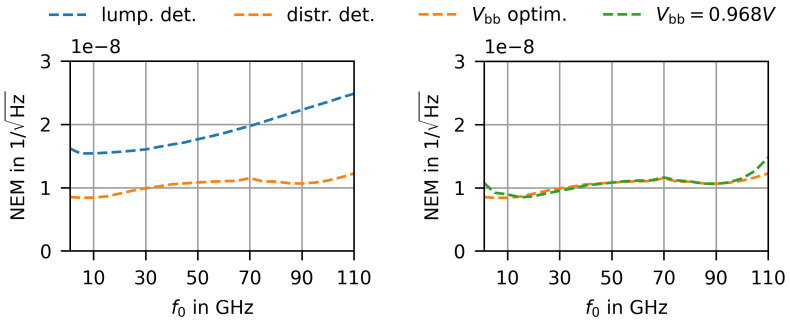

Figure 5.24: Simulated NEM results for (a) the lumped and distributed detector at an input power of $P_0 = 3$ dBm and (b) for the distributed detector obtained using a frequency-optimized V_{bb} compared to using a fixed base supply voltage of $V_{bb} = 0.968$ V.

5.2.7 Performance Comparisons and Summary

The performance of the lumped and distributed integrated circuits is first compared with the commercial detector used in the EPR measurement setup shown in Fig. 3.1. In addition, both detectors are benchmarked against state-of-the-art silicon-based detectors. The chapter concludes with a discussion and summary of the results.

Comparison with Commercial Detector

The commercial detector is a planar-doped barrier diode in a GaAs technology. It is input matched to 50 Ω and is specified for the frequency range from 0.01 GHz to 50 GHz. The responsivities $\mathcal{R}_m$ and $\mathcal{R}_p$ are measured in the same way as for the integrated detector circuits.

Fig. 5.25 compares the performance of the three detectors operated as rectifier. It is important to note that for frequencies above 50 GHz, the commercial detector operates beyond its specified range. Its noise voltage spectral density was already presented in Fig. 3.12 of Section 3.2.3 and is evaluated at 1 MHz, yielding $v_n = 2.4\,\mathrm{nV}/\sqrt{\mathrm{Hz}}$. The responsivity is again measured at an input

power of $P_0 = -21\,\mathrm{dBm}$. The commercial detector shows a relatively linear NEP up to a frequency of 35 GHz. The lumped detector achieves a similar NEP within the measured frequency range while offering a very compact design. Simulation results further indicate that it maintains a reasonable NEP up to 110 GHz. The distributed detector demonstrates a distinct improvement in NEP compared to the commercial detector, with an enhancement factor ranging from 1.1 to 2.6 within the commercial detector's specified frequency range. Additionally, it supports operation up to 110 GHz, providing a substantially wider bandwidth while maintaining a low NEP.

When operated as demodulators, v_n at 100 kHz is considered. At this frequency, the commercial detector exhibits a noise voltage spectral density of $v_\mathrm{n} = 4.6\,\mathrm{nV}/\sqrt{\mathrm{Hz}}$. Fig. 5.26 shows the NEM as a function of input power at a carrier frequency of 10 GHz. Both integrated detectors achieve a lower NEM across all input powers, with the distributed detector exhibiting an improvement by a factor of 1.9 – 2.4 compared to the commercial detector.

Fig. 5.27 shows the NEM as a function of carrier frequency for two input powers, $P_0 = -21\,\mathrm{dBm}$ and $P_0 = 3\,\mathrm{dBm}$. The observed NEM trends are consistent with the NEP results and confirm that the distributed detector achieves the lowest NEM values overall. The performance advantage becomes more pronounced

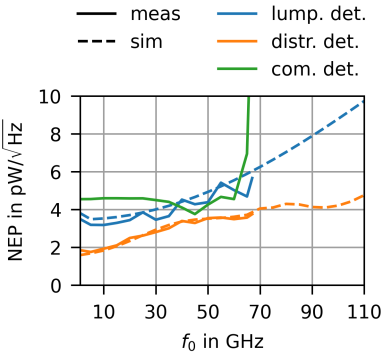

Figure 5.25: Comparison of the designed detectors with a commercial GaAs diode operated as rectifiers. NEP as a function of the frequency at an input power of $P_0 = -21\,\mathrm{dBm}$ is shown. The noise voltage spectral density is extracted at 1 MHz.

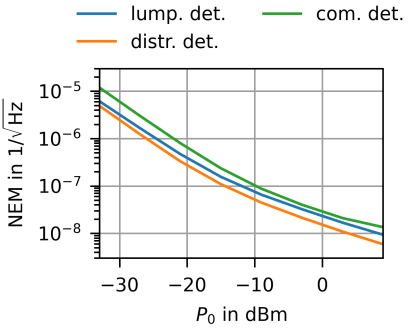

Figure 5.26: Comparison of the designed detectors with a commercial GaAs diode operated as demodulators. NEM as a function of input power at a carrier frequency of $f_0 = 10\,\mathrm{GHz}$ is shown. The noise voltage spectral density is extracted at 100 kHz.

at higher input powers, which is particularly relevant for EPR experiments, where, to a first approximation, a higher input power produces a larger EPR signal voltage. At $P_0 = -21\,\mathrm{dBm}$, both simulation and measurement results are shown. As explained in the previous section, at $P_0 = 3\,\mathrm{dBm}$ the noise voltage spectral density of the integrated circuits decreases. However, these input-power-dependent bias conditions cannot be reproduced in the measurement, and therefore only the simulation results are presented. Since the commercial detector is a passive device, its performance does not benefit from higher input powers, and its noise voltage spectral density remains independent of input power.

However, it should be noted that the commercial detector is already packaged, in contrast to the bare integrated circuits of the other detectors, making the comparison not entirely fair. Furthermore, the noise performance of the integrated circuits is influenced by the relatively high noise contribution from the SMU. As a result, careful design and filtering of the DC supply paths are required to suppress noise injection from the DC supply into the measurement setup.

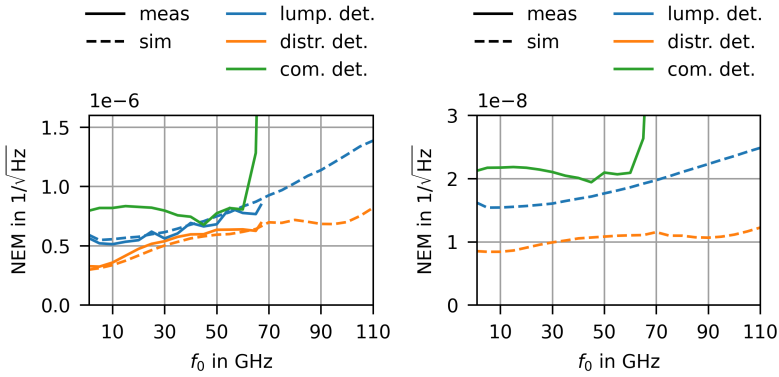

Figure 5.27: Comparison of the designed detectors with a commercial GaAs diode operated as demodulators. NEM as a function of frequency at an input power of (a) $P_0 = -21\,\mathrm{dBm}$ and (b) $P_0 = 3\,\mathrm{dBm}$.

Comparison with State-of-The-Art Silicon Detectors

Although detectors are a key component of EPR spectrometers, EPR remains a relatively uncommon application area in detector development. Therefore, the detectors developed in this work are compared with state-of-the-art designs based on their minimum NEP. Tab. 5.4 shows the comparison, where the bandwidth is denoted by BW, a common-gate configuration by CG, and a common-source configuration by CS.

Among the published broadband detectors surveyed here, only two report NEP values. The detector presented by Qayyum and Negra operates only up to 5 GHz and is based on packaged Schottky diodes rather than an integrated implementation [QN18]. Its reported NEP of $9.6\,\mathrm{pW}/\sqrt{\mathrm{Hz}}$ was measured at a modulation frequency of $f_\mathrm{m} = 100\,\mathrm{MHz}$. The distributed detector reported by Wang et al. exhibits a very large bandwidth from 30 GHz to 300 GHz, but its NEP of $55\,\mathrm{pW}/\sqrt{\mathrm{Hz}}$ measured at 100 kHz is comparatively high [WCC+23].

The lumped detector developed in this work achieves a minimum measured NEP of $3.5\,\mathrm{pW}/\sqrt{\mathrm{Hz}}$ at 1 MHz, while the distributed detector achieves a minimum

measured NEP of 1.8 pW/$\sqrt{\text{Hz}}$ at the same modulation frequency. Simulated NEP results for the distributed detector as a function of modulation frequency (see Fig. 5.21) indicate a value of approximately 10 pW/$\sqrt{\text{Hz}}$ at 100 kHz, which is well below the previously reported results. All published broadband detectors listed in Table 5.4 have been implemented in CMOS processes, whereas the detector presented in this work was realized in a BiCMOS technology.

Since there are not many broadband detectors reported that work down to the single-digit GHz frequencies, the detectors are also compared to W-Band (75 GHz – 110 GHz), F-Band (90 GHz – 140 GHz), and D-Band (110 GHz – 170 GHz) detectors in Tab. 5.5. In the table, CD denotes a common-drain configuration, SOI refers to silicon-on-insulator technology, GF stands for Global Foundries, and IBM for International Business Machines Corporation. Detectors in those frequency bands are often used for passive imaging systems.

Early studies [MR10, TGV10, GJH11] were among the first to publish works on integrated Dicke radiometers, in which power detectors play a crucial role. Differential topologies are used in [TGV10] and [GJH11] to reduce the noise introduced from power supply variations. The designs reported in [UTB+20, KGY+20, TCYG20, YE21] originate from the same research group and consistently employ a cascode topology. In this configuration, the breakdown voltage of the CB stage is increased as the CB transistor is biased with a forced emitter current. This allows for the use of a larger collector resistor without inducing breakdown in the transistors, thereby enabling higher responsivity. The distributed detector presented in this work, representing the better-performing design, achieves a NEP of the same order of magnitude as the reported detectors in Tab. 5.5 while maintaining a wide bandwidth. Further improvements of the circuit are discussed in the following section.

Table 5.4: Performance comparison of broadband silicon detectors.

Reference	Technology	Topology	BW GHz	$\mathcal{R}_p$ kV/W	NEP pW/$\sqrt{\text{Hz}}$	f_m Hz	P_{dc} mW	Area mm^2
[WQN17]	65 nm CMOS	17-stages distr. CG	0.01–110	0.7–0.068	n.a.	n.a.	0	0.456[(1)]
[QN17b]	65 nm CMOS	1-stage CS	0.01–110	0.1	n.a.	6 G	0.029	0.001[(2)]
[QN17a]	130 nm CMOS	2-stages distr. CS	7–70	2.2–5.6	n.a.	n.a.	0.156	0.068[(2)]
[QN18]	Schottky diodes	3-stages distr.	0.1–5.3	2.5–17.57	< 9.6[(4)]	100 M	150	846[(3)]
[WCC+23]	65 nm CMOS	2-stages distr. CS	30–300	> 0.8[(5)]	< 11[(5)]	100 k	7[(6)]	0.176
[NOW+25]	130 nm SiGe BiCMOS	2-stages distr. casc.	2.5–64	14.58 –45.23	n.a.	n.a.	7.79	0.033[(1)]
This work	130 nm SiGe BiCMOS	1-stage CE	0.01–25	> 1.3[(4)]	< 3.9[(4)]	1 M	11.3	0.0008[(2)]
This work	130 nm SiGe BiCMOS	10-stages distr. CE	0.01–110[(7)]	6.2–2.1	1.8–4.8	1 M	11.1	0.025[(2)]

[(1)] incl. pads, [(2)] core, [(3)] complete printed circuit board (PCB), [(4)] entire BW, [(5)] at 100 GHz; estimated from plot [(6)] with buffer, [(7)] meas. up to 67 GHz

Table 5.5: Performance comparison of W-, F-, D-band detectors.

Reference	Technology	Topology	BW GHz	$\mathcal{R}_p$ kV/W	NEP pW/$\sqrt{\text{Hz}}$	f_m Hz	I_c µA	R_c kΩ
[MR10]	120 nm SiGe BiCMOS IBM8HP	CE	94	12	3–4	10 k	150	0.75
[TGV10]	65 nm CMOS	diff. CD+CG	70–95	0.17	149	400 k	200	0.36
[GJH11]	180 nm SiGe BiCMOS TowerJazz	diff. CE	70–110	11	5	1 M	42	23
[UR13]	45 nm CMOS SOI	CS	150–210	3	8–10	10 M	200	1
[UTB+20]	130 nm SiGe BiCMOS IHP	cascode	80–107	772	0.43	1 k	n.a.	100
[KGY+20]	130 nm SiGe BiCMOS IHP	cascode	76–81	64	1.25	12.5 k	n.a.	100
[TCYG20]	130 nm SiGe BiCMOS IHP	cascode	110–155	883	0.7	10 k	50	100
[YE21]	120 nm SiGe BiCMOS GF	CB	90–100	24	1.4	1 k	n.a.	2

Summary and Outlook

In this section, the noise-equivalent modulation index was proposed as a figure of merit to quantify the smallest detectable modulation index per square root bandwidth, analogous to the commonly used noise-equivalent power. The modulation index m is proportional to the measured EPR voltage and is thus the quantity of interest in context of EPR measurements.

Two detector architectures were developed and analyzed: a lumped design and a distributed design. The lumped detector provides a compact implementation and serves as a reference for the distributed design. Its input reflection coefficient remains below $-10\,\mathrm{dB}$ up to 25 GHz, while both simulation and measurement results indicate reasonable NEP and NEM performance beyond this frequency. When operated as a rectifier, it achieves a minimum measured NEP of $3.5\,\mathrm{pW}/\sqrt{\mathrm{Hz}}$ at 1 MHz. As a demodulator, it yields a measured NEM between $5.6 \times 10^{-7}\,1/\sqrt{\mathrm{Hz}}$ and $1.4 \times 10^{-6}\,1/\sqrt{\mathrm{Hz}}$.

To enable broadband operation and achieve lower NEM values, a distributed architecture was designed. The parasitic input capacitances of the transistors are absorbed by inductive transmission lines between the transistor stages, enabling operation up to 110 GHz. Ten stages were selected as a trade-off between minimum NEM and DC power consumption. A larger collector resistor reduces the minimum achievable NEM but increases power consumption.

The main noise contributor of the distributed detector is the flicker noise of the matching resistors at the input. To reduce the flicker noise, instead of using R_{b1} and R_{b2} as input matching resistors as well as the bias resistors, separate large biasing resistors can be used for R_{b1} and R_{b2}. The matching resistor would need to be placed before the blocking capacitor to not influence the operating point. This would reduce the base bias current, leading to a lower flicker noise of the input resistors. Increasing the physical size of the resistors also decreases the flicker noise, since it is inversely proportional to the square root of the physical size. As is often done in Dicke radiometers, an additional low noise amplifier could be placed in front of the detector to further reduce the overall noise. However, the design of a broadband low noise amplifier is challenging, and its actual performance benefits would require a detailed analysis.

The noise measurements showed that the SMU has a large effect on the noise voltage spectral density for modulation frequencies up to 200 kHz. To suppress

the common-mode noise of the supply lines, a differential detector design would likely be highly beneficial. To optimize the noise measurement setup, twisted pair cables could be used to connect the DC probes to the SMU to suppress injected common mode noise by the SMU. To eliminate any ground loops, a battery instead of the SMU could be used. Large filter capacitors on an additional PCB could further decrease the injected noise. Those measures should also be used when integrating the distributed detector into an on-chip EPR spectrometer.

The input reflection coefficient of the distributed detector remains below −10 dB across the entire bandwidth. When operated as a rectifier, it achieves a NEP between $1.8\,\mathrm{pW}/\sqrt{\mathrm{Hz}}$ and $4.8\,\mathrm{pW}/\sqrt{\mathrm{Hz}}$, with v_n extracted at 1 MHz. This represents one of the lowest NEP values reported for broadband detectors. The simulation results, validated by measurements up to 67 GHz, indicate broadband operation extending to at least 110 GHz.

When operated as demodulator, the distributed detector yields a NEM ranging from $3.2 \times 10^{-7}\,1/\sqrt{\mathrm{Hz}}$ to $8.2 \times 10^{-7}\,1/\sqrt{\mathrm{Hz}}$ for an input power of −21 dBm across the full bandwidth. The noise voltage spectral density is evaluated at 100 kHz, as it is a typical modulation frequency used in standard EPR spectrometers. For higher input powers, a lower base supply voltage is required to maintain the same collector current, which reduces the detector's noise. Combined with the increased responsivity at higher input powers, this leads to a further improvement in the NEM.

Compared to the commercial detector used in the EPR measurement setup, both the lumped and distributed detectors developed in this work achieve lower NEM values within the commercial detector's specified frequency range at $P_0 = -21$ dBm. The distributed detector, representing the better-performing design, achieves a consistently lower NEM by a factor of 1.9 to 2.4 and operates up to 110 GHz, which significantly extends the usable bandwidth beyond the commercial detector's 50 GHz limit.

6 Conclusions and Outlook

Conclusions

By progressing from the analysis of system architectures, through the realization of a TL-based measurement setup, to the development of optimized non-resonant microwave probes, and ultimately to the design of integrated circuit components, this thesis establishes a coherent framework for broadband integrated EPR spectrometers. The presented results demonstrate that an on-chip, broadband implementation is not only feasible but constitutes a meaningful extension of the EPR toolbox, complementing established resonator-based systems and enabling experimental capabilities that are difficult if not impossible to achieve with conventional approaches.

In the first part of this thesis, different TL-based detection architectures and their potential for broadband operation were examined. The main difference compared to conventional spectrometers lies in the use of a TL microwave probe instead of a resonator. Such a probe inherently works over a broad frequency range, but this advantage introduces two main challenges: a potentially lower sensitivity due to the lack of resonator-like magnetic field build-up and the difficulty of separating the small EPR signal from the large transmitted microwave signal.

Three system architectures were analyzed and experimentally demonstrated: quadrature, interferometric, and lock-in detection. The quadrature detection performs the separation of the transmission and EPR signals only during post-processing, requiring the receiver to handle the full transmission signal. As a result, the effective dynamic range and sensitivity are limited.

The interferometric detection overcomes this limitation by suppressing the transmitted signal through destructive interference before detection. This configuration is therefore not limited by the receiver's dynamic range and,

in its operating principle, most closely resembles the conventional resonator-based approach, where the background signal is likewise canceled so that absorption and dispersion unfold in a similar manner. Both the quadrature and interferometric implementations, however, rely on broadband IQ mixers, which remain technically demanding to realize.

The lock-in detection scheme, on the other hand, separates the large transmission carrier and the weak EPR response in the frequency domain by applying magnetic-field modulation and using a detector for demodulation. After detection, the EPR signal appears as an isolated component at the modulation frequency, which can be measured using a lock-in amplifier. This architecture eliminates the need for a broadband IQ mixer, provides strong noise rejection through narrowband detection, and relaxes broadband circuit requirements, making it the most suitable starting point for an on-chip broadband implementation.

An analytical model was developed for the lock-in detection scheme, showing that the demodulated signal corresponds directly to the absorption component. For the interferometric detection, a dedicated post-processing algorithm was developed to separate absorption and dispersion more efficiently than previously published methods.

Building on this analysis, a complete broadband TL-based spectrometer was realized based on the lock-in detection scheme combined with field modulation. It is based on conventional laboratory instruments combined with the TL microwave probes developed based on the results of this thesis. The measurement setup revealed an unwanted interference path that arises when planar microwave probes are placed inside the modulation coil. Without correction, this path distorts the EPR spectra and prevents accurate interpretation. A dedicated post-processing scheme was therefore developed to automatically remove this influence, enabling accurate and repeatable measurements without manual phase tuning between the I- and Q-channel of the lock-in amplifier. Amplitude noise from the signal generator and potentially flicker noise from the detector were identified as the dominant noise sources in the system at higher input powers.

A comparison with a high-end commercial resonator-based spectrometer confirms that the latter achieves a higher sensitivity than the presented custom TL-based setup. When both spectrometers are operated close to the onset of

saturation, the observed sensitivity difference can be attributed primarily to the spatial overlap between the microwave magnetic field and the sample volume, as well as to the effective noise performance of the respective excitation and receive chains. A direct quantitative comparison of the underlying noise contributions is not feasible, as the internal signal chain of the commercial spectrometer is not accessible. It is assumed that the broadband requirements imposed on the individual components of the custom-built TL-based spectrometer, particularly the signal source, lead to an increased overall noise contribution. Nevertheless, the presented broadband approach provides a complementary alternative that extends EPR capabilities toward broadband measurements, which is particularly important for complex spectra and for the direct determination of zero-field splitting parameters.

The investigation of TL microwave probes focused on improving the magnetic field strength in the sample area, which is a key parameter in continuous-wave EPR because the signal amplitude scales linearly with the microwave magnetic field. Coplanar waveguide and microstrip structures were analyzed in simulation and measurement, and design guidelines were established for both. The results showed that the CPW configuration provides the highest effective magnetic field and is therefore well suited for qualitative experiments requiring high sensitivity. For applications where a homogeneous magnetic field distribution is important, the inverted microstrip line offers clear advantages and represents a valuable alternative for specific sample types. These findings provide a consistent basis for designing future TL probes in broadband EPR spectrometers.

Two components, which are key parts of the path toward on-chip miniaturization, were developed and implemented in SiGe BiCMOS technology: a broadband amplifier and two variants of a broadband detector. The amplifier was realized as a compact two-stage lumped circuit consisting of an emitter-follower and a cascode stage with inductive peaking. Despite its very small core area of 0.007 mm^2, it achieved a 3 dB bandwidth of 60 GHz and a saturated output power of 10 dBm, demonstrating that compact lumped designs can deliver sufficient output power for EPR excitation.

For the detector design, the NEM was introduced as a dedicated figure of merit for EPR detection, describing the minimum detectable modulation index associated with the EPR-induced signal. To apply this metric, the measured EPR voltage amplitudes were mapped to the corresponding effective modulation indices. This approach enables a direct comparison between

the achieved detector performance and the modulation depths required for EPR measurements. Both a lumped and a distributed ten-stage detector were developed. Compared with the lumped implementation, the distributed design extends the bandwidth of the input matching ($|S_{11}| < -10$ dB) from 25 GHz to 110 GHz while maintaining low-noise performance. It achieved NEP values between 1.8 pW/$\sqrt{\text{Hz}}$ and 4.8 pW/$\sqrt{\text{Hz}}$, and NEM values ranging from 3.2×10^{-7} 1/$\sqrt{\text{Hz}}$ to 8.2×10^{-7} 1/$\sqrt{\text{Hz}}$ at an input power of −21 dBm over the frequency range up to 110 GHz. The NEM further decreased at higher input powers. These minimum detectable modulation indices are sufficiently low to measure the EPR effect. Compared to the commercial 50 GHz planar-doped GaAs diode detector used in the implemented measurement setup, the integrated design exhibited lower NEM and a significantly broader bandwidth. Broadband detection over the frequency range from 0.01 GHz to 110 GHz has not been a primary focus of previous work. The detector presented here therefore demonstrates that low NEP values can be achieved simultaneously with broadband operation, thereby extending the range of achievable performance in integrated detector concepts.

In summary, this work establishes the conceptual and technological basis for on-chip broadband EPR spectrometers. The presented system architecture, measurement methods, probe designs, and integrated components show that the trade-offs between sensitivity, bandwidth, and integration can be addressed through careful co-design. The resulting approach enhances the flexibility and scope of EPR spectroscopy and provides a solid foundation for further developments toward compact and versatile broadband systems.

Outlook

Future developments can build directly on these results at both the system and component levels. A primary focus should be placed on further enhancing spectrometer sensitivity by reducing system noise, which is currently dominated by the amplitude noise of the signal source and potentially by flicker noise in the detector. To suppress amplitude noise, a fully differential system architecture is proposed. In this concept, the input signal is split into two identical paths that feed a main transmission line containing the sample and a reference transmission line with identical geometry. This configuration follows

the principle of the interferometric approach but eliminates the need for a phase shifter and attenuator by using a matched reference line instead. The two output signals are then combined by a differential detector, which inherently suppresses common-mode noise and cancels the large transmission background. In addition, operating the magnetic-field modulation at higher frequencies shifts the detection bandwidth away from the detector's flicker-noise-dominated region. In combination with lock-in detection, this scheme is expected to provide a broadband, low-noise platform with improved sensitivity and dynamic range.

Signal averaging can further enhance sensitivity. The geometry of the TL microwave probe can be tailored to individual samples to increase the effective interaction region, taking advantage of the flexibility of planar fabrication while adhering to EPR field criteria. Introducing a mechanical rail system for positioning the probe would facilitate reproducible alignment within the magnet and allow systematic variation of the sample position, enabling more versatile measurement configurations.

To guide future integration efforts, each component along the signal path in the EPR setup is subsequently examined. All components are envisioned to be implemented in a differential manner to fit into the overall differential system vision. The next logical step toward further miniaturization is to shift the focus of integrated design to the microwave source, as a commercial signal generator has been used thus far. In this context, particular emphasis should be placed on minimizing amplitude noise.

For the amplifier, extending the current design to a multi-stage lumped or distributed architecture could increase both bandwidth and output power, while active power combining may further enhance performance without sacrificing wideband behavior.

For the microwave probe, co-design with the amplifier and detector would allow tailored impedance matching rather than adherence to a fixed $50\,\Omega$ interface. This co-optimization can enhance the magnetic field strength through a tailored design approach for the microwave probe and may also reduce losses, since the input and output impedances of the circuits can be chosen to match more closely the natural impedance of the active transistor cores. To experimentally verify the $\vec{H}_1$ field strength and homogeneity, dedicated measurements will be required. So far, only indirect estimations have been made. The $\vec{H}_1$ strength could be derived from saturation experiments using samples with well-known

saturation behavior by relating the input power at which saturation occurs to the corresponding magnetic field. To assess the $\vec{H}_1$ homogeneity, the approach proposed by Hagen could be applied, where a sample sheet containing one and multiple BDPA crystals is used to analyze how the shape of the EPR peak changes [Hag23].

In line with the proposed differential system architecture, the detector must also operate in a differential configuration. Beyond being a functional requirement for the system setup, this implementation offers the additional benefit of suppressing common-mode noise coupled through the supply lines. Further noise reduction could be achieved through battery operation, twisted-pair DC wiring, and large filtering capacitors. The potential of including a broadband low-noise amplifier before the detector should also be evaluated to determine whether it can further reduce the overall NEM.

On the experimental side, measurements at cryogenic temperatures would offer new opportunities. At low temperatures, thermal population differences between the spin energy levels increase, leading to a higher net spin polarization in the EPR sample and, consequently, to an enhanced signal amplitude [GS18]. This increased sensitivity would enable the direct measurement of zero-field splitting parameters, for example in gadolinium-based samples.

Beyond EPR, the same broadband architecture is directly applicable to ferromagnetic resonance (FMR) which is used to study magnetic thin films that play a key role in data storage and magnetic memory technologies. EPR and FMR share a common physical origin and can be investigated with the same experimental setup but FMR is governed by the collective dynamics of strongly exchange-coupled spins, in contrast to EPR, which probes resonances of weakly interacting paramagnetic spin ensembles [CP21].

Compared to paramagnetic samples, ferromagnetic materials exhibit an internal effective field that arises from exchange and anisotropy effects and can be stronger than the externally applied magnetic field. In FMR, broadband operation is essential for locating the resonance of a given sample and characterizing its frequency dependence. From the resulting frequency-dependent linewidth, the magnetic damping factor, which governs device speed and efficiency, can be extracted [MK15]. A homogeneous microwave field is crucial for the accurate interpretation of these experimental results, which makes

the inverted microstrip structure a promising candidate for future broadband FMR studies.

Finally, the degree of integration should be explored. A fully monolithic spectrometer could improve efficiency by eliminating interconnect losses, reducing system cost, and enabling operation at higher microwave frequencies. Alternatively, a modular architecture based on individually packaged components may offer increased robustness and greater flexibility to accommodate different sample environments. Evaluating these two strategies will help define the most practical route toward scalable and user-friendly integrated spectrometers.

Declarations

The author declares that the findings reported in this manuscript are the result of her original research. The manuscript's clarity and language have been enhanced with the assistance of AI-based tools, including generative AI.

A Details on Detector Biasing

Detailed values for the supply voltages and operating points are provided for the optimization of the design of the detector. In addition, the specific values for the base supply voltage V_{bb} are listed for the characterization of the lumped and distributed detector for the determination of the NEM.

A.1 Optimization

The optimization of the detector is described in Section 5.2.4. This section provides specific details about the optimal supply voltage and operating points used for various presented results.

Number of Fingers

In Fig. 5.8b, the input reflection coefficient is presented for various transistor fingers. The optimal operating point chosen for each number of transistor fingers is listed in Tab. A.1.

Table A.1: Choice of supply voltages and operating point for results shown in Fig. 5.8b.

N_x	$I_{c,bias}$	V_{bb}	V_{cc}	V_{be}	V_{ce}
	in µA	in V	in V	in V	in V
1	150	1.605	1.475	0.803	1.4
2	200	1.580	1.500	0.790	1.4
4	250	1.550	1.525	0.775	1.4
8	250	1.515	1.525	0.758	1.4

Number of Stages

In Fig. 5.10a, the influence of the number of stages of the distributed detector design on the NEP and P_{dc} are discussed. The choice of the optimal supply voltages and operating points for each stage is listed in Tab. A.2.

Table A.2: Choice of supply voltages and operating point for different number of stages of the distributed detector design.

X_s	$I_{bb,bias}$	$I_{cc,bias}$	V_{bb}	V_{cc}	V_{be}	V_{ce}
	in mA	in µA	in V	in V	in V	in V
1	7.88	200	1.579	1.500	0.776	1.4
2	7.74	250	1.552	1.525	0.757	1.4
4	7.55	250	1.514	1.525	0.746	1.4
6	7.45	250	1.492	1.525	0.746	1.4
8	7.37	250	1.477	1.525	0.739	1.4
10	7.31	250	1.465	1.525	0.733	1.4
12	7.26	250	1.455	1.525	0.728	1.4

A.2 Measurements of the NEM

Tab. A.3 shows the values for V_{bb} for the determination of the NEM as a function of the input power shown in Fig. 5.23a. The values are chosen so that the collector supply current of 100 µA and 350 µA are achieved for the lumped and distributed detector, respectively. The frequency is chosen to be $f_0 = 10\,\text{GHz}$.

Table A.3: Choice of V_{bb} for input power sweep to determine NEM.

	Lump. det.	Distr. det.
P_0 in dBm	V_{bb} in V	V_{bb} in V
−33	1.541	1.484
−27	1.539	1.482
−21	1.530	1.473
−15	1.500	1.443
−9	1.415	1.360
−3	1.221	1.171
3	0.809	0.771
9	−0.039	−0.049

In Tab. A.4, the values for V_{bb} are shown for the NEM as a function of carrier frequency shown in Fig. 5.23b. The values are chosen so that the collector supply current of 100 µA and 350 µA are achieved for the lumped and distributed detector, respectively. The input power is chosen to be $P_0 = -30\,\text{dBm}$.

Table A.4: Choice of V_{bb} for the frequency sweep to determine NEM.

	Lump. det.	Distr. det.
f_0 in GHz	V_{bb} in V	V_{bb} in V
1	0.839	0.712
5	0.804	0.735
10	0.809	0.771
15	0.817	0.814
20	0.829	0.856
25	0.843	0.890
30	0.859	0.916
35	0.876	0.935
40	0.894	0.954
45	0.913	0.961
50	0.933	0.968
55	0.953	0.973
60	0.972	0.975
65	0.991	0.974
70	1.010	0.974
75	1.027	0.985
80	1.044	0.971
85	1.061	0.963
90	1.077	0.963
95	1.091	0.973
100	1.105	0.991
105	1.118	1.014
110	1.131	1.040

Bibliography

[AAB12] Jens Anders, Alexander Angerhofer, and Giovanni Boero. K-band single-chip electron spin resonance detector. *Journal of Magnetic Resonance*, 217:19–26, 2012.

[AFAS15] Faisal Ahmed, Muhammad Furqan, Klaus Aufinger, and Andreas Stelzer. Compact broadband amplifiers with up to 105 GHz bandwidth in SiGe BiCMOS. In *2015 IEEE Radio Frequency Integrated Circuits Symposium (RFIC)*, pages 3–6. IEEE, 2015.

[AL19] Jens Anders and Klaus Lips. MR to go. *Journal of Magnetic Resonance*, 306:118–123, 2019.

[Ale21] Mehdi Alem. Noise spectral density measured with lock-in amplifiers, 2021. `https://www.zhinst.com/ch/de/blogs/noise-spectral-density-measured-lock-amplifiers`. Accessed: 2025-02-19.

[ATL23] Ohara Augusto, Daniela Ramos Truzzi, and Edlaine Linares. Electron paramagnetic resonance (EPR) for investigating relevant players of redox reactions: Radicals, metalloproteins and transition metal ions. *Redox Biochemistry and Chemistry*, 5:100009, 2023.

[Bar03] R. C. Barklie. Characterisation of defects in amorphous carbon by electron paramagnetic resonance. *Diamond and Related Materials*, 12:1427–1434, 2003.

[BC93] R L Belford and R B Clarkson. *Multifrequency Electron Paramagnetic Resonance Spectroscopy*, volume 229. American Chemical Society, 1993.

[BHL+12] Ilja N Bronstein, Juraj Hromkovic, Bernd Luderer, Hans-Rudolf Schwarz, Jochen Blath, Alexander Schied, Stephan Dempe, Gert Wanka, and Siegfried Gottwald. *Taschenbuch der Mathematik*, volume 1. Springer-Verlag, 2012.

[Boh24] Christian Bohn. *Broadband Circuits for High-Speed Short Reach Optical Transceivers*. PhD thesis, Karlsruhe Institute of Technology, 2024.

[Bre] Ben Breeze. EPR spectrometers. `https://warwick.ac.uk/research/~rtp/spectroscopy/epr/eprspectrometers/`. Accessed 2025-10-19.

[Bro03] Elliott R. Brown. Fundamentals of terrestrial millimeter-wave and THz remote sensing. *International Journal of High Speed Electronics and Systems*, 2003.

[Bru07] Andrew S Brush. Measurement of microwave power. *IEEE Instrumentation & Measurement Magazine*, 10:20–25, 2007.

[BS83] Richard Bramley and Steven J Strach. Electron paramagnetic resonance spectroscopy at zero magnetic field. *Chemical Reviews*, 83:49–82, 1983.

[CBK+13] Conrad Clauss, Daniel Bothner, Dieter Koelle, Reinhold Kleiner, Lapo Bogani, Marc Scheffler, and Martin Dressel. Broadband electron spin resonance from 500 MHz to 40 GHz using superconducting coplanar waveguides. *Applied Physics Letters*, 102, 2013.

[CCM16] Victor Chechik, Emma Carter, and Damien Murphy. *Electron Paramagnetic Resonance*. Oxford University Press, USA, 2016.

[CKK+23] Anh Chu, Michal Kern, Khubaib Khan, Klaus Lips, and Jens Anders. A 263 GHz 32-channel EPR-on-a-chip injection-locked VCO-array. In *2023 IEEE International Solid-State Circuits Conference (ISSCC)*, pages 318–320. IEEE, 2023.

[Col07] Robert E. Collin. *Foundations for Microwave Engineering*. John Wiley & Sons, Inc., 2007.

[CP21] Michael Coey and Stuart S. P. Parkin. *Handbook of Magnetism and Magnetic Materials*. Springer, 2021.

[CSB13] Charles Chen, Payam Seifi, and Aydin Babakhani. A silicon-based, fully integrated pulse electron paramagnetic resonance system for mm-wave spectroscopy. In *2013 IEEE MTT-S International Microwave Symposium (IMS)*. IEEE, 2013.

[CSL+18] Anh Chu, Benedikt Schiecker, Klaus Lips, Maurits Ortmanns, and Jens Anders. An 8-channel 13 GHz ESR-on-a-chip injection-locked VCO-array achieving 200 µm-concentration sensitivity.

In *2018 IEEE International Solid-State Circuits Conference (ISSCC)*, volume 61, pages 354–356. IEEE, 2018.

[CSW17] Zhe Chen, Jiwei Sun, and Pingshan Wang. Broadband ESR spectroscopy with a tunable interferometer. *IEEE Transactions on Magnetics*, 53, 2017.

[DBK+24] Sadegh Rajabi Doulataabadi, Seyed Hossein Hosseini Biuki, Farid Khoshkhati, Seyed Abbas Jazayeri Moghadas, Mohammad Masoudi Mohammadi, and Mehdi Ahmadi-Boroujeni. Design and fabrication of a microstrip phase shifter based on liquid crystal. In *2024 32nd International Conference on Electrical Engineering (ICEE)*. IEEE, 2024.

[Dic46] Robert Henry Dicke. The measurement of thermal radiation at microwave frequencies. *Review of Scientific Instruments*, 17:268–275, 1946.

[DNC+90] I. Dale, S. Neylon, A. Condie, M. Hobden, and M. J. Kearney. The 1/f noise performance of GaAs planar doped barrier mixed diodes. In *1990 20th European Microwave Conference*. IEEE, 1990.

[EAR19] Omar El-Aassar and Gabriel M. Rebeiz. A DC to 108 GHz CMOS SOI distributed power amplifier and modulator driver leveraging multi-drive complementary stacked cells. *IEEE Journal of Solid-State Circuits*, 54:3437–3451, 2019.

[EE12] Sandra S. Eaton and Gareth R. Eaton. The world as viewed by and with unpaired electrons. *Journal of Magnetic Resonance*, 223:151–163, 10 2012.

[EEBW10] Gareth R. Eaton, Sandra S. Eaton, David P. Barr, and Ralph T. Weber. *Quantitative EPR*. Springer Science & Business Media, 2010.

[Ell07] Frank Ellinger. *Radio Frequency Integrated Circuits and Technologies*. Springer-Verlag, 2007.

[Eri66] Lynden E Erickson. Electron-paramagnetic-resonance absorption by trivalent neodymium ions in single crystals of lanthanum trichloride and lanthanum ethyl sulphate in zero magnetic field. *Physical Review*, 143, 1966.

[ETF96] Keith A Earle, Dmitriy S Tipikin, and Jack H Freed. Far-infrared electron-paramagnetic-resonance spectrometer utilizing

a quasioptical reflection bridge. *Review of Scientific Instruments*, 1996.

[Fan50] Robert Mario Fano. Theoretical limitations on the broadband matching of arbitrary impedances. *Journal of the Franklin Institute*, 249, 1950.

[Feh56] George Feher. Sensitivity considerations in microwave paramagnetic resonance absorption techniques. *The Bell System Technical Journal*, 36, 1956.

[FLB16] Kelvin Fang, Cooper S. Levy, and James F. Buckwalter. Supply-scaling for efficiency enhancement in distributed power amplifiers. *IEEE Journal of Solid-State Circuits*, 51:1994–2005, 2016.

[FM82] Piotr Fajer and Derek Marsh. Microwave and modulation field inhomogeneities and the effect of cavity Q in saturation transfer ESR spectra. Dependence on sample size. *Journal of Magnetic Resonance*, 1982.

[FM98] Keng Leong Fong and Robert G. Meyer. High-frequency nonlinearity analysis of common-emitter and differential-pair transconductance stages. *IEEE Journal of Solid-State Circuits*, 33, 1998.

[GAS+14] Gabriele Gualco, Jens Anders, Andrzej Sienkiewicz, Stefano Alberti, László Forró, and Giovanni Boero. Cryogenic single-chip electron spin resonance detector. *Journal of Magnetic Resonance*, 247:96–103, 2014.

[GFWK12] Ahmed Gharib, Georg Fischer, Robert Weigel, and Dietmar Kissinger. A broadband 1.35 THz GBP 120 mW common-collector feedback amplifier in SiGe technology. In *2012 IEEE Bipolar/BiCMOS Circuits and Technology Meeting (BCTM)*. IEEE, 2012.

[GJH11] Leland Gilreath, Vipul Jain, and Payam Heydari. Design and analysis of a W-band SiGe direct-detection-based passive imaging receiver. *IEEE Journal of Solid-State Circuits*, 46:2240–2252, 2011.

[GM06] Eugenio Garribba and Giovanni Micera. Determination of the hyperfine coupling constant and zero-field splitting in the ESR

spectrum of Mn2+ in calcite. *Magnetic Resonance in Chemistry*, 44:11–19, 2006.

[GS18] Daniella Goldfarb and Stefan Stoll. *EPR spectroscopy: Fundamentals and Methods*. John Wiley & Sons, Inc., 2018.

[GZV+16] Jéssica Gutiérrez, Kaoutar Zeljami, Enrique Villa, Beatriz Aja, Maria Luisa De La Fuente, Sergio Sancho, and Juan Pablo Pascual. Noise conversion of schottky diodes in mm-wave detectors under different nonlinear regimes: Modeling and simulation versus measurement. *International Journal of Microwave and Wireless Technologies*, 8:479–493, 2016.

[Hag13] Wilfred R. Hagen. Broadband transmission EPR spectroscopy. *PLoS ONE*, 8, 3 2013.

[Hag19] Wilfred R. Hagen. Broadband tunable electron paramagnetic resonance spectroscopy of dilute metal complexes. *Journal of Physical Chemistry A*, 123:6986–6995, 2019.

[Hag23] Wilfred R. Hagen. Conversion of a single-frequency X-band EPR spectrometer into a broadband multi-frequency 0.1–18 GHz instrument for analysis of complex molecular spin hamiltonians. *Molecules*, 28, 2023.

[HC07] Jeffrey L. Hesler and Thomas W. Crowe. Responsivity and noise measurements of zero-bias schottky diode detectors. In *18th International Symposium on Space Terahertz Technology*, 2007.

[HGHP13] Richard Al Hadi, Janusz Grzyb, Bernd Heinemann, and Ullrich R. Pfeiffer. A terahertz detector array in a SiGe HBT technology. *IEEE Journal of Solid-State Circuits*, 48:2002–2010, 2013.

[HHL04] Chris D. Holdenried, James W. Haslett, and Michael W. Lynch. Analysis and design of HBT cherry-hooper amplifiers with emitter-follower feedback for optical communications. *IEEE Journal of Solid-State Circuits*, 39:1959–1967, 2004.

[HKC+22] Mohamed Atef Hassan, Michal Kern, Anh Chu, Gatik Kalra, Ekaterina Shabratova, Aleksei Tsarapkin, Neil Mackinnon, Klaus Lips, Christian Teutloff, Robert Bittl, Jan Gerrit Korvink, and Jens Anders. Towards single-cell pulsed EPR using VCO-based EPR-on-a-chip detectors. *Frequenz*, 76:699–717, 2022.

[Hoo94] F. N. Hooge. 1/f noise sources. *IEEE Transactions on Electron Devices*, 41, 1994.

[HSM19] James S. Hyde, Jason W. Sidabras, and Richard R. Mett. Uniform field resonators for EPR spectroscopy: A review. *Cell Biochemistry and Biophysics*, 77:3–14, 2019.

[HSW+16] Jonas Handwerker, Benedikt Schlecker, Ulrich Wachter, Peter Radermacher, Maurits Ortmanns, and Jens Anders. A 14 GHz battery-operated point-of-care ESR spectrometer based on a 0.13 µm CMOS ASIC. In *2016 IEEE International Solid-State Circuits Conference (ISSCC)*, volume 59, pages 476–477. IEEE, 2016.

[Ins23] Zurich Instruments. Principles of lock-in detection and the state-of-the-art. Technical report, 2023. `https://www.zhinst.com/sites/default/files/documents/2023-04/zi_whitepaper_principles_of_lock-in_detection_0.pdf`. Accessed: 2025-07-10.

[IUM+08] J. Isoya, T. Umeda, N. Mizuochi, N. T. Son, E. Janzén, and T. Ohshima. EPR identification of intrinsic defects in SiC. *Physica Status Solidi (B) Basic Research*, 245:1298–1314, 2008.

[JGW20] Rolf Jakoby, Alexander Gaebler, and Christian Weickhmann. Microwave liquid crystal enabling technology for electronically steerable antennas in SATCOM and 5G millimeter-wave systems. *Crystals*, 10:1–56, 2020.

[JHPB74] B. Johansson, S. Haraldson, L. Pettersson, and O. Beckman. A stripline resonator for ESR. *Review of Scientific Instruments*, 45:1445–1447, 1974.

[JLS+19] Ke Jing, Ziheng Lan, Zhifu Shi, Shiwei Mu, Xi Qin, Xing Rong, and Jiangfeng Du. Broadband electron paramagnetic resonance spectrometer from 1 to 15 GHz using metallic coplanar waveguide. *Review of Scientific Instruments*, 90, 2019.

[JNL+96] Jinjie Jiang, Toshiaki Nakashima, Ke Jian Liu, Fuminori Goda, Toshi Shima, and Harold M Swartz. Measurement of pO2 in liver using EPR oximetry. *Journal of Applied Physiology*, 1996.

[JSC+08] Z. H. Jang, B. J. Suh, M. Corti, L. Cattaneo, D. Hajny, F. Borsa, and M. Luban. Broadband electron spin resonance

at low frequency without resonant cavity. *Review of Scientific Instruments*, 79, 2008.

[KB09] Joohwa Kim and James F. Buckwalter. A DC–102 GHz broadband amplifier in 0.12 µm SiGe BiCMOS. In *2009 IEEE Radio Frequency Integrated Circuit Symposium (RFIC)*. IEEE, 2009.

[KCD+06] Martin Kopáni, Peter Celec, Luboš Danišovič, Peter Michalka, and Csaba Biró. Oxidative stress and electron spin resonance. *Clinica Chimica Acta*, 364:61–66, 2006.

[Kel25] Timothy J. Keller. Demystifying phase noise. *EPR Newsletter*, 35:32–33, 2025. `https://ieprs.org/wp-content/uploads/2025/05/eprnl.3512.pdf`. Accessed: 2025-07-10.

[KFHF+23] Gyan Khatri, Gregory Fritjofson, Jacob Hanson-Flores, Jaesuk Kwon, and Enrique Del Barco. A 220 GHz–1.1 THz continuous frequency and polarization tunable quasi-optical electron paramagnetic resonance spectroscopic system. *Review of Scientific Instruments*, 94, 2023.

[KGY+20] Hamza Kandis, Berke Gungor, Melik Yazici, Mehmet Kaynak, and Yasar Gurbuz. A 0.9 mW compact power detector with 30 dB dynamic range for automotive radar applications. In *2020 IEEE 63rd International Midwest Symposium on Circuits and Systems (MWSCAS)*. IEEE, 2020.

[KSE11] Christian Knochenhauer, Behnam Sedighi, and Frank Ellinger. A comparative analysis of peaking methods for output stages of broadband amplifiers. *IEEE Transactions on Circuits and Systems I: Regular Papers*, 58:2581–2589, 2011.

[Lee76] Young-Hoon Lee. EPR studies of defects in electron-irradiated silicon: A triplet state of vacancy-oxygen complexes. *Physical Review B*, 13, 1976.

[Lee04] Thomas H. Lee. *The Design of CMOS Radio-Frequency Integrated Circuits*. Cambridge University Press, 2nd edition, 2004.

[LZK16] Jinlin Liu, Ashraf Uz Zaman, and Per-Simon Kildal. Design of transition from WR-15 to inverted microstrip gap waveguide. In *Global Symposium on Millimeter Waves (GSMM) & ESA*

Workshop on Millimetre-Wave Technology and Applications. IEEE, 2016.

[MCB86] H. Mahdjour, W. G. Clark, and K. Baberschke. High-sensitivity broadband microwave spectroscopy with small nonresonant coils. *Review of Scientific Instruments*, 57:1100–1106, 1986.

[MDS20] Björn Miksch, Martin Dressel, and Marc Scheffler. Cryogenic frequency-domain electron spin resonance spectrometer based on coplanar waveguides and field modulation. *Review of Scientific Instruments*, 91, 2020.

[MGJ+17] Alessandro V. Matheoud, Gabriele Gualco, Minki Jeong, Ivica Zivkovic, Jürgen Brugger, Henrik M. Rønnow, Jens Anders, and Giovanni Boero. Single-chip electron spin resonance detectors operating at 50 GHz, 92 GHz, and 146 GHz. *Journal of Magnetic Resonance*, 278:113–121, 2017.

[Mis11] Sushil K. Misra. *Multifrequency Electron Paramagnetic Resonance: Theory and Applications*. John Wiley & Sons, Inc., 2011.

[MK15] Ivan S. Maksymov and Mikhail Kostylev. Broadband stripline ferromagnetic resonance spectroscopy of ferromagnetic films, multilayers and nanostructures. *Physica E*, 69:253–293, 2015.

[MK25] Thorsten Maly and Timothy J. Keller. Instrumentation for high-field dynamic nuclear polarization and electron paramagnetic resonance spectroscopy. *European Physical Journal A*, 61, 2025.

[MMS+05] Atsuko Matsumoto, Shingo Matsumoto, Anastasia L. Sowers, Janusz W. Koscielniak, Nancy J. Trigg, Periannan Kuppusamy, James B. Mitchell, Sankaran Subramanian, Murali C. Krishna, and Ken Ichiro Matsumoto. Absolute oxygen tension (pO2) in murine fatty and muscle tissue as determined by EPR. *Magnetic Resonance in Medicine*, 54:1530–1535, 2005.

[MR10] Jason W. May and Gabriel M. Rebeiz. Design and characterization of W-band SiGe RFICs for passive millimeter-wave imaging. In *IEEE Transactions on Microwave Theory and Techniques*, volume 58, pages 1420–1430. IEEE, 2010.

[MS16] E.S. Malotaux and M. Spirito. Characterization of broadband low-NEP SiGe square-law detectors for mm-wave passive

imaging. In *2016 IEEE MTT-S International Microwave Symposium (IMS)*. IEEE, 2016.

[MSB18] Alessandro V. Matheoud, Nergiz Sahin, and Giovanni Boero. A single chip electron spin resonance detector based on a single high electron mobility transistor. *Journal of Magnetic Resonance*, 294:59–70, 2018.

[NBM+18] P. Neugebauer, D. Bloos, R. Marx, P. Lutz, M. Kern, D. Aguilà, J. Vaverka, O. Laguta, C. Dietrich, R. Clérac, and J. Van Slageren. Ultra-broadband EPR spectroscopy in field and frequency domains. *Physical Chemistry Chemical Physics*, 20:15528–15534, 2018.

[NCG+23] Kyriaki Niotaki, Nuno Borges Carvalho, Apostolos Georgiadis, Xiaoqiang Gu, Simon Hemour, Ke Wu, Diogo Matos, Daniel Belo, Ricardo Pereira, Ricardo Figueiredo, Henrique Chaves, Bernardo Mendes, Ricardo Correia, Arnaldo Oliveira, Valentina Palazzi, Federico Alimenti, Paolo Mezzanotte, Luca Roselli, Francesca Benassi, Alessandra Costanzo, Diego Masotti, Giacomo Paolini, Aline Eid, Jimmy Hester, Manos M. Tentzeris, and Naoki Shinohara. RF energy harvesting and wireless power transfer for energy autonomous wireless devices and RFIDs. *IEEE Journal of Microwaves*, 3:763–782, 2023.

[NHBS17] Joscha Nehrkorn, Karsten Holldack, Robert Bittl, and Alexander Schnegg. Recent progress in synchrotron-based frequency-domain fourier-transform THz-EPR. *Journal of Magnetic Resonance*, 280:10–19, 2017.

[NOW+25] Mark Johannes Neff, Burak Gueven Oezat, Janis Nikolai Woermann, Prakhar Singhal, Benjamin Schoch, and Ingmar Kallfass. 2.5 to 64 GHz nonuniform distributed power detector in 130nm SiGe BiCMOS. In *2025 20th European Microwave Integrated Circuits Conference (EuMIC)*. IEEE, 2025.

[OIH+23] Kaisarbek Omirzakhov, Mohamad Hossein Idjadi, Tzu Yung Huang, S. Alex Breitweiser, David A. Hopper, Lee C. Bassett, and Firooz Aflatouni. An integrated reconfigurable spin control system on 180 nm CMOS for diamond NV centers. *IEEE Transactions on Microwave Theory and Techniques*, 71:4052–4063, 2023.

[OOTO21] Eiji Ohmichi, Tsubasa Okamoto, Hideyuki Takahashi, and Hitoshi Ohta. Mechanically detected terahertz electron spin resonance. *Applied Magnetic Resonance*, 52:283–304, 2021.

[PDM+25] Lukasz Polewski, Daria Dymnikova, Weronika Malicka, Maike Lettow, Gert von Helden, Christian Teutloff, Matthias Ballauff, Matthias Taupitz, Robert Bittl, and Kevin Pagel. Glycan-induced transchelation of gadolinium from magnetic resonance imaging contrast agent-complexes. *Analytical Chemistry*, 97:11436–11442, 2025.

[Poo96] Charles P.. Poole. *Electron Spin Resonance: A Comprehensive Treatise on Experimental Techniques*. Dover Publications, 1996.

[Poz21] David M. Pozar. *Microwave Engineering*. John Wiley & Sons, Inc., 4th edition, 2021.

[PS08] John G. Proakis and Masoud Salehi. *Digital Communications*. McGraw-Hill, 5th edition, 2008.

[PWK+04] W Perndl, W Wilhelm, H Knapp, M Wurzer, K Aufinger, T F Meister, J Böck, W Simbürger, and A L Scholtz. A 60 GHz broadband amplifier in SiGe bipolar technology. In *IEEE BCTM 15.4*. IEEE, 2004.

[PZZ+22] Haofeng Peng, Yongwei Zhang, Senlai Zhu, Murat Temiz, and Ahmed El-Makadema. Determining dielectric properties of nematic liquid crystals at microwave frequencies using inverted microstrip lines. *Liquid Crystals*, 49:2069–2081, 2022.

[QN17a] Saad Qayyum and Renato Negra. 0.16 mW, 7–70 GHz distributed power detector with 75 dB voltage sensitivity in 130 nm standard CMOS technology. In *2017 12th European Microwave Integrated Circuits Conference (EuMIC)*, pages 13–16. IEEE, 2017.

[QN17b] Saad Qayyum and Renato Negra. 0.8 mW, 0.1-110 GHz RF power detector with 6 GHz video bandwidth for multigigabit software defined radios. In *2017 IEEE MTT-S International Microwave Symposium (IMS)*. IEEE, 2017.

[QN18] Saad Qayyum and Renato Negra. Analysis and design of distributed power detectors. *IEEE Transactions on Microwave Theory and Techniques*, 66:4191–4203, 2018.

[Raz12a] Behzad Razavi. *Design of Integrated Circuits for Optical Communications*. John Wiley & Sons, Inc., 2012.

[Raz12b] Behzad Razavi. *RF Microelectronics*, volume 2. Pearson Education, 2012.

[RHF12] Holger Rücker, Bernd Heinemann, and Alexander Fox. Half-terahertz SiGe BiCMOS technology. In *2012 IEEE Topical Meeting on Silicon Monolithic Integrated Circuits in RF Systems (SiRF)*. IEEE, 2012.

[RS18] Maxie M. Roessler and Enrico Salvadori. Principles and applications of EPR spectroscopy in the chemical sciences. *Chemical Society Reviews*, 47:2534–2553, 2018.

[RSM+24] Sofia Rustioni, Lorenzo Silvestri, Stefania Marconi, Gianluca Alaimo, Ferdinando Auricchio, and Maurizio Bozzi. A dielectric permittivity sensor based on inverted microstrip/3D-printing hybrid technology. In *2024 IEEE MTT-S International Microwave Symposium (IMS)*, pages 883–886. IEEE, 2024.

[SA82] Rainee Navin Simons and Rajendra K Arora. Coupled slot line field components. *IEEE Transactions on Microwave Theory and Techniques*, 1982.

[SAA+19] Pragya R. Shrestha, Nandita Abhyankar, Mark A. Anders, Kin P. Cheung, Robert Gougelet, Jason T. Ryan, Veronika Szalai, and Jason P. Campbell. Nonresonant transmission line probe for sensitive interferometric electron spin resonance detection. *Analytical Chemistry*, 91:11108–11115, 9 2019.

[SBL+09] Alexander Schnegg, Jan Behrends, Klaus Lips, Robert Bittl, and Karsten Holldack. Frequency domain fourier transform THz-EPR on single molecule magnets using coherent synchrotron radiation. *Physical Chemistry Chemical Physics*, 11:6553–6554, 2009.

[SDS10] C. Schlegel, M. Dressel, and J. Van Slageren. Broadband electron spin resonance at 4–40 GHz and magnetic fields up to 10 T. *Review of Scientific Instruments*, 81, 2010.

[SG51] Abraham Savitzky and Marcel J.E. Golay. Smoothing and differentiation of data by simplified least squares procedures. *Analytical Chemistry*, 40:1832, 1951.

[She13] Hani Mahmoud Sherry. *Terahertz Circuits and Systems in CMOS*. PhD thesis, University of Wuppertal, Germany, 2013.

[SMV+20] Victoria N. Syryamina, Anna G. Matveeva, Yan V. Vasiliev, Anton Savitsky, and Yuri A. Grishin. Improving B_1 field homogeneity in dielectric tuberesonators for EPR spectroscopy via controlled shaping of the dielectric insert. *Journal of Magnetic Resonance*, 311, 2020.

[SS06] Stefan Stoll and Arthur Schweiger. Easyspin, a comprehensive software package for spectral simulation and analysis in EPR. *Journal of Magnetic Resonance*, 178:42–55, 2006.

[SSCG21] Adel S. Sedra, Kenneth C. Smith, Tony Chan Carusone, and Vincent C. Gaudet. *Microelectronic Circuits*. Oxford University Press, 2021.

[SVG+03] J. Van Slageren, S. Vongtragool, B. Gorshunov, A. A. Mukhin, N. Karl, J. Krzystek, J. Telser, A. Müller, C. Sangregorio, D. Gatteschi, and M. Dressel. Frequency-domain magnetic resonance spectroscopy of molecular magnetic materials. *Physical Chemistry Chemical Physics*, 5:3837–3843, 2003.

[SW98] M. Seck and P. Wyder. A sensitive broadband high-frequency electron spin resonance/electron nuclear double resonance spectrometer operating at 5–7.5 mm wavelength. *Review of Scientific Instruments*, 69:1817–1822, 1998.

[SWQS24] Jui Hung Sun, Difei Wu, Peter Qin, and Constantine Sideris. Design and implementation of integrated dual-mode pulse and continuous-wave electron paramagnetic resonance spectrometers. *IEEE Transactions on Biomedical Circuits and Systems*, 18:1209–1219, 2024.

[SWYGG24] Zeng Hui Shi, Feng Wei, Li Yang, and Roberto Gomez-Garcia. High-selectivity inverted microstrip gap waveguide bandpass filter using hybrid cavity and stub-loaded ring resonant modes. *IEEE Transactions on Circuits and Systems II: Express Briefs*, 71:146–150, 2024.

[TBP+15] Paolo Valerio Testa, Guido Belfiore, Robert Paulo, Corrado Carta, and Frank Ellinger. 170 GHz SiGe-BiCMOS loss-compensated distributed amplifier. *IEEE Journal of Solid-State Circuits*, 50:2228–2238, 2015.

[TCC+09] C. C. Tsai, J. Choi, Sunglae Cho, S. J. Lee, B. K. Sarma, C. Thompson, O. Chernyashevskyy, I. Nevirkovets,

and J. B. Ketterson. Microwave absorption measurements using a broadband meanderline approach. *Review of Scientific Instruments*, 80, 2009.

[TCE16] Paolo Valerio Testa, Corrado Carta, and Frank Ellinger. Analysis and design of a 220 GHz wideband SiGe BiCMOS distributed active combiner. *IEEE Transactions on Microwave Theory and Techniques*, 64:3049–3059, 2016.

[TCYG20] Esref Turkmen, Barbaros Cetindogan, Melik Yazici, and Yasar Gurbuz. Design and characterization of a D-band SiGe HBT front-end for dicke radiometers. *IEEE Sensors Journal*, 20:4694–4703, 2020.

[TGV10] Alexander Tomkins, Patrice Garcia, and Sorin P. Voinigescu. A passive W-band imaging receiver in 65 nm bulk CMOS. *IEEE Journal of Solid-State Circuits*, 45:1981–1991, 2010.

[TKA+07] Saverio Trotta, Herbert Knapp, Klaus Anfinger, Thomas F. Meister, Josef Böck, Bernhard Dehlink, Werner Simbürger, and Arpad L. Scholtz. An 84 GHz bandwidth and 20 dB gain broadband amplifier in SiGe bipolar technology. In *IEEE Journal of Solid-State Circuits*, volume 42, pages 2099–2105, 2007.

[TS91] V. F. Tarasov and G. S. Shakurov. Applied magnetic resonance submillimetre EPR spectrometer. Technical report, 1991.

[TS13] Ulrich Tietze and Christopher Schenk. *Halbleiter-Schaltungstechnik*. Springer-Verlag, 2013.

[UR13] Mehmet Uzunkol and Gabriel M. Rebeiz. A low-noise 150–210 GHz detector in 45 nm CMOS SOI. *IEEE Microwave and Wireless Components Letters*, 23:309–311, 2013.

[UTB+20] Berktug Ustundag, Esref Turkmen, Abdurrahman Burak, Berke Gungor, Hamza Kandis, Barbaros Cetindogan, Melik Yazici, Mehmet Kaynak, and Yasar Gurbuz. Front-end blocks of a W-band dicke radiometer in SiGe BiCMOS technology. *IEEE Transactions on Circuits and Systems II: Express Briefs*, 67:2417–2421, 2020.

[VLG14] Leonardo Vera, John R. Long, and B. Jeffrey Gross. A low-power SiGe feedback amplifier with over 110 GHz bandwidth. In *2014 IEEE Bipolar/BiCMOS Circuits and Technology Meeting (BCTM)*, pages 1–4. IEEE, 2014.

[Voi13] Sorin Voinigescu. *High-frequency Integrated Circuits*. Cambridge University Press, 2013.

[VSZK00] S. Sendhil Velan, Richard G.S. Spencer, Jay L. Zweier, and Periannan Kuppusamy. Electron paramagnetic resonance oxygen mapping (EPROM): Direct visualization of oxygen concentration in tissue. *Magnetic Resonance in Medicine*, 43:804–809, 2000.

[WB07] John A. Weil and James R. Bolton. *Electron Paramagnetic Resonance: Elementary Theory and Practical Applications*. John Wiley & Sons, Inc., 2007.

[WCC+23] Yunshan Wang, Tzu Yang Chiu, Te Yen Chiu, Kai Jie Yu, Yu Min Teng, Guo Wei Huang, Chun Hsing Li, Chien Nan Kuo, Chau Ching Chiong, and Huei Wang. A Ka- to G-band detector with 5.5 GHz video bandwidth using a modified traveling-wave structure in 65 nm CMOS technology. *IEEE Transactions on Circuits and Systems II: Express Briefs*, 70:1371–1375, 2023.

[Wie72] Werner Wiesbeck. *Stromverteilung und Hochfrequenzeigenschaften der ungeschirmten Streifenleitung*. PhD thesis, 1972.

[Wil60] Ernest J Wilkinson. An n-way hybrid power divider. *IRE Transaction on Microwave Theory and Techniques*, 1960.

[WMI24] Yannick Wenger, Bernd Meinerzhagen, and Vadim Issakov. Built-in self-test of millimeter-wave integrated front-end circuits: How far have we come? *IEEE Access*, 12:78572–78588, 2024.

[WPTJ22] Dongwei Wang, Ersin Polar, Henning Tesmer, and Rolf Jakoby. Compact interference based microstrip single-pole double-throw utilizing liquid crystal phase shifter. In *2022 IEEE MTT-S International Microwave Symposium (IMS)*, pages 363–366. IEEE, 2022.

[WQN17] Muh-Dey Wei, Saad Qayyum, and Renato Negra. 0.01 GHz to 110 GHz distributed common-gate power detector in standard CMOS 65 nm technology. In *2017 IEEE MTT-S International Microwave Symposium (IMS)*, pages 634–637. IEEE, 2017.

[WSC+15] Yvonne Wiemann, Julian Simmendinger, Conrad Clauss, Lapo Bogani, Daniel Bothner, Dieter Koelle, Reinhold Kleiner, Martin Dressel, and Marc Scheffler. Observing electron spin resonance between 0.1 and 67 GHz at temperatures between 50 mK and

300 K using broadband metallic coplanar waveguides. *Applied Physics Letters*, 106, 2015.

[YB08] T. Yalcin and G. Boero. Single-chip detector for electron spin resonance spectroscopy. *Review of Scientific Instruments*, 79, 2008.

[YB15] Xuebei Yang and Aydin Babakhani. A single-chip electron paramagnetic resonance transceiver in 0.13 µm SiGe BiCMOS. *IEEE Transactions on Microwave Theory and Techniques*, 63:3727–3735, 2015.

[YB16] Xuebei Yang and Aydin Babakhani. A full-duplex single-chip transceiver with self-interference cancellation in 0.13 µm SiGe BiCMOS for electron paramagnetic resonance spectroscopy. *IEEE Journal of Solid-State Circuits*, 51:2408–2419, 2016.

[YE21] Roee Ben Yishay and Danny Elad. Low power 75–110 GHz SiGe dicke radiometer front-end. In *2021 IEEE MTT-S International Microwave Symposium (IMS)*, pages 885–887. IEEE, 2021.

[ZCP19] Magdalena Zdybel, Ewa Chodurek, and Barbara Pilawa. Application of EPR spectroscopy to determine the influence of simvastatin concentration on free radicals in A-375 human melanoma malignum cells. *Toxicology in Vitro*, 61, 2019.

[ZFB19] Dimitrios C. Zografopoulos, Antonio Ferraro, and Romeo Beccherelli. Liquid-crystal high-frequency microwave technology: Materials and characterization, 2019.

[ZN21] Luya Zhang and Ali M. Niknejad. An ultrasensitive 14 GHz 1.12 mW EPR spectrometer in 28 nm CMOS. *IEEE Microwave and Wireless Components Letters*, 31:819–822, 2021.

[ZUSC05] Xiaoliang Zhang, Kamil Ugurbil, Robert Sainati, and Wei Chen. An inverted-microstrip resonator for human head proton MR imaging at 7 tesla. *IEEE Transactions on Biomedical Engineering*, 52:495–504, 2005.

Own Publications

Journal Papers

[1] Selina Eckel, Julian Nagel, Mazin Jouda, Jan Gerrit Korvink, and Ahmet Çağrı Ulusoy. Design of planar transmission line microwave probes for broadband EPR spectroscopy. *Journal of Magnetic Resonance*, 374:107866, 2025.

[2] Selina Eckel, Matthias Oliver Beck, and Ahmet Çağrı Ulusoy. Microwave probe based on an inverted microstrip line for broadband electron paramagnetic resonance spectroscopy. *IEEE Microwave and Wireless Technology Letters*, 2026.

Conference Papers

[3] Selina Eckel and Ahmet Çağrı Ulusoy. Complex-valued signal recovery in interferometric electron paramagnetic resonance spectroscopy. In *2026 17th German Microwave Conference (GeMiC)*. IEEE, 2026.

[4] Selina Eckel and Ahmet Çağrı Ulusoy. Post-processing scheme for EPR spectroscopy based on planar microwave structures. In *2024 54th European Microwave Conference (EuMC)*, pages 309–312. IEEE, 2024.

[5] Selina Eckel and Ahmet Çağrı Ulusoy. Design of a SiGe BiCMOS broadband amplifier for an electron paramagnetic resonance spectrometer. In *2025 IEEE Texas Symposium on Wireless and Microwave Circuits and Systems, (TSWMCS)*, pages 1–4. IEEE, 2025.

[6] Selina Eckel and Ahmet Çağrı Ulusoy. Analysis of a SiGe BiCMOS detector for a broadband mmW-integrated EPR spectrometer. In *2024 IEEE 24th Topical Meeting on Silicon Monolithic Integrated Circuits in RF Systems (SiRF)*, pages 71–74. IEEE, 2024.